GEOLOGICA ULTRAIECTINA

Mededelingen van de
Faculteit Aardwetenschappen
Universiteit Utrecht

No. 113

RHEOLOGY OF SYNTHETIC ROCKSALT

with emphasis on the influence of deformation history and geometry on the flow behaviour

Raymond Franssen

GEOLOGICA ULTRAIECTINA

Mededelingen van de
Faculteit Aardwetenschappen
Universiteit Utrecht

No. 113

RHEOLOGY OF SYNTHETIC ROCKSALT

with emphasis on the influence of deformation history and geometry on the flow behaviour

Raymond Franssen

RHEOLOGY OF SYNTHETIC ROCKSALT

with emphasis on the influence of deformation history and geometry on the flow behaviour

Reologie van synthetisch steenzout

met de nadruk op de invloed van deformatie geschiedenis en geometrie op het vloeigedrag
(met een samenvatting in het Nederlands)

PROEFSCHRIFT

TER VERKRIJGING VAN DE GRAAD VAN DOCTOR AAN DE UNIVERSITEIT UTRECHT, OP GEZAG VAN RECTOR MAGNIFICUS, PROF. DR. J.A. VAN GINKEL, INGEVOLGE HET BESLUIT VAN HET COLLEGE VAN DEKANEN IN HET OPENBAAR TE VERDEDIGEN OP DINSDAG 23 NOVEMBER 1993, DES NAMIDDAGS TE 12.45 UUR

door

RAIMUNDUS CHRISTIANUS MARIA WILHELMUS FRANSSEN

Geboren op 20 februari 1959 te Heerlen

PROMOTOR: PROF. DR. S.H. WHITE
COPROMOTOR: DR. C.J. SPIERS

Hurrah for positive science! long live exact demonstration!
Fetch stonecrop mixt with cedar and branches of lilac,
This is the lexicographer, this the chemist, this made grammar of old cartouches,
These mariners put ship through dangerous unknown seas
This is the geologist, this works with the scalpel, and this is a mathematician.

Gentlemen, to you the first honours always!
Your facts are useful, and yet they are not my dwelling,
I but enter by them into an area of my dwelling.

Walt Whitman, Song of Myself (1881).

Vormgeving: Bert Janssen, Utrecht
Druk: Drukkerij Elinkwijk, Utrecht

CIP-GEGEVENS KONINKLIJKE BIBLIOTHEEK, DEN HAAG

Franssen, Raimundus Christianus Maria Wilhelmus

Rheology of synthetic rocksalt with emphasis on the influence of deformation history and geometry on the flow behaviour / Raimundus Christianus Maria Wilhelmus Franssen. - Utrecht: Faculteit Aardwetenschappen Universiteit Utrecht (Geologica Ultraiectina, ISSN 0072-1026; no. 113)
Proefschrift Universiteit Utrecht. - Met Lit. opg. - Met samenvatting in het Nederlands.
ISBN 90-71577-67-8
Trefw.: synthetisch steenzout; reologie.

CONTENTS

Chapter 4
DEFORMATION OF POLYCRYSTALLINE SALT IN COMPRESSION AND IN SHEAR AT 250-350 °C

Chapter 5
INFLUENCE OF DEFORMATION GEOMETRY ON THE FLOW BEHAVIOUR OF POLYCRYSTALLINE HALITE AT TEMPERATURES IN THE RANGE 250-600 °C

SUMMARY

The present study consists of an experimental investigation into the deformation behaviour of synthetic polycrystalline rocksalt (NaCl) in uniaxial compression and in simple shear. While there exists an extensive body of experimental work regarding the deformation behaviour of synthetic and natural rocksalt in compression, a number of important questions remains unanswered. In particular, though recognized that deformation history and geometry can strongly influence rheological behaviour and microstructural and texture development via so-called "memory' effects", such effects have not been systematically investigated. In addition, there still is widespread disagreement in the literature regarding the detailed dislocation creep mechanisms, rate-controlling processes and microstructural processes operating in polycrystalline NaCl.

This study aims at helping to resolve these questions. However, special attention is given to the influence of deformation geometry/history on the mechanical behaviour of rocksalt and to testing the validity of the assumptions underlying methods normally used to generalize experimentally obtained (axi-symmetric) flow laws, where stress and strain rate are treated as scalars, into forms suitable for 3-dimensional numerical modelling, where these quantities are treated as tensors. The results not only provide insight into the influence of deformation geometry and/or history on the deformation behaviour of NaCl, but allow general principles to be distilled that are also relevant to the effects of deformation geometry and history on the deformation behaviour of other rock-forming minerals.

In CHAPTER 1, the problems addressed in this thesis are introduced in detail, and the aims of the present study are defined.

This is followed in CHAPTER 2 with an investigation of the mechanical behaviour of synthetic rocksalt in uniaxial compression, in relation to microstructural evolution, crystallographic preferred orienta-

tion development and strain-rate history. To these ends, synthetic polycrystalline halite was deformed in uniaxial compression in the temperature range 250-780 °C (0.5-0.98 T_m) at strain rates between 10^{-3} and 10^{-7} s^{-1}, using both constant strain-rate and strain-rate stepping methods. At temperatures from 250 to 450 °C, the dominant mechanism of deformation was inferred to be climb-controlled dislocation creep, where climb is controlled by pipe diffusion through dislocation cores. The corresponding steady state flow law is given by:

$$\dot{\varepsilon} = 5.75 \exp(-129/RT)\, \sigma^{5.7}$$

where $\dot{\varepsilon}$ is the strain-rate, the pre-exponential constant is expressed in $MPa^{-n}s^{-1}$, the activation energy for creep is in kJ/mol, the temperature T is in K, the gas constant R is in kJ/Kmol and σ is the applied stress in MPa. At temperatures in the range 500 - 780 °C, the observed steady state flow behaviour follows an empirical creep equation given by:

$$\dot{\varepsilon} = 6.57 \times 10^7 \exp(-227/RT)\sigma^{4.4}$$

and was inferred to be dominated by lattice diffusion-controlled dislocation creep. With regard to microstructural development, in the temperature range 250-350 °C, polygonization and rotation recrystallization are the dominant microstructural processes. At higher temperatures, however, strain-induced grain-boundary migration becomes increasingly important. Interestingly, the transition from pipe to lattice diffusion-controlled creep coincides with the transition to migration recrystallization dominated microstructures. This is explained in relation to Derby's (1992) dynamic recrystallization model as due to relative changes of grain boundary mobility, nucleation rate and driving force, which allow a balance to be established between the migration rate of nucleated grains and the nucleation rate of new grains. Turning to the strain-rate history, below 450 °C this has a profound effect upon the observed microstructural development and mechanical behaviour, namely that stresses do not fall, and subgrain sizes do not increase, to the expected steady state values upon a lowering in strain-rate. This results in a relative hardening effect and in an increase of the stress sensitivity of strain rate to 7 - 10. Above 450 °C, however, the strain-rate history does not affect microstructural development and steady state behaviour is always attained because migration recrystallization is very efficient. Across the entire range of conditions investigated, the crystallographic preferred orientations developed during deformation show a strong tendency for the weaker $\{110\}\langle 1\bar{1}0\rangle$ slip planes to rotate perpendicu-

lar to the compression direction. The observed recrystallization processes appear to have no influence on the texture development.

CHAPTER 3 documents simple shear experiments carried out on the same salt starting material used for the uniaxial tests. The aim of the experiments was to gain insight into the mechanical behaviour, microstructural evolution and crystallographic preferred orientation development characterizing shear deformation. Both constant stress and constant strain-rate tests were performed at temperatures in the range 250 - 600 °C (0.5 - 0.8T_m), varying the imposed shear strain rates between 10^{-5} and 10^{-7} s^{-1} and the applied shear stress between 0.6 and 2.75 MPa. Expressed in terms of shear stress (τ) and shear strain rate ($\dot{\gamma}$), the steady state flow law obtained for the temperature range 250 - 450 °C is given:

$$\dot{\gamma} = 0.72 \exp(-93/RT)\, \tau^{5.2}$$

As in the uniaxial experiments, this lower temperature behaviour was inferred to represent pipe-diffusion controlled dislocation creep. However, at temperatures from 500-600 °C, the steady state flow law was characterized by the equation:

$$\dot{\gamma} = 2.65 \times 10^{8} \exp(-209/RT)\, \tau^{4.3}$$

In parallel with the results obtained in uniaxial compression for the same temperature range, this was inferred to describe lattice-diffusion controlled dislocation creep. As far as microstructural development is concerned, similar microstructural processes were also found to operate in shear, compared to those observed in the uniaxially shortened samples. Thus, polygonization and rotation recrystallization dominate microstructural development in the temperature range 250 - 365°C, whereas with increasing temperature, grain boundary migration becomes more important. The crystallographic preferred orientation developed under all conditions investigated in shear is characterised by an alignment of the {110} planes towards the flow plane and of the <111> direction parallel to the shear direction. However, while the preferred orientation pattern was found to be independent of deformation condition, the intensity of the {110} component increased above 500 °C.

In CHAPTER 4, a simple comparison of the results obtained in the uniaxial compression and simple shear experiments, between 250 and 350 °C, is presented. The mechanical behaviour seen in the two geo-

metries is compared in terms of equivalent stress and strain, as defined in the theory of perfect isotropic plasticity. For a given equivalent strain rate, the uniaxially deformed samples were found to be stronger in terms of equivalent flow stress. From a detailed consideration of the data, it is inferred that this difference in flow strength is largely due to the development of anisotropy during deformation, presumably in association with the observed texture development. The results thus suggest that the assumptions underlying the classical theory of isotropic plasticity and the standard "associative" methods of generalizing uniaxial flow data to 3-dimensions are not applicable for the conditions considered.

CHAPTER 5 aims at a more detailed and rigorous verification of the validity of the assumptions underlying the "associative" method of generalizing axisymmetric flow laws to 3-D. This is done for the temperature range 250-600 °C, using the extensive experimental datasets presented in Chapters 2 and 3. Following the approach adopted in Chapter 4, the mechanical behaviour and the flow laws obtained in uniaxial compression and shear are compared in terms of equivalent stress, strain and strain-rate, using the associated flow rule as defined in the theory of isotropic plasticity. Below 400 °C, i.e. in the pipe-diffusion controlled field, the equivalent stresses supported in shear are smaller than those in compression (at similar equivalent strain rate and temperatures) for all strains, from the initial work hardening stage of deformation through into the steady state stage. Thus, strain hardening is anisotropic at lower temperatures. However, at temperatures above 400-450 °C, in the lattice-diffusion controlled field, the strain hardening and steady state behaviour obtained in both test geometries is similar (isotropic). It is argued that the hardening behaviour is not necessarily unique and may depend on the number and combination of slip systems activated, which may in turn depend on the deformation mode imposed. Such behaviour has been observed in Cu polycrystals (Tomé et al., 1984) and similar mechanisms may also occur in polycrystalline halite. Texture simulations suggest that in general fewer slip systems are needed to accommodate an increment of simple shear compared to an increment of uniaxial compression, and this would imply fewer dislocation interactions in shear than in compression. At the same time, the slip systems activated in shear tend to be preferentially 'softer', and hence the flow stresses in shear will tend to be lower than in compression. The effects of these two processes is most pronounced at temperatures below 400 °C, where the three principal types of slip systems in halite have widely differing strengths, so that the single crystal

yield surface is highly anisotropic. In the pipe-diffusion controlled creep regime (250-450 °C), the flow law for compression is characterised by a significantly higher activation energy (129 kJ/mol) than the flow law for shear (93 kJ/mol). This is tentatively explained by variations in dislocation substructures developed in simple shear and compression as a result of the different activation of slip systems. In view of the anisotropic hardening and steady state flow behaviour observed at lower temperatures, it is concluded that the associated flow rule does not offer an adequate method of generalizing the creep behaviour of polycrystalline salt in the pipe-diffusion controlled dislocation creep field. However, dislocation creep laws reflecting lattice-diffusion control can be generalized using the associated flow rule. Notably, under geological conditions, the generalization of the pipe-diffusion controlled flow law for rocksalt using the associated flow rule, may lead to serious errors. Similarly, the generalization of the axi-symmetric deformation data of other rock forming minerals with highly anisotropic single crystal yield surfaces, that deform under conditions when pipe diffusion controls the dislocation creep rate or when recovery is limited and recrystallization suppressed, may also lead to serious errors if the associated flow rule is used.

The purpose of CHAPTER 6 is to draw together general conclusions, based on the findings presented in Chapter 2 to 5. In addition, questions which remain unanswered are identified and suggestions are made for further research.

INTRODUCTION: Definition of problems and aims

1.1 GENERAL BACKGROUND AND SCOPE

While halite (NaCl) is the principal constituent of evaporite deposits, it is of rather limited volumetric importance in the continental crust. Nonetheless, because of its low density ($2.2*10^3$ kg/m^3), unusually high ductility, and very low creep strength (resistance to plastic deformation) under crustal conditions, salt formations play an important and dramatic role in crustal tectonic processes. First, for example, layered salt formations often form major decollement horizons. Second, the density of salt, which varies little with depth, is lower than the density of most compacted sediments, and this often leads to gravitational instabilities giving rise to salt pillows and domes. In addition, salt formations often interact with extensional tectonic processes, and with sedimentation during basin evolution, giving rise to major structural and stratigraphic hydrocarbon traps. Last, the high ductility, the generally plastic behaviour, low permeability and low creep strength of salt, coupled with its easy mineability (conventional or solution), make stable salt formations attractive sites for disposal of radioactive and chemical wastes, and for the development of strategic storage caverns.

For these reasons, there has long been interest in the mechanical properties of rocksalt, and in the associated deformation mechanisms and microstructural development. Data on these are essential both for modelling natural salt flow and repository or storage cavern performance, and for interpreting structures and microstructures preserved in natural salt tectonites. Consequently, a great deal of experimental work has been done on the mechanical behaviour of both natural and synthetic rocksalt. In particular, the dislocation creep behaviour of natural and synthetic polycrystalline rocksalt has been investigated experimentally by numerous authors (Heard, 1972; Arieli et al., 1982; Burke et al,. 1981; Carter and Hansen, 1983; Wawersik and Zeuch, 1986; Horseman and Handin, 1990; Carter et al., 1993; Senseny, 1992), and it is well established that rocksalt deforms by dislocation creep mechanisms under laboratory, natural, and geotechnically relevant conditions

(e.g. Carter et al., 1993). During slow natural deformation, rocksalt can also deform by pressure solution mechanisms provided the brine content is in excess of ~0.01% (Spiers et al., 1990), such that both dislocation and pressure solution mechanisms are probably important in nature (Urai et al., 1986b; Spiers et al., 1990; Carter et al., 1993). In summary, the experiments performed to date have yielded both flow laws and palaeopiezometers for salt (Carter et al., 1993). In addition, considerable interest exists in salt as a rock analogue material, and numerous experiments have also been performed in this context (e.g. Guillopé and Poirier, 1979; Banerdt and Sammis, 1985, Chester, 1989; Shimamoto, 1989ab; Chester and Logan, 1990).

Despite the extensive experimental work referred to above, a number of important gaps have remained in our understanding of the deformation behaviour of rocksalt. In particular, while it is recognized that deformation geometry (i.e. mode of deformation) and history may strongly influence the deformation behaviour of salt in the dislocation creep field (i.e. memory effects), and indeed other geological materials (for example Wenk et al., 1986), this has not been systematically investigated or quantitatively evaluated in a useful manner. Furthermore, there still is widespread disagreement in the literature regarding the detailed dislocation creep mechanisms, rate controlling processes and microstructural processes operating in NaCl, and how/whether laboratory data can be extrapolated to natural and geotechnical relevant conditions (Senseny et al., 1992; Carter et al., 1993).

The research reported in this thesis is directed at helping to resolve these questions. In particular, attention is focused on developing a microphysically based understanding of the influence of deformation geometry and/or history on deformation behaviour and microstructural and textural development in NaCl under laboratory conditions, where dislocation creep is dominant. The results provide useful insight not only into NaCl, but general principles distilled are also relevant to the effect of deformation geometry and history on the deformation behaviour of other rock-forming minerals.

In the remainder of this chapter, the various questions to be addressed are elaborated upon, and the specific aims of the present work are defined.

1.2 THE ROLE OF SALT IN TECTONIC PROCESSES

As indicated above, rocksalt exerts an important control on the development of many tectonic structures in the Earth's crust. For example, it has long been recognized that thrusting is facilitated by the presence of evaporites. In fold-and-thrust belts such as the Salt Range of Pakistan and the Jura (Alps), a detachment in salt permits the development of long thrust sheets and broad thrust belts with very narrow cross-sectional tapers and no consistent vergence direction (Davis and Engelder, 1985, 1987; Butler et al., 1987). Salt detachments also extend the range of shortening deformation into the foreland. This can be observed in the Alpine foreland, for example, where Jura folding has developed over the Triassic Keuper, whereas in Bavaria, where the salt is missing, the Alpine thrust belt stops abruptly.

The role of salt tectonics in basin evolution and the associated development of hydrocarbon accumulations is manifold and of economic importance. It is controlled by the interaction between sedimentation, regional extensional tectonics and the rheological behaviour of the rocksalt, and is manifested in the following ways.

First, salt has a density which is intermediate between the densities of uncompacted sediments near the surface and the densities of compacted sediments at depth. However, the density of salt varies little during burial, so that at some point in a basin's evolution, the salt will become gravitationally unstable and attempt to rise, resulting in the formation of salt pillows and domes. During the evolutionary stages of a diapiric salt dome, differential burial and uplift leads to facies changes, unconformities, off- and onlap relations between stratigraphic units deposited above and around the dome and to the development of rim synclines and so-called 'turtleback' structures (Lerche and O'Brien, 1987). The recognition of differential loading and of downbuilding (Jackson and Talbot, 1991) as a mode of diapiric growth during regional thin-skinned extension has recently led to a new understanding of the rise and subsidence of diapirs (Vendeville and Jackson, 1992ab) in these tectonic settings, and of the importance of the rheological role of salt.

Second, on some passive continental margin, gravitational gliding of the uppermost sediments occurs on a basal detachment layer consisting of evaporites. This can give rise to extreme thin-skinned extension, or "raft tectonics". Examples include the Kwanza Basin of Angola (Duval et al., 1992; Lundin, 1992) and the Santos Basin of Brazil (Cobbold and Szatmari, 1991). In these settings, the structural development and the formation of hydrocarbon traps depends on the

interplay between sedimentary processes, regional extensional tectonics and the flow behaviour of the rocksalt. Adequate salt supply and low sedimentation rates promote diapir growth by downbuilding. Restricted salt supply and high sedimentation rates, however, promote growth faulting (Vendeville and Jackson, 1992ab).

Finally, consider the role of salt in delta tectonics, of which the United States Gulf Coast is the best documented example. The extreme mobility of the Middle Jurassic Louan salt during the Late Mesozoic and Tertiary cover deformation resulted in salt being squeezed towards the delta front by differential loading of the prograding sediments in the shelf upper-slope (Worral and Snelson, 1989). The allochtonous salt sheets, massifs, nappes and decollements are interpreted to reflect the large-scale horizontal displacements of salt (Worral and Snelson, 1989; Wu et al., 1990). The allochtonous salt nappe at the Sigsbee escarpment is one of the largest structural features in North America and is about three times the size of Alpine nappes. The allochtonous salt itself acts as a secondary source layer for diapirs formed by downbuilding of minibasins (Jackson and Talbot, 1991).

From these examples, it is clear that the dynamical evolution of subsurface salt bodies has an important control on basin evolution. It is therefore essential that the flow behaviour of salt is well understood and incorporated in basin modelling studies in order to understand basin evolution, and hydrocarbon migration and trapping (see for example Weijermars et al., 1993).

From this perspective, there has been a longstanding interest in the rheological behaviour of rocksalt, in its deformation mechanisms and microstructural development (see for example reviews by Carter and Hansen, 1983; Senseny et al., 1992; Carter et al., 1993). As mentioned already, evidence for both the operation of dislocation and fluid-assisted diffusional creep processes is found in naturally deformed rocksalt (Urai et al., 1987). Recent numerical experiments by Van Keken et al. (1993) have shown that for strain rates typical of salt diapirism driven by buoyancy alone (10^{-12} - 10^{-15} s^{-1}), the diffusion creep mechanism is likely to be dominant in most cases (grain size < 1 cm). However, for higher strain rates, which occur in cases of differential loading, salt extrusion and in active tectonic environments, the dislocation creep mechanism should be more important (Van Keken et al., 1993). Despite the extensive body experimental work on salt, however, important details of the dislocation creep mechanisms are not well understood; indeed substantial disagreement exists regarding the magnitude for the apparent activation energy for creep, the rate-controlling mechanisms and the role of recrystallization. Questions also remain as to how laborato-

ry data can be extrapolated to natural conditions and how dislocation creep and fluid-assisted diffusional creep processes compete. Other gaps in our understanding of the mechanical behaviour of salt concern memory effects, for example i) to what extent does deformation geometry influence the deformation behaviour of rocksalt in the dislocation creep field, and ii) are experimentally derived subgrain size palaeopiezometers (for example Carter et al., 1982) sensitive to deformation history?

1.3 GEOTECHNICALLY RELATED QUESTIONS

Salt has long been recognized as a relatively favourable medium for the disposal of radioactive and chemical wastes, and for the development of strategic storage caverns. This is because of its relatively high ductility, low creep strength, low permeability and hence high containment capabilities (natural salt permeability is $< 10^{-22}$ m^2, c.f. 10^{-16} m^2 for a relatively tight sandstone, Peach, 1991), coupled with its easy mineability (conventional or solution).

Now, the construction of storage caverns or disposal systems in a salt formation will lead to mechanical and/or thermal perturbations of the entire geological system. In particular, mechanical and thermal perturbations will lead to plastic deformation of the surrounding salt in a time-dependent manner, governed by the deformation properties of the salt and the evolution of the thermal pulse. Although it is expected that these perturbations will be small (Prij, 1983), for an accurate analysis of the facility performance it is nonetheless necessary to quantitatively model the intermediate and long term response of the geological system (Janssen et al., 1984).

On this basis, it is apparent that a thorough performance analysis requires a detailed understanding of the rheological behaviour of the salt. In particular, requirements for predictions of the intermediate and long term behaviour of a storage system demand a thorough, fundamental understanding of the mechanical behaviour of rocksalt at temperatures below 250 °C. This includes an understanding of the effects of strain-rate on stress-strain behaviour and the rate-controlling mechanisms (cross-slip vs. climb-controlled creep), and of the magnitude of the apparent activation energy for creep. These provide the basis for the development of constitutive models that can be used to predict the behaviour of the salt body (Krieg, 1982; Russel et al., 1990). However, such constitutive models should also incorporate the rheological behaviour of salt for different loading conditions with due consideration of

the history dependent nature of the rheological behaviour of salt (memory effects) (Aubertin et al., 1991). Laboratory investigations indicate that steady-state flow of rock salt is not strongly influenced by previous loading history when the loading geometry is relatively simple, for example coaxial (Heard and Ryerson, 1986; Russel et al., 1990). However the effect of complex, non-coaxial histories is not known. In addition, it is recognized that transient flow is very sensitive to previous deformation history (Aubertin et al., 1991), and this has never been systematically investigated. Both of these areas clearly require further study, then.

1.4 GENERALIZATION OF LABORATORY CREEP EQUATIONS

To numerically model the mechanical behaviour of a rock body under given boundary conditions, it is necessary to generalize experimentally obtained one-dimensional flow laws to two or three dimensions (McClintock and Argon, 1966; Ranalli, 1987; Twiss and Moores, 1992). For example, almost all flow laws available for olivine rocks have been obtained from axially symmetric experiments and relate axial strain rate to axial differential stress; in order to model large-scale mantle flow processes in 2-D or 3-D, these have to be generalized into relations linking the strain rate tensor $\dot{\varepsilon}_{ij}$ to the deviatoric stress state σ_{ij} (Stocker and Ashby, 1973; Ranalli, 1987; Van Keken, 1993). The same type of generalization procedure must also be applied to axi-symmetric data on rocksalt in order to model tectonic processes as well as the (thermo)mechanical response of salt formations to the construction of waste repositories and/or storage caverns (Prij, 1983; Janssen et al. 1984; Van Keken et al., 1993). This type of generalization is usually done using the theory of perfect isotropic plasticity known from metallurgy, applied to incompressible media in a form often referred to as the associated flow rule (for example Malvern, 1969). This theory implies that the principal axes of stress coincide with the principal axes of strain rate (Nye, 1953a, Drucker, 1956, 1959; Paterson, 1976; Hobbs et al., 1990). The assumptions underlying this method of generalization are that i) the material is isotropic, remains isotropic during deformation and has no memory for incremental strain history (i.e. path independent behaviour), ii) deformation is isovolumetric and iii) the material response is independent of the third invariant of the deviatoric stress tensor (Nye, 1953ab; Ranalli, 1987; Schmid et al, 1987).

While the above method of generalization is widely applied in al-

most all modelling studies of large scale deformation phenomena, it is well-known that most plastically deforming materials have some microstructural memory for incremental strain history. It therefore may be expected, and occasionally has been observed, that the incremental deformation history influences the mechanical behaviour to some extent (for example: Ghosh and Backofen, 1973; Tomé et al., 1984). Furthermore, it has been clearly demonstrated from theory that axi-symmetric deformation experiments on materials with "memory" are insufficient to fully characterise the material behaviour (Hobbs, 1972; Ferguson, 1979). Since most flow laws for rocks are obtained from axi-symmetric compression experiments, there is thus no *a priori* justification for generalizing these flow laws using the associated flow rule, and experimentally based information on the validity of the associated flow rule for individual materials, such as rocksalt and olivine, is clearly needed.

1.5 ANISOTROPY DEVELOPMENT AND SHEAR LOCALIZATION DURING DISLOCATION CREEP

Material strain softening is commonly taken as a requirement for the localization behaviour demonstrated in natural ductile shear zones. Strain softening mechanisms proposed to explain shear localization include recrystallization softening, grain-size reduction softening, crystallographic preferred orientation softening, phase-change softening, reaction softening and thermal softening (White et al., 1980; Poirier, 1980; Evans and Wong, 1985, Kirby, 1985). However, shear localization does not always have to be associated with macroscopic strain softening, as has been observed in compression experiments in which localization of deformation occurred (for example Burrows et al., 1979). Localization of deformation under strain-hardening conditions also may occur and can arise from i) non-associated flow behaviour, which is characterized by the development of mechanical anisotropy during deformation (Rice, 1976; Leroy and Ortiz, 1990; Hobbs et al., 1990); and ii) the development of vertices on the yield surface, arising from the presence of randomly oriented small cracks or small faults, which will promote further localization (Rudnicki and Rice, 1975). The localization behaviour of pressure-sensitive, dilatant, rate-independent materials has been investigated rather extensively (for example Rudnicki and Rice, 1975; Hobbs et al., 1990; Ord, 1991), but less so of presssure-insensitive, rate dependent materials (Anand et al., 1987; Harren et al., 1988). The flow behaviour of rate-dependent poly-

crystals, deforming by cross-slip or climb-controlled creep, may be non-associated (Rice, 1976). For example, Asaro and Needleman (1985) developed a constitutive model for deformation of rate-dependent polycrystals that predicts that flow in an initially isotropic material becomes non-associated with increasing deformation.

If the flow behaviour of rocksalt (or other geological materials) is non-associated (i.e. associated flow rule does not offer an adequate method of generalizing the creep law), shear localization is possible under particular loading conditions. As explained above, this is because non-associated behaviour is characterized by the development of mechanical anisotropy during deformation giving rise to truly different strengths of the material, depending on the deformation geometry. Now, localization may occur as long as the material in a particular zone (for example where non-coaxial flow dominates) flows at lower stresses than in the adjacent rock body (for example where coaxial flow dominates) resulting in higher strain rates in that particular zone. Thus, the onset of shear localization may result from boundary conditions of the system causing inhomogeneous deformation coupled with relative and not necessarily structural strain softening (Hobbs et al., 1990). During the subsequent evolution of the zone of localized deformation into a 'mature' shear zone, typical mylonitic microstructures and crystallographic preferred orientations may develop as a result, and not necessarily as the cause of shear localization.

From the above, it is clear that the influence of deformation geometry (i.e. mode of deformation) and history on the flow behaviour of rocksalt needs to be assessed. This may not only provide insight into the process of shear localization in relation to the development of mechanical anisotropy, but is also important for modelling flow of salt in natural deformation and in geotechnical applications. Furthermore, a general understanding of the process of shear localization can be distilled from the results, which may be applicable to other rock-forming minerals deforming in the dislocation creep field.

1.6 AIMS OF THE PRESENT STUDY

Having outlined some of the principal problems which remain outstanding as regards the deformation behaviour of salt, and information which may be gained relating to other materials, the general aim of the present work can be stated as to investigate the dependence of the rheology of synthetic rocksalt upon deformation history in the dislocation creep field, and the detailed nature of dislocation creep mechanisms in NaCl.

The *specific aims* of the study were:

- to investigate the mechanical behaviour, microstructural processes and texture development in polycrystalline halite deformed in uniaxial compression and in simple shear;
- to compare the behaviour seen in the two deformation geometries;
- to determine the deformation mechanisms and rate-controlling processes operating in halite deformed in both geometries investigated;
- to determine the dependence of the uniaxial flow behaviour on strain-rate history;
- to test if the associated flow rule offers an accurate method of generalizing creep laws obtained for polycrystalline halite;
- to assess the implications of the results for salt and other materials.

In order to achieve these aims, uniaxial and simple shear experiments have been carried out on synthetic polycrystalline rocksalt in the temperature range 250-780 °C with strain rates between 10^{-3} and 10^{-7} s^{-1}. Under these conditions, rocksalt deforms by dislocation creep mechanisms (Verall et al., 1977; Frost and Ashby, 1982). Both the uniaxial and the shear apparatus used in the study were specially designed for this study.

UNIAXIAL DEFORMATION
experiments on synthetic polycrystalline salt*

ABSTRACT

Synthetic polycrystalline halite (rocksalt) has been deformed in uniaxial compression in the temperature range 250-780 °C (0.5-0.98 T_m) at strain rates between 10^{-3} and 10^{-7} s^{-1}. Constant strain rate and strain-rate decrement, increment and cycling tests have been carried out. At temperatures from 250-450 °C the steady state flow law is given by

$$\dot{\varepsilon} = 5.75 \exp(-129/RT)\sigma^{5.7}$$

which is thought to describe climb-controlled dislocation creep, in which climb is controlled by diffusion through dislocation cores (pipe diffusion). The flow law in the temperature range 500 - 780 °C is given by

$$\dot{\varepsilon} = 6.57 \times 10^{7} \exp(-227/RT)\sigma^{4.4}$$

which is inferred to describe lattice diffusion-controlled dislocation creep. In the temperature range 250-350 °C, polygonization and rotation recrystallization are the dominant microstructural processes. However, with increasing temperature, grain boundary migration becomes important. The transition to migration recrystallization dominated microstructures, at c. 450 °C, coincides with the change from pipe diffusion to lattice diffusion controlled creep. This is explained as due to relative changes of grain boundary mobility, nucleation rate and driving force, which allow a balance to be established between the migration rate of nucleated grains and the nucleation rate of new grains.

* *This chapter has been submitted to Tectonophysics as: Franssen, R.C.M.W. The rheology of synthetic rocksalt in uniaxial compression.*

Below 450 °C the strain-rate history has a profound effect upon the observed microstructural development and mechanical behaviour. The subgrains do not increase and the stresses do not fall to the expected steady state values upon a lowering in strain-rate. This process of subgrain refinement results in relative hardening effects and in an increase of the stress sensitivity upon strain rate up to 10. Above 450 °C, however, the strain-rate history does not affect the microstructural development and steady state behaviour is always attained because migration recrystallization resets the microstructure which adjusts to the newly imposed conditions.
The crystallographic preferred orientation under all conditions investigated is characterised by rotation of the {110} poles towards the compression direction. Recrystallization processes appear to have no influence on the texture development.

2.1 INTRODUCTION

The dislocation creep behaviour of natural and synthetic polycrystalline salt (halite) has been investigated experimentally by numerous authors (Heard, 1972; Arieli et al., 1982; Burke et al., 1981; Carter and Hansen, 1983; Wawersik and Zeuch, 1986; Horseman and Handin, 1990; Horseman et al., 1992; Senseny et al., 1992; Carter et al., 1993), because of the interest in modelling salt tectonics and the behaviour of geotechnical structures, such as caverns for the storage of waste material or energy reserves. Microstructural development has also been investigated in detail to provide useful information for the interpretation of microstructures developed in naturally deformed salt rocks (Carter et al., 1982; Friedman et al. 1984; Skrotzki and Haasen, 1984; Urai et al., 1987). For example, sub-grain-size stress relations have been established for application as a palaeopiezometer to estimate steady state flow stresses in naturally deformed salt rock (Guillopé and Poirier, 1979; Carter et al. 1982; Carter et al. 1984, Carter et al., 1993). While all this work has provided much insight into the behaviour of salt, a number of questions remain unanswered. These include the following:

1) There still is considerable disagreement in the literature regarding the detailed deformation mechanisms and rate-controlling processes operating in halite, and which of these are relevant to natural deformation (e.g. cross-slip vs. climb control, vs. pressure solution creep; Wawersik and Zeuch, 1986; Wawersik, 1988; Carter et al, 1993).
2) While it is known that the rheology of salt in the dislocation creep field is to some extent history dependent, very little is known about the transient behaviour of salt from a microphysical point of view. Such information is of potentially major importance for accurate geotechnical modelling (Aubertin, 1991).

3) Similarly, it still is debated what the effect is of deformation history is on the microstructural development in NaCl, notably on subgrain size development (e.g. Robinson et al., 1974; Carter et al., 1984; Poirier, 1985).
4) Also, while evidence exists for several dynamic recrystallization mechanisms in NaCl, the conditions under which these occur and their influence on crystallographic preferred orientation (texture) development and mechanical behaviour are poorly understood and even controversial (Guillopé and Poirier, 1979; Skrotzki and Welch, 1983; c.f. Urai et al., 1986a; 1987).

In this paper, the results of a total of 40 uniaxial compression experiments on synthetic polycrystalline NaCl are reported. The experiments were carried out under conditions favouring dislocation creep behaviour, namely in the temperature range 250-780 °C ($T/T_m \approx 0.5$ - 0.98) at atmospheric pressure (in air) and at strain rates between 10^{-3} and 10^{-7} s^{-1}. The objective was to provide new data relating to the above questions by 1) determining the mechanical behaviour of synthetic salt in relation to microstructural evolution and crystallographic preferred orientation (textures), 2) identifying the microphysical processes operating and, in particular, 3) investigating the influence of strain-rate history as a function of temperature.

Viewing NaCl as a rock analogue (e.g. Shimamoto, 1989ab; Fransen and Spiers 1990; Chester and Logan, 1990), an additional aim was to gain insight into the likely influence of strain-rate history on mechanical behaviour and microstructural development in rocks in general, for deformation by dislocation creep mechanisms. A point of special interest here concerns to what extent subgrain palaeopiezometers may be influenced by strain rate history.

2.2 EXPERIMENTAL METHODS

2.2.1 *Samples*

In this study, synthetic polycrystalline halite samples were used. The samples were prepared as follows. First, analytical grade NaCl powder (Merck), jacketed in rubber tubes, was hydrostatically cold-pressed at 100 MPa for 10 to 20 minutes into irregular billets. From these billets, cylindrical samples were machined. These samples measured 20 mm in length by 10 mm in diameter. After machining, the samples were annealed for 12-14 hrs in an argon atmosphere at 720-725 °C (i.e. ~0.9 T_m) and stored in a low humidity room (RH ≤ 15%; Peach, 1991) before testing.

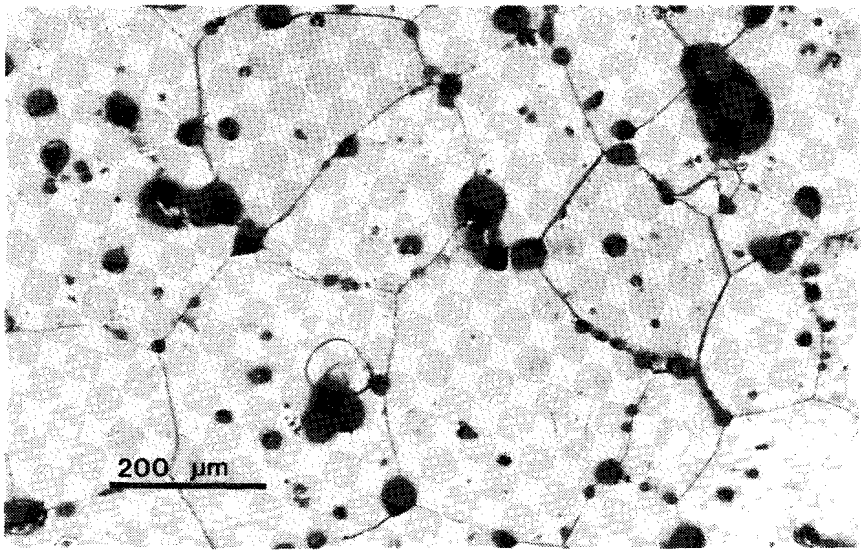

Figure 2.1
The annealed starting material typically possesses a foam microstructure with a grain size of 100 - 400 µm. The recrystallized grains contain no visible microstructure. The grain boundaries contain arrangements of gas-filled inclusions. The circular dark spots within the grains are artefacts resulting from the etching procedure. These artefacts are visible in all micrographs.

After annealing, the samples possessed a recrystallized polygonal "foam" microstructure with a grain size 100 to 400 µm (Fig. 2.1). The grains contained no optically visible substructure. Grain boundaries contained gas-filled tubular and spherical inclusions of about 10-20 µm in diameter and isolate pores up to 30 µm in diameter. The total porosity of the samples ranged from 2% to 2.5%. Neutron diffraction analysis showed that no significant starting crystallographic preferred orientation was developed (Fig. 2.2). The trace element content of the samples, analyzed by Inductively Coupled Plasma (ICP) emission spectrophotometry, was found to be below 75 ppm and the total divalent impurity content was approximately below 30 ppm. The main impurities were, in decreasing order of importance: K, Ca, Cs and S. The trace element composition and concentration remained unchanged after the annealing stage. The water content of the annealed samples, as determined by thermogravimetric analysis (TGA), was below 35 ppm.

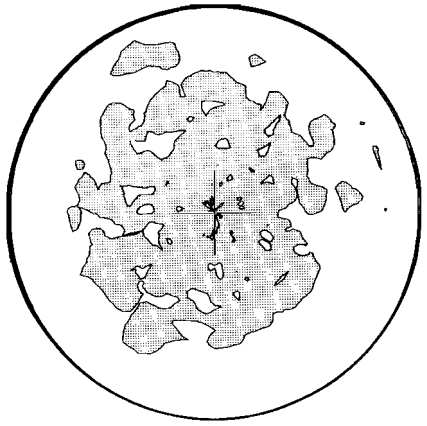

Figure 2.2
The starting material contain no significant preferred orientation as is shown by this pole figure of the {200} reflection. Contour intervals are 0.25 times uniform.

2.2.2 *Deformation apparatus*

The experiments were carried out in uniaxial compression, using a modified Instron 1193 constant displacement rate apparatus (Fig. 2.3), i.e. with a cross head speed (constant within 4%) variable over more than five orders of magnitude. The machine was equipped with a high temperature furnace and superalloy loading pistons. Temperature was controlled using a Eurotherm (type 093) controller connected to a Chromel-Alumel (Cr-Al) thermocouple positioned on the furnace wall (Fig. 2.3). A second thermocouple was used for temperature measurement of the sample. The temperature was kept constant to within ~3°C. The axial force applied to the sample was measured using a 5kN load cell, with an absolute error less than 0.025 kN.

2.2.3 *Testing procedure*

As mentioned previously, the tests were done at 250-780 °C (T/T_m = 0.5 - 0.98) at atmospheric pressure and strain rates between 10^{-3} and 10^{-7} s^{-1}. The following tests were carried out:

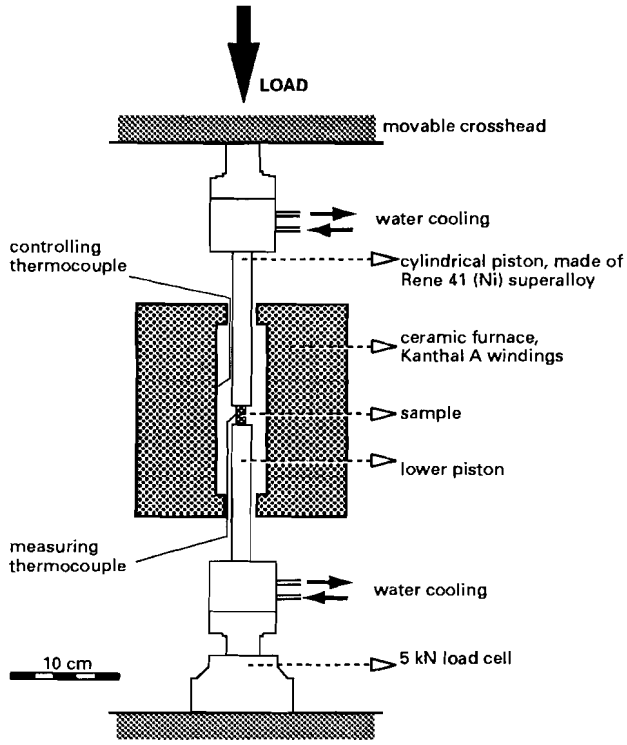

Figure 2.3:
Schematic diagram of the experimental apparatus used in the present tests.

1) *constant strain-rate tests* (i.e. at constant cross-head speed);
2) *strain-rate increment tests*, in which the lowest strain rate was imposed at the beginning of the test and the strain rate increased stepwise during the test;
3) *strain-rate decrement tests*, in which the highest strain rate was imposed at the beginning of the test and the strain rate then decreased stepwise but not necessarily sequentially;
4) *strain-rate cycling tests*, in which the same strain rates were imposed in cycles.

In all of these tests, the sample was first inserted into the apparatus and brought to the desired test temperature. A small load was then applied, and the desired strain rate was selected and imposed. In various

stepping tests (i.e. 2-4 above), the strain reached during the first step was always more than 6% and the strain during each subsequent step was at least 2%. To terminate each test, the load was instantaneously removed and the sample quenched with compressed air. Within 5 minutes after termination, the sample temperature was below 100 °C.

For reasons of convenience, we henceforth refer to a constant strain-rate test as being 'equivalent' to a step test if the strain rate imposed during the *last* step ($\dot{\varepsilon}_f$) is the same as the strain rate of the constant strain rate test.

2.2.4 *Data processing*

True stress-strain curves were obtained by digitizing and processing chart records of force vs. time. Strains were calculated from loading piston velocity, elapsed time and sample length, applying corrections for apparatus stiffness and for thermal expansion of the sample. Strains and strain rates were calculated with respect to the starting dimensions of the sample. Since the last strain-rate steps were in general applied at total accumulated strains less then 15%, the difference compared with the true strain rate is very small (calculated strain rate is <6% lower than the true strain rate). For strains less than 20%, the strain rate is constant to within about 10%. Sheets of gold foil or Teflon inserted between the piston and the sample reduced the friction at the sample ends and minimized barrelling. Stress calculations assumed homogeneous deformation with no volume change, but did include dimensional changes of the sample.

2.2.5 *Other techniques*

The microstructures of both the deformed and undeformed samples were studied by means of reflected light microscopy carried out on polished sections. Grain boundaries and dislocation substructures were made visible by etching the polished sections. Details of the section preparation techniques and etching procedures used are given in Spiers et al. (1986). In addition, some selected samples have been investigated using SEM and SEM-BSE techniques.

Texture measurements were carried out using the neutron diffraction goniometers at GKSS-Research Centre in Geesthacht, Germany and at Institut Laue-Langevin in Grenoble, France under supervision of Dr. H.G. Brokmeier. For a detailed description of the texture diffractometer at GKSS, the reader is referred to Brokmeier et al. (1988).

2.3 MECHANICAL DATA

2.3.1 *Stress - strain behaviour*

The complete set of tests reported here is listed in Tables 2.1 to 2.4 where tests are grouped according to testing method.

Constant strain-rate experiments

Typical stress-strain curves of constant strain-rate tests are shown in Figs. 2.4 and 2.5. (see also Table 2.1). The flow stress and the rate of work hardening decrease with increasing temperature and decreasing strain rate. At high temperatures (≥ 550 °C), occasionally some strain softening is observed (for example experiment C51 in Fig. 2.5). The reproducibility of the constant strain-rate tests is better than 10% of the measured stress.

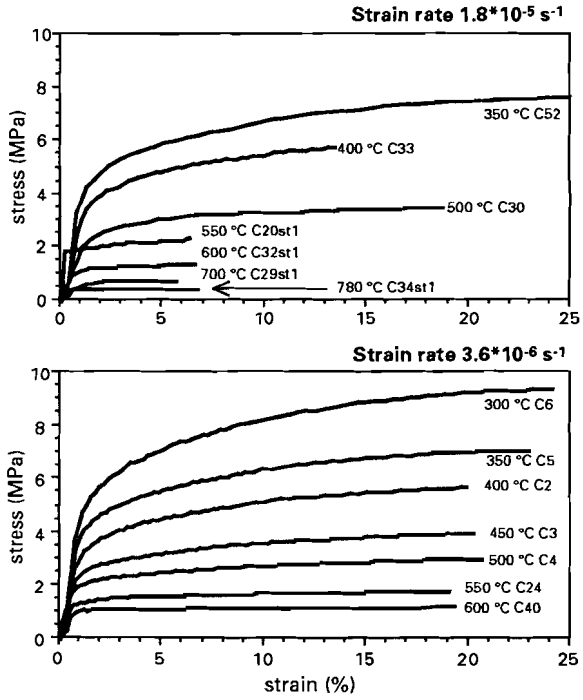

Figure 2.4:
*(a) Stress-strain curves for uniaxially compressed synthetic rocksalt at a constant strain-rate of 1.8*10^{-5} s^{-1} between 350-780 °C*
*(b) Stress-strain curves at a constant strain-rate of 3.6*10^{-6} s^{-1} between 300-600 °C . Each curve is labelled with test temperature and test number.*

Table 2.1. *Summary of mechanical data of constant strain rate experiments*

Test number	Temperature (°C)	Strain rate (s^{-1})	Stress at 10% strain (MPa)	Final stress	Final strain
C15	250	$1.8*10^{-6}$	13.9	14.8	14.5%
C6	300	$3.6*10^{-6}$	8.3	9.4	24.0%
C53	300	$1.8*10^{-6}$	7.5	7.7	14.2%
C52	350	$1.8*10^{-5}$	6.8	7.4	39.0%
C5	350	$3.6*10^{-6}$	6.4	7.1	23.0%
C10	350	$1.8*10^{-6}$	8.7	9.0	13.0%
C42	350	$1.8*10^{-6}$	7.1	7.3	13.9%
C46	350	$1.8*10^{-6}$	6.7	6.9	14.6%
C45	350	$1.8*10^{-7}$	--	5.0	8.9%
C28	400	$1.8*10^{-5}$	5.1	5.2	13.1%
C33	400	$1.8*10^{-5}$	5.5	5.8	13.4%
C2	400	$3.6*10^{-6}$	5.2	5.7	19.9%
C8	400	$1.8*10^{-6}$	4.2	4.2	14.0%
C27	400	$1.8*10^{-6}$	3.7	3.8	14.3%
C3	450	$3.6*10^{-6}$	3.6	4.0	20.2%
C7	450	$1.8*10^{-6}$	3.6	3.8	15.0%
C30	500	$1.8*10^{-5}$	3.3	3.5	18.7%
C31	500	$1.8*10^{-5}$	3.3	3.5	18.3%
C4	500	$3.6*10^{-6}$	2.8	3.0	20.6%
C9	500	$1.8*10^{-6}$	2.7	2.7	14.5%
C24	550	$3.6*10^{-6}$	1.7	1.8	19.1%
C19	550	$1.8*10^{-6}$	1.5	1.5	15.2%
C51	550	$1.8*10^{-7}$	0.56	0.54	13.6%
C40	600	$3.6*10^{-6}$	1.2	1.2	19.3%

Strain-rate stepping experiments

The data obtained from the strain-rate increment experiments are summarized in Table 2.2 and typical examples are shown in Fig. 2.6. The trends observed are similar to those seen in constant strain rate experiments: the rate of work hardening decreases with strain rate and the flow stress decreases with increasing temperature. During any one experiment, steady state flow may be attained at lower strain rates, whereas this can be replaced by continuous work hardening at higher rates. Similar stress levels (within ±1 MPa) are obtained from strain-rate increment tests compared to constant strain-rate tests.

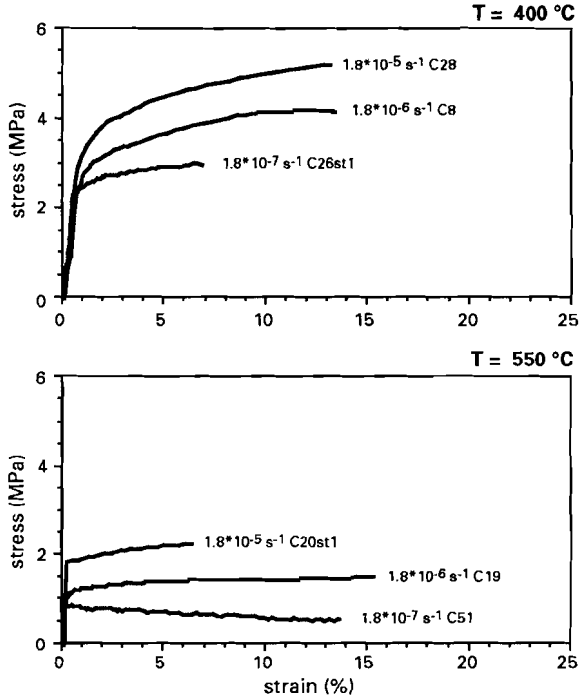

Figure 2.5:
(a) Stress - strain curves for constant strain-rate tests at 400 °C. and (b) at 550 °C. Each curve is labelled with the imposed strain rate and test number.

Examples of strain-rate decrement tests are shown in Fig. 2.7 (Table 2.3). Again, similar trends as mentioned above have been observed. Though, in the temperature range 250 - 450 °C, consistently higher stresses are attained in the decrement strain rate tests compared to the other test types, the differences in stress, at comparable strain-rates, being up to 4 MPa. At temperatures above 450 °C, however, the stresses obtained from decrement step-tests are within ±0.5 MPa of the stresses obtained from the other test types.

Table 2.2 *Summary of mechanical data of incremental strain-rate stepping tests*

Test number	Temperature (°C)	Strain rate (s^{-1})	Stress (MPa)	Strain (%)
C35st1	250	$2.88*10^{-7}$	9.8	6.6
C35st2	250	$3.6*10^{-7}$	10.5	9.4
C35st3	250	$1.8*10^{-6}$	11.9	12.0
C35st4	250	$3.6*10^{-6}$	13.0	15.0
C43st1	300	$3.6*10^{-7}$	7.6	8.6
C43st2	300	$1.8*10^{-6}$	8.6	11.1
C43st3	300	$3.6*10^{-6}$	9.5	14.3
C43st4	300	$1.0*10^{-5}$	10.5	17.3
C43st5	300	$1.8*10^{-5}$	11.7	20.4
C38st1	350	$2.88*10^{-7}$	5.4	9.3
C38st2	350	$3.6*10^{-7}$	5.5	12.3
C38st3	350	$1.8*10^{-6}$	6.5	15.6
C38st4	350	$3.6*10^{-6}$	7.1	19.5
C38st5	350	$1.8*10^{-5}$	9.1	21.5
C44st1	450	$3.6*10^{-7}$	2.3	9.0
C44st2	450	$1.8*10^{-6}$	3.0	12.0
C44st3	450	$3.6*10^{-6}$	3.4	14.8
C44st4	450	$1.0*10^{-5}$	3.9	18.3
C44st5	450	$1.8*10^{-5}$	4.4	21.4
C44st6	450	$1.0*10^{-4}$	5.5	24.4
C54st1	500	$1.8*10^{-6}$	2.0	11.2
C54st2	500	$3.6*10^{-6}$	2.3	14.9
C54st3	500	$1.0*10^{-5}$	2.8	18.3
C54st4	500	$1.8*10^{-5}$	3.1	20.9
C54st5	500	1.0*10-4	4.1	24.0
C32st1	600	$1.8*10^{-5}$	1.4	6.6
C32st2	600	$1.0*10^{-5}$	1.2	10.5
C32st3	600	$1.0*10^{-4}$	2.0	14.7
C32st4	600	$1.0*10^{-3}$	3.5	47.5
C41st1	600	$3.6*10^{-7}$	0.6	11.6
C41st2	600	$1.8*10^{-6}$	0.8	14.4
C41st3	600	$3.6*10^{-6}$	1.0	17.9
C41st4	600	$1.8*10^{-5}$	1.5	22.0
C41st5	600	$1.8*10^{-4}$	2.3	22.7
C29st1	700	$1.8*10^{-5}$	0.7	5.7
C29st2	700	$1.0*10^{-5}$	0.6	9.4
C29st3	700	$1.0*10^{-4}$	1.1	12.9
C29st4	700	$1.0*10^{-3}$	2.0	42.6
C34st1	780	$1.8*10^{-5}$	0.4	6.7
C34st2	780	$1.0*10^{-5}$	0.4	10.5
C34st3	780	$1.0*10^{-4}$	0.7	14.3
C34st4	780	$1.0*10^{-3}$	1.3	47.0

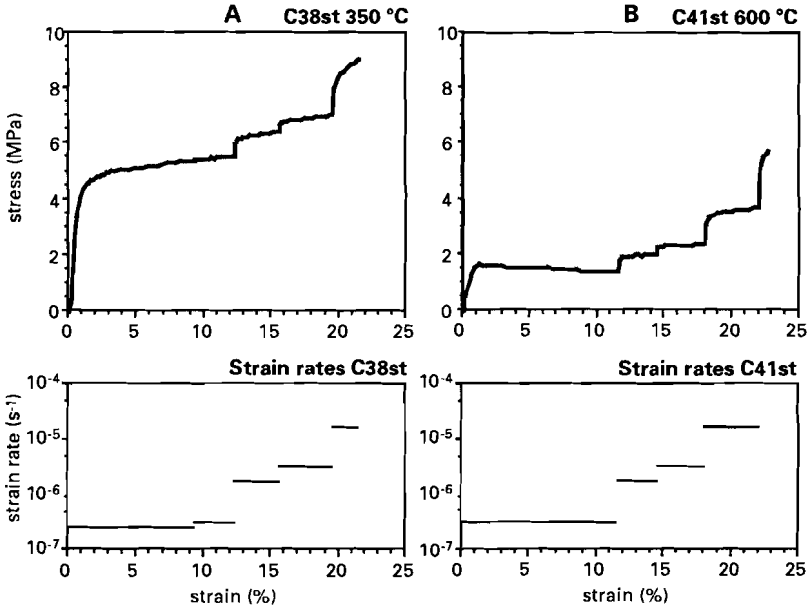

Figure 2.6:
Stress-strain curves for increment strain-rate stepping experiments at (a) 350 °C and (b) 600 °C. The imposed strain rates are indicated below the curves. The stress data of these tests correspond favourably with constant strain rate experiments.

Only two strain-rate cycling tests were carried out, namely at 400 °C (Table 2.4) (Fig. 2.8). In experiment C13st (Fig. 2.8b), the highest strain-rate was imposed at the start (cf. decrement step test), whereas in case of test C26st, the lowest strain-rate was applied at the start (cf. increment step test). Experiment C13st is characterized by consistently higher flow stresses (up to c. 2.9 MPa), compared with the results obtained from the other test types. This is consistent with the results presented above. In case of C26st (Fig. 2.8a), the measured flow stresses were similar to those obtained from constant strain rate experiments except the last two ('decrement') steps; these show a decrease in stress with strain and somewhat higher stress levels are attained compared to constant strain-rate tests.

Table 2.3 *Summary of mechanical data of decremental strain-rate stepping tests*

Test number	Temperature (°C)	Strain rate (s^{-1})	Stress (MPa)	Strain (%)
C18st1	250	$1.8*10^{-6}$	11.1	10.9
C18st2	250	$3.6*10^{-7}$	10.5	12.3
C18st3	250	$2.88*10^{-7}$	10.5	14.3
C18st4	250	$1.8*10^{-7}$	10.3	17.3
C16st1	300	$1.8*10^{-5}$	11.8	7.3
C16st2	300	$3.6*10^{-6}$	11.9	10.2
C16st3	300	$3.6*10^{-7}$	10.3	12.4
C16st4	300	$1.8*10^{-6}$	11.7	15.5
C14st1	350	$1.8*10^{-5}$	9.6	7.0
C14st2	350	$3.6*10^{-6}$	9.1	9.8
C14st3	350	$3.6*10^{-7}$	7.8	12.0
C14st4	350	$1.8*10^{-6}$	8.7	14.1
C14st5	350	$1.8*10^{-7}$	7.0	15.4
C12st1	450	$1.8*10^{-5}$	5.0	6.6
C12st2	450	$3.6*10^{-6}$	4.6	9.0
C12st3	450	$1.8*10^{-6}$	4.2	11.4
C12st4	450	$3.6*10^{-7}$	3.5	14.0
C17st1	500	$1.8*10^{-5}$	3.1	6.0
C17st2	500	$3.6*10^{-7}$	1.8	8.5
C17st3	500	$3.6*10^{-6}$	2.5	11.0
C17st4	500	$1.8*10^{-6}$	2.3	13.5
C17st5	500	$1.8*10^{-7}$	1.6	16.2
C20st1	550	$1.8*10^{-6}$	2.3	6.3
C20st2	550	$3.6*10^{-6}$	1.7	8.5
C20st3	550	$3.6*10^{-7}$	1.1	11.4
C20st4	550	$1.8*10^{-6}$	1.4	13.9
C20st5	550	$1.8*10^{-7}$	0.9	15.4

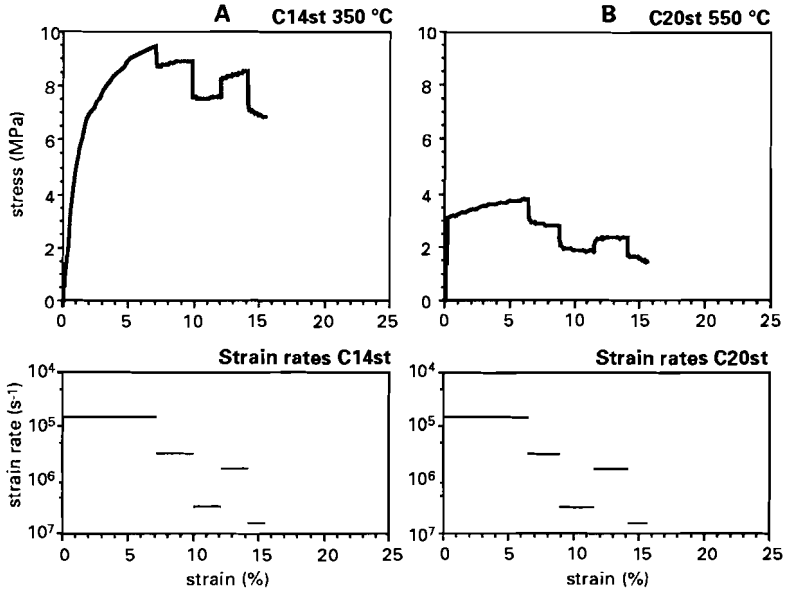

Figure 2.7:
Stress-strain curve for decrement strain-rate stepping tests at (a) 350 °C and (b) 550 °C. The imposed strain rates are indicated. See text for discussion.

2.3.2 *Dependence of flow stress on strain rate and temperature*

In Fig. 2.9, the flow data obtained in the increment, decrement, and constant strain rate tests, carried out in the temperature interval 300-450 °C, are plotted in log stress vs. (- log strain rate)-space. As has been shown above, the stress levels obtained in the decrement step tests are higher compared to the other test type. In addition, the dependence of strain rate upon stress is different for the decrement stepping tests compared to the increment and constant strain-rate tests (Fig. 2.9). The increment and constant strain-rate tests show that the strain rate depends on the stress to the power 5 to 6. In the decrement tests, this power exponent is significantly larger (7-10). These results show that a decremental strain-rate history has a significant effect upon the stress vs. strain and stress vs. strain-rate relations for temperatures below 450 °C (memory effect).

Table 2.4 *Summary of mechanical data of cycling strain-rate stepping tests*

Test number	Temperature (°C)	Strain rate (s^{-1})	Stress (MPa)	Strain (%)
C13st1	400	$1.8*10^{-5}$	7.0	7.5
C13st2	400	$3.6*10^{-6}$	6.4	10.4
C13st3	400	$1.8*10^{-6}$	6.0	12.5
C13st4	400	$3.6*10^{-7}$	5.0	14.7
C13st5	400	$1.8*10^{-6}$	5.7	16.2
C13st6	400	$3.6*10^{-6}$	6.4	17.6
C13st7	400	$1.8*10^{-7}$	4.3	21.4
C26st1	400	$1.8*10^{-7}$	3.0	6.8
C26st2	400	$3.6*10^{-7}$	3.3	10.0
C26st3	400	$1.8*10^{-6}$	4.0	12.1
C26st4	400	$3.6*10^{-6}$	4.4	14.1
C26st5	400	$1.8*10^{-5}$	5.4	16.8
C26st6	400	$3.6*10^{-6}$	4.7	18.3
C26st7	400	$3.6*10^{-7}$	3.6	20.5

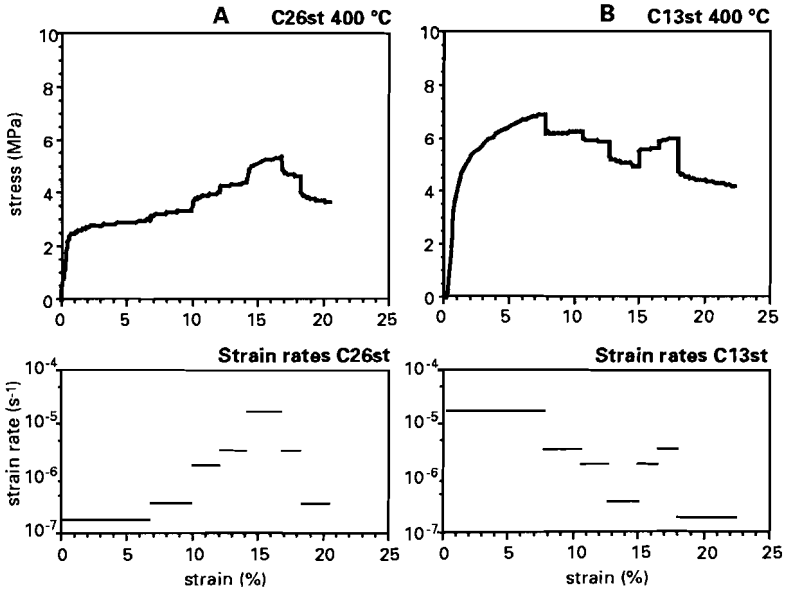

Figure 2.8:
Stress-strain curves for cycling strain-rate stepping tests (a) C26st and (b) C13st at 400 °C. The imposed strain rates are indicated below the stress-strain curves. See text for discussion.

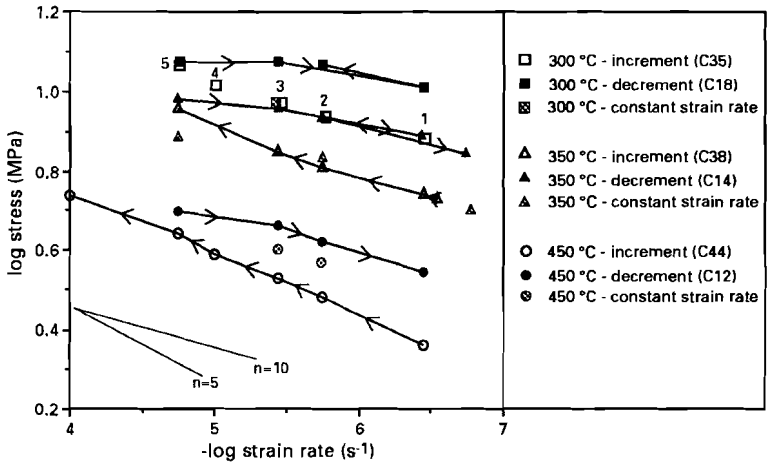

Figure 2.9:
Experimental stress-strain rate data of decrement and increment step tests data in the temperature range 300-450 °C plotted as log(stress) vs. -log (strain rate). The step tests data are connected through lines and the arrow heads indicate the sequence of imposed strain rates.

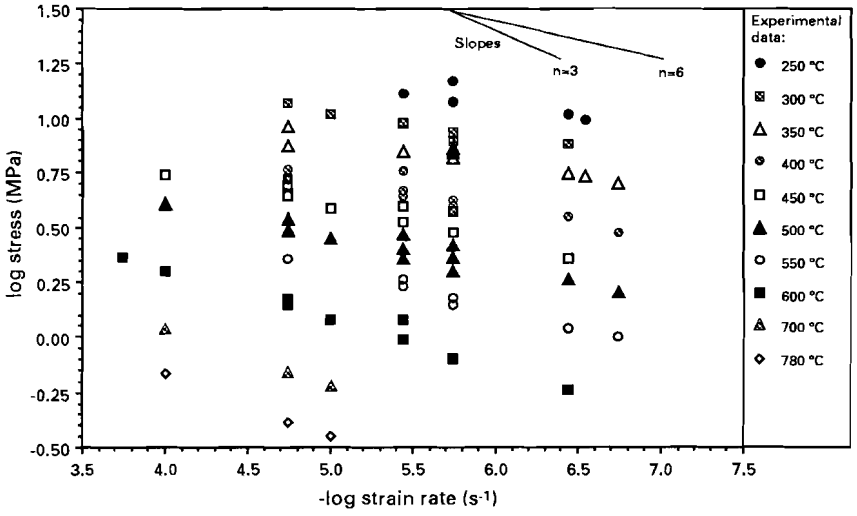

Figure 2.10:
Experimental stress-strain rate plotted in log(stress) vs. -log (strain rate) space. For a constant temperature the strain rate depends on the power 3 to 6 of the applied stress. These data are used to the determine the flow parameters.

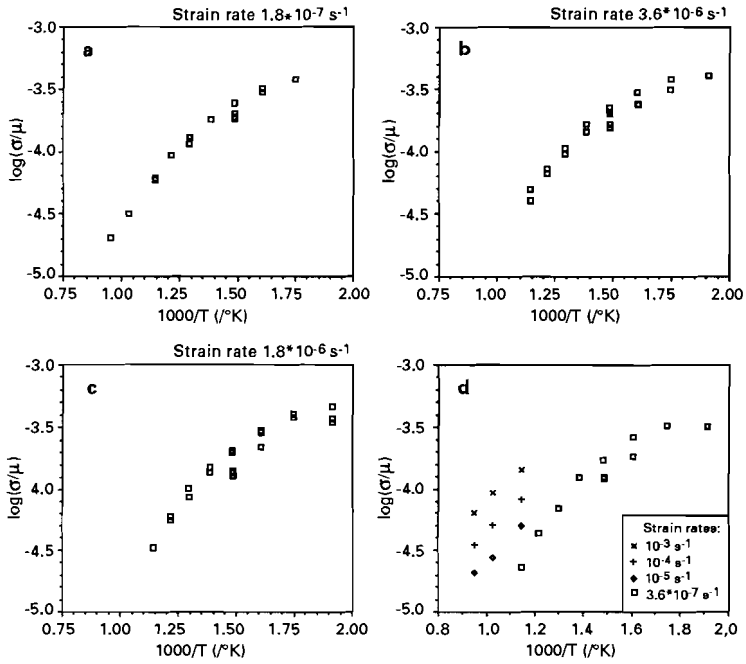

Figure 2.11:
Arrhenius-plots of the quantity log (σ/μ) vs. temperature for seven different strain rates. The stress has been normalized against the temperature compensted shear modulus μ. In (d) the data cover four orders of magnitude in strain rate.

The data obtained in the temperature range 250-450 °C, shown in Fig. 2.10, contain increment and constant strain-rate experiments and the data of the first step of the strain-rate decrement tests. In addition, all data obtained in the temperature range 500-780 °C are plotted. The data show that all test types represented in Fig. 2.10 yield similar results at temperatures above 450 °C, and that the constant strain-rate and strain-rate increment tests also yield consistent results at temperatures below 450 °C. Thus, it appears that strain-rate history effects are only significant for decreasing strain rates at temperatures from 250-450 °C. Accordingly, the data set plotted in Fig. 2.10 can be viewed as mechanical data which are not significantly influenced by strain-rate history, i.e. true steady state data. These data indicate that, for a constant temperature, the strain rate depends on the stress to the power 3 to 6.

The dependence of flow stress upon temperature is illustrated in

Arrhenius-plots for six different strain rates in Fig. 2.11, using the same data as shown in Fig. 2.10. These plots show that the quantity $\log(\sigma/\mu)$ decreases with reciprocal absolute temperature and the data can be approximated by two straight line segments, with the Arrhenius plot being curved in the intervening regions, $1.4 < 1000/T < 1.5$.

2.4 MICROSTRUCTURAL OBSERVATIONS

The microstructures developed in the deformed samples were found to depend strongly upon temperature. Three temperature intervals could be distinguished on the basis of characteristic microstructural development, namely: 250-350 °C, 400-500 °C and 550-780 °C. First, the microstructures developed during the constant strain-rate tests will be described, followed by a description of the microstructural evolution of various stepping tests. Data on subgrain size vs. stress will be given next. This section is concluded with crystallographic preferred orientation data.

2.4.1 *Microstructural development during constant strain-rate experiments*

250 - 350 °C (Fig. 2.12)

The halite deformed at 250-350 °C comprises flattened polygonal grains containing subgrains arranged in a linear fashion (Fig. 2.12a) and irregular patterns of cellular subgrains (Fig. 2.12b). The latter sometimes show incomplete boundaries (Figs. 2.12c). The linear substructures consist of straight-edged and rhomboidal subgrains and develop more commonly at higher strain rates. The irregular patterns of incomplete subgrain boundaries indicate incipient polygonization involving climb (Friedman et al. 1984). The subgrain shapes vary from polygonal to slightly irregular. Due to the optically isotropic nature of the halite, the orientation differences between subgrains could not be established. Epitaxial overgrowth experiments indicate that orientation differences of up to 10°-15° between subgrains developed. This may suggest that rotation recrystallization has occurred. The thin subparallel etch lines with irregular subgrains resemble wavy slip lines, e.g. grain A in Fig. 2.12a, and are indicative of polygonization by a combination of cross slip and limited climb (Skrotzki 1987).

In addition to the mentioned grain flattening, the samples deformed at 250-350 °C show a marked change in grain-boundary morphology. At low strains, most grain boundaries remain straight (Fig. 2.12c). However, with increasing deformation the grain boundaries

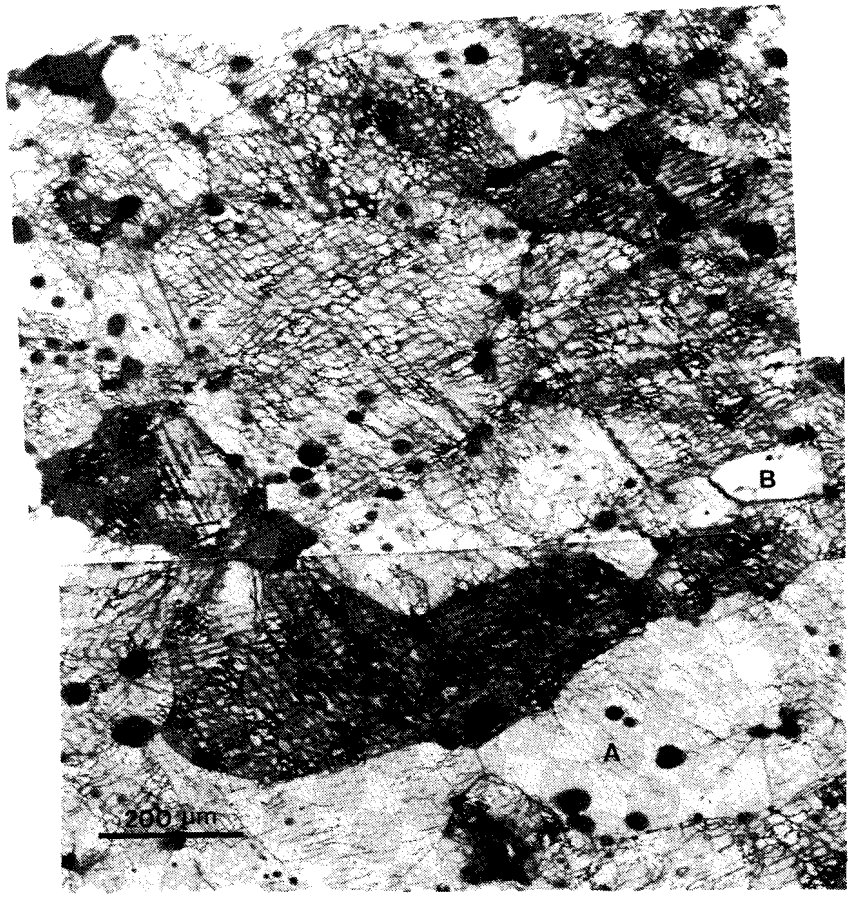

Figure 2.12a:
Optical micrographs of constant strain rate experiments deformed in the temperature range 250-350 °C.
The development of linear arrangements of subgrains is typical for deformation below 350 °C. In the two dark grains, just below the centre, two intersecting sets of linear substructures give rise to the formation of rhomboidal subgrains. In grain A (bottom right) thin etch lines resemble wavy slip lines.
(Sample C15, 250 °C, $\dot{\varepsilon} = 1.8 * 10^{-6}\ s^{-1}$, $\varepsilon = 14.5\%$, compression direction is vertical).

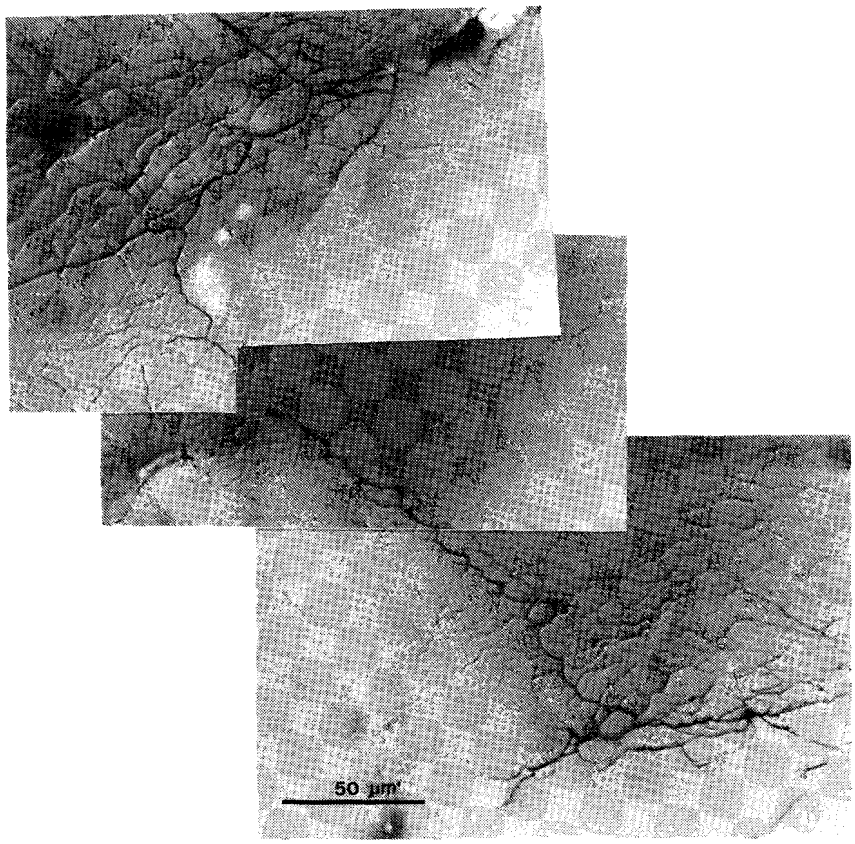

Figure 2.12b:
Optical micrographs of constant strain rate experiments deformed in the temperature range 250-350 °C.
Close inspection of clear grain B (in a) reveals a fine network of etch lines. The grain boundary traces are bulged and the spacing of the bulges depends on the subgrain size.
(Sample C15, 250°C, $\dot{\varepsilon} = 1.8*10^{-6}$ s^{-1}, $\varepsilon = 14.5\%$, compression direction is top right to bottom left).

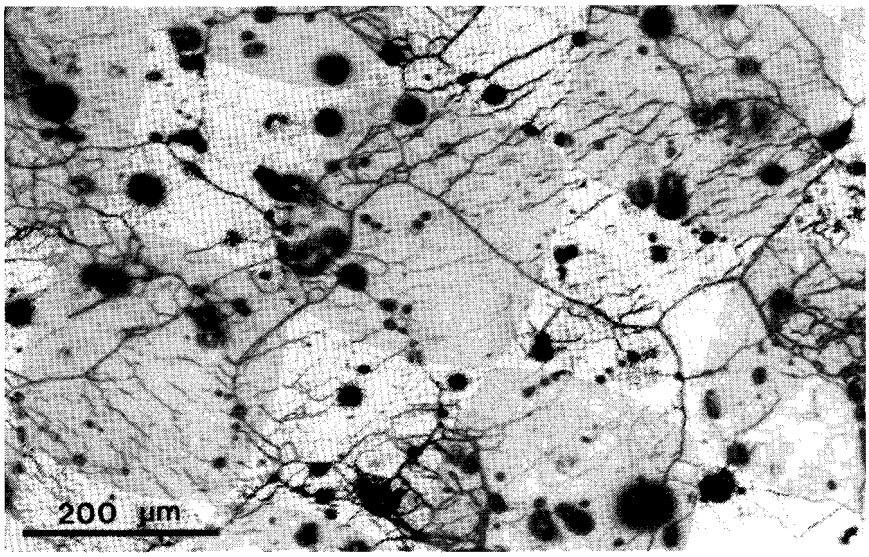

(Figure 2.12*c*) *Sometimes an irregular pattern of incomplete subgrains developed, indicating incipient polygonization. (Sample C45, 350°C, $\dot{\varepsilon} = 1.8*10^{-7}\ s^{-1}$, $\varepsilon = 8.9\%$, compression direction is vertical).*

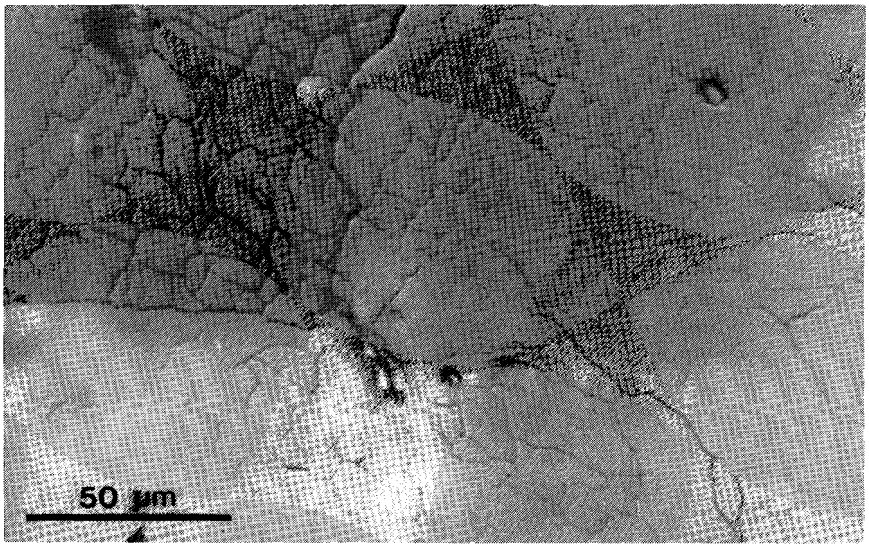

Figure 2.12*d*: *Grain boundaries were mobile to some extent as is suggested by the cuspate grain boundaries, which were not observed in the starting material.(Sample C15, 250°C, $\dot{\varepsilon} = 1.8*10^{-6}\ s^{-1}$, $\varepsilon = 14.5\%$, compression direction is vertical).*

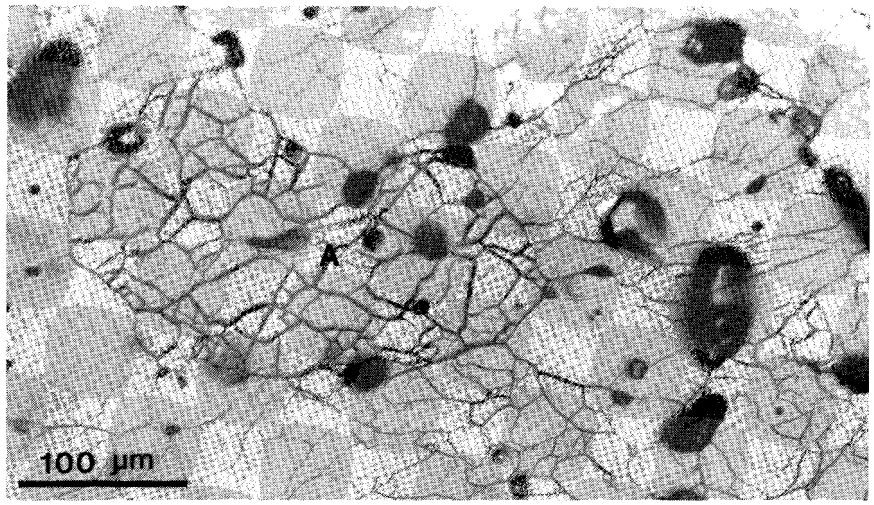

Figure 2.13a:
Microstructures developed during constant strain-rate deformation at 400-500 °C.
Dark and heavily etched grains (e.g. grain A in the centre of the micrograph) with concave grain shapes are surrounded by a network of clear grains. In both dark and light grains, well developed cellular networks of subgrains are visible. The grain boundaries of the clear grains are inferred to migrate towards the dark grains on basis of the cusp polarity.
(Sample C33, 400 °C, $\dot{\varepsilon} = 1.8 * 10^{-5}$ s^{-1}, $\varepsilon = 13.4\%$, compression direction is vertical).

show small bulges and cusps (Figs. 2.12b-d) with consistent polarities. These bulges develop at subgrain-boundary/grain-boundary intersections and they have wavelengths similar to the subgrain size. The grain boundaries thus show evidence of some mobility, but migration distances are very small (smaller than the initial grain size) .

400-500 °C (Fig. 2.13)

Microstructural development in this temperature range is characterised by the absence of a strong grain shape fabric. Indeed, flattened grains are relatively rare, but grain boundary migration is widespread, presumably weakening the development of a grain-flattening fabric. Commonly, dark-etched and light-etched grains with concavo-convex grain contacts are observed. All contain networks of cellular subgrains. However, dark-etched grains contain higher densities of dislocation substructures. The grain boundaries develop bulges or cusps, and the

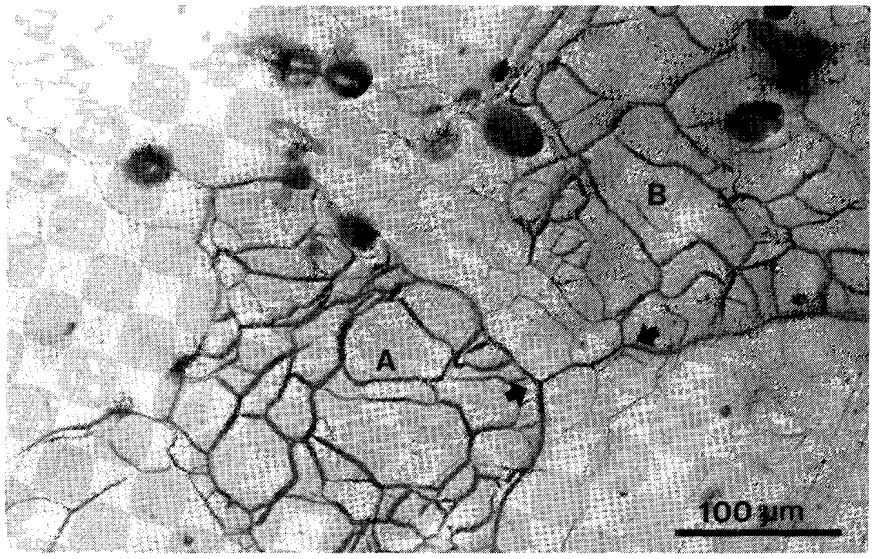

Figure 2.13b:
Microstructures developed during constant strain-rate deformation at 400-500 °C.
The grains A and B shown in this micrograph possess similar substructures and are darker etched than the surrounding grains. The concave shape of grain A indicates migration recrystallization and pinning of grain boundaries by subgrains. The grain boundary shape (between the arrows) is strongly influenced by the presence of subgrains.
(Sample C8, 400 °C, $\dot{\varepsilon} = 1.8 * 10^{-6}\ s^{-1}$, $\varepsilon = 14\%$, compression direction is vertical).

dark-etched grains are typically located at the convex side (Fig. 2.13b). The width of the cusps of the grain boundaries is determined by the subgrain-boundary spacing. The consistent polarity of the cusps suggests that grain boundaries migrate away from the centre of curvature and that subgrain boundaries exert pinning forces on such migrating grain boundaries. Nuclei for migration recrystallization are formed by subgrains bordering grain boundaries. These features suggest that grain boundaries of the light-etched grains migrate into neighbouring dark-etched grains and that grain boundary migration is driven by strain-induced energy (Nicolas and Poirier, 1976; Karato, 1988). At the same time, the subgrain boundaries propagate in an edge-wise fashion during the grain boundary migration (Means and Ree, 1988). This style of

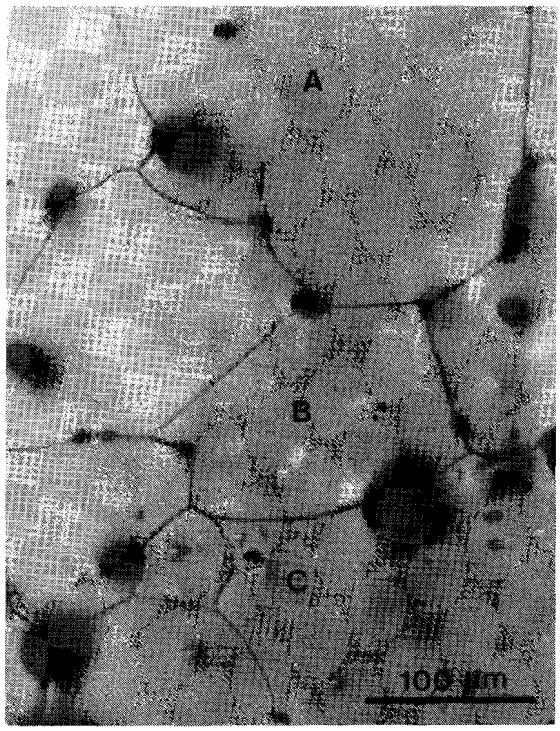

Figure 2.14a:
Microstructures observed in temperature range 500-600 °C.
At high temperatures large subgrains develop and extensive migration of grain boundaries leads to the development of concavo/convex grain contact. Grain boundaries inclusions may exert dragging forces (arrow). The grain boundaries are straight to slightly curved and tend to intersect at 120° triple junctions.

grain-boundary migration is characteristic of the temperature range 400-500 °C. The mobile grain boundaries have migrated distances in the order of the original grain size. The proportion of "relic", dark-etched grains still present (~20 - 50%), suggests that though dynamic, the observed grain boundary migration does not pervade the microstructure.

550 - 600 °C (Fig. 2.14)

Compared to lower temperatures, the microstructure developed in this temperature range is characterised by large grains with relatively few substructures (Fig. 2.14a). The microstructure is clearly dominated by grain-boundary migration. The grain boundaries tend to be straight

Figure 2.14b:
Microstructures observed in temperature range 550-600 °C.
Pinning of the migrating grain boundary by subgrain boundaries and by grain boundary inclusions (arrow). Behind this pinning point a subgrain is developed in the recrystallized grain. Note the increase in radius of curvature of the concave grain boundary in comparison with Figs. 2.12 or 2,13.
(Sample C19, 550 °C, $\dot{\varepsilon} = 1.8 * 10^{-6}\ s^{-1}$, $\varepsilon = 15.2\%$, compression direction is vertical).

to slightly curved and intersect at 120° triple junctions. However, migrating grain boundaries may be pinned by grain boundary inclusions, subgrain boundaries or triple junctions. The recrystallized grains show widespread development of large subgrains, indicating the dynamic character of the migration recrystallization process. Only a very few dark-etched grains with convex outlines are observed (Fig. 2.14b). This observation combined with the presence of many relatively 'clear' grains, suggests that dynamic recrystallization is continuously and pervasively active, even at the low strain rates (Drury and Urai 1990).

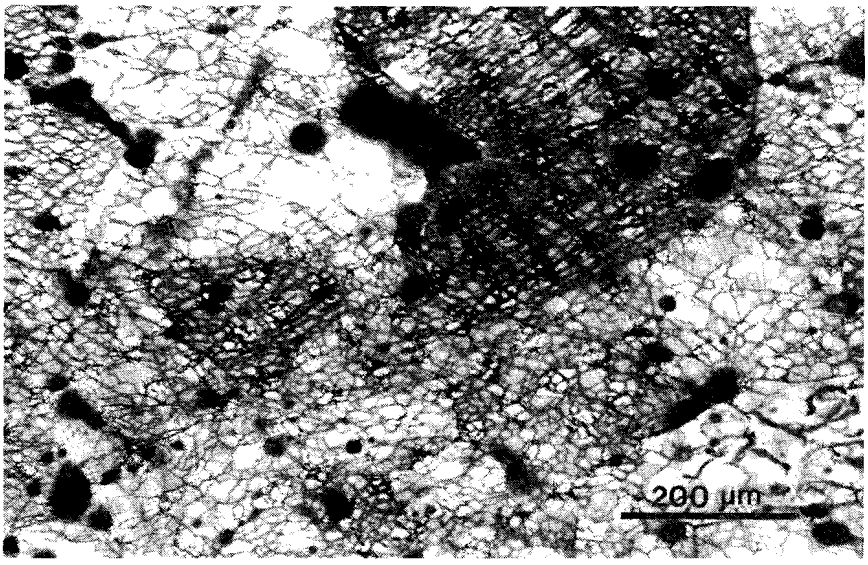

Figure 2.15a:
Microstructures developed during strain rate increment stepping tests in the temperature range 250-350 °C.
Microstructure reveals linear dislocation substructures and very small subgrains, comparable in size to the those developed in constant strain rate tests with high strain rates and low temperatures, (cf. Fig. 2.12a).
Sample C43st, 300 °C, $\dot{\varepsilon}_f = 1.8 * 10^{-5}$ s^{-1}, $\varepsilon_f = 3\%$, $\varepsilon_t = 20.4\%$, compression direction is vertical.

In summary, below 400 °C, the microstructural evolution is controlled by polygonization, possibly rotation recrystallization, and very limited grain boundary migration. With increasing temperature, grain-boundary migration becomes progressively more important. At temperatures above 500 °C, the microstructural development is controlled by migration recrystallization.

2.4.2 *Microstructural development during strain-rate stepping experiments*

Again, three temperature intervals could be distinguished, and the results will be presented according to test type.

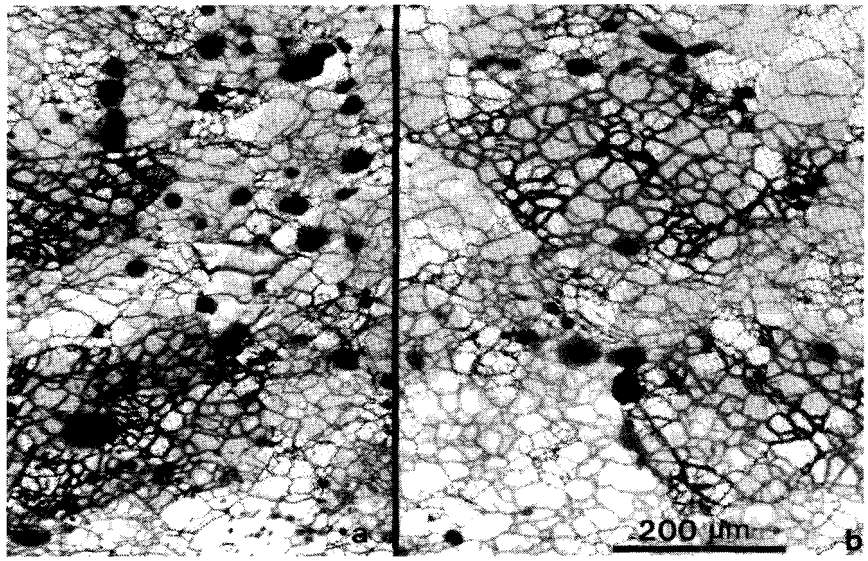

Figure 2.15b:
Microstructures developed during strain rate increment tests in the temperature range 250-350 °C.
Despite the difference in strain-rate history and total imposed strain, the microstructure of the increment step test (left) is very similar to the microstructure of the constant strain rate test (right).
(left) Sample C38st, 350 °C, $\dot{\varepsilon}_f = 1.8*10^{-5}$ s^{-1}, $\varepsilon_f = 2\%$, $\varepsilon_t = 21.5\%$.
(right) Sample C52, 350 °C, $\dot{\varepsilon}_f = 1.8*10^{-5}$ s^{-1}, $\varepsilon = 39\%$. Compression direction is vertical.

250 - 350 °C

The microstructures developed in strain rate *increment* tests (Fig. 2.15) are similar to those developed in equivalent constant strain rate experiments. For example, the microstructure of increment stepping test C38st ($\dot{\varepsilon}=1.8*10^{-5}$ s^{-1}) and of the equivalent constant-strain rate experiment C52 are virtual identical (Fig. 2.15b). Although migration recrystallization is considered to be rather unimportant at temperatures from 250 to 350 °C, one spectacular example illustrates the dramatic effect grain boundary migration can have on the microstructure even at low temperatures (Fig. 2.15c).

The microstructures of strain rate *decrement* tests also comprise flattened polygonal grains containing dense networks of cellular or rhomboidal subgrains (Fig. 2.16ab). The microstructures of the decrement tests are not similar to equivalent constant strain rate in that the subgrains developed in decrement tests are significantly smaller than those observed in equivalent constant strain rate tests (e.g. Fig. 2.16c).

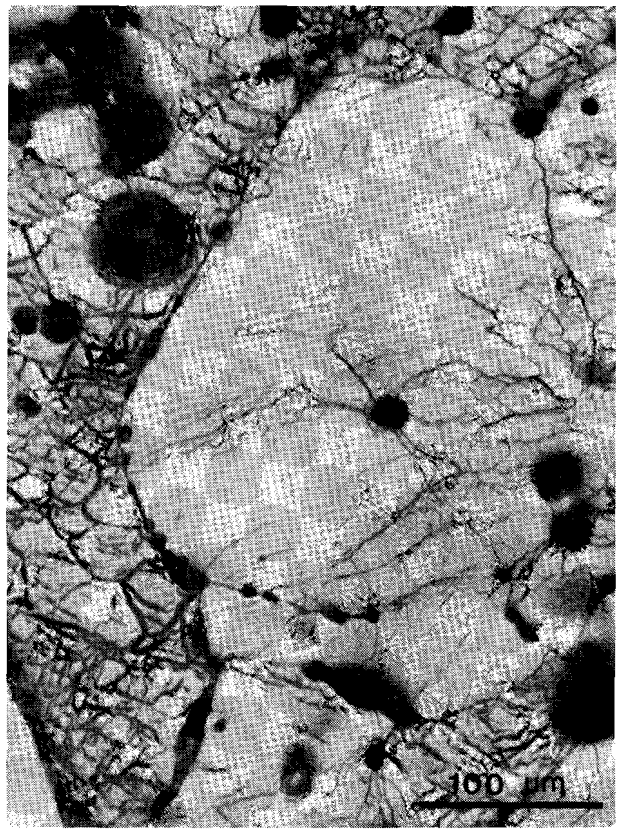

Figure 2.15c:
Microstructures developed during strain rate increment tests in the temperature range 250-350 °C.
Spectacular example of grain boundary migration resulting in concavo-convex grain contacts between dark- and light-etched grains. The boundary on the left-hand side of the light-etched grain is inferred to move to the left, consuming the heavily polygonized grain. The light-etched grains is being polygonized.
Sample C35st, 250 °C, $\dot{\varepsilon}=3.6*10^{-6}\ s^{-1}$, $\varepsilon_f=3\%$, $\varepsilon_t=15$.

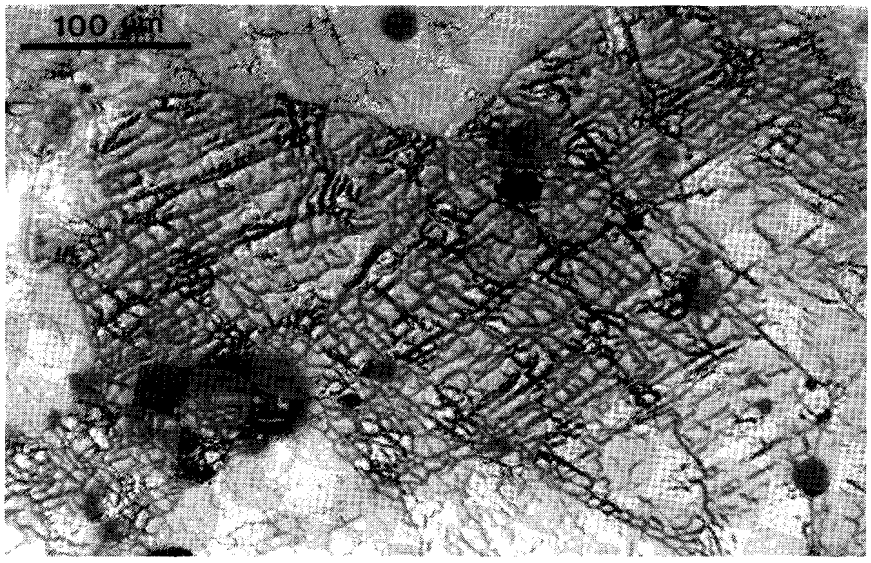

Figure 2.16a-c:
Microstructures developed during strain rate decrement stepping tests in the temperature range 250-350 °C.

(a) A conjugate set of linear dislocation substructures is developed in this decrement stepping test. Note that the development of these dislocation substructures is characteristic of deformation at low temperatures and high strain rates.
(Sample C18st, 250 °C, $\dot{\varepsilon}_f = 1.8 * 10^{-7}$ s^{-1}, ε_f =3%, ε_t =17.3%, compression direction is vertical).

(b) SEM image of mechanically parted grain boundaries. A single grain (starting grain size 100-400 µm) evolved into a an aggregate of 10 to 30 µm large grains by rotation recrystallization.
(Sample C18st, 250 °C, $\dot{\varepsilon}_f = 1.8 * 10^{-7}$ s^{-1}, ε_f =3%, ε_t =17.3%).

(c) At 300 °C, the microstructure of the decrement step test C16st (left). comprises very small subgrains in linear arrangements indicative of high stress/high strain-rate deformation at low temperatures. The microstructure developed during an equivalent constant strain rate test (right) shows well developed cellular networks of subgrains. The subgrain size developed during the constant strain rate experiment is substantially larger compared to the decrement step test.

left: Sample C16st, 300 °C, $\dot{\varepsilon}_f = 1.8 * 10^{-6}$ s^{-1}, ε_f=3.1%, ε_t =15.5%,
right: Sample C53, 300 °C, $\dot{\varepsilon} = 1.8 * 10^{-6}$ s^{-1}, ε =14%.
Compression direction is horizontal.

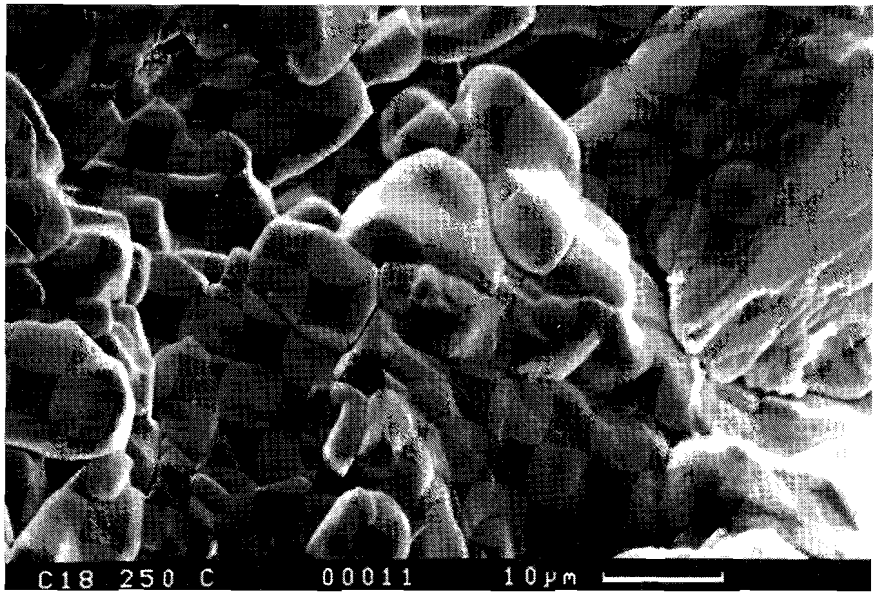

Figure 2.16b: *Microstructures developed during strain rate decrement stepping tests in the temperature range 250-350 °C.*

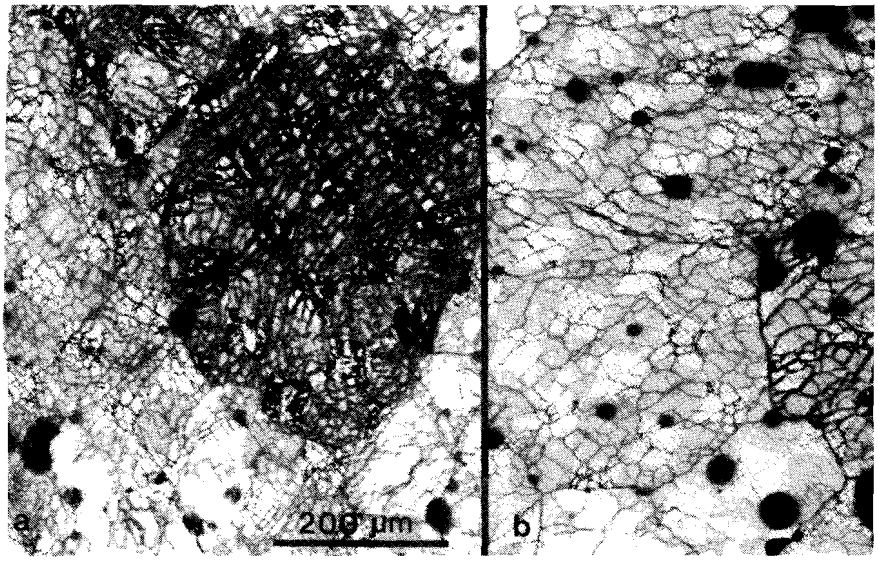

Figure 2.16c: *Microstructures developed during strain rate decrement stepping tests in the temperature range 250-350 °C.*

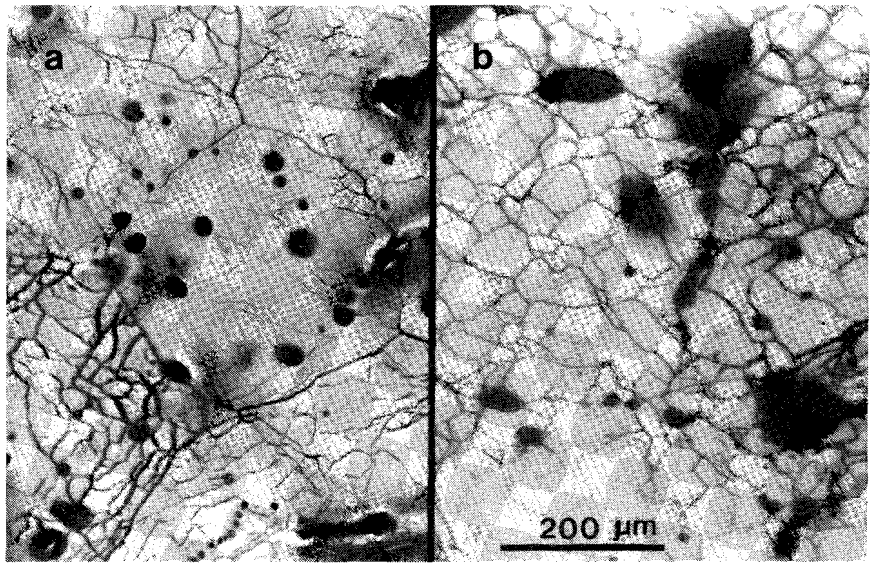

Figure 2.17:
The microstructure developed during strain-rate decrement test at temperatures in the range 400-500 °C.
At 450-500 °C, the well-developed cellular networks of subgrains observed in the decrement tests (left) are comparable to those developed in constant strain-rate tests. Some grain boundary migration occurred.
left: Sample C12st, 450 °C, $\dot{\varepsilon}_f = 1.8*10^{-7}\ s^{-1}$, $\varepsilon_f = 2.6\%$, $\varepsilon_t = 14\%$,
right: Sample C17, 500 °C, $\dot{\varepsilon}_f = 1.8*10^{-7}\ s^{-1}$, $\varepsilon_f = 1.6\%$, $\varepsilon_t = 16.2\%$,
Compression direction is vertical.

Thus, microstructures in the *decrement* tests resemble those observed in constant strain rate experiments carried out at higher rates (compare Fig. 2.16a with 2.12a). SEM images of mechanically parted grain boundaries provide some evidence for rotation recrystallization (Fig. 2.16b). Subgrain boundaries have developed into grain boundaries and this process gives rise to an aggregate constituting of 10 to 30 µm large grains derived from initial grains 100 - 400 µm in size.

400 - 500 °C

At these temperatures, the *increment* stepping tests show the same type of microstructural features and subgrain sizes as the equivalent constant strain rate experiments described above. Darker-etched grains with convex outlines are surrounded by light-etched, with both grain

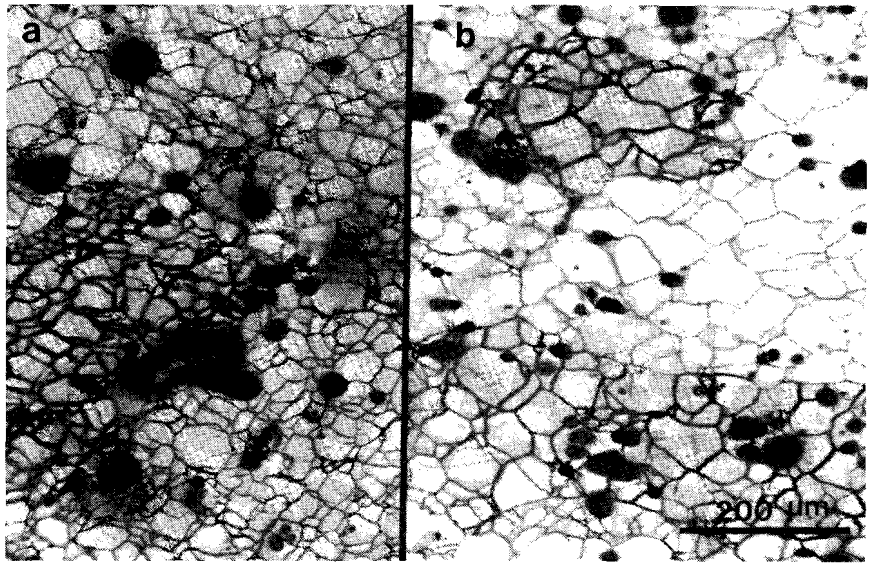

Figure 2.18:
The microstructure developed during the strain-rate cycling tests at 400 °C.
The microstructure of the decrement test (left) compares rather well with the microstructure developed during the increment test (right). The slight difference in subgrain-size is in accordance with the difference in stress observed during the last 3.5 - 5% strain (Fig. 2.8).
left: Sample C13st, 400 °C, $\dot{\varepsilon}_f = 1.8*10^{-7}$ s^{-1}, $\varepsilon_f = 3.8\%$, $\varepsilon_t = 21.4\%$,
right: Sample C26st, 400 °C, $\dot{\varepsilon}_f = 1.3.6*10^{-7}$ s^{-1}, $\varepsilon_f = 2.2\%$, $\varepsilon_t = 20.5\%$,
Compression direction is vertical.

types containing well-developed subgrain networks. The strain rate *decrement* tests also showed similar microstructural features as described for the equivalent constant strain-rate tests (Fig. 2.17). However, the subgrains are somewhat smaller compared to equivalent constant strain-rate experiments (Fig. 2.17) and increment step tests. The microstructures of the strain rate *cycling* tests (C13st/C26st, see Fig. 2.18) are comparable with those observed in constant strain-rate experiment C33 (Fig. 2.13a). However, the subgrain size of "decrement-starting" test C13st is smaller than the subgrains of "increment-starting" test C26st. Note that the strain rate imposed in test C33 ($\dot{\varepsilon}=1.8*10^{-5}$ s^{-1}) is equal to the highest strain rate imposed during the cycling tests, which is approximately two orders of magnitude higher than the strain rate of last step of the cycling test.

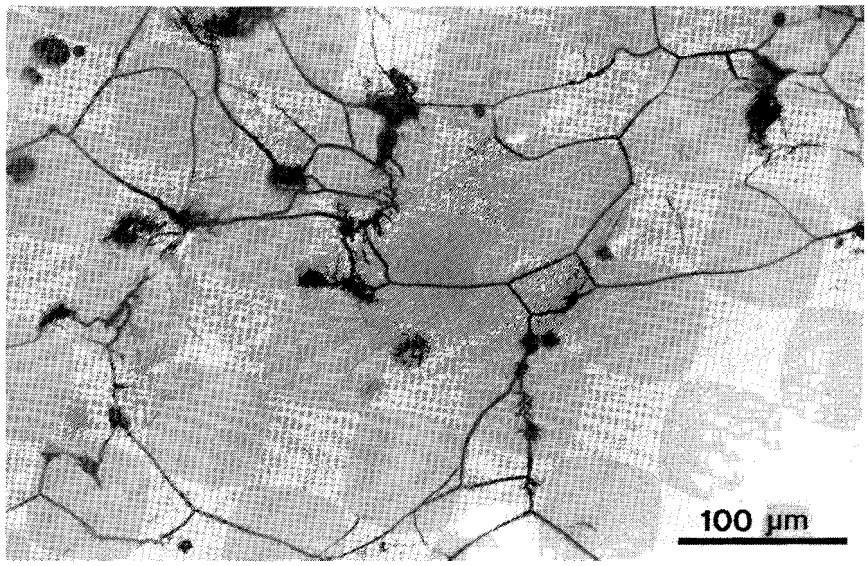

Figure 2.19:
The microstructure developed during strain-rate step tests at 550 °C. consists of completely recrystallized grains. The grains contain subgrains (top right), and have straight boundaries
(Sample C20st, 550 °C, $\dot{\varepsilon}_f = 1.8 * 10^{-7}$ s^{-1}, $\varepsilon_f = 1.5\%$,$\varepsilon_t = 15.4\%$, compression direction is vertical).

550 - 780 °C

Above 500 °C dynamic recrystallization by grain boundary migration dominates the microstructural evolution of the *increment* and *decrement* strain-rate step tests (Fig. 2.19), i.e. the step tests yield microstructures which are indistinguishable from the constant strain-rate experiments (compare Fig. 2.19 and Fig. 2.14).

2.4.3 *Subgrain size vs. stress data*

Subgrain-size data characteristic of constant strain-rate and strain-rate stepping tests are plotted against applied stress in Fig. 2.20. No systematic differences were observed between the constant strain-rate, the increment and decrement stepping tests. In addition, the present data are reasonably consistent with existing relationships such as those of

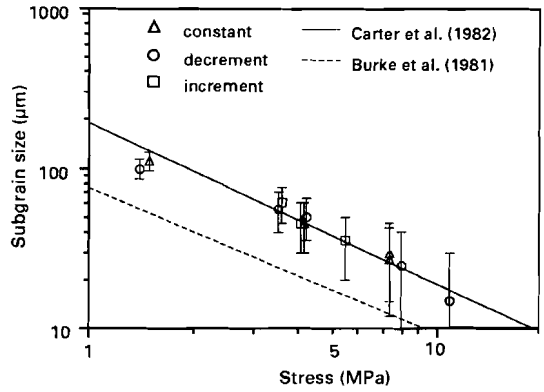

Figure 2.20:
Plot showing the subgrain-size vs. stress for constant strain-rate and strain-rate stepping tests. The lines represent the subgrain size - stress relations derived by Carter et al. (1982) and by Burke et al. (1981).

Carter et al. (1982), $d_{sg}(\mu m) = 190\ \sigma^{-1}$ (MPa), and Burke et al. (1981), $d_{sg}(\mu m) = 75\ \sigma^{-0.9}$. Note that all previously reported subgrain size - stress data for salt fall between the relations obtained by Carter et al. (1982) and Burke et al. (1981).

2.4.4 *Crystallographic preferred orientation data*

Pole figures have been measured for the {220} and {200} reflections for samples C2, C3, C4, C15 and C24 (Table 2.1), deformed in the temperature range 250-550 °C. From the pole figures, the orientation distribution function and inverse pole figures were calculated for each sample (Bunge, 1982; Dahms and Bunge, 1989; Dahms, 1992). The textures are illustrated in Fig. 2.21 as inverse pole figures (Wenk and Kocks, 1987) for the compression direction.

Regardless of temperature, all samples developed a maximum around <110> with a shoulder towards <100>. The texture development is not strong, with the maximum intensities varying between only 1.5 and 2.0 times uniform. At 250 °C, a submaximum around <115> is also developed. With increasing temperature, this submaximum decreases in intensity. At the same time, the shoulder towards <100> becomes stronger, and the orientation distribution moves towards the <100>-<110> symmetrale. Note that the <100> shoulder disappears at 550 °C.

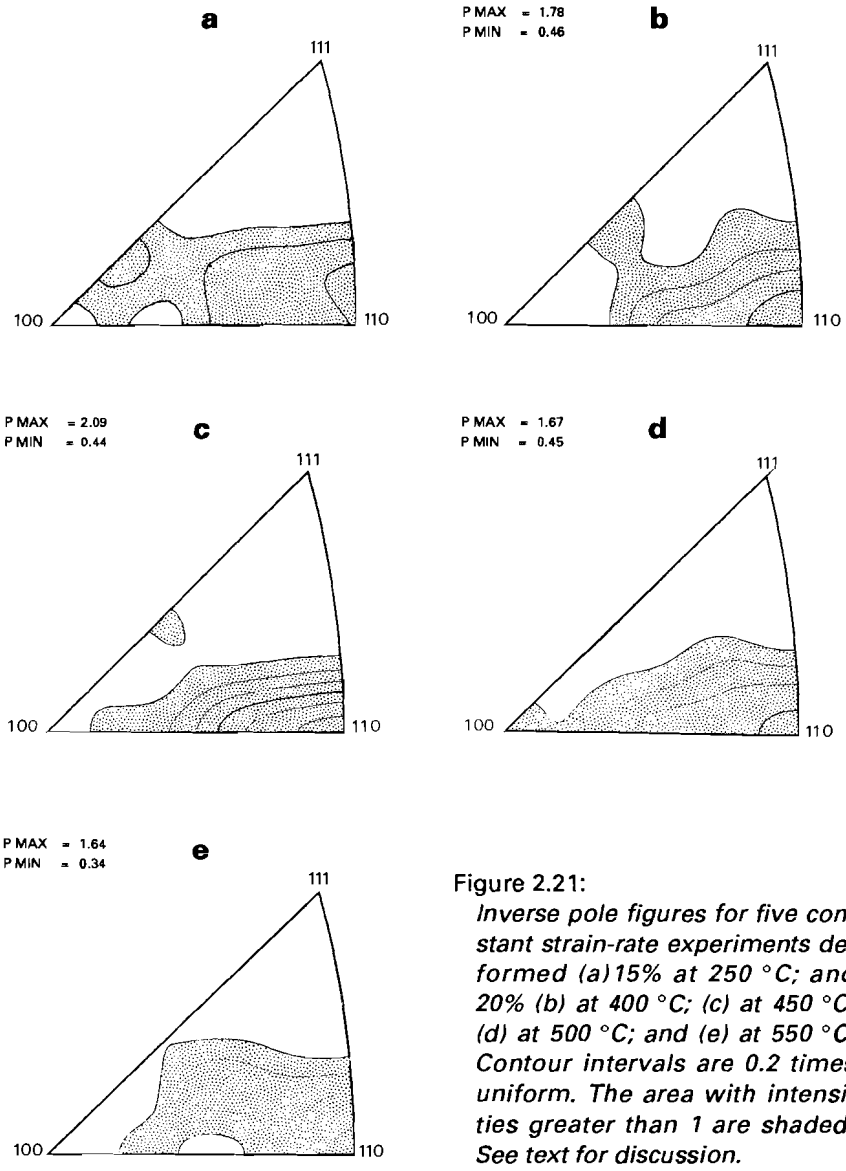

Figure 2.21:
Inverse pole figures for five constant strain-rate experiments deformed (a)15% at 250 °C; and 20% (b) at 400 °C; (c) at 450 °C; (d) at 500 °C; and (e) at 550 °C. Contour intervals are 0.2 times uniform. The area with intensities greater than 1 are shaded. See text for discussion.

2.5 THE OBSERVED FLOW BEHAVIOUR: DATA ANALYSIS AND DISCUSSION

2.5.1. *Analysis of flow data*

The above-reported microstructural and crystallographic preferred orientation development, in addition to the dependency of flow stress upon strain rate and upon reciprocal absolute temperature, indicate that deformation occurs by thermally activated dislocation creep processes. Previous studies (Heard 1970; Burke 1981; Arieli et al. 1982; Frost and Ashby, 1982; Carter & Hansen 1983) suggest that the relationship between stress, strain rate and temperature for salt deformed above $0.5T_m$ should be described by a Dorn-type power-law equation of the form:

$$\dot{\varepsilon} = A\exp(-\Delta H/RT)(\sigma/\mu)^n \qquad (2.1)$$

where $\dot{\varepsilon}$ is the strain rate (s^{-1}), A is a pre-exponential constant ($MPa^{-n}s^{-1}$), ΔH is the activation energy for creep (kJ/mol), R is the gas constant (kJ/Kmol), T is the temperature (K), σ the stress (MPa), μ is the temperature-compensated shear modulus (MPa) and n is the power-law exponent. Neither the pressure dependency (because all experiments were carried out at atmospheric pressure) nor the grain size dependency of creep can be determined (because all samples contained similar initial grain sizes) from the present data set. Thus the flow behaviour can be described empirically by a surface defined by

$$f(\ln\dot{\varepsilon}, \ln\sigma, 1/T) = 0 \qquad (2.2)$$

(Poirier, 1985). In order to derive values for the parameters A, ΔH and n the experimental data, shown in Fig. 2.10, were fitted to Eq. 2.1, using a global inversion method of Tarantola and Valette (1982), as adapted by Sotin and Poirier (1984) for processing creep data (see Appendix A and Poirier et al., 1990). The strain-rate decrement tests carried out at temperatures below 500 °C were excluded from the analysis, since these clearly showed history effects and cannot be regarded as reflecting true steady-state behaviour. Furthermore, the data set shown in Fig. 2.10 was divided into two sets. Separate solutions were sought for the creep parameters in the temperature range 250-450 °C and 500-780 °C. The reasons for this subdivision are 1) that the Arrhenius plots show a curvature in the temperature range 400-450 °C, indicating that two different rate-controlling processes exist (Poirier,

1985), 2) that this subdivision separates the field where migration recrystallization is the predominant microstructural process from the field where other processes control the microstructural development and, 3) that this subdivision yields an optimal data fit (Appendix A).

In the *250-450 °C* temperature range, the inversion procedure yielded, after only 5 iterations, the following flow law parameters:

$$\ln A(\text{in MPa}^{-n}\text{s}^{-1}) = 1.75 \pm 4.0$$
$$n = 5.7 \pm 0.33$$
$$\Delta H = 129 \pm 7.9 \text{ kJ/mol}$$

The data obtained in the *500-780 °C* range yielded, after only 4 iterations, the following values:

$$\ln A(\text{in MPa}^{-n}\text{s}^{-1}) = 18.0 \pm 2.3$$
$$n = 4.4 \pm 0.22$$
$$\Delta H = 227 \pm 10 \text{ kJ/mol}$$

Other temperature intervals always yielded poorer fits of the data to Eq. 2.1 (Appendix A).

At low temperatures and relatively high stress levels, the power law relation is generally expected to break down (see e.g. Frost and Ashby, 1982; Tsenn and Carter, 1987) with an exponential dependence of strain rate upon stress then describing the flow behaviour, i.e.:

$$\dot{\varepsilon} = B\exp(\Delta H/RT)\exp(\beta\sigma) \qquad (2.3)$$

where B and β are constants. Fitting the present low temperature data to this, again using the inversion method, yielded

$$\ln B = -11.3 \pm 0.873$$
$$\beta = (6.86 \times 10^{-2}) \pm 0.000315$$
$$\Delta H = 87.8 \pm 13.8 \text{ kJ/mol}$$

with convergence after 8 iterations.

According to Poirier et al. (1990), the best rheological description is the one which leads to the quickest inversion with the smallest residuals and standard deviations. From this, it is hence clear that the power-law (Eq. 2.1) yields best-fit descriptions of the experimental data. The results for the optimal inversions are summarized in Table 2.5.

Table 2.5 *Flow law parameters lnA, n and ΔH for the present experimental data, obtained using the global inversion method of Sotin & Poirier (1984). The mechanical data have been fitted to a general power law creep equation (Frost & Ashby, 1982):*
$\dot{\varepsilon} = A\exp(-\Delta H/RT)(\sigma)^n$

Temperature interval (°C)	250-450°C	500-780°C
Initial values:		
lnA=	-20±100	-20±100
n=	5±5	5±5
ΔH=	250±250	250±250
Results:		
lnA	1.75±4.0	18.0±2.3
n	5.7±0.33	4.4±0.22
ΔH	129±7.9	227±10
n_i	45	40
k	5	4
$\Sigma res^2/n_i$	1.85	0.9

Meaning of symbols: $\dot{\varepsilon}$: the shear strain rate (s^{-1}); σ: the applied shear stress (MPa); n: the power-law exponent; ΔH: apparent activation energy for creep (kJ/mol); A is a constant ($MPa^{-n}s^{-1}$); R: the gas constant (kJ/Kmol); T: temperature (K), μ: the temperature-compensated shear modulus (MPa); n_i: number of tests; k: number of iterations before convergence tests were fulfilled; Σres^2: sum of the squared residuals (measure for goodness-of-fit); ln: natural logarithm.

2.5.2 *Deformation mechanisms and rate-controlling processes*

The networks of cellular subgrains and the texture development indicate that climb-controlled dislocation creep processes are operative in the deformed polycrystalline halite under the stress-temperature conditions investigated. The presence of well-developed subgrains requires climb of edge segments of dislocations and cross-slip of the screw segments (Poirier, 1985; Carter et al., 1993). In the previous section, the parameters which best describe the flow laws for two different temperature regimes have been determined (Table 2.5). We will now examine the behaviour in these two regimes in more detail.

In the *500-780 °C* temperature range, i.e. 0.7 - 0.98 T_m, the best-fit flow law obtained is given by:

Table 2.6 *Comparison of creep activation energies and stress exponents of synthetic rocksalt deformed in uniaxial compression and published data*

Source/material	Temperature interval (°C)	n-value	ΔH (kJ/mol)
this study:			
uniaxial compression	250 - 450	5.7	129
Burke et al. (1981)	365 - 475	5 - 6	105
Heard (1972)	200 - 400	5.6	98
Arieli et al. (1982)[1)]			
low stress	200 - 400	5.3	102
high stress	200 - 400	11.3	166
Heard/Arieli et al. -re-evaluated[2)]			
low stress	200 - 400	5.8	115
high stress	200 - 400	6.5	120
Heard and Ryerson (1986)[1)]	200 - 400	5.8	96.1
this study:			
uniaxial compression	500 - 780	4.4	227
Burke et al. (1981) and Robinson et al. (1974)	500 - 740	4 - 5	210
Carter et al. (1993):			
natural salt: high $\dot{\varepsilon}$	50 - 200	5.3	68.1
natural salt: low $\dot{\varepsilon}$	50 - 200	3.4	51.6

Notes:
All data are derived from experiments on synthetic polycrystalline salt with the exception of Carter's (1993) data.

1) Data from Arieli et al. (1982) and Heard and Ryerson (1986) are based on Heard's (1972) experimental data which have been corrected for jacket strength and some new data collected by the authors.

2) Values for n and ΔH presented here are based on Heard and Arieli et al.'s data and have been derived using the inversion method of Sotin and Poirier (1984). The low stress data correspond to Arieli et al.'s (1982) power law creep field . The high stress data include tests with strain rates < 10^{-2} s^{-1}.

$$\dot{\varepsilon} = 6.57 \times 10^7 \exp(-227/RT)\sigma^{4.4} \qquad (2.4)$$

In most solids, creep in temperature range 0.7 - 0.98 T_m is controlled by lattice-diffusion controlled dislocation-climb (for example Sherby and Burke, 1967) and theoretical models for climb-control dislocation creep predict a power-law with a stress exponent between 3 and 6 (Weertman 1968; Sherby & Weertman, 1979; Poirier, 1985). The value of the stress exponent obtained at 500 - 780 °C ($n = 4.4 \pm 0.22$) thus agrees favourably with these models, and with previously determined values (Table 2.6) for polycrystalline halite.

In ionic polycrystals, the creep rate is often believed to be controlled by lattice diffusion of the slowest moving ion. In case of sodium chloride, the rate of diffusion of the cation exceeds that of the anion (Laurent & Bénard, 1957, 1958). In NaCl, the activation energy for lattice diffusion of the anion, $(Q_l)_{Cl^-}$, ranges from 205 to 221 kJ/mol in the temperature range 450 to 795 °C (Laurent & Bénard, 1957, 1958; Laurance, 1960; Barr et al., 1965). The activation energy for creep determined here, $\Delta H = 227 \pm 10$ kJ/mol, therefore falls in the range of diffusion activation energies for the anion, and is approximately equal to activation energies for high temperature creep determined by previous authors, see Table 2.6.

Combining these arguments, it is thus suggested that deformation of the present polycrystalline halite, in the temperature range 500-780 °C, occurred by climb-controlled dislocation creep, with climb controlled by anion lattice diffusion.

For the temperature range *250-450 °C*, i.e. 0.5- 0.7 T_m, the flow law obtained in the present study is given by:

$$\dot{\varepsilon} = 5.75 \exp(-129/RT)\sigma^{5.7} \qquad (2.5)$$

At such homologues temperatures, short-circuit diffusion through dislocation cores (pipe diffusion) often becomes an important rate-controlling process in the creep of ionic and ceramic materials (Verrall et al., 1977; Langdon, 1985; Cannon and Langdon, 1988). If pipe diffusion is the rate-controlling mechanism, the flow law is characterized by a decrease in activation energy and higher stress exponents compared to lattice-diffusion controlled dislocation climb (Cannon and Langdon, 1983; Langdon, 1985; Poirier, 1985).

Now, below 530 °C dislocation cores in NaCl carry an excess charge of Cl^- and are surrounded by a positive space-charge caused by an excess of divalent impurities (Verrall et al., 1977). This imbalance

seems to enhance diffusion at or near the dislocation core (Frost and Ashby, 1982). Significantly, the activation energy for dislocation core diffusion Q_c is typically 0.5 - 0.7 Q_l (Gjostein, 1972), where Q_l is the activation energy for lattice diffusion of the slowest moving species, i.e. equal to $(Q_l)_{Cl^-}$. In case of NaCl, Q_c therefore ranges from 102.5 to 155 kJ/mol (see also Barr et al., 1960). The activation energy for creep of polycrystalline NaCl in the temperature range 250-450 °C obtained here ($\Delta H = 129 \pm 7.9$ kJ/mol) is in good agreement with the range of activation energies expected for core diffusion.

Turning to the question of n-values, pipe diffusion occurs through dislocation cores and consequently the rate of core diffusion depends also on the density of dislocations present. In addition, the dislocation density depends on the magnitude of the applied stress (Poirier 1985). Thus, the stress exponent for core-diffusion controlled creep is expected to increase compared to the stress exponent for lattice-diffusion controlled creep (Cannon and Langdon, 1983; Langdon 1985; Poirier, 1985), since in the latter process the dislocations do not exert significant control on the diffusion rate. Clearly, the amount by which the stress exponent is increased depends on the relevant dislocation density - stress relation. Beeman & Kohlstedt (1988) have determined the dislocation density - stress relation for synthetic NaCl deformed in the temperature range 20 - 600 °C with differential stress varying from 2 to 20 MPa, and obtained:

$$\rho_{disl} = C(\sigma/\mu)^{1.3} \qquad (2.6)$$

where ρ_{disl} is the dislocation density (m^{-2}) and C is a material constant. If the same dislocation density - stress relation holds for the samples tested in the present study, it is expected that the stress exponent for pipe-diffusion controlled creep should thus increase by 1.3 relative for the stress exponent of lattice diffusion creep (n = 4.4). The stress exponent obtained for pipe diffusion is n = 5.7 and hence agrees well with this model.

In summary, the present data for the flow behaviour in the 250-450 °C temperature range (Eq. 2.5) agree favourably with theoretical models for climb-controlled dislocation creep. The diffusion activation data and the values for the stress exponent, which agree with independently obtained experimental data, suggest that deformation occurs by climb-controlled dislocation creep with climb controlled by pipe diffusion through dislocation cores.

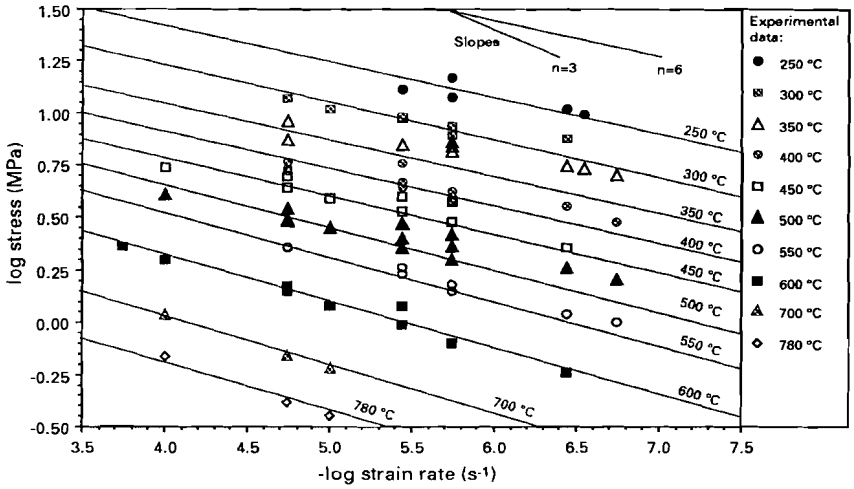

Figure 2.22:
The derived two-mechanism flow law (Eq. 2.7) plotted in log(stress) vs. -log (strain rate) space together with the experimental data. The correspondence between the modelled flow behaviour and the experiments is good for the temperature range 250 - 780°C over 4 orders of magnitude in strain rate.

2.5.3 *Two-mechanism flow law*

Lattice-diffusion and dislocation-core diffusion are independent processes which act simultaneously. They each contribute to the total strain rate which is given by the sum of the strain rates of the individual processes (Poirier, 1985). On the basis of the conclusions drawn in the preceding section, we therefore propose the following two-mechanism flow law for synthetic rocksalt, by adding the flow equations for the two temperature regimes. The two-mechanism equation is:

$$\dot{\varepsilon}_{tot} = 6.57 \times 10^{7} \exp(-227/RT)\, \sigma^{4.4} + 5.75 \exp(-129/RT)\sigma^{5.7} \qquad (2.7)$$

This two-component flow law is compared with the original data in Figs. 2.22 and 2.23. The agreement is excellent for the temperature and strain-rate range investigated (Fig. 2.22). The surface described by Eq. 2.7 (Fig. 2.23) is curviplanar with different stress exponents along the isotherms. The process with the highest activation energy (lattice diffu-

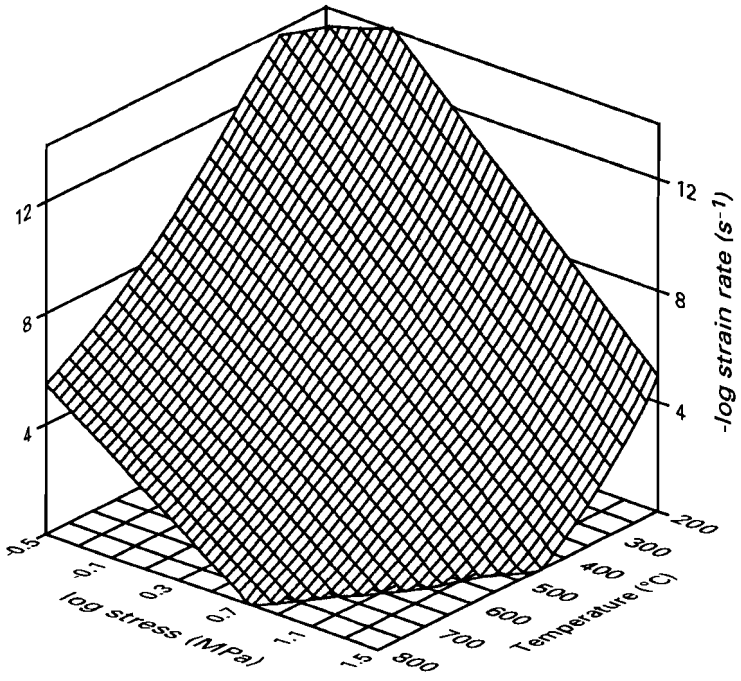

Figure 2.23:
The strain-rate dependency on stress and temperature (Eq. 2.7) is described by a curvi-planar surface in 3D.

sion creep) controls the total strain rate at high temperatures, and pipe diffusion controls the creep rate at lower temperatures. In the temperature range where the activity of both processes is comparable ($1.4 < 1000/T < 1.5$), the Arrhenius plots is curved (Fig. 2.11).

2.5.4 *Comparison with previous studies*

Burke et al. (1981) carried out a set of creep experiments on synthetic polycrystalline halite in the temperature range 365-740 °C. These authors concluded that above 475-500 °C, lattice diffusion creep controlled the deformation rate, whereas below 450-475 °C pipe diffusion was the rate-controlling process. This interpretation and the values of the activation energies obtained by Burke et al. (1981) agree well with the present study (Table 2.6).

Heard (1972) and Arieli et al. (1982) analysed the mechanical behaviour of synthetic polycrystalline halite deformed in the temperature range 23 to 400 °C and strain rates between 10^{-8} and 10^{-1} s^{-1} under 200 MPa confining pressure. These authors recognised two flow regimes between 200 and 400 °C: one at low stresses with a stress exponent around 5 and creep activation energy (ΔH) between 98 and 102 kJ/mol, and a high stress flow regime characterized by n = 11.3 and ΔH = 166 kJ/mol (see Table 2.6). These findings do not seem to agree well with the present results.

Heard (1972) and Arieli et al. (1982) argued that the activation energy obtained for the high stress regime indicated creep controlled by Cl^- lattice diffusion. However, this interpretation does not agree with the activation energies for lattice diffusion of the anion, $(Q_l)_{Cl^-}$, which ranges from 205 to 221 kJ/mol (Laurent & Bénard; 1957, 1958, Laurance, 1960; Barr et al., 1965). In addition, the activation energy for the low stress regime was argued to agree with the activation energy for Na^+ self-diffusion. However, the available data on Na^+ self-diffusion activation energies have a very wide range, from 74 to 155 kJ/mol (Mapother et al., 1950; Laurent & Bénard, 1957, 1958). Since the presence of grain boundaries in polycrystalline NaCl is known to enhance diffusion of Cl^- but not of Na^+ (Laurent & Bénard 1958), Heard (1972) and Arieli et al. (1982) argued that for larger grain sizes diffusion and hence creep would be limited by Cl^- diffusion, whereas at finer grain sizes Na^+ diffusion would be rate limiting. Heard and coworkers proposed that Na^+ diffusion would control the creep rate in the low stress regime, and hence it would control the creep at low stresses in natural rocksalt (Handin et al., 1986; Russel et al., 1990). However, careful inspection of the original experimental diffusion data (Laurent & Bénard 1958; their Fig. 3) shows that even for the finest grain size (50 μm), at 750 °C, the diffusivity of Cl^- approaches but does not exceed the Na^+ diffusivity. With decreasing temperature the Na^+ diffusivity is always larger than the Cl^- diffusivity. Thus, anion diffusion should always be slower than cation diffusion, also at low temperatures and for large grain sizes (see also Wawersik & Zeuch, 1986).

To make a proper quantitative comparison with the data reported in this Chapter, the mechanical data obtained by Heard (1972) and Arieli et al. (1982) have been re-evaluated using the Sotin & Poirier's (1984) inversion method (Table 2.6). Considering their *low* stress data *only* yields the following flow law parameters: $\ln A = 2.11 \pm 3.45$ $MPa^{-n}s^{-1}$ n

= 5.8±0.25 and ΔH = 115± 8.4 kJ/mol. The present data, for temperatures below 450 °C, are thus in good agreement with those of Heard (1972) and Arieli et al. (1982) when treated in the same manner. Fitting Heard's (1972) and Arieli et al.'s (1982) *low and high* stress data to a power law yields lnA = 2.25±2.5 $MPa^{-n}s^{-1}$, n = 6.46±0.17 and ΔH = 120± 6.95 kJ/mol. Again, these flow law parameters are in reasonable agreement with the flow law parameters derived in the present study for the pipe diffusion field, and agree with theoretical values for climb controlled dislocation creep. This agreement between Arieli et al.'s (1982) data and the flow law given in Eq. 2.5, suggests that the flow law (Eq. 2.7) should describe the mechanical behaviour of synthetic rocksalt in the temperature range 200 - 780 °C, regardless of factors such as grain size. The deformation of the polycrystalline halite tested by Heard (1972) and Arieli et al. (1982) thus is interpreted to occur by climb-controlled dislocation creep, where climb is controlled by Cl^- limited pipe-diffusion rather then by bulk Na^+ diffusion.

Recently, Carter et al. (1993) reviewed the rheology of natural rocksalt, primarily focusing on experimental results from Avery Island, Lousiana, U.S.A. domal salt. Avery Island is the purest (99% NaCl) and most homogenous natural rocksalt yet discovered (Handin et al., 1986). The grain size ranges from 2.5 - 15 mm, the content of any foreign ion is fewer than about 100 ppm, in-situ water content is 50 ppm and the porosity is less than 0.5%. The experiments on this rocksalt have been carried out in the temperature range 50-200 °C with strain rates varying between 10^{-5} and 10^{-9} s^{-1}.

The steady state flow field for Avery Island rocksalt has been separated by Carter and co-workers into a high stress/high strain-rate and a low stress/low strain-rate flow regime, each fitted by a power law, but with different n-values and activation energies (Carter et al., 1993; Horseman et al. 1992) (Table 2.6). The change in behaviour was attributed to a change in rate-controlling mechanism, from cross slip in the high strain rate regime to climb in the low strain rate regime. Now, principal differences between the low temperature flow laws for climb-controlled creep of synthetic salt and Avery Island rocksalt are the much lower activation energies, the smaller stress exponent and the smaller pre-exponential (about five order of magnitude smaller) seen in Avery Island rocksalt (see also Carter and Hansen, 1983; Handin et al., 1986; Russel et al., 1990). These differences clearly suggest different mechanisms in Avery Island rocksalt compared with the present experiments. At temperatures below 300 °C and stresses below 10 MPa, the strain-rate predicted by Eq. 2.7 is lower than the strain rate predicted

by Carter et al.'s climb-controlled or cross-slip equations (approximately one order of magnitude smaller for 10 MPa and 200 °C). At higher temperatures, Eq. 2.7 predicts faster strain rates. Thus, although a reasonable agreement between the steady state flow stresses of natural and synthetic rocksalt may be obtained at typical laboratory strain rates (10^{-4} and 10^{-7} s^{-1}), the behaviour of a natural salt body over longer term may be very different from the predictions based on flow laws for synthetic rocksalt (see application by Heard and Ryerson, 1986). More work thus is still needed to ascertain the rate controlling mechanisms in natural rocksalt, since these are evidently different from those seen in synthetic rocksalt. A particular problem concerns are the very low values of the activation energy for creep seen in Avery Island rocksalt.

2.6 MICROSTRUCTURAL AND TEXTURE DEVELOPMENT: DISCUSSION OF OPERATING PROCESSES

2.6.1 *Mechanisms of dynamic recrystallization*

Subgrain formation by polygonization, rotation recrystallization and recrystallization by grain boundary migration are microstructural processes observed in dry deformed polycrystalline NaCl (Carter and Hansen, 1983; Friedman et al., 1984; Guillopé and Poirier, 1979; Urai et al., 1986a). Dynamic recrystallization processes in alkali halides have been studied in single crystals (Yan et al. 1975, Guillopé & Poirier 1979, 1980, Kopetskii et al. 1982) and bi- or tricrystals (Sun & Bauer 1970). Relatively little attention has been paid to polycrystalline halite (Nadgornyi & Strunk 1987).

Commonly, three types of recrystallization mechanisms are distinguished for crystalline materials (Guillopé & Poirier, 1979; Drury & Urai 1990). Rotation recrystallization involves the progressive misorientation of subgrain boundaries resulting in the formation on new high-angle grain boundaries and the old grains become subdivided into a number of new grains. Two regimes of migration recrystallization are distinguished, depending on whether or not impurity atoms exert a dragging force on the migrating boundary (Guillopé & Poirier 1979). These regimes correspond to slow solute-loaded migration and fast solute-escape migration (Guillopé & Poirier, 1979; Urai et al., 1986a; Drury & Urai 1990). Fast solute-escape migration occurs only after a critical amount of strain (in case of NaCl > 60% shortening) and above a critical curve in σ - T space. The location of this curve has been determined by Guillopé and Poirier (1979) for uniaxially compressed NaCl single crystals (Fig. 2.24). The position of the curve depends on

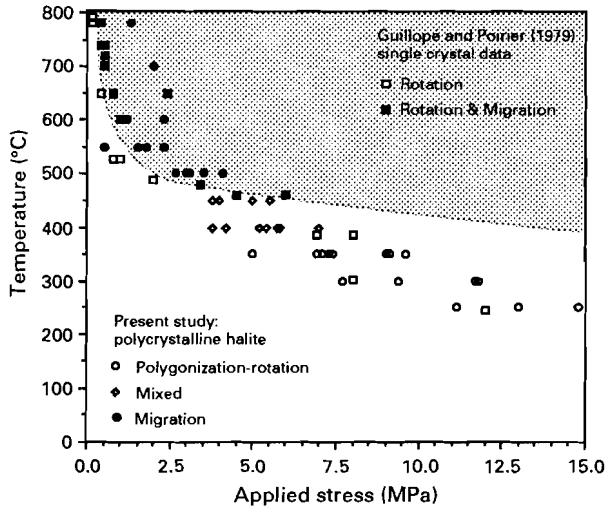

Figure 2.24:
Microstructural summary plot showing the predominant processes as function of temperature and applied stress. Note that in the present study grain boundary migration has been observed under all experimental conditions. The critical curve above which migration recrystallization is possible in synthetic NaCl single crystals (Guillopé and Poirier, 1979) is also shown. The stress - temperature conditions for which migration recrystallization in polycrystalline salt occurs plot well below this critical curve.

the impurity content: the more impure the NaCl the higher stresses and temperatures are needed for fast solute-escape migration to occur.

The driving force for rotation recrystallization is generally considered to be elastic distortional energy (Urai et al. 1986a). The driving force for grain-boundary migration in monomineralic materials are differences in stored (strain-induced) lattice defect energy (from dislocations and subgrains) and grain-boundary energy. In case of NaCl, the driving-force due to grain-boundary energy is commonly much lower than the driving force generated by lattice defects (Guillopé & Poirier 1979, Poirier & Guillopé 1979, Urai et al. 1986a). However, at high temperatures, grain boundary migration driven by surface-energy may be important, because the increased rate of polygonization may reduce lattice defect energies.

In the temperature range *250-300 °C* polygonization and rotation recrystallization were the dominant processes in the present experiments though minor grain boundary migration was observed. The 2-D geometry of the grain boundaries changed from initial planar to undulating with small valleys defined by subgrain - grain boundary intersections (Fig. 2.25a). The corresponding stress - temperature data plot well below the critical curve (Fig. 2.24), suggesting that the limited grain boundary migration observed is of the slow solute loaden type.

In the temperature range *400-500 °C* polygonization and migration recrystallization control microstructural evolution. The applied stress-temperature data plot below the critical curve (Fig. 2.24) and it is inferred that migration recrystallization is probably of the slow solute-loaden type.

In the temperature range *500 - 780 °C* migration recrystallization is the dominant microstructural process with recrystallized grains containing only a few large subgrains (50 - 150 μm). The migrating boundaries may be pinned by inclusions, grain boundary triple junctions and subgrain boundaries. Grain boundary migration may be driven by lattice-defect energy (since migration directions tend to be away from the centre of curvature) and by grain boundary energy (as suggested by the straight or slightly curved grain boundaries, intersecting at 120° triple junction develop, Figs. 2.14a, 2.25b) (Vernon, 1976). The clear microstructure, the low densities of defects and the complete obliteration of the old deformed grains suggest that grain-boundary migration is continual (Drury & Urai 1990). In the 500-780 °C temperature regime, the experimental data plot well above the critical curve in σ - T space. This suggests that fast solute-escape migration may have occurred. However, the stress- recrystallized grain size relation for fast solute-escape migration is given by (Guillopé and Poirier, 1979):

$$\sigma_m = 57\mu(b/D)^{0.78} \qquad (2.8)$$

where, σ_m is the applied stress (in MPa), D is the recrystallized grain size (μm) and in their analysis in the shear modulus μ is taken as 10 GPa and the Burger's vector b equals 3.98 x 10^{-4} μm. Assuming that this relation also applies to polycrystalline halite, then applied stresses between 0.5 and 1.5 MPa would yield recrystallized grain sizes between 0.5 and 2.2 x 10^4 μm. The observed recrystallized grain sizes are significantly smaller (0.5 - 1 x10^3 μm). Thus it is not likely that the same fast migration recrystallization mechanism proposed by Guillopé and Poirier (1979) is operating in the polycrystalline salt presently studied. In addition, the total strains imposed are smaller than

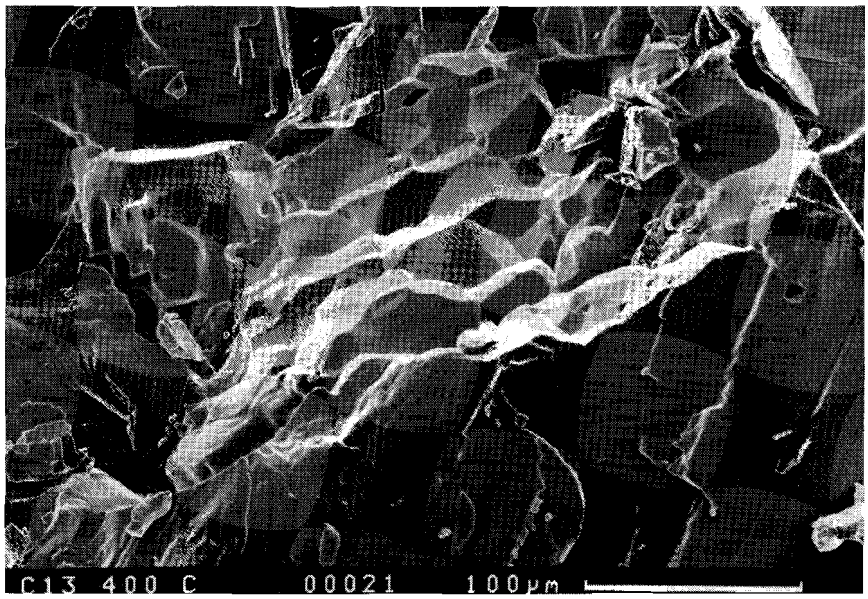

Figure 2.25a: *SEM images of mechanically parted grain boundaries in deformed synthetic rock salt.*
A parted grain boundary of a sample deformed at 400 °C. Grain boundary migration is faster that edge-wise propagation of subgrain boundaries and this results in three dimensional cuspate grain boundaries. The planes with a lineations represent stepped cleavage planes.

the critical strains (60%) needed for fast solute-escape migration to occur as suggested by Guillopé and Poirier (1979) and the gradual increase in migration recrystallization activity with temperature suggest that migration recrystallization is of the slow solute-loaden type over the whole temperature range investigated. Furthermore, the grain boundary structure of the recrystallized polycrystalline halite obtained in this study (Fig. 2.25a) does not resemble the high-angle grain boundaries developed in the single crystals which exhibit fast migration recrystallization. Further work is needed to establish whether an entirely different process is operating in the present experiments.

2.6.2 *The relationship between migration recrystallization and creep behaviour*

Derby (1990, 1991, 1992) has developed a model for dynamic recrystallization by grain boundary migration that may explain the stress

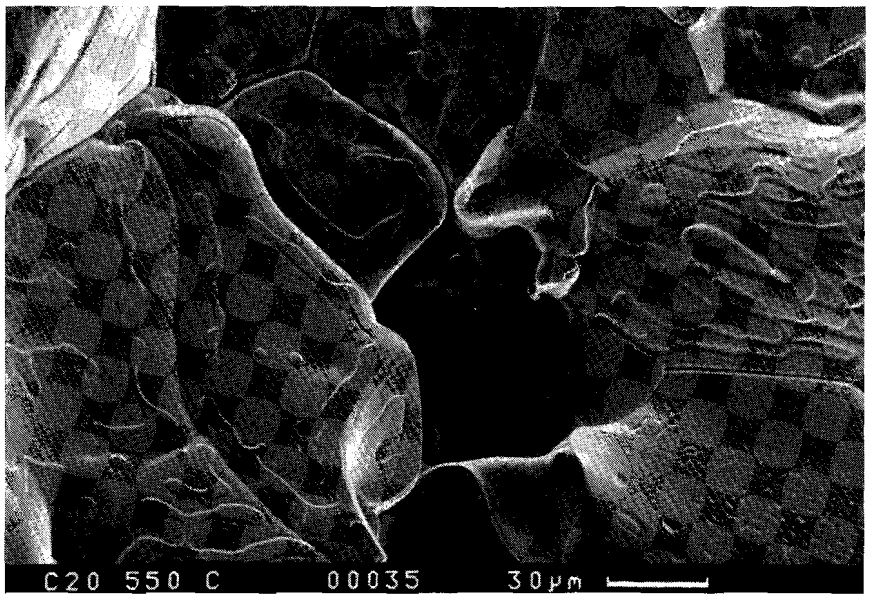

Figure 2.25b: *SEM images of mechanically parted grain boundaries in deformed synthetic rock salt.*
At 550 °C, the mechanically parted mobile grain boundaries contain an intricate channel-and-island structure. The grains intersect at triple junctions.

- steady state grain-size relations found in various metals and rock-forming minerals. This model assumes that recrystallization occurs by bowing out of grain boundary segments between subgrain boundaries. A nucleation criterion is developed which is based on the distribution of subgrain boundaries in the polygonized grains *prior* to recrystallization. For steady state to occur, the model assumes that a dynamic balance exists between the *nucleation rate* of new grains and the *migration rate* of already nucleated grains. Derby expresses this balance as follows: in the time taken for a moving grain boundary to sweep a volume equivalent to the steady state grain size, the nucleation rate I should be sufficient to allow one nucleation event to occur in each equivalent volume averaged over the microstructure. If nucleation is confined to the pre-existing grain boundaries, this balance can be expressed as:

$$\frac{CD^3I}{g} = 1 \qquad (2.9)$$

where C is a geometrical constant equal to about 3 (Derby, 1992), D is the recrystallized grain size, I is the nucleation rate and g is the grain boundary migration rate.

The migration recrystallization/nucleation process observed in the polycrystalline halite is similar to the processes described in Derby's recrystallization model. Now, the microstructural development of the polycrystalline halite will be considered against the background of Derby's recrystallization model. One interesting observation is that migration recrystallization becomes the dominant microstructural process when the rate-controlling process for creep changes from pipe diffusion to lattice diffusion (i.e. for temperatures above 500 °C). At temperatures above 500 °C, migration recrystallization controls the microstructural development and it is assumed that Eq. 2.9 applies, whereas below 500 °C no steady state grain size develops, since old deformed grains are always present. At temperatures below 500 °C, the volume *to be* swept by a moving grain boundary during the unit time necessary for one nucleation event to occur is larger than the volume *actually* swept by the moving grain boundary. This can be expressed as:

$$CD^3I > g \qquad (2.10)$$

If during a temperature increase, say for example from 450 to 550 °C, migration recrystallization becomes the dominant microstructural process, Eq. 2.10 is then replaced by Eq. 2.9 over that particular temperature interval. For a fixed strain rate, an increase in temperature from 450 to 550 °C would mean that the inequality of Eq. 2.10 is replaced by Eq. 2.9 such that:

$$1 = \frac{CD^3I \text{ (at 550 °C)}}{g \text{ (at 550 °C)}} < \frac{CD^3I \text{ (at 450 °C)}}{g \text{ (at 450 °C)}} \qquad (2.11)$$

This can be achieved by a decrease on the left-hand side of the product CD^3I (in Eq. 2.10) or by an increase in grain boundary migration rate g, over the temperature range 450-550 °C. In what follows, the dependence of the individual parameters of Eq. 2.9 on temperature will be discussed qualitatively (in other words the strain rate is kept constant).

The steady state grain size D is related to the applied stress: $D \propto \sigma^{-3/2}$ (Derby 1991, 1992). Thus, for a fixed strain rate, an increase in temperature will result in larger recrystallized grain sizes.

The nucleation rate I depends on the stored energy of the deformed grains and the majority of the stored dislocation energy will be in the subgrain boundaries (Derby, 1991). The nucleation rate thus depends on the number of subgrains per grain:

$$I \propto D/d_{sg}$$

In halite, the subgrain size d_{sg} depends on the inverse of the stress (see above), therefore:

$$I \propto D\sigma$$

Thus, for a fixed strain rate the nucleation rate will increase with temperature since $D \propto \sigma^{-3/2}$ and consequently $I \propto \sigma^{-1/2}$. Thus, the product on the left-hand side of Eq. 2.10 is proportional to σ^{-5} and will increase with temperature and changes in nucleation rate or steady state grain size cannot explain the microstructural observations. From the above, it is clear that g must increase with temperature. The increase in g from 450 °C to 550 °C must exceed the increase of the product CD^3I such that:

$$\frac{CD^3I \text{ (at 550 °C)}}{CD^3I \text{ (at 450 °C)}} < \frac{g \text{ (at 550 °C)}}{g \text{ (at 450 °C)}}$$

The migration rate g is related to the stored energy F by a mobility term such that g = MF. The stored energy F of a dislocation network is given by (Derby, 1991):

$$F = C_2\gamma_s/d_{sg}$$

where C_2 is a geometric factor equal to about 3 and γ_s is the mean energy per unit area of the sub-boundaries (the majority of the stored energy is in subgrain boundaries). The energy of a subgrain boundary is relatively temperature independent. From this it follows that the driving force F is proportional to the inverse of the subgrain size and from the stress - subgrain size relations it can be deduced that the driving force $F \propto \sigma$. In other words, for a fixed strain rate, the driving force decreases with increasing temperature and this cannot explain the microstructural observations. In order to obtain a microstructure controlled by migration recrystallization, over the temperature interval 450 - 550 °C, the grain boundary mobility term must increase strongly. The grain boundary mobility is given by a diffusion relation:

$$M = \delta D_b \exp(-Q_b/RT) \qquad (2.12)$$

where δ is the mean grain boundary width, D_b is the grain boundary diffusion coefficient and Q_b is the grain boundary diffusion activation energy. The pre-exponential in Eq. 2.12 is temperature independent and does not influence the relative increase in M. Commonly, the grain boundary activation energy in NaCl is taken to be equal to the pipe diffusion activation energy (Verall et al., 1977; Frost and Ashby, 1982; Derby, 1992). The mobility term M increases with increasing temperature and for migration recrystallization to be dominant this increase must at least compensate the decrease in driving force F and the increase of the term on the left-hand side of Eq. 2.10. Thus, the condition for migration recrystallization to be the dominant microstructural process, with a temperature increase from 450 to 550 °C, is given by:

$$\frac{CD^3I \text{ (at 550 °C)} \times F\text{(at 450 °C)}}{CD^3I \text{ (at 450 °C)} \times F\text{(at 550 °C)}} < \frac{M\text{(at 550 °C)}}{M\text{(at 450 °C)}} \qquad (2.13)$$

The term CD^3I is proportional to σ^{-5} (see above) which in turn is proportional to the $\dot{\varepsilon}^{n/5}$. The driving force F is proportional to the stress, i.e. proportional to the $\dot{\varepsilon}^{1/n}$. For a constant strain rate, the relative decrease in driving force by increasing temperature T_1 to T_2 is given by:

$$\frac{\sigma(T_1)}{\sigma(T_2)} = \frac{\exp(-\Delta H/nRT_2)}{\exp(-\Delta H/nRT_1)} \qquad (2.14)$$

The value for ΔH in Eq. 2.14 is taken to be the lattice diffusion activation energy ΔH at 550 °C (227 kJ/mol) and the pipe diffusion activation energy at 450 °C (129 kJ/mol). The stress exponents are taken as 4.4 and 5.7 respectively. Combining Eqs. 2.13 and 2.14 gives, for the temperature rise from 450 to 550 °C:

$$1.5 \times 10^{-10} < 13.6$$

which is true and a condition for migration recrystallization is fulfilled. In the pipe diffusion field, however, this condition is not fulfilled: in other words the mobility term increases less than the left-hand term of Eq. 2.13 for a temperature increase of 350 to 450 °C and Eq. 2.9 does not apply.

The increase in grain boundary mobility coincides with a change in grain boundary morphology (Fig. 2.25). Mobile grain boundaries con-

tain inclusion-like channel structures (Fig. 2.25b), typical of recrystallized grains (Drury and Urai, 1990) and are similar to those observed in recrystallizing wet salt aggregates (Spiers et al., 1990) and in hot pressed healed calcite (Olgaard and Fitz Gerald, 1993). At lower temperatures, the less mobile grain boundaries are characterized by subgrain boundary intersection and the channel structures are not developed (Fig. 2.25a).

In summary, the microstructural evolution in polycrystalline halite can at least be qualitatively explained by Derby's (1990, 1991, 1992) dynamic recrystallization model. Below 500 °C, the boundary migration rate is too low to sweep a volume equivalent to the recrystallized grain size in the time that one nucleation event occurs or the nucleation rate is so low that by the time an equivalent volume is swept by the migrating boundary less then one nucleation event has occurred. It should be noted, however, that some grain boundary migration occurs at low temperatures, although it is not dominating the microstructural development and presumably steady state recrystallized grain sizes do not develop.

2.6.3 *Subgrain-size evolution and strain rate history effects*

The concept whether the creep rate of a polycrystal depends on the subgrain size has been a point of controversy (Robinson et al., 1974; Pontikis and Poirier, 1975; Miller et al., 1977; Poirier, 1985). It is commonly accepted that if steady state microstructures develop, the mechanical behaviour is not dependent on the subgrain size. The crucial point in the discussion is if and for how long the subgrain size remains unchanged and stable after an abrupt change in strain-rate (Poirier, 1985). Especially subgrain refinement before a stress/strain-rate drop may have an effect on the transient behaviour of the material (Sherby et al., 1977).

In various materials the subgrain size has been seen to decrease with increasing stress. In case of synthetic or natural rock salt (Carter et al. 1982, Carter & Hansen 1983), AgCl (Pontikis and Poirier 1975) and olivine (Ross et al. 1980), the subgrain size does not appear to increase with decreasing stress or after annealing. This means that in such materials only the highest stress levels will be recorded. Stress drop experiments in metals show that the strain required to reach the new steady-state subgrain-size increases with the ratio of the steady-state subgrain-size to the subgrain size immediately before the stress drop (Miller et al., 1977). Thus, the imposed strains may not have been large enough in the experimental work described here.

Carter et al. (1984) claim that subgrains in NaCl enlarge upon lo-

wering in stress. In their strain-rate decrement experiments on Avery Island rock salt (T= 200 °C), the strain rate was changed abruptly after 4% strain (from 10^{-4} to 10^{-6} s^{-1}). The subgrains have been reported to grow to nearly equilibrium size, after 5 - 9% steady-state strain, by subgrain-boundary dissolution and migration.

With respect to the present study, first the influence of strain-rate history on the microstructural development of the polycrystalline halite will be discussed, followed by a discussion of the effects of strain-rate history on the mechanical behaviour.

The microstructures show that over the temperature range investigated the subgrains decrease in size with an increase in strain rate independent of test type (compare Figs. 2.12 and Fig. 2.16). The microstructural response to a decrease in strain rate appears to be temperature dependent.

Below *400-450 °C*, the subgrains in a strain rate decrement test remain small compared to equivalent constant strain-rate or increment step tests. Thus, the microstructural evolution during a decrement testis influenced by the strain rate history. This microstructural imprint, developed during the high strain-rate increments, is inherited during the subsequent steps, even if total strains in excess of 10% are subsequently imposed. Application of Miller et al.'s criterion to the present data would imply that the new steady state subgrain size would be at least twice the initially generated subgrain size. Or expressed in terms of stress, the expected stress during the lower strain-rate step would be half the stress attained during the highest strain-rate increment. The steady state stresses are higher than the values predicted by Miller et al. (1977). Apparently, in this temperature range processes like subgrain-boundary dissolution and migration are insufficiently effective to increase the subgrain sizes to the expected steady state size during the imposed subsequent strain increments.

Above *450-500 °C*, the subgrain sizes observed in the decrement step tests increase with decreasing strain rate after 3 - 5% strain. Grain boundary migration controls the microstructural development and the dislocation substructures in old deformed grains are renewed after a recrystallizing grain boundary sweeps through the grain interior afterwhich new steady state subgrains can develop.

The subgrain size-stress relations of the constant strain-rate and the various strain-rate step tests agree with existing relationships (Fig. 2.20).

The mechanical response of step tests is also temperature dependent (Fig. 2.9). Between 250 and 450 °C, the stress levels attained in steps, after the highest strain rate increment has been imposed, are con-

sistently higher than in equivalent constant strain-rate and increment step tests (Fig. 2.8). Above 500 °C, the mechanical results of all tests agree with each other (Fig. 2.10).

Only in case of decrement step tests has the strain-rate history an effect on the transient mechanical response in the 250-450 °C temperature range. This particular strain-rate history results in subgrain refinement, which is essentially a non-equilibrium microstructure. The small subgrains developed during this subgrain refinement process act as barriers to creep (Robinson et al., 1974). The effect of subgrain size d_{sg} on the creep rate is given by (Robinson et al., 1974; Sherby et al., 1977):

$$\dot{\varepsilon} = B\,(d_{sg})^{p}(\sigma/\mu)^{N}\exp(-(\Delta H/RT) \qquad (2.15)$$

where p is about 3 to 4 for NaCl.

When dealing with steady state subgrains the strain rate is proportional to $(\sigma/\mu)^{N-p}\exp(-(\Delta H/RT)$ where n = N-p (Robinson et al., 1974, Poirier, 1985). In other words, the creep rate is independent of subgrain size. If no steady state is attained, the strain rate is proportional to $(\sigma/\mu)^{N}$.

The decrement tests (in the 250-450 °C temperature range) can be considered as strain-rate step experiments with approximately constant structure (Miller et al., 1977; Sherby et al., 1977). In that case, since n=5.7 and p≈3 - 4 the value of the stress exponent N ranges between 8.7 and 9.7. The stress exponents N of the decrement step tests, which have been shown to contain a constant subgrain size d_{sg}, range between 7 and 10 (Fig. 2.9). The steady-state stress exponents n of constant strain-rate and increment step tests, where steady state subgrains develop, are approximately 5 to 6 (Fig. 2.10). In other words, the subgrain refinement imposed during the first high strain rate steps gives rise to a relative hardening effect of the samples in the subsequent steps according to Eq. 2.15. In the temperature range 250 to 450 °C, the nature and amplitude of a change in strain rate and the microstructural characteristics of the material before that change both determine the mechanical response (memory effect). Above 450 °C, however, recovery and recrystallization processes are sufficiently efficient and the microstructure re-adjusts with the new imposed conditions relatively rapidly (within 1% strain). In other words, the material no longer has a memory and the rheology is no longer history dependent.

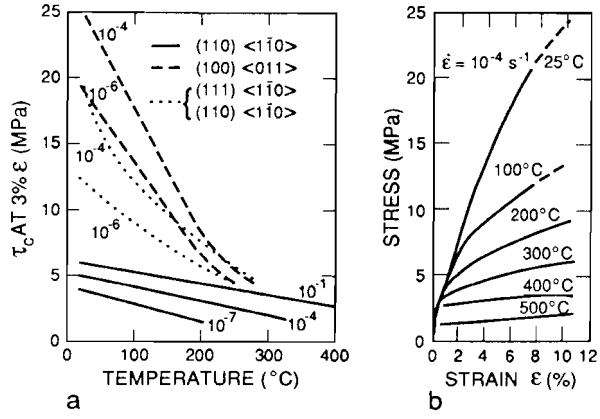

Figure 2.26:

(a) Critical resolved shear stress of the different slip systems in NaCl as function of temperature at different strain rates .(from Carter and Heard, 1970)

(b) Strain hardening illustrated by stress - strain curves for single slip on (110)[1$\bar{1}$0] as function of temperature at strain rate of 10^{-4} s^{-1} (from Carter and Heard, 1970).

2.6.4 *Crystallographic preferred orientations development*

In the temperature range 250 - 550 °C the textures of the uniaxially compressed samples show a strong tendency for the {110} planes of the relatively weak {110}<1$\bar{1}$0> slip system to rotate perpendicular to the compression direction (Fig. 2.21). At 250 °C, a weak <115> texture component is observed, which decreases with temperature. Dynamic recrystallization by grain boundary migration, the dominant microstructural process at 550 °C, appears to have no significant influence on texture development (Fig. 2.21e).

Texture development in synthetic polycrystalline halite with comparable deformation geometries has been studied by Kern & Braun (1973), Kern (1977), Kern & Richter (1985). Kern and co-workers deformed dry synthetic rock salt (grain size 0.05-0.4 mm) under uniaxial and true triaxial stress conditions, in the temperature range 20-200 °C, and with strain rates of the order of 10^{-6} s^{-1}. The uniaxial experiments showed axially symmetric pole figures, with {110}-planes perpendicular to the compression direction (maximum intensity 2 times uniform).

These textures compare reasonably well with the present results.

At low temperatures the slip systems in halite are strongly anisotropic and their rate and temperature dependency are known (Carter & Heard, 1970; Fig. 2.26). The easiest slip system in halite is {110} <1$\bar{1}$0> and at room temperature the {111}<1$\bar{1}$0> and {100}<1$\bar{1}$0> slip systems are about 6-7 times stronger. Extrapolation of the data shown in Fig. 2.26a suggests that at temperatures above 400 °C they all have comparable critical resolved shear stresses (crss).

Texture development in halite has been simulated by Wenk et al. (1989a), using a viscoplastic Taylor model and a viscoplastic self-consistent approach. The viscoplastic Taylor model assumes homogeneous strain and requires that all grains deform in the same way as the polycrystalline sample. In contrast to the "classic" Taylor theory, the viscoplastic Taylor model allows for rate dependency of the active slip systems instead of a rigid plastic behaviour. In addition to this, the viscoplastic self-consistent approach allows unfavourably oriented grains to deform less than favourably oriented grains. In other words, the viscoplastic self-consistent theory does not require strain compatibility and is suitable for modelling strongly anisotropic materials (Molinari et al., 1987).

Inverse pole figures predicted by the texture modelling simulating room temperature deformation at a strain rate of 10^{-4} s^{-1}, are shown in Fig. 2.27 (Wenk et al. 1989a). The Taylor model predicts a weak orientation around <110> and <100> whereas the self-consistent texture is characterised by a rotation towards <100>, i.e. a soft orientation (Fig. 2.27ab). In the Taylor model, most strain is accommodated by the harder {100} system only if the slip systems do not harden, whereas in the SC approach the strain is almost exclusively accommodated by the {110} system. If hardening is included, the {100} and later the {111} slip systems become significant as well in the SC approach. In the Taylor simulation a broad concentration near <110> develops, whereas in the self-consistent model two maxima at <110> and <100> develop (Fig. 2.27cd).

The experimentally obtained textures resemble the Taylor models more than the self-consistent simulations. The maximum around <110> with a weak shoulder towards <100> (Fig. 2.21) is predicted by the Taylor model with hardening (Fig. 2.27c) (and by self-consistent models with crss data of 400 °C quoted in Wenk et al. 1989a, p. 2027). With increasing temperature, the shoulder towards <100> appears to become stronger and the texture more resembles the Taylor model without hardening (Fig. 2.27a). This change is consistent with the decrease in hardening rate at elevated temperature (see Fig. 2.26b). The ab-

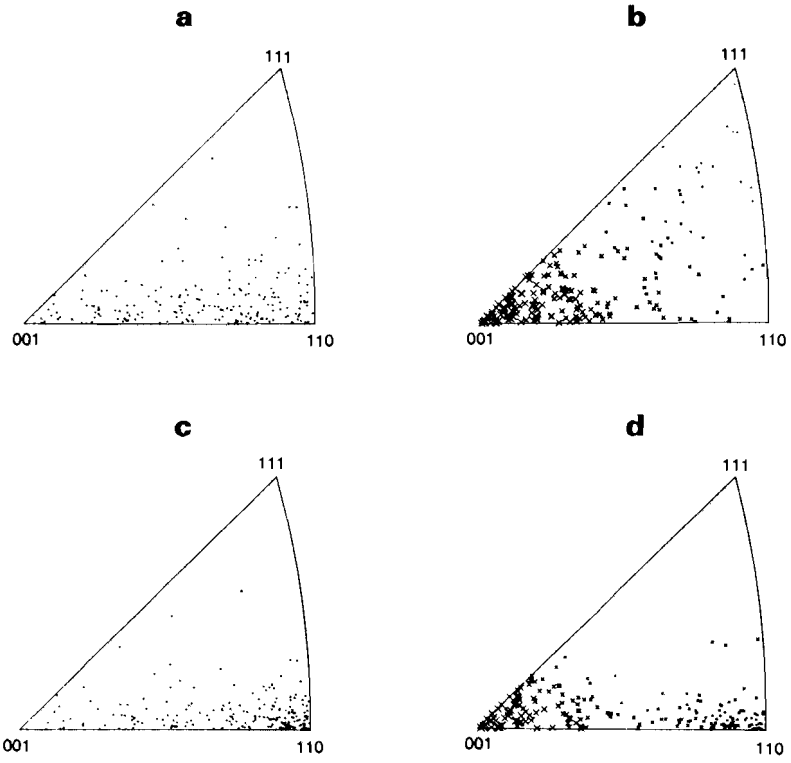

Figure 2.27:
Inverse pole figures for the compression direction, representing texture development in halite using Taylor and self-consistent theories (from Wenk et al., 1989a). The size of the symbols in b and d indicate relative average change in grain shape.

(a) Taylor model with no hardening
(b) Self-consistent model with no hardening
(c) Taylor model with hardening
(d) Self-consistent model with hardening

sence of a <100> component in the texture developed at 550 °C and the presence of a weak (insignificant?) <115> component observed at 250 °C cannot be explained at present. In conclusion, the textures of the uniaxial deformed salt do not resolve the question which texture model may best be used.

2.7 CONCLUSIONS

Synthetic polycrystalline halite has been deformed in uniaxial compression in the temperature range 250-780 °C ($0.5< T/T_m< 0.98$) at strain rates between $10^{-3}< \dot{\varepsilon}< 10^{-7}$ s^{-1}. Constant strain-rate, increment, decrement and cycling strain-rate step tests have been carried out. The main results can be summarized as follows:

1) Deformation occurred by climb-controlled dislocation creep. Between 450 and 780 °C, the creep rate is controlled by anion lattice-diffusion.
   In the temperature range 250 and 450 °C flow law is controlled by pipe diffusion. A quantitative comparison has shown that the present interpretation of the creep mechanism is consistent with published data on the deformation of synthetic rocksalt (Heard, 1972; Burke et al., 1981; Arieli et al., 1982).
2) In the temperature range 250 and 400 °C, the microstructural development is controlled by polygonization, rotation recrystallization and limited grain-boundary migration. The development of concavo-convex grain boundaries is consistent with strain-induced migration recrystallization. With increasing temperature, migration recrystallization becomes more important. At temperatures above 500 °C, migration recrystallization is the dominant microstructural process.
3) The transition to a migration recrystallization dominated microstructure coincides with the change from pipe-diffusion to lattice diffusion controlled dislocation creep. This is explained in relation to Derby's (1990, 1991, 1992) recrystallization model as due to relative changes between the driving force, the nucleation rate and grain boundary velocity, so that a balance can be established between the nucleation rate of new grains and the migration rate of nucleated grains.
4) Below 450 °C, the mechanical behaviour and the microstructural evolution of polycrystalline halite are strain-rate history dependent. Subgrains do not grow in size upon a lowering in strain-rate. This

process of subgrain refinement results in relative hardening effect and in an increase of the stress exponent from c. 6 to a 7 - 10.

Above 450 °C, recovery processes and especially migration recrystallization are sufficiently efficient to establish new steady state subgrain sizes. The mechanical behaviour and the microstructural evolution are no longer strain-rate history dependent (no memory effects).

In order to obtain useful mechanical data from strain rate stepping tests, it is necessary to ensure microstructural steady state in each step. In other words, the earlier loading history should not cause microstructural changes which may *influence* the mechanical behaviour of the subsequent steps (cf. stress relaxation technique; Rutter et al., 1978, Carter and Kirby 1978).

5) During uniaxial compression the {110} poles rotate parallel to the compression direction. The observed crystallographic preferred orientations agree favourably with viscoplastic Taylor and self-consistent texture simulations (Wenk et al. 1989). However, the experimental results do not constrain the model which most effectively applies to the deformation of polycrystalline halite.
6) Migration recrystallization does not appear to have a significant influence on texture development.

It is generally accepted that steady-state flow is essentially independent of the previous loading history and that the transient flow is very susceptible to the previous history (Aubertin et al., 1991). Studies modelling the mechanical response of geotechnical structures should account for the strain-rate history-dependent transient response. For analysis of salt tectonics the steady-state flow properties are crucial and the strain-rate history effect may not play a significant role.

In analogy with halite, rocks deforming by dislocation creep may also exhibit deformation-history dependent behaviour in the dislocation creep field at low temperatures ($0.5<T/T_m<0.7$).

SIMPLE SHEAR DEFORMATION
experiments on synthetic polycrystalline halite*

ABSTRACT

Synthetic polycrystalline halite (rocksalt) has been deformed in simple shear in both constant stress and constant strain-rate tests in the temperature range 250-600 °C (0.5 - 0.8T_m). The shear strain rates varied between 10^{-5} and 10^{-7} s^{-1} and the applied shear stress from 0.6 to 2.75 MPa. Steady state flow can be described by two flow regimes. At temperatures from 250-450 °C the flow law is given by:

$$\dot{\gamma} = 0.72 \exp(-93/RT)\, \tau^{5.2}$$

which is inferred to describe climb-controlled dislocation creep where climb is controlled by pipe diffusion through dislocation cores. At temperatures between 250-365°C polygonization and rotation recrystallization are the main processes influencing microstructural development. With increasing temperature, strain-induced grain boundary migration becomes more important, resulting in concavo-convex grain and cuspate grain boundaries. At temperatures from 500-600 °C the flow law is given by:

$$\dot{\gamma} = 2.65 \times 10^{8} \exp(-209/RT)\, \tau^{4.3}$$

which is inferred to describe climb-controlled dislocation creep where climb is controlled by lattice diffusion. In this temperature range, migration recrystallization, driven by strain-induced lattice-defect energy and by grain boundary energy, dominates microstructural development. The crystallographic preferred orientation developed at all temperatures is characterized by <110> poles perpendicular to the shear plane and the <111> direction parallel to the shear direction. The crystallographic preferred orientation pattern is independent of temperature, but its intensities are temperature dependent.

* *This chapter has been submitted to Mechanics of Materials as: Franssen, R.C.M.W. The rheology of synthetic rocksalt in shear deformation.*

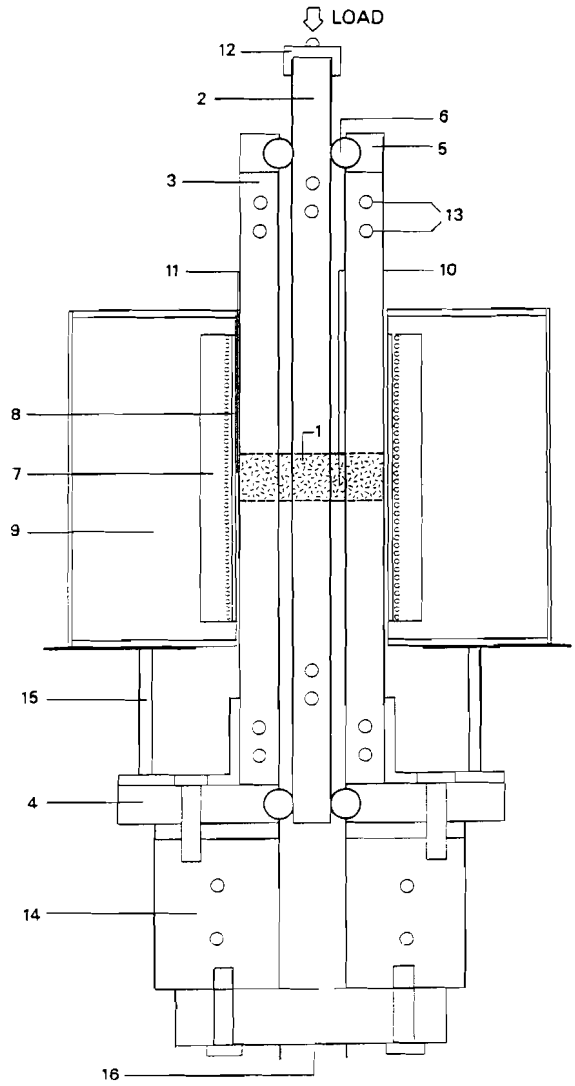

Figure 3.1:
Schematic diagram of the shear apparatus.
Key:

1: Cylindrical sample with reduced sections;
2: mobile middle bar;
3: fixed outer bars;
4: bottom platen fixating other bars;
5: idem, top platen;
6: roller bearings reducing friction of the middle bar and constraining its movement to vertical;
7: furnace windings in ceramic material;
8: insulating mica sheets;
9: ceramic fibre insulation;
10: sample thermocouple;
11: controller thermocouple;
12: spherical seat;
13: water-cooling access;
14: spacers;
15: furnace support;
16: Instron loading ram.

3.1 INTRODUCTION

Ductile deformation within the earth's crust is often inhomogeneous and localized in narrow zones where a non-coaxial deformation history dominates (Ramsay & Graham 1970; Ramsay, 1980). It is commonly assumed that such ductile shear zones evidence strong localization of deformation and may form major displacement zones. Such zones are therefore expected to control the bulk strength of the rock bodies in which they occur. There is ample evidence that localization of flow into shear zones plays an important role in the mechanical behaviour of the lower crust (Kirby, 1985; Ord and Hobbs, 1989; Rutter and Brodie, 1992) and upper mantle (Wernicke, 1985; Drury et al., 1991; Vissers et al., 1991).

Material strain softening is commonly taken as a requirement for the localization of deformation in natural ductile shear zones. Deformation processes proposed to explain shear localization by strain softening include recrystallization, lattice rotation and grain-size reduction (Poirier, 1980; White et al., 1980; Evans and Wong, 1985, Kirby, 1985). However, shear localization does not always have to be associated with macroscopic softening as has been observed in compression experiments in which localization of deformation occurred (for example Burrows et al., 1979). Localization may occur under strain-hardening conditions if the flow behaviour is characterized by the development of mechanical anisotropy during deformation (Leroy and Ortiz, 1990). Ductile shear zones can develop if the material in the shear zone flows at lower stresses than in the adjacent rock body. The onset of shear localization may result from the boundary conditions of the system, causing inhomogeneous deformation coupled with relative and not necessarily absolute strain softening (Hobbs et al. 1990; Jessel and Lister, 1991). The difference in flow strength between the localized shear zone and the adjacent rock body will subsequently maintain localization of deformation into the ductile shear zone. Insight into the conditions which favour localization and whether localization is ac-

companied by strain softening, is of importance for understanding the development of ductile shear zones and the rheology of the lower crust and upper mantle.

In natural deformation by intracrystalline plasticity, microstructural changes occur with large strains. These include grain shape fabric and crystallographic preferred orientation. The strain mode is an important control on the development of these microstructural changes and may lead to an anisotropic mechanical behaviour (Wenk et al., 1986; Takeshita, 1989). In addition, Tomé et al. (1984) have shown that the hardening rate of a deforming polycrystal may also depend on the deformation geometry (coaxial vs. non-coaxial).

Despite the geological relevance, non-coaxial deformation experiments are relatively rare in comparison to coaxial deformation experiments. Examples of non-coaxial deformation tests include 1) hollow cylinders subjected to torsional strains (Bouchez & Duval, 1982; Jessel & Lister, 1991), 2) thin rock wafers or gouge deformed in oblique cuts through cylindrical specimens subjected to triaxial loading conditions (Shimamoto & Logan, 1986; Knapp et al.,1987; Schmid et al., 1987; Borradaile & Alford, 1988; Dell'Angelo and Tullis, 1989), 3) extrusion type configurations (Kunze & Avé Lallement 1981), 4) indentation-type experiments (Kern & Wenk, 1983; Masuda, 1989; Ralser, 1989) and, 5) direct-shear box experiments (Price & Torok, 1989; Williams & Price, 1990; Cogné and Canot-Laurent, 1992). The reason for the lack of non-coaxial deformation experiments is the difficulty in obtaining a well-constrained non-coaxial deformation path while still being able to control and measure experimental variables such as the state of stress in the sample.

Ideally, one would like to perform simple shear experiments on silicate minerals making up the major constituents of the crust. However, with the current experimental techniques, small specimens have to be used to produce plastic deformation in silicate minerals under high temperature and pressure conditions, and there are severe limitations for obtaining relatively large strains and simultaneously obtaining good quality data.

In this study, simple shear experiments were carried out on a mineral analogue. Halite was used as the analogue because it deforms plastically without confining pressure at temperatures above 250 °C. This allows simple shear deformation, under atmospheric pressure, of relatively large samples in a relatively simple deformation apparatus. In addition, the mechanical properties of halite have been well described (e.g. Carter and Hansen, 1983) and the elementary intracrystalline

deformation mechanisms are similar to those seen to operate in silicate minerals.

The experiments were carried out on synthetic polycrystalline NaCl deformed in "simple shear" at intermediate to high temperatures ($0.5 < T/T_m < 0.8$). The aims of the study were to gain insight into the mechanical behaviour, microstructural evolution and development of crystallographic preferred orientation (textures) of synthetic rocksalt in simple shear deformation and to identify the microphysical processes operating during flow. Later, the role of deformation geometry on the flow behaviour and on the rate-controlling processes will be investigated by comparing the results with those obtained from uniaxial compression tests.

3.2 EXPERIMENTAL METHODS

In this study, dry synthetic polycrystalline NaCl samples were used. Analytical grade NaCl powder was hydrostatically cold-pressed at 100 MPa into a dense synthetic rocksalt. From these rocksalt billets, right cylindrical samples were machined with slots giving rise to reduced sections. These samples were 75 mm long and two sample diameters were used, namely 15 and 25 mm. The smaller diameter samples are denoted with an 's' in Table 3.1. After machining, the samples were annealed in an argon atmosphere at 720-725 °C for 12 - 14 hours. The starting material obtained possessed a recrystallized polygonal foam texture with a grain size between 100 and 400 μm (Fig. 2.1). Grain boundaries contained gas inclusions (tubular and sphericaly shaped) of 10 to 20 μm diameter. Etched thin sections revealed that the grains contained no optically visible internal microstructure. No significant crystallographic preferred orientation developed in the samples (Fig. 2.2). The porosity of the starting material ranged from 2% to 2.5%.

The shear experiments were carried out in a deformation apparatus shown in Fig. 3.1, mounted in an Instron 1362 loading frame. The geometry of the sample and of the shear rig are in broad lines similar to the set-ups used by Williams (1962) and Cogné and Canot-Laurant (1992). The shear rig basically consists of three parallel loading bars, of which the two outer bars are fixed to end-platens and are immobile. The middle bar is free to move parallel to the fixed outer bars only. Cylindrical samples with reduced sections were fitted lengthwise through aligned holes in the three loading bars. Advancing the middle bar downwards imposes a shear deformation on the reduced sections of the sample. A 10 kN load cell with an absolute accuracy better than

Table 3.1 *Experimental data of the constant shear strain experiments.*

Test number	Temperature (°C)	Shear strain rate (s^{-1})	Shear stress at γ=0,5 (MPa)	Final Shear stress	Final Shear strain
119s	250	$5.76 * 10^{-7}$	—	3.56	0.17
120s	250	$5.76 * 10^{-7}$	3.97	3.97	0.66
118s	300	$3.6 * 10^{-6}$	2.85	2.89	1.22
123	300	$3.6 * 10^{-6}$	3.40	3.46	0.56
125	300	$9 * 10^{-7}$	—	3.13	0.16[1)]
124	365	$7.2 * 10^{-6}$	2.29	2.23	0.99
121	365	$3.6 * 10^{-6}$	—	2.54	0.34
105	365	$5.76 * 10^{-7}$	1.84	1.94	0.61
117s	400	$7.2 * 10^{-6}$	2.17	2.22	1.19
122	400	$3.6 * 10^{-6}$	2.16	2.27	0.96
114s	400	$3.6 * 10^{-6}$	2.58	2.67	1.58
112s	450	$7.2 * 10^{-6}$	1.87	2.20	1.80
104	450	$3.6 * 10^{-6}$	1.50	1.50	0.59[2)]
113s	450	$3.6 * 10^{-6}$	1.80	1.74	0.59
127	450	$3.6 * 10^{-6}$	1.46	1.46	0.50
101	500	$7.2 * 10^{-6}$	1.41	1.41	0.55
110s	500	$7.2 * 10^{-6}$	1.43	1.43	0.66
111s	500	$7.2 * 10^{-6}$	1.37	1.5	1.95
106	495	$2.5 * 10^{-6}$	1.00	1.02	0.63
115s	550	$9 * 10^{-6}$	1.09	1.31	1.62
109	550	$7.2 * 10^{-6}$	1.09	1.12	1.38
116s	550	$7.2 * 10^{-6}$	1.27	1.30	1.18
108	550	$3.6 * 10^{-6}$	0.76	0.75	0.96
126st1	600	$3.6 * 10^{-6}$	—	0.52	0.32
126st2	600	$7.2 * 10^{-6}$	0.58	0.58	0.70
126st3	600	$3.6 * 10^{-5}$	—	0.8	

1) Sample failed during the experiment.

2) Due to an erroneous termination of this test, the sample was subjected to a higher but unknown final strain than given in the Table.

0.5% and a resolution better than 0.01% of the full load was used to measure the applied load and hence the total shear stress supported by the sample. Normal stresses acting parallel to the length of the sample could not be measured. Displacement (hence shear strain γ) was mea-

Table 3.2 *Experimental data of the creep tests in shear*

Test number	Temperature (°C)	Shear stress (MPa)	Strain rate (s^{-1})	Shear strain at end of test
203	365	2.75	$1.29*10^{-5}$	0.63
206st1	400	1.23	$6.61*10^{-8}$	0.019
206st2	400	.59	$5.37*10^{-7}$	0.105
201	450	1.4	$1.86*10^{-6}$	0.63
204st1	445	1.0	$4.79*10^{-7}$	0.10
204st2	445	1.24	$1.41*10^{-6}$	0.184
202	495	0.94	$1.86*10^{-6}$	0.72
207	550	0.97	$1.10*10^{-5}$	0.59

sured using the linear variable differential transformer (LVDT) located in the drive unit of the Instron 1362.

Shear experiments were carried out in the temperature range 250-600 °C, under unconfined (i.e. atmospheric pressure) conditions. Typically, the temperature was kept constant to within 5 °C. Constant shear strain rates varied between 10^{-5}-10^{-7} s^{-1} (Table 3.1). In addition, a limited number of creep tests were carried out with constant applied shear stress between 0.59 and 2.75 MPa (Table 3.2).

Stress-strain curves and strain-time curves were calculated from strip-chart records of force and displacement vs. time. The stresses were corrected for the weight of the middle bar. Strain and strain rates were calculated with respect to the starting dimensions of the sample. The microstructures of both the deformed and undeformed samples were studied by means of reflected light microscopy carried out on polished sections and by SEM. Grain boundaries and dislocation substructures were made visible by etching the polished sections (Spiers et al., 1986).

Crystallographic preferred orientations of selected samples were measured using neutron diffraction to determine pole figures for {220}, {200} and {111} reflections. From the pole figures, the orientation distribution function was calculated for each sample. From this, the inverse pole figures for the shear direction and the normal to the shear plane were determined (Bunge 1982; Dahms and Bunge, 1989; Dahms, 1992).

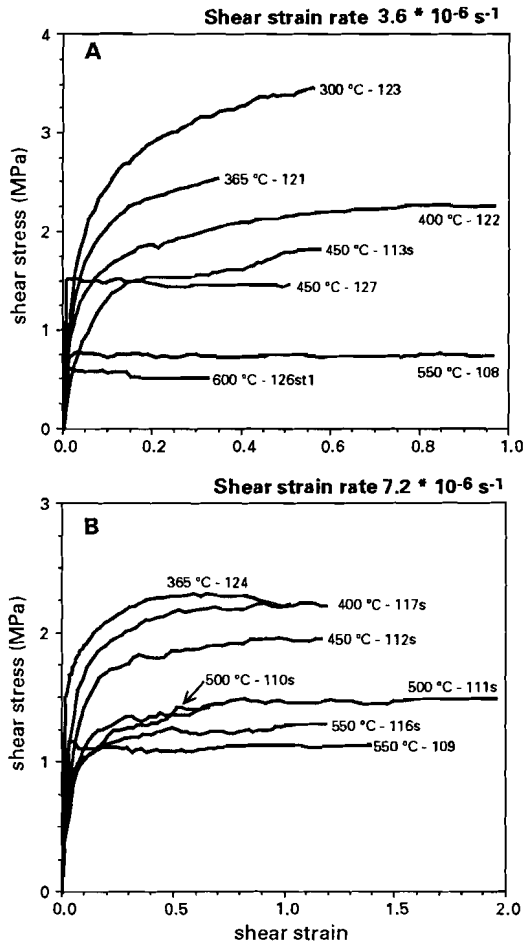

Figure 3.2:
Applied shear stress versus shear strain plots for polycrystalline halite samples deformed in shear. Each curve is labelled with test temperature and test number (italics).

(a) For temperatures between 300 and 600 °C and an applied shear strain-rate of $3.6*10^{-6}$ s^{-1}.

(b) For temperatures between 365 and 550 °C and an applied shear strain-rate of $7.2*10^{-6}$ s^{-1}.

Note the different horizontals scales in (a) and (b).

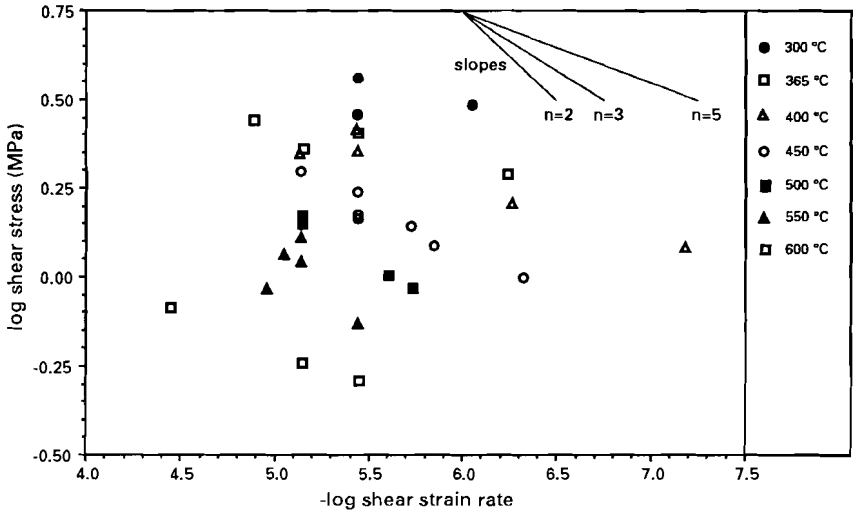

Figure 3.3:
Experimental shear stress and shear strain-rate data plotted in log-log space for temperatures between 300 and 600 °C. The shear strain-rate depends on the power 3 to 5 of the shear stress. These data are used to determine the flow law parameters.

3.3 EXPERIMENTAL RESULTS

3.3.1. *Mechanical behaviour*

The experimental results are summarized in Tables 3.1 and 3.2. Typical shear stress (τ) vs. shear strain (γ) plots for two different constant shear strain-rates are shown in Fig. 3.2. Below 450 °C, all curves show considerable work-hardening at shear strain up to 0.2 - 0.4. With increasing deformation steady state is approached and the flow stresses range from 2 to 4 MPa. With increasing temperature, the amount of work-hardening decreases. At 600 °C, for example, steady state is attained within a shear strain of 0.1 and the flow stress thereafter is only 0.5 MPa.

The flow stress may fluctuate within 4% of the steady state value; these small stress variations can be attributed to laboratory temperature variations. Samples with different diameter (15 or 25 mm) yield similar steady state stress values (within 10% of each other), for example tests 116s and 109, see Fig. 3.2b.

The dependency of stress upon strain rate is shown in Fig. 3.3. The data listed in Tables 3.1 and 3.2 were used to construct -log shear strain-rate (-log$\dot{\gamma}$) versus log applied shear-stress (logτ) plot. Assuming

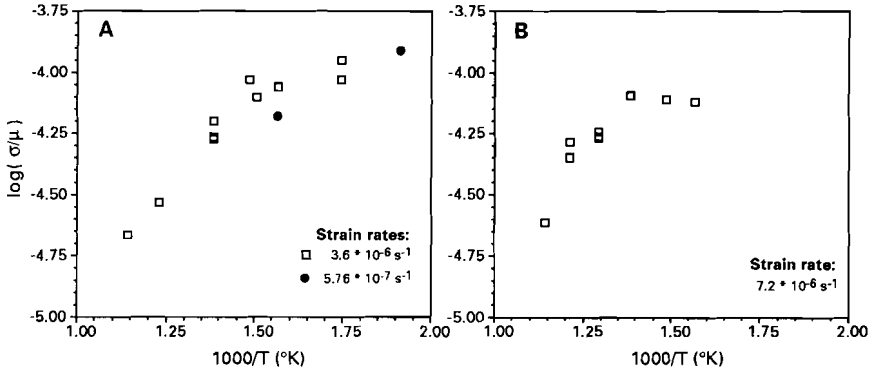

Figure 3.4:
Arrhenius-type plot of the quantity log(τ/μ) vs. 1000/T for constant shear strain-rates.
(a) Shear strain-rate of $3.6*10^{-6}$ s^{-1}. In addition two data points with shear strain-rate of $5.76*10^{-7}$ s^{-1} are shown.
(b) Shear strain-rate of $7.2*10^{-6}$ s^{-1}.

a power-law relation, the shear strain-rate depends on the shear stress to the power of 3 to 5. The dependency of flow stress upon temperature is illustrated in Arrhenius plots (Fig. 3.4). In these plots the quantity $\log(\tau/\mu)$, which is the shear stress normalized against the temperature-compensated shear modulus (μ) (Robinson et al., 1974; Burke et al., 1981) is plotted against the quantity (1000/T), which represents the reciprocal absolute temperature. The data can be approximated by two straight line segments, and the Arrhenius plot is curved in the interval $1.4 < 1000/T < 1.5$ where the two lines inter-vene.

3.3.2 *Microstructural observations*

The microstructural development of deformed polycrystalline halite was found to depend on temperature. As with the microstructural development observed in uniaxially compressed halite (Chapter 2), three temperature intervals could be distinguished each with their own characteristic microstructural evolution. The microstructure of the undeformed starting material is shown in Fig. 2.1.

250-365 °C (Fig. 3.5)

At shear strains below 0.2, the deformed salt shows slightly deformed grains (Fig. 3.5a). Subgrains with incomplete boundaries indicate incipient polygonization involving climb (Friedman et al., 1984).

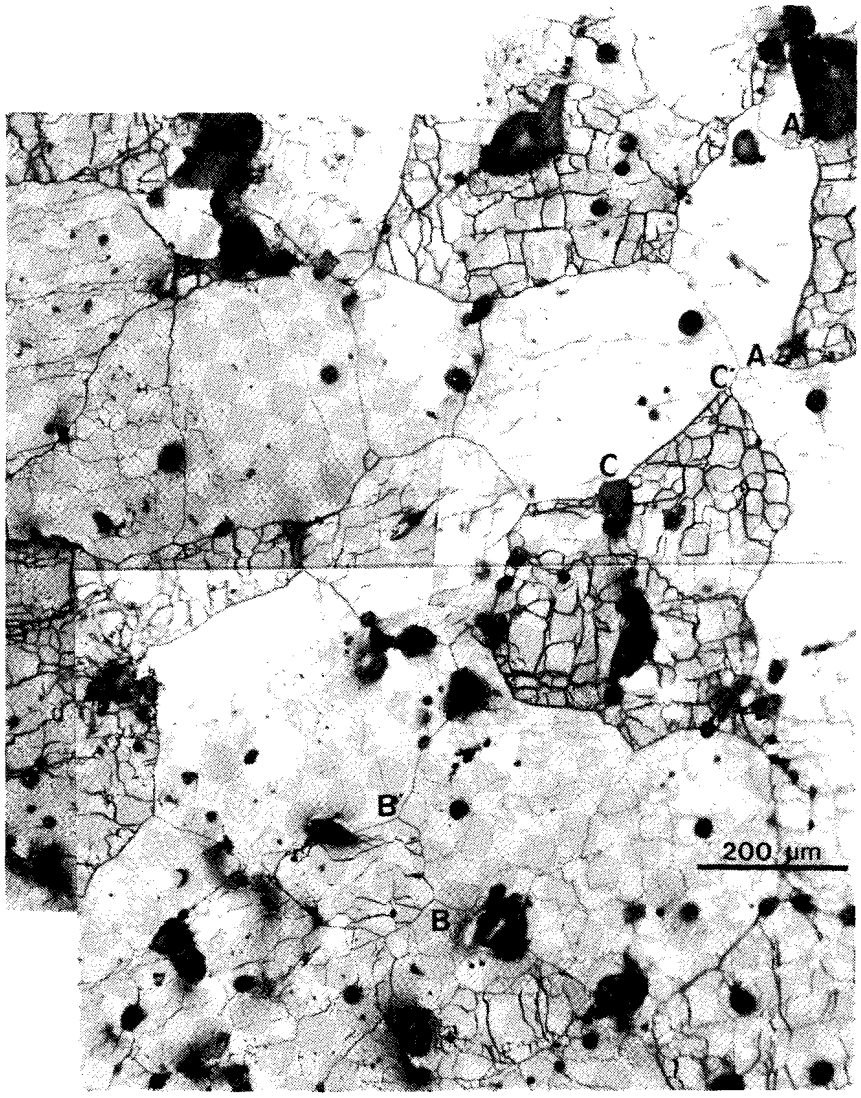

Figure 3.5a: *Microstructures developed in sheared polycrystalline synthetic rocksalt at 250-365 °C. Some micrographs may contain circular dark spots in grain interiors, these are artefacts resulting from etching.*

At low shear strains a deformed network of polygonal grains containing subgrains developed. The grain boundaries remain straight (for example CC')
(Sample 121, 365°C, $\gamma = 0.34$, sinistral sense of shear).

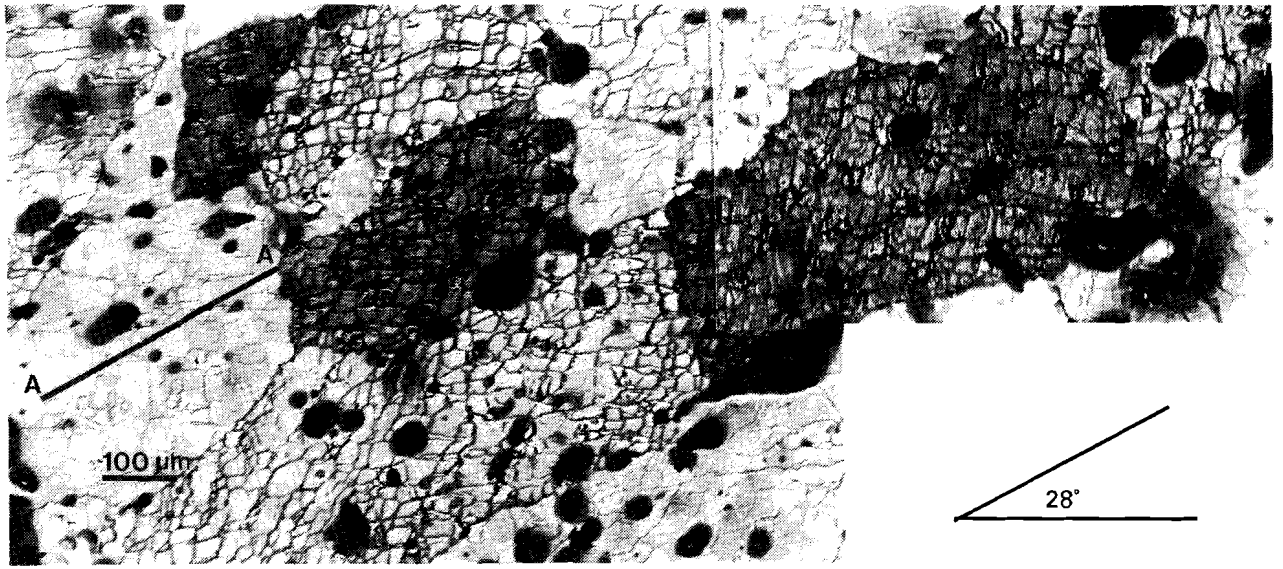

Figure 3.5b: *Microstructures developed in sheared polycrystalline synthetic rocksalt at 250-365 °C. Some micrographs may contain circular dark spots grain interiors, these are artefacts resulting from etching.*

Subgrain development and grain flattening are the controlling the microstructural processes, resulting in a foliation defined by flattened grains.

(Sample 118s, 300°C, γ = 1.22, left lateral shear zone). The orientation of the foliation (AA') is parallel to the orientation of the plane of finite flattening. The latter makes an angle of 28° with the shear plane for a shear strain of 1.22.

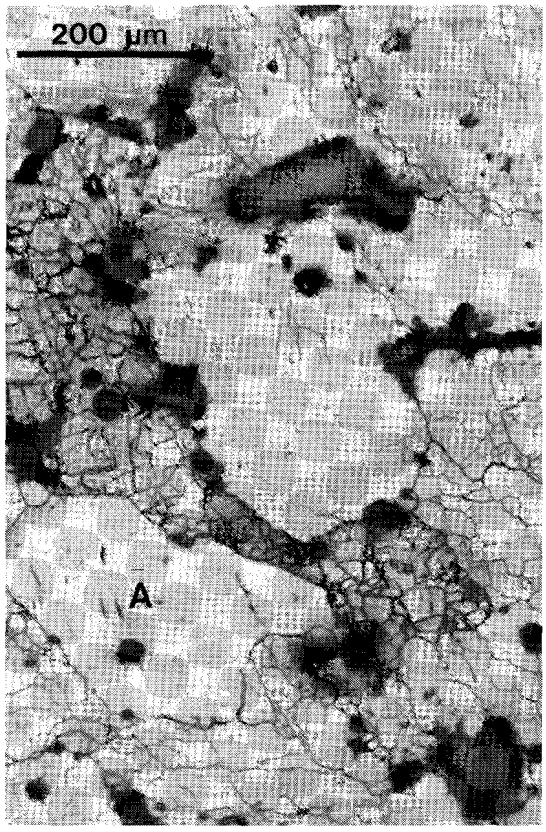

Figure 3.5c: *Microstructures developed in sheared polycrystalline synthetic rocksalt at 250-365 °C. Some micrographs may contain circular dark spots grain interiors, these are artefacts resulting from etching.*

Some grain boundary migration, controlled by subgrain-boundary intersections, is seen to occur at temperatures as low as 300 °C. (Sample 123, 300°C, γ = 0.56, left lateral shear zone).

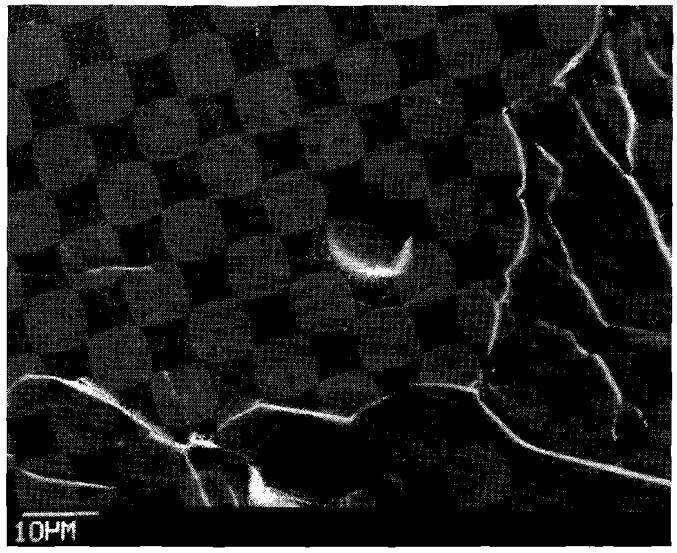

Figure 3.5d: *Microstructures developed in sheared polycrystalline synthetic rocksalt at 250-365 °C. Some micrographs may contain circular dark spots grain interiors, these are artefacts resulting from etching.*

SEM micrograph of grain boundary containing small bulges with wavelengths controlled by subgrain - grain boundary intersections. Detail of grain A shown in Fig. 3.5c.

With increasing shear strain ($\gamma = 1.22$), subgrain development and grain flattening are more pronounced, resulting in a strong grain-shape fabric. The transition zone from undeformed "wall rock" into the shear zone is narrow and is approximately equal to the initial grain size (Fig. 4.6). The lack of deformation features in the "wall rock" outside the transition zone indicates that the deformation is *confined* to the imposed shear zone. The orientation of the foliation defined by the flattened grains is in close agreement with the orientation of the plane of finite flattening of the strain ellipse calculated for the imposed shear strain (Fig. 3.5b). This indicates that deformation was close to *homogeneous* simple shear. Subgrain shapes have a blocky shape with one wall approximately parallel to the shear zone boundary. Since halite is optically isotropic, optical microscopy does not reveal the orientation differences between subgrains.

With increasing shear strain, a well-defined grain shape fabric develops, and the grain-boundary morphology changes significantly.

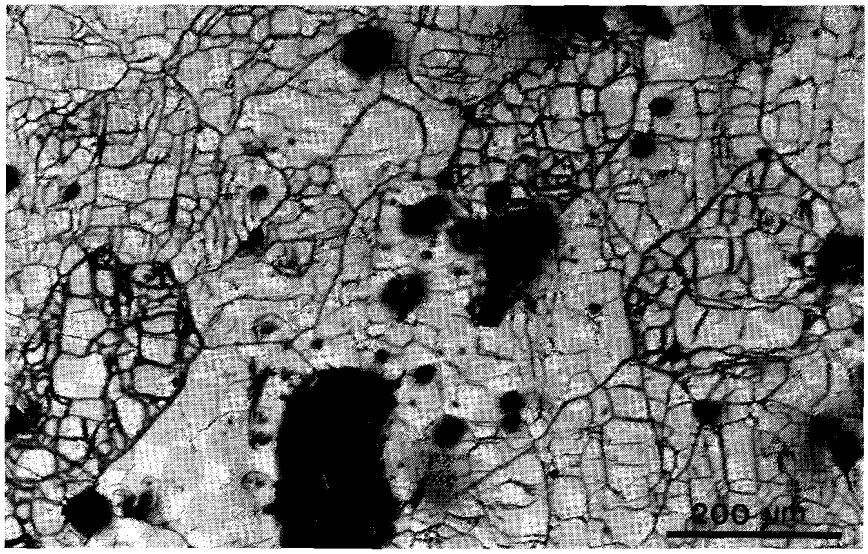

Figure 3.6a: *Microstructures developed in sheared polycrystalline halite at 400-500 °C.*
At low shear strains a network of deformed polygonal grains, containing blocky subgrains developed.
(Sample 204, 450°C, γ = 0.18, right lateral sense of shear).

Whereas at low shear strains most grain boundaries are relatively straight (Fig. 3.5a), at high shear strains the grain boundaries contain bulges and become cuspate (Fig. 3.5c, d). The small bulges and cusps develop where subgrain-boundaries intersect with grain-boundaries. The grain boundary cusps have a consistent polarity. Irregular lobate grains may develop, changing the geometry of the deformed polygonized network considerably (Fig. 3.5c).

400-500 °C (Fig. 3.6)
At low strains (γ = 0.18), a network of deformed polygonal grains can be discerned (Fig. 3.6a). The grains contain a well-developed cellular network of blocky subgrains indicating efficient polygonization.

With increasing strain (γ = 1), two counteracting processes occur (Fig. 3.6b, c). Grain flattening tends to define a foliation whereas grain-boundary migration tends to weaken this fabric. Examination of numerous thin sections suggests that between dark-etched and light-

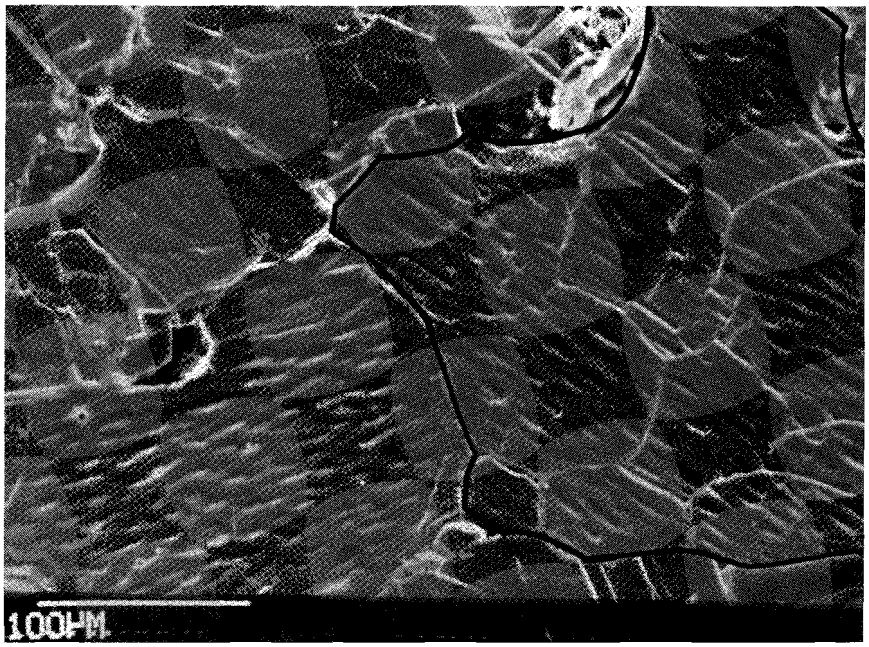

Figure 3.6b: *Microstructures developed in sheared polycrystalline halite at 400-500 °C.*

(b) SEM micrograph of concavo-convex grain contacts. The grains contain cellular networks of subgrains as is indicated by etching and the small epitaxial overgrowths. The grain boundaries of grains in the lower left and top right of the micrograph are inferred to migrate into outlined grain A.
(Sample 101, 500°C, γ = 0.55, left lateral shear zone).

(c) Migrating grain boundaries become cuspate with the bulges defining a consistent polarity. The bulges are controlled by subgrain-boundary - grain boundary intersections. The polarity of the cusps indicate the migration direction. Amplitude and wavelengths of the cusps increase with temperature.
(Sample 122, 400°C, γ = 0.96, left lateral shear zone).

(d) Irregular grain boundaries are visualised by the different orientations of epitaxial overgrowth structures. The lobes and bulges may have small radii of curvature and indicate a high grain boundary mobility.
(Sample 101, 500°C, γ = 0.55, left lateral shear zone).

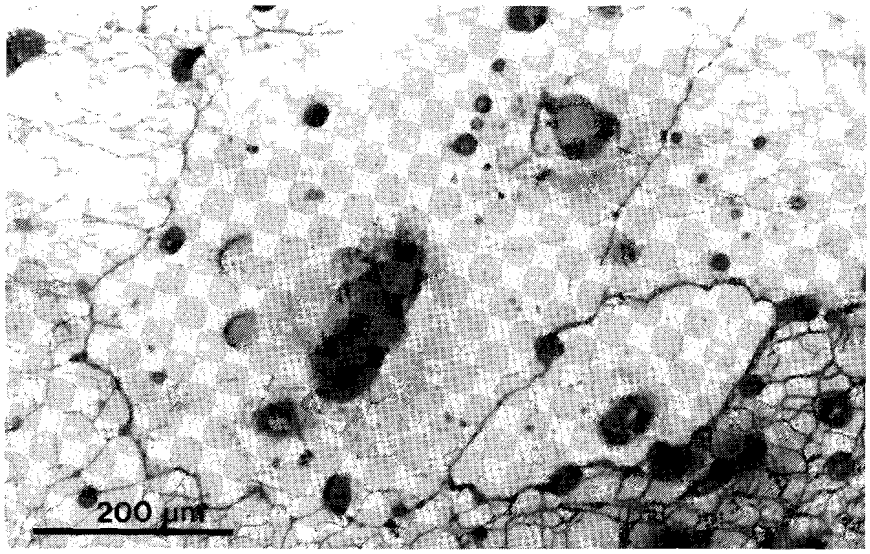

Figure 3.6c: *Microstructures developed in sheared polycrystalline halite at 400-500 °C.*

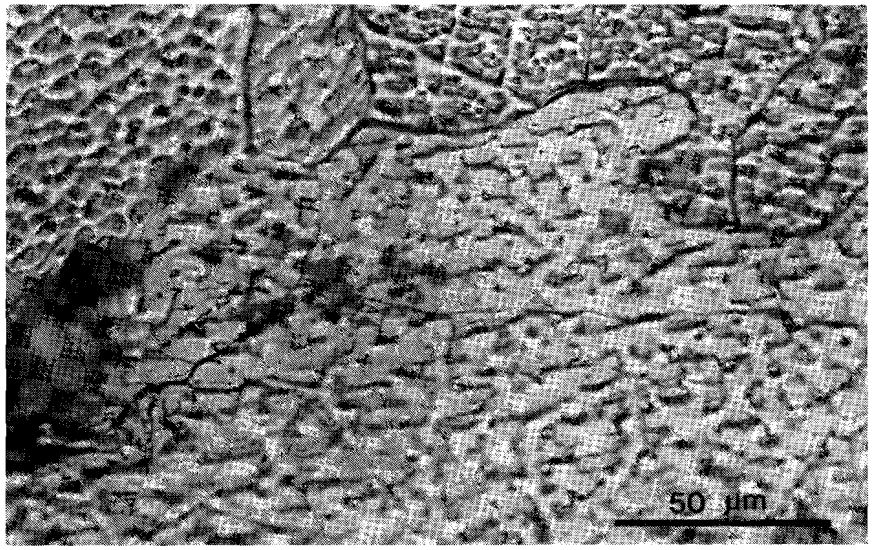

Figure 3.6d: *Microstructures developed in sheared polycrystalline halite at 400-500 °C.*

etched grains, concavo-convex cuspate contacts develop. Dark-etched grains contain higher densities of substructures (subgrains, etch-pits, slip lines) than light-etched grains. Predominantly, the dark-etched grains are at the convex side and the light-etched grains are at the concave side of these cusps. These features suggest that the boundaries of the light-etched grains migrate into the darker grains. This is interpre-

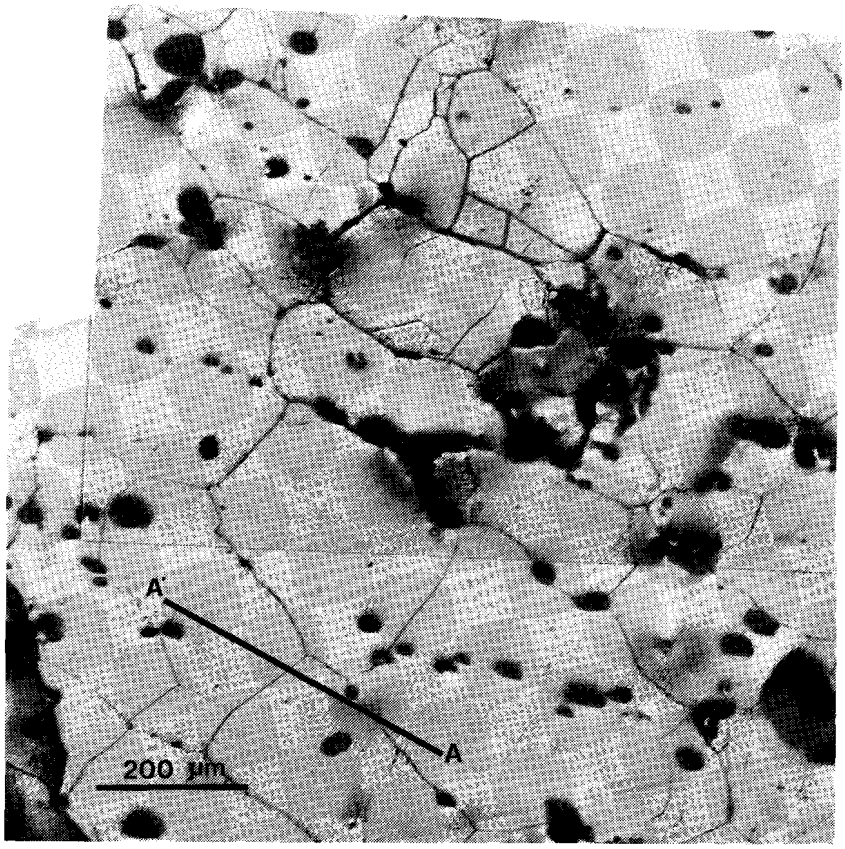

Figure 3.7a: *Microstructures developed in sheared polycrystalline salt at 550-600 °C.*
(a) An almost completely recrystallized fabric defines a weak grain shape preferred orientation. The grain shape fabric makes a larger angle with the shear plane compared to the plane of finite flattening. The grain boundaries are straight or slightly curved. The grains contain few large subgrains.
(Sample 109, 550°C, γ = 1.38, left lateral shear zone).

ted to indicate grain-boundary migration with migration away from the centre of curvature. The wavelength of the cusps of the migrating grain boundaries is determined by the subgrain-size spacing (Fig. 3.6c). This suggests that the subgrains at the concave side of the grain boundary exert some control on the migration process. However, locally inclusions at the grain boundaries control the presence of grain boundary cusps. With increasing temperature, the amplitude and wavelength of the cusps increases, indicating enhanced grain boundary mobility (compare Fig. 3.6c with Fig. 3.5c). Locally, sometimes very irregular grain lobes are observed (Fig. 3.6d). The grain boundaries resemble the grain-boundary geometries in dynamically recrystallized bischofite (Urai, 1983).

In the temperature interval 400-500 °C, polygonization (plus possible rotation recrystallization) and grain boundary migration are the dominant microstructural processes.

550-600 °C (Fig. 3.7)

Compared to lower temperatures, relatively large grains with fewer substructures are observed. A weak grain shape foliation is sometimes observed, but the orientation of this foliation does not coincide with the plane of finite flattening corresponding to the imposed shear strain (Fig. 3.7a). The foliation appears to lag behind in terms of shear strain and consequently the foliation makes a larger angle with the shear plane than plane of finite flattening. The foliation defined by the passively rotated grain boundary inclusions corresponds closely to the plane of finite flattening.

The subgrains developed at 550-600 °C are large and may be of the order of the grain size. The subgrains are no longer blocky in shape and intersect at equilibrium 120° triple junctions. The grain boundaries tend to be straight or slightly curved (weak concavo-convex grain contacts), and intersect at 120° triple junctions. Grain boundary inclusions, present at the grain boundaries in the starting material, may be incorporated in the recrystallized grains (Fig. 3.7a). Occasionally, pinning of migrating grain boundaries by inclusions is observed, causing small radii of curvature at the grain boundaries (Fig. 3.7b). Relatively few dark-etched grain are present. The relatively "clear" microstructure, the grain boundary morphology, and the weak development of a grain shape foliation, which does not keep pace with the total imposed deformation, suggest that recrystallization is continually operating during the tests (Drury & Urai, 1990).

It is inferred that the microstructural evolution above 500 °C is dominated by grain boundary migration.

Figure 3.7b: *Microstructures developed in sheared polycrystalline salt at 550-600 °C.*
A migrating grain boundary is pinned by grain boundary inclusions (arrows) and a grain boundary bulge with a small radius of curvature develops.
(Sample 108, 550°C, γ = 0.96, left lateral shear zone).

Table 3.3 *Calculated intensities (times uniform) for texture components of the inverse pole figures.*

Sample	T (°C)	Shear strain	<111>	<100>	<110>
123	300	0.56	1.68	1.15	1.46
122	400	0.96	2.36	1.4	1.89
104	450	0.59[1]	2.49	1.34	2.01
106	500	0.63	1.84	1.34	1.48
103	550	0.7	2.05	1.45	1.79
108	550	0.96	2.46	1.6	2.64
109	550	1.38	2.91	1.6	3.17

1) Due to an erroneous termination of this test, the sample was subjected to a higher but unknown final strain than given in the Table.

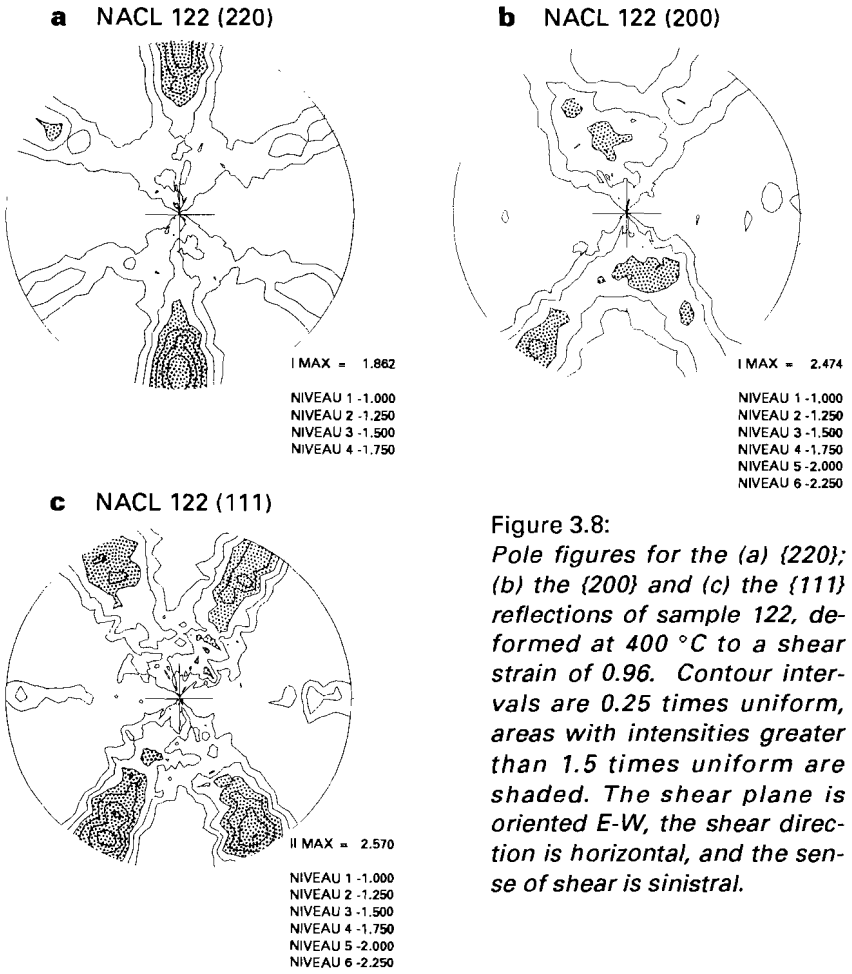

Figure 3.8:
Pole figures for the (a) {220}; (b) the {200} and (c) the {111} reflections of sample 122, deformed at 400 °C to a shear strain of 0.96. Contour intervals are 0.25 times uniform, areas with intensities greater than 1.5 times uniform are shaded. The shear plane is oriented E-W, the shear direction is horizontal, and the sense of shear is sinistral.

3.3.3 *Textures*

Pole figures of the {220}, {111} and {200} reflections were measured of seven samples (Table 3.3). The final shear strains range from 0.6 to 1.4 and the samples were deformed in the temperature range 300 to 550 °C. This data set describes the development of crystallographic preferred orientation with varying temperature and strain.

Pole figures of samples 122 (γ= 0.96, T= 400 °C) and 109 (γ= 1.4, T= 550 °C) are shown in Figs. 3.8 and 3.9 respectively. The microstructural development of sample 122 is characterized by polygonization and grain boundary migration processes (Fig. 3.6c) whereas the

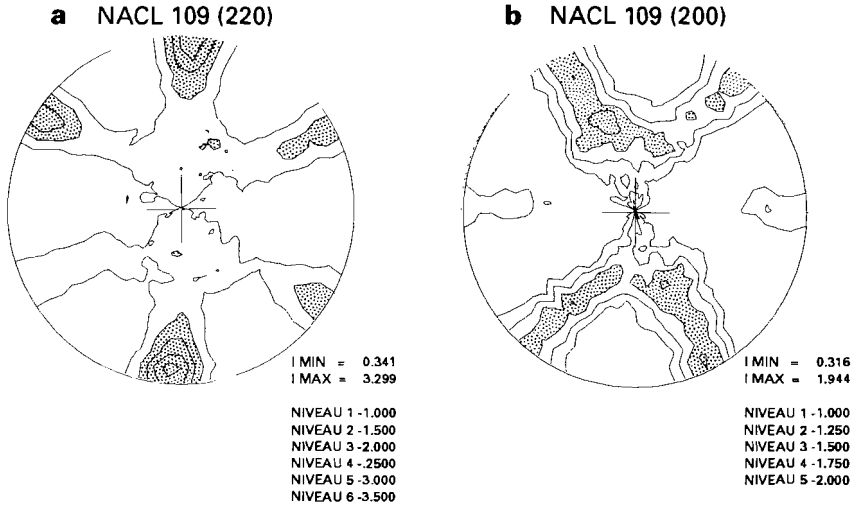

Figure 3.9:
Pole figures for the (a) {220} and (b) the {200} crystallographic directions for sample 109, deformed at 550 °C to a shear strain of 1.38. Contour interval for (a) is 0.5 and for (b) 0.25 times uniform. Areas with intensities greater than 1.5 times uniform are shaded. The shear plane is oriented E-W and the shear direction is horizontal, the sense of shear is sinistral.

microstructural development of sample 109 is dominated by continual recrystalization by grain boundary migration (Fig. 3.7a). The textures presented here are representative for all samples studied.

All pole figures possess an almost orthorhombic symmetry with respect to the shear plane and, taking all samples into account, no consistent relation is found between the sense of shear and the occasional slight asymmetry of the pole figures (for example in Fig. 3.9). The pole figure geometries appear not to change with increasing deformation and only the intensity of the maxima increase with deformation. The geometry of the pole figures is also independent of temperature.

The {220} pole figures contain a maximum perpendicular to the shear plane (Figs. 3.8a and 3.9a). The {200} and {111} pole figures comprise crossed-girdle distributions, symmetrically oriented with respect to the shear plane. The maximum intensities of the {200} pole figures are smaller than the maximum intensities of the {220} and {111} reflections.

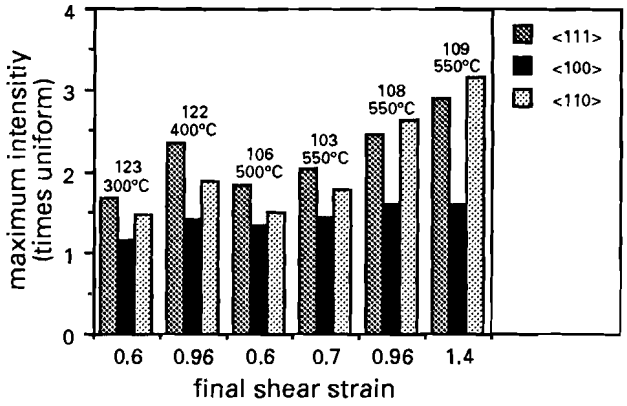

Figure 3.11:
Maximum intensities observed in the inverse pole figures (Fig. 3.10) plotted against final shear strain and temperature.

The inverse pole figures (Wenk and Kocks, 1987) for the shear direction and shear plane normal have been calculated from the orientation distribution function (Bunge, 1982; Dahms and Bunge, 1989; Dahns, 1992) (Fig. 3.10). The inverse pole figures for the shear direction exhibit a maximum around <111> and a submaximum around <100>. The inverse pole figures for the shear plane normal show a maximum around <110>, spreading towards the <100> and <111>. The maximum intensities of the texture components of the inverse pole figures are given in Table 3.3 and shown in Fig. 3.11 (excluding experiment 104, because the final shear strain imposed on this sample is unknown, see Table 3.3). The following observations can be made: the <100> texture component has an intensity around 1 time uniform which is hardly affected by strain and/or temperature. The intensities of the <111> and the <110> components increase with shear strain. In addition, the intensity of the <110> component also appears to increase with temperature above 500 °C (compare intensities of the <110> components of samples 122 and 108). Consequently, the <111> component is stronger at temperatures below 500 °C, whereas the <110> component is stronger at the higher temperatures (Fig. 3.11).

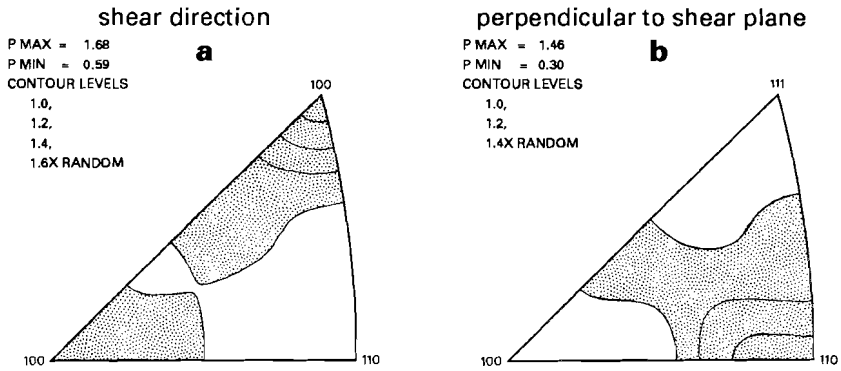

No. 123, T=300 °C, shear strain 0.6.

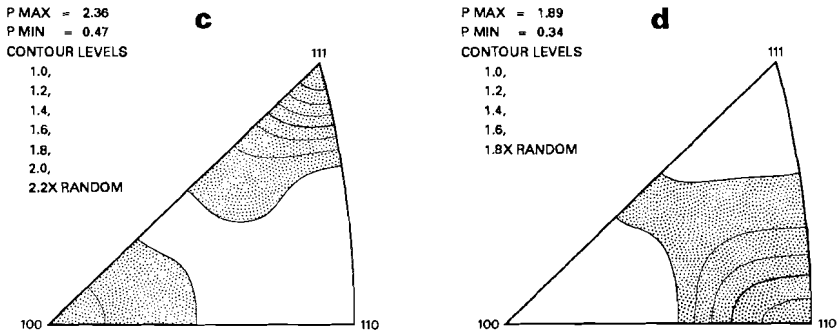

No. 122, T=400 °C, shear strain 0.96.

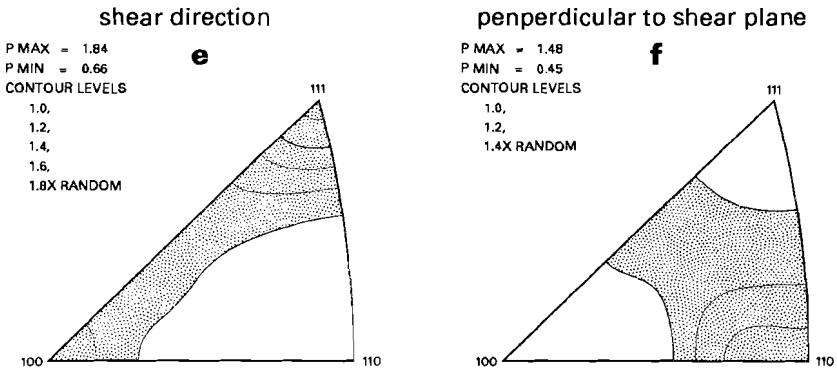

No. 106, T=500 °C, shear strain 0.6

Figure 3.10 a-f:
Inverse pole figures for the shear direction (left side: (a), (c), (e), (g), (i) and (k)) and the shear plane normal (right side: (b), (d), (f), (h), (i) and (l)).

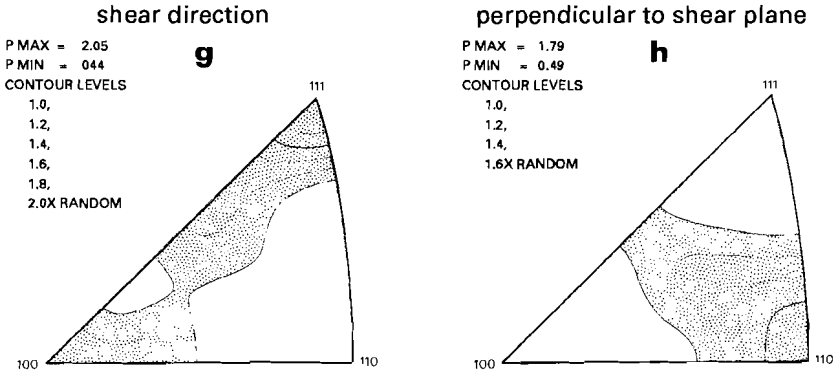

No. 103, T=550 °C, shear strain 0.7.

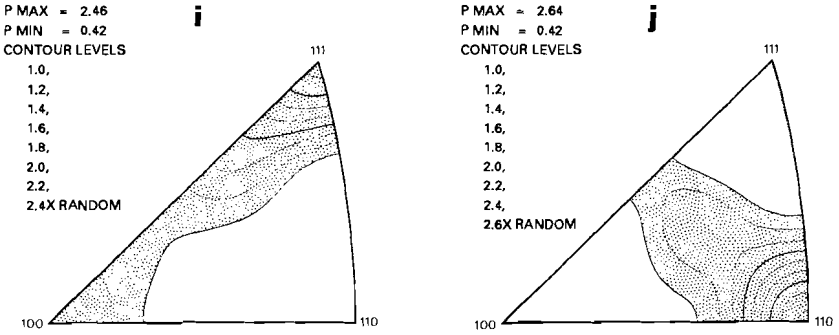

No. 108, T=550 °C, shear strain 0.96.

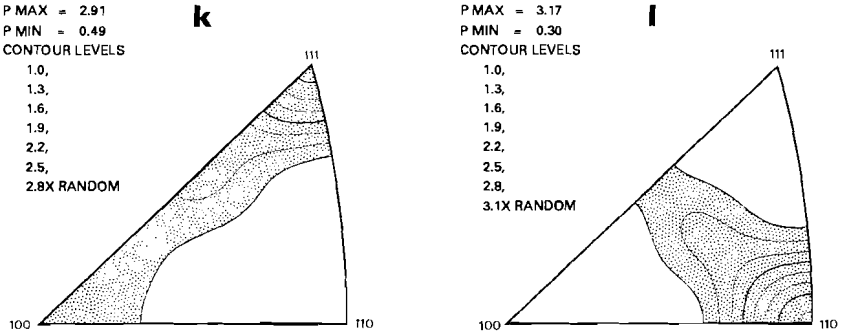

No. 109, T=550 °C, shear strain 1.4.

Figure 3.10 g-l:
Sample number, maximum intensities, minimum intensities and contour intervals are given in times uniform. Areas with intensities greater than 1 time uniform are shaded.

3.4 ANALYSIS OF FLOW BEHAVIOUR

A number of observations indicate that deformation in the present samples occurs by a thermally-activated dislocation creep process. These observations are the operating microstructural processes (subgrain development and recrystallization), the development of crystallographic and shape preferred orientations and the observed dependencies of stress upon strain rate and temperature. For shear deformation, thermally-activated dislocation creep is commonly described by a power-law equation (see for example Frost & Ashby, 1982):

$$\dot{\gamma} = A\exp(-\Delta H/RT)(\tau/\mu)^n \qquad (3.1)$$

where $\dot{\gamma}$. is the shear strain rate (s^{-1}), A is a pre-exponential constant ($MPa^{-n}s^{-1}$), ΔH is the activation energy for creep (kJ/mol), R is the gas constant (kJ/Kmol), T is the temperature (K), τ the applied stress (MPa), μ is the temperature-compensated shear modulus (MPa) and n is the power-law exponent. We will analyse the mechanical data using such a power law relation.

The mechanical data are fitted to Eq. 3.1 to determine the parameters A, ΔH and n. The global inversion method of Tarantola & Valette (1982) was used to obtain the flow law parameters. This method has recently been used by Sotin & Poirier (1984), specifically for this type of purpose. For a more extensive discussion of this method the reader is referred to Poirier et al. (1990), where a comparison with other more traditional techniques is given. The iterative method aims at finding the best solution for the equation

$$f(\ln\dot{\gamma}, \ln\tau, 1/T) = 0 \qquad (3.2)$$

The method implicitly assumes normal distributions for the stress and temperature and a log-normal distribution for strain rate data (Appendix B). The best rheological law is the one that leads to the quickest inversion with the smallest residuals and smallest standard deviations (Poirier et al., 1990).

Separate solutions were sought for the flow law in the temperature range 250-450 °C and 500-600 °C. Three reasons may be offered to support this subdivision. First, this subdivision gives flow law parameters with the smallest standard deviations obtained within the smallest number of iterations (Appendix B). Second, the Arrhenius plots (Fig. 3.4) show a curvature in the temperature range 400 to 500 °C indicating that two different rate-controlling processes exist above and below

these temperatures (Poirier, 1985). Third, this subdivision also defines two different microstructural domains with migration recrystallization as the dominant process in the temperature range 500-600 °C.

Furthermore, in order to optimize the goodness-of-fit, two data inversions were carried out with different initial values for lnA, n and ΔH. This optimization was inspired by the quality of fit obtained from the well-constrained data set of the uniaxial compression experiments (Chapter 2). In the first attempt, the initial values for the iterative data fitting procedure were lnA = -20 ± 100 $MPa^{-n}s^{-1}$, n = 5±5 and ΔH = 250 ± 250 kJ/mol. The results of the inversion are shown in Table 3.4, upper half. In order to see whether a still better fit could be obtained, flow law parameters obtained from the uniaxial compression tests were used as initial values for the iteration process, see Table 3.4 .

The second attempt, using the flow law parameters of the uniaxial compression tests as initial estimates, yielded, for both temperature intervals, best-fit flow laws. The *250-450 °C* data-set yielded, after only 5 iterations:

$$\ln A \text{ (in } MPa^{-n}s^{-1}) = -0.33 \pm 3.0$$
$$n = 5.17 \pm 0.2$$
$$\Delta H = 92.7 \pm 7.0 \text{ kJ/mol.}$$

and the flow law in the *500-600 °C* temperature range is described by:

$$\ln A \text{ (in } MPa^{-n}s^{-1}) = 19.5 \pm 2.7$$
$$n = 4.3 \pm 0.28$$
$$\Delta H = 209 \pm 18.3 \text{ kJ/mol}$$

A remark relating to the global inversion scheme used should be made here. The stress exponents obtained during the first attempts (using a broad range of initial values for lnA, N and ΔH, see above) were around 3.5 for both temperature ranges. In the second run, using more constrained initial values (Table 3.4), stress exponents of 4.4±0.3 and 5.2±0.2 were obtained for the two temperature intervals respectively. Inspection of Fig. 3.3 shows that stress exponents of 4.4 and 5.2 yield better fits then stress exponents of 3.5. In addition, the number of iterations and the standard deviations were minimized during the second run which yielded values for n and ΔH which are more consistent with microphysical creep models than the first run (see next section).

If the experimental data set is too small and/or too clustered, the global inversion method may not immediately yield an optimal data fit and a careful analysis of the results is needed. In case of the uniaxial

Table 3.4
Flow law parameters lnA, n and ΔH for the present mechanical data, obtained using the global inversion method of Sotin & Poirier (1984). The mechanical data have been fitted to a general power law creep equation (Frost & Ashby, 1982):
$\dot{\gamma} = A\exp(-\Delta H/RT)(\tau)^n$.

Temperature interval (°C)	250-450°C	500-600°C
Initial values:		
lnA=	-20±100	-20±100
n=	5±5	5±5
ΔH=	250±250	250±250
Results:		
lnA	-2.1±7.2	14.5±5.0
n	3.42±0.58	3.49±0.53
ΔH	72±9.4	179±28.3
n_i	15	11
k	6	6
$\Sigma res^2/n_i$	1.64	1.15
Uniaxial results used as initial values:		
lnA=	1.75±10	18±10
n=	5.7±1	4.4±1
ΔH=	130±50	230±50
Results:		
lnA	-0.33±3.0	19.5±2.7
n	5.17±0.2	4.3±0.28
ΔH	92.7±7.0	209±18.3
n_i	15	11
k	5	5
$\Sigma res^2/n_i$	2.17	1.48

Meaning of symbols: $\dot{\gamma}$: the shear strain rate (s^{-1}); τ: the applied shear stress (MPa); n: the power-law exponent; ΔH: apparent activation energy for creep (kJ/mol); A is a constant ($MPa^{-n}s^{-1}$); R: the gas constant (kJ/Kmol); T: temperature (K); n_i: number of tests; k: number of iterations before convergence tests were fulfilled; Σres^2: sum of the squared residuals (measure for goodness-of-fit); ln: natural logarithm.

experiments (Chapter 2), the data set was well-defined and the ranges of experimental data were large enough to allow derivation of flow law parameters independent of the initial values of these parameters.

3.5 DISCUSSION

3.5.1 Deformation mechanisms and rate-controlling processes

In the previous section we have determined the parameters which best describe the flow behaviour of salt in simple shear. The values of the stress exponents and of the activation energies for the two temperature fields are consistent with dislocation climb models (Weertman 1968, Poirier, 1985). The flow laws are now considered in relation to the rate-controlling processes that may govern the creep behaviour of salt in shear.

In the *500-600 °C* temperature range (0.7 - 0.8 T_m), the flow law is given by:

$$\dot{\gamma} = 2.65 \times 10^8 \exp(-209/RT)\, \tau^{4.3} \qquad (3.3)$$

where τ in MPa. The creep behaviour of ionic polycrystals at high temperatures is generally controlled by lattice diffusion of the slowest moving species (Frost and Ashby, 1982; Poirier, 1985). Independent, direct measurements by Laurent & Bénard (1957) have shown that the slowest moving species in NaCl is the anion Cl^-. The lattice-diffusion activation energy of the anion, $(Q_l)_{Cl^-}$, ranges from 205 - 221 kJ/mol in the temperature range 450 - 795°C (Laurent & Bénard, 1957, 1958; Laurance, 1960; Barr et al. 1965; Benière et al., 1968) and the activation energy for creep found here is in good agreement with these diffusion activation energies. Published values of creep activation energies derived from coaxial experiments conducted at high temperatures also agree well with the present data (Table 3.5).

Theoretical models for climb-controlled dislocation creep predict a stress exponent between 3 and 6 (Weertman 1968; Poirier, 1985). The value of the stress exponent, $n = 4.3 \pm 0.28$, agrees favourably with these models and with other experimentally derived values (Table 3.5).

The agreement between the present data, theoretical dislocation creep models and experimental diffusion data strongly suggest that shear deformation of polycrystalline salt in the temperature range 500-

Table 3.5

Comparison of creep activation energies and stress exponents of synthetic rocksalt deformed in simple shear and published data derived from coaxial deformation experiments .

Source	Temperature interval (°C)	n-value	ΔH (kJ/mol)
this study:			
shear deformation	250 - 450	5.2	92.7
	500 - 600	4.3	209
this study:			
uniaxial compression	250 - 450	5.7	129
	500 - 780	4.4	227
Burke et al. (1981)	365 - 475	5 - 6	105
Burke et al. (1981) and			
Robinson et al. (1974)	500 - 740	4 - 5	210
Schuh et al. (1970)[1)]	460 - 600		180 - 240
Arieli et al. (1982)[2)]	200 - 400	5.3	102
Heard (1972)[3)]	200 - 400	5.8	115

Notes:

[1)] Based on single crystal creep data with 12 and 66 ppm Ca^{2+}.

[2)] Data from Arieli et al. (1982) are based on Heard's (1972) experimental data which have been corrected for jacket strength and new data collected by the authors.

[3)] Values for n and ΔH presented here are based on Heard's data and have been derived using the inversion method of Sotin and Poirier (1984) used in the present study. Only tests carried within the dislocation climb-regime (i.e. strain rates < 10^{-3} s^{-1} and stresses below 10 MPa) have been used (see Heard, 1972).

600 °C occurs by climb-controlled dislocation creep, where climb is controlled by lattice diffusion.

In the temperature range *250-450 °C* (0.5 - 0.7 T_m), the flow law for sheared salt is given by:

$$\dot{\gamma} = 0.72 \ \exp(-93/RT)\ \tau^{5.2} \qquad (3.4)$$

Differences with the creep behaviour in the temperature range 500-600 °C are the increase of stress exponent and the strong decrease of the activation energy.

In the temperature range of 0.5 - 0.7 T_m, pipe diffusion along dislocation cores often becomes an important rate-controlling process in the creep behaviour of ceramic and ionic materials (Langdon, 1985; Cannon & Langdon, 1988, Verall et al. 1977). If pipe diffusion is the rate-controlling process, the creep behaviour is characterized by a decrease in activation energy and higher values of the stress exponent compared to lattice-diffusion controlled dislocation climb (Cannon & Langdon, 1983).

The activation energy for diffusion through dislocation cores, Q_c, is typically 0.5 - 0.7 Q_l (Gjostein, 1972). In case of NaCl, Q_l is equal to the activation energy of the slowest moving species $(Q_l)_{Cl^-}$, which ranges from 205 - 221 kJ/mol. Thus, the activation energy for pipe diffusion is expected to range from 102.5 to 155 kJ/mol (see also Barr et al., 1960). Hence, in the temperature range 0.5 - 0.7T_m, the creep activation energy ΔH of polycrystalline NaCl deformed in shear falls close to the range of values expected for pipe diffusion control.

Various creep models involving diffusion-controlled dislocation-climb as the rate-controlling process allow the generalized creep equation to be written as (Frost and Ashby, 1982):

$$\dot{\gamma} = A_2 D_{eff}(\tau)^n/(kT) \qquad (3.5)$$

where A_2 is roughly constant and D_{eff} is the effective diffusivity. The effective diffusivity is determined by the relative contributions of lattice diffusion and pipe diffusion (i.e. $D_{eff} = f_l D_l + f_c D_c$). When the contribution of pipe diffusion is negligible, D_{eff} equals the self-diffusion coefficient for the slowest moving species. However, if lattice diffusion is negligible and pipe diffusion dominates, the bulk rate of diffusion depends also on the dislocation density, which in turn depends on the applied stress ($\rho_{disl} = C(\sigma/\mu)^p$) (Sherby and Weertman, 1979; Burke et al., 1981). Consequently, the stress exponent n in Eq. 3.5 is expected to increase by p compared to the stress exponent for lattice-

diffusion controlled creep (Cannon and Langdon, 1983; Langdon, 1985). The effective diffusivity in the pipe-diffusion field is given by:

$$D_{eff} = C_2(\sigma/\mu)^p \exp(-Q/RT) \qquad (3.6)$$

where C_2 is a constant. The stress - dislocation density relation for synthetic NaCl, deformed coaxially in the temperature range 20 - 600 °C with differential stresses ranging from 2 to 20 MPa, has been determined by Beeman & Kohlstedt (1988) and is given by :

$$\rho_{disl} = C_3(\sigma/\mu)^{1.3} \qquad (3.7)$$

where ρ_{disl} is the dislocation density (m^{-2}), C_3 is a material constant and σ is the applied stress. Combining Eqs. 3.4, 3.5 and 3.6, and assuming that Eq. 3.7 holds for shear deformation, it is expected that the stress exponent in the pipe-diffusion field is raised by a factor 1.3, compared to the stress exponent for lattice diffussion-controlled dislocation creep. The stress exponent is n = 5.2±0.2, and agrees with a stress exponent of 5.6±0.3 which is expected for pipe diffusion controlled dislocation creep.

The data obtained for shear deformation match broadly with theoretical dislocation creep models and the limited experimental data for lattice and pipe diffusion.

The flow law of rocksalt in compression is characterized by a significantly higher activation energy (by ~35 kJ/mol) than the flow law for shear deformation in the temperature range 250-450 °C for exactly the same starting material and deformed under comparable strain rates (Table 3.5). This difference in activation energy can tentatively be explained by different dislocation substructures developing in the rocksalt deformed in the two deformation geometries. At higher temperatures, the activation energies for shear and uniaxial deformation are not significantly different (within one S.D.). In Chapter 5 the flow laws obtained in compression and shear deformation are compared and discussed in more detail.

Lattice-diffusion and dislocation-core diffusion are parallel-concurrent processes. They each act simultaneous and each contribute to the total strain rate. The total strain rate can therefore best be written as the sum of the creep rates of the two processes (Poirier, 1985). On basis of the conclusions drawn above, we therefore propose the following two-mechanism flow law, by adding the creep equations for the two temperature regimes:

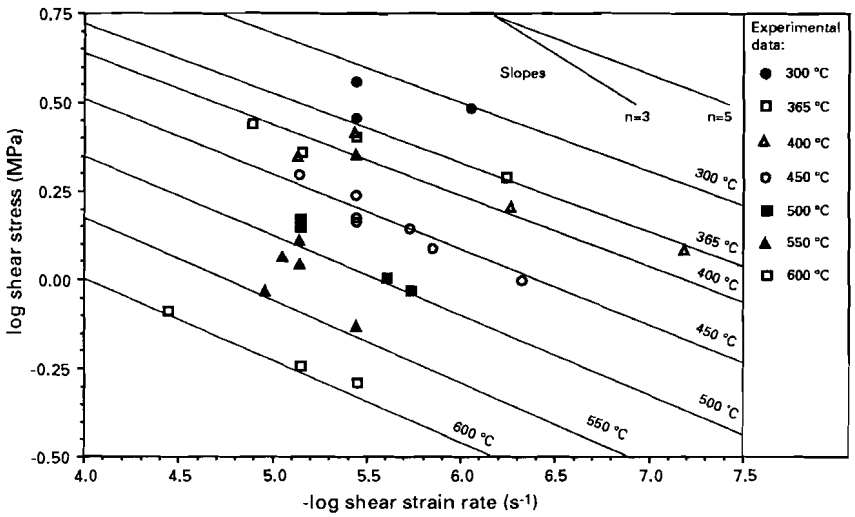

Figure 3.12:
Comparison between the two-mechanism flow law (Eq. 3.8) and the experimental data. The modelled flow behaviour corresponds with the experimental data for the applied ranges of shear strain-rate and temperature.

$$\dot{\gamma}_{tot} = 0.72 \exp(-93/RT)\, \tau^{5.2} + 2.65 \times 10^{8} \exp(-209/RT)\, \tau^{4.3} \quad (3.8)$$

The process with the highest activation energy gives the dominant contribution at high temperatures and the other process is dominant at low temperatures. In the temperature range where the activity of both processes is comparable, the Arrhenius plot is curved ($1.4 < 1000/T < 1.5$, see Fig. 3.4). The two-component flow law (Eq. 3.8) is compared with the experimental data in Fig. 3.12. The agreement between the flow law and the experimental data is fairly good, considering the variability of the experimental data set. Thus, a single two-component flow law describes the mechanical behaviour of sheared salt over almost 3 orders of magnitude in strain-rate allowing for two different rate-controlling mechanisms. The flow law described by Eq. 3.8 defines a curvi-planar surface in 3D (Fig. 3.13) with different stress exponents along the isotherms.

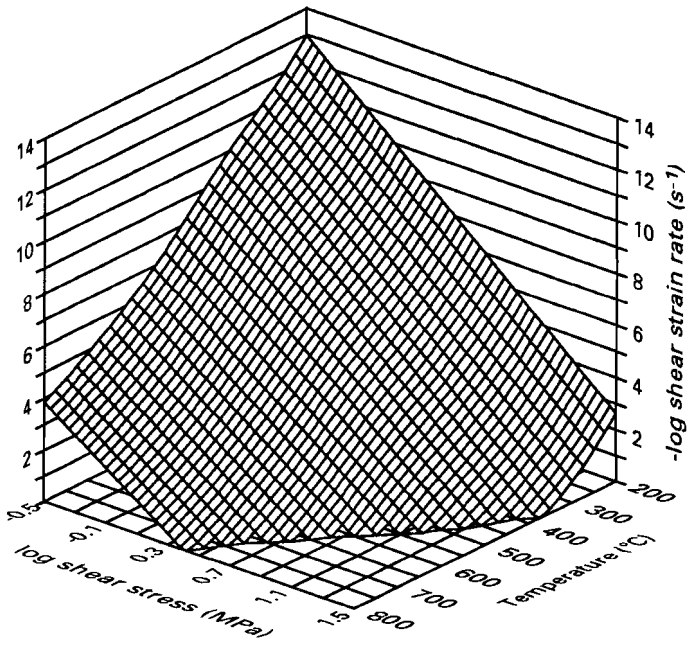

Figure 3.13:
The shear strain-rate dependency on shear stress and temperature (Eq. 3.8) is described by a curvi-planar surface in 3D.

3.5.2 Microstructural development

Subgrain formation by polygonization, rotation recrystallization and grain-boundary migration are microstructural processes, which previously have been observed in dry deformed single and polycrystalline halite (Carter and Hansen, 1983; Friedman et al., 1984; Guillopé and Poirier, 1979; Urai et al., 1986a; Nadgornyi and Strunk, 1987). Two regimes of migration recrystallization have been distinguished by Guillopé and Poirier (1979). These regimes correspond to slow solute-loaded migration and fast solute escape migration (Guillopé and Poirier, 1979; Urai et al., 1986a; Drury and Urai, 1990). The transition between fast and slow migration recrystallization is defined by a critical curve in σ - T space. This curve has been determined by Guillopé and Poirier (1979) for uniaxially compressed NaCl single crystals (Fig. 3.14). The location of the curve depends on the impurity content of the crystal: in more impure material higher temperatures and stresses are

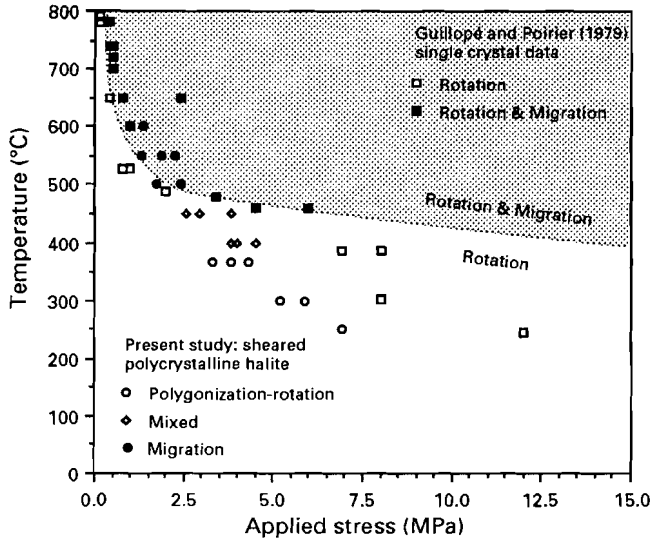

Figure 3.14:
Summary plot showing which microstructural processes are predominant in temperature vs. applied stress space. Note that in the present study grain boundary migration has been observed under all conditions. *However, migration recrystallization is not necessarily the process dominating the microstructural evolution as is indicated. Observations of Guillopé and Poirier (1979) on NaCl single crystals imply a critical curve above which migration recrystallization occurs. The temperature-stress conditions for which migration recrystallization is observed in the present study are well below this critical curve. Differential stress values in coaxial creep are compared with shear stress values through the second invariant of deviatoric stress (see Franssen & Spiers, 1990; Chapter 4).*

needed for fast-solute escape migration to occur (Guillopé and Poirier, 1979).

The driving forces for migration recrystallization in mono-mineralic, dry materials are strain-induced differences in lattice-defect energy and grain-boundary energy (Nicolas and Piorier, 1976, Urai et al., 1986). In the case of NaCl, the driving force of lattice defects is generally much higher than driving forces exerted by grain boundaries (Guillopé and Poirier, 1979; Urai et al., 1986a). However, at high temperatures, the differences in stored lattice defect energies may be relatively low, due to an increased rate of polygonization processes, and mi-

gration recrystallization driven by grain boundary energy may dominate the microstructural development. Similarly, surface-energy driven grain-boundary migration may play a role when boundaries with small radii of curvature develop due to the pinning of migrating grain boundaries by subgrain boundaries or inclusions.

In the present experiments, the microstructural development of the sheared polycrystalline salt, in the temperature range *250-350 °C*, was found to be dominated by polygonization (Fig. 3.5). The subgrains are small (10 - 20 μm). By analogy with uniaxially compressed polycrystalline salt (Chapter 2), it is inferred that rotation recrystallization also may have occurred, but firm evidence is lacking. In the temperature range *400-500 °C*, polygonization is controlling the microstructural evolution at low strains (Fig. 3.6a). Grain boundary migration occurs with increasing deformation and this leads to the formation of grain boundary bulges with consistent polarities (Fig. 3.6bc). The bulges or cusps are located at subgrain-grain boundary intersections and this suggests that the subgrains act as nuclei for migration recrystallization (Derby, 1990, 1992). The edge-wise propagation of subgrain boundaries (Means and Ree, 1988) commonly appears to be slower than the grain boundary migration velocity. As a result cuspate grain boundaries with consistent polarities develop. Grain boundary inclusions also exert a dragging force on the mobile grain boundary. The consistent polarity (Fig. 3.6c) suggests that migration direction is away from the centre of curvature and that migration recrystallization is driven by differences in lattice-defect energy (Nicolas and Poirier, 1976; Urai et al., 1986, Karato, 1988; Drury and Urai, 1990). The lobate and concavo-convex grain contacts (Figs. 3.6b and d), commonly observed in samples deformed in the 400-500 °C temperature range, indicate that the grain boundary mobility is increased compared to lower temperatures. The applied stress - temperature data (Fig. 3.14) plot well below the critical curve and it is inferred that migration recrystallization is of the slow solute-loaden type. In Guillopé and Poirier's (1979) experiments, slow grain boundary migration was also an important microstructural process in the rotation recrystallization field.

Above *500 °C*, continual grain boundary migration is the process dominating the microstructural development. Recrystallized grains contain large subgrains. Inclusions located at the grain boundaries in the starting material (Fig. 2.1), are either dragged along by the migrating grain boundaries or they broke away, leaving grain interiors with small voids (Fig. 3.7a). Possibly grain boundary migration is driven by a combination of grain-boundary energy and strain-induced energy.

Straight or slightly curved grain boundaries are seen to develop which intersect at 120° triple junctions. This grain boundary configuration indicates the development of low surface energy configurations (similar to annealed microstructures, Fig. 2.1) driven by grain-boundary energy (Vernon, 1976). The microstructure shown in Fig. 3.7b, where a pinned grain boundary appears to migrate away from the centre of curvature, despite the development of very small radii of curvature (±40 μm), indicates that strain-induced energy still provides a significant driving force for the recrystallization process.

The experimental data in fhe 500-600 °C temperature range plot well above the critical curve in σ - T space (Fig. 3.14). This may suggest that fast solute-escape migration recrystallization has occurred. The stress - grain size relation for fast solute-escape migration recrystallization is given by Guillopé and Poirier (1979):

$$\sigma_m = 57\mu(b/D)^{0.78} \qquad (3.9)$$

where σ_m is the applied stress (in MPa), D is the grain size (μm) and in their analysis the shear modulus m is taken as 10 GPa and the Burger's vector b equals 3.98 x 10^{-4} μm. Assuming that this relation would hold for shear deformation, an applied shear stress between 0.5 and 1 MPa would yield recrystallized grain sizes of 1 - 2 x 10^4 μm. However, the observed recrystallized grain sizes are significantly smaller (1 - 2 x 10^3 μm).

It is not likely that fast solute-escape migration recrystallization mechanism is operating in the polycrystalline salt presently studied, since the recrystallized grain sizes are much smaller than those predicted for the fast migration recrystallization model (Eq. 3.9). In addition, thin section observations suggest that the mobile grain boundaries in sheared polycrystalline halite may also contain inclusion-like channels similar to those observed in recrystallized rocksalt deformed in uniaxial compression (Fig. 2.24b). These grain boundary channels are similar to the structures observed in the grain boundaries of recrystallized wet salt aggregates (Spiers et al., 1990) and in healed calcite grain boundaries (Olgaard and Fitz Gerald, 1993). These are significantly different from the high angle grain boundary structures of the NaCl single crystals where fast solute-escape grain occurred (Guillopé and Poirier, 1979).

Derby (1990, 1991, 1992) proposed a dynamic recrystallization model that explains the stress - steady-state grain size relation commonly observed in rock-forming materials and metals. The recrystallization process involves a bowing out of grain boundary segments be-

tween subgrains. For steady-state to occur the model assumes a dynamic balance between the *nucleation* rate of new grains and the *migration* rate of nucleated grains, in other words: in the time taken for a moving grain boundary to sweep a volume equivalent to the steady-state grain-size one nucleation event occurs in each equivalent volume averaged over the microstructure. A nucleation criterion is formulated and is based on the distribution of subgrain boundaries in the polygonized grain prior to recrystallization. The dynamic balance between the nucleation rate I and grain boundary migration-rate g is expressed as (Derby, 1992):

$$\frac{CD^3I}{g} = 1 \qquad (3.10)$$

where D is the recrystallized grain size and C is a geometrical constant equal to about 3. The migration recrystallization process observed in sheared polycrystalline halite involves bowing out of grain boundary segments between subgrain boundaries (Fig. 3.6c) similar to Derby's recrystallization model and similar to uniaxially deformed halite (Chapter 2). Derby's recrystallization model has been evaluated using the microstructural processes observed in uniaxially compressed halite (Chapter 2). It was proposed that migration recrystallization was to be the dominant microstructural process for a temperature increase from T_1 to T_2, if the following condition is met (Chapter 2):

$$\frac{CD^3I\,(\text{at } T_2) \times F(\text{at } T_1)}{CD^3I\,(\text{at } T_1) \times F(\text{at } T_2)} < \frac{M(\text{at } T_2)}{M(\text{at } T_1)} \qquad (3.11)$$

where F is the driving force for recrystallization (proportional to the applied stress) and M is the grain boundary mobility (depending through an Arrhenius-type equation on the pipe diffusion activation energy). In halite, this condition is met when the rate controlling mechanism changes from pipe-diffusion to lattice diffusion controlled dislocation creep, i.e. for a temperature increase from 450-550 °C. For this particular temperature increase, the increase in grain boundary mobility is strong enough to compensate for any decrease in driving force or for an increase in equilibrium recrystallized grain size. In other words, the grain boundary mobility terms are differently affected by the temperature increase than the terms on the left-hand side of Eq. 3.11, and that allows a dynamic balance to be established between the grain boundary migration rate and the nucleation rate.

3.5.3 *Crystallographic preferred orientations*

In the temperature range investigated, the textures of the sheared samples show a strong tendency for the {110} planes of the relatively weak {110}<1$\bar{1}$0> slip system to align parallel to the shear plane (Figs. 3.8 - 3.10). The <111> direction and not the slip direction of the "easiest" slip system tends to align in the shear direction (Fig. 3.10). The geometry of the developed textures does not change with increasing temperature or increasing deformation. This suggests that migration recrystallization has limited influence on the development of the crystallographic preferred orientation.

We are not aware of any previous experimental studies on texture development in sheared rocksalt. Wenk and co-workers (Wenk et al., 1989a) have applied Taylor and self-consistent (SC) texture simulation models (Molinari et al., 1987) to the development of crystallographic preferred orientations in halite. At low temperatures (<250 °C), the slip systems in halite are strongly anisotropic (Fig. 2.26a). Slip on {110}<1$\bar{1}$0> is about 6 - 7 times easier as slip on the {111}<1$\bar{1}$0> and {100}<001> systems. Extrapolation of the critical resolved shear stress (crss) data to higher temperatures suggests that all slip systems have comparable crss at temperatures above 400 °C (Carter & Heard, 1970). The only available texture simulations are for sheared halite deformed at room temperature (i.e. highly anisotropic) to a shear strain of 1 (Fig. 3.15). Without strain hardening of the slip systems, the Taylor and the SC approach predict weak textures, as is shown by the {110} pole figures (Fig. 3.15a, b). The texture development is enhanced if hardening of the slip systems is included (Fig. 3.15c, d). The simulated Taylor and SC {110} pole figures resemble the experimentally obtained {110} pole figures (Figs. 3.8 and 3.9), although the latter are obtained at much higher temperatures.

Textures with near orthorhombic geometries have been predicted for f.c.c. metals deformed in torsion exhibiting isotropic hardening (Molinari et al., 1987). Textures obtained from experimentally sheared copper and iron also show near orthorhombic symmetry (Williams, 1962). The slip systems of f.c.c., and b.c.c. metals are {111}<1$\bar{1}$0> and {110}<111> respectively and these are different from those in NaCl. A detailed comparison between the textures found in NaCl and by Williams, (1962) is therefore not allowed. The orthorhombic symmetry of textures developed in (monoclinic) simple shear of cubic materials is at least remarkable.

It has been shown that above 500 °C migration recrystallization is the dominant microstructural process and that compared to lower temperatures the <110> texture component increases more strongly with

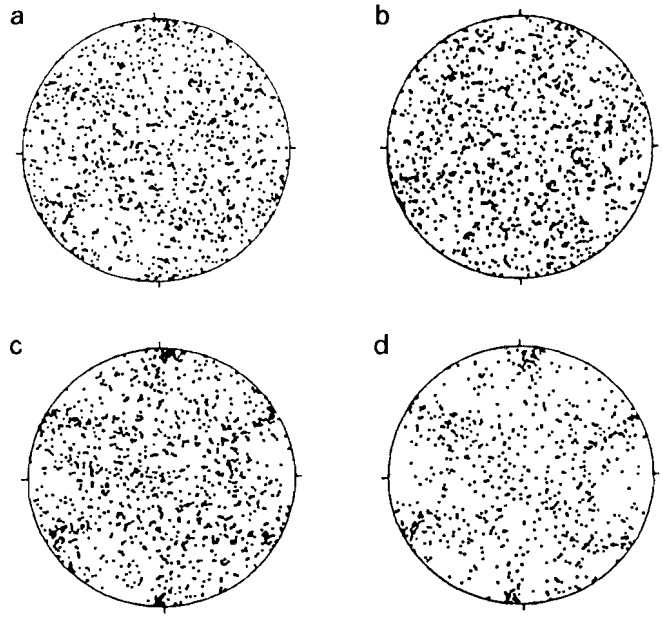

Figure 3.15:
{110} pole figures representing texture simulation of halite deformed in simple shear to a shear strain γ=1. 200 grains are modelled using room temperature critical resolved shear stress data.
(a) Taylor models without hardening
(b) Self-consistent model without hardening
(c) Taylor model with hardening
(d) Self-consistent model with hardening
Note that the shear plane is E-W and the sense of shear is sinistral. From Wenk et al. (1989a).

increasing shear strain than the <111> component (Fig. 3.11). Since the crss of all slip systems in NaCl are expected to be equal above 400 °C (Carter & Heard, 1970), it seems unlikely that the increase of the <110> component with temperature is related to preferred slip on the $\{110\}\langle 1\bar{1}0\rangle$ system over the other slip systems.

An alternative explanation for the increase of the <110> texture component may be lattice re-orientation by migration recrystallization. Grain-boundary migration can change the orientation of crystals substantially (e.g. Jessel and Lister, 1990). Ice polycrystals, for example,

develop strong c-axis preferred orientations (an orientation for easy slip) by dynamic recrystallization (Wilson, 1986). In case of olivine, grain boundary migration only produces preferred orientations when lattice-defect energy is the driving force and not when grain-boundary energy is the driving force (Karato, 1988).

In polycrystalline halite deformed above 500 °C, the driving forces for grain boundary migration are lattice-defect and grain boundary energies. In analogy with observations in other materials (Wilson, 1986; Karato, 1988; Jessel and Lister, 1990), we infer that strain-induced grain boundary migration in halite may give rise to lattice re-orientation. Although complete recrystallization may have occurred in the sheared halite, the crystallographic preferred orientations observed are relatively weak (2 - 3 times uniform). This may imply that not all the grain volumes, which have been swept by migrating grain boundaries, are re-oriented substantially. Strain-induced grain boundary migration merely enhances texture development rather than changes it.

Further discussion of the relations between texture simulations, dynamic recrystallization and the experimentally-obtained crystallographic preferred orientations is not justified and the exact significance of the texture development remains speculative (see also for a discussion on this topic Wenk and Christie, 1991). In order to reach firm conclusions it is necessary to perform texture simulations using mechanical data (crss, hardening rates of the slip systems) relevant to the experimental conditions of the present study and to carry out simple shear experiments under conditions relevant to the simulations which model the strongly anisotropic behaviour of halite at low temperature.

3.5.4 *Comparison with other shear experiments on rocksalt material*

Various triaxial deformation experiments have been carried out on cylindrical specimens of sandstone with halite gouge sheared along 35°-precut surfaces (Shimamoto, 1986; Shimamoto and Logan, 1986; Hiraga and Shimamoto, 1987; Knapp et al., 1987; Shimamoto, 1989ab; Chester, 1989; Chester and Logan, 1990). In these experiments, thin layers (0.2 - 1.0 mm) of granular halite were sheared to high shear strains (γ amounts to 70) at room temperature under confining pressures up to 250 MPa with relatively high shear rates (between $\sim 10^{-1}$ and $\sim 10^{-6}$ s^{-1}). A transition from homogeneous plastic deformation to potentially unstable heterogeneous deformation has been observed to occur at much higher shear strains ($\gamma > 10$) than those achieved in the present study (Shimamoto and Logan, 1986; Hiraga and Shimamoto, 1987). Triaxial shear experiments carried out in the ductile field were

characterized by very high shear stresses (between 50 and 130 MPa) and a high stress exponent (n= 17.3) (Shimamoto, 1986) compared to the present data. Furthermore, under conditions favouring intracrystalline deformation sheared *synthetic* and *crushed natural* salt produced flattened grain fabrics, that were possibly modified by metadynamic and/or static recrystallization (Shimamoto and Logan, 1986; Hiraga and Shimamoto, 1987; Chester, 1989).

The differences in experimental conditions and the operation of different processes between the published studies and the present experiments do not justify a comparison of the results.

3.6 CONCLUSIONS

Polycrystalline salt has been deformed in simple shear, in the temperature range 250-600 °C with strain rates between 10^{-5} and 10^{-7} s^{-1}. The deformation within the shear zone is homogeneous and maximum finite shear strains of 1.4 are archieved. No remarkable strain softening has been observed. The main findings and conclusions can be summarized as follows:

1) The activation energies and the stress exponents for creep are consistent with the interpretation that deformation occurred by climb-controlled dislocation creep. In the temperature range 500-600 °C, the creep rate is controlled by lattice-diffusion. In the temperature range 250-450 °C, creep is controlled by diffusion through dislocation cores.
2) Application of the global inversion method proposed by Sotin and Poirier (1984) to obtain a rheological law from laboratory deformation experiments may yield misleading results, if the experimental data are poorly constrained and/or highly clustered.
3) In the temperature range 250 - 400 °C, the microstructure is controlled by polygonization, rotation recrystallization and limited migration of the boundaries. The development of cuspate grain boundaries with consistent polarities in this temperature range indicates that grain boundary migration is driven by stored lattice defect energies. With increasing temperature, migration recrystallization becomes more important till at 500-600 °C the microstructural development is dominated by this process. In this temperature range migration recrystallization is inferred to be driven by differences in stored lattice defect energy and by grain boundary energy.

4) The microstructural observations can at least be qualitatively explained by the dynamic recrystallization model proposed by Derby (1990, 1991, 1992). The transition from pipe-diffusion to lattice-diffusion controlled dislocation creep affects the driving force for recrystallization and the grain boundary mobility in such a way that the grain boundary migration rate and nucleation rate are in balance and consequently migration recrystallization becomes the dominant microstructural process.
5) During simple shear deformation the {110} planes of the relatively weak $\{110\}\langle 1\bar{1}0\rangle$ slip system tend to align parallel to the shear plane. Notably, the $\langle 1\bar{1}0\rangle$ slip direction does not orient itself parallel to the shear direction, instead the <111> crystallographic direction tends to align parallel to the shear direction. The texture does not change with increasing deformation, only the intensity of the maxima increases with deformation.
6) Dynamic recrystallization does not appear to have an influence on the geometry of the developed texture. However, the onset of migration recrystallization as dominant microstructural process coincides with an increase in the intensity of the <110> texture component. It is inferred that this strenghtening of this texture component could result from dynamic recrystallization.

DEFORMATION OF POLYCRYSTALLINE SALT IN COMPRESSION AND IN SHEAR AT 250 - 350 °C*

ABSTRACT

Dry synthetic polycrystalline salt (NaCl) has been deformed in uniaxial compression and in shear in order to gain insight into the influence of deformation mode on the development of crystallographic preferred orientation, microstructural evolution and mechanical behaviour (flow strength). The experiments were carried out between 250 and 350 °C, at strain rates between 10^{-5} and 10^{-7} s^{-1}. Under these conditions halite deforms by diffusion climb-controlled dislocation creep. In our samples, the presence of deformed grains containing cellular networks of subgrains, and the development of texture are consistent with such mechanisms. The weaker {110}<1$\bar{1}$0> slip plane appears to align parallel to the shear plane and perpendicular to the uniaxial compression direction. In the sheared samples, a <111> maximum is observed parallel to the shear direction. The textures obtained agree favourably with texture simulations. When the mechanical behaviour seen in uniaxial compression and shear is compared in terms of equivalent stress and strain, as defined in von Mises theory of isotropic plasticity, the uniaxially deformed samples appear to be stronger. From a detailed consideration of the data, it is inferred that the difference in flow strength is largely due to anisotropy resulting from texture development. The results suggest that the assumptions underlying the von Mises theory of isotropic plasticity are not applicable in the present case, and that the associated flow rule does not offer an accurate method of generalizing creep laws for salt under the conditions investigated.

* *This chapter has been published as: Franssen, R.C.M.W. and Spiers, C.J. 1990. Deformation of polycrystalline salt in compression and shear at 250 - 350 °C. In: Deformation mechanisms, rheology and tectonics. Knipe, R.J. and Rutter, E.H. (eds.) Geol. Soc. Spec. Publ., 54: 201-212.*

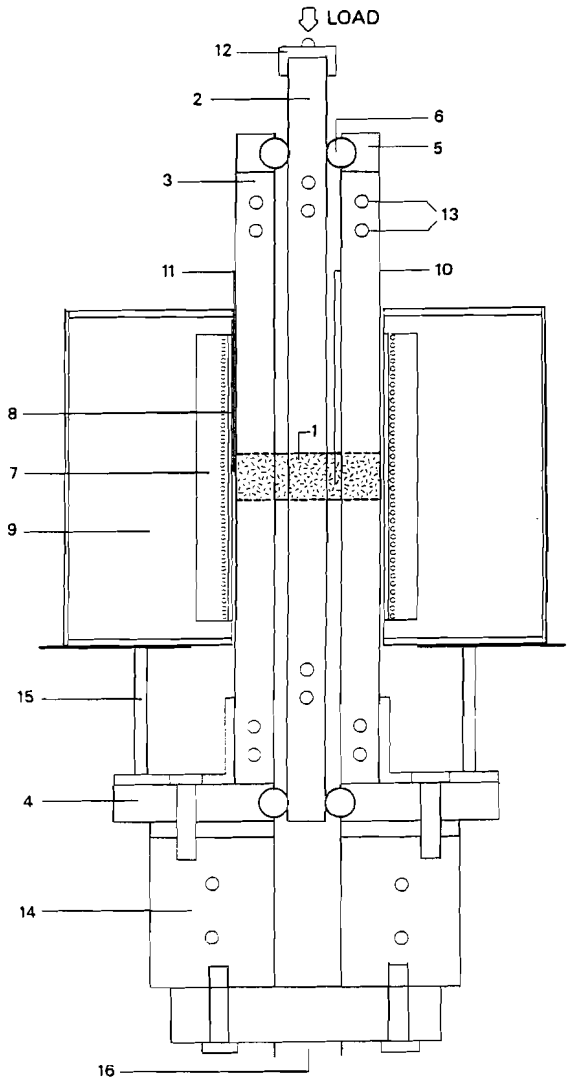

Figure 4.1b:
Schematic diagram of the shear apparatus.
Key:

1: Cylindrical sample with reduced sections;
2: mobile middle bar;
3: fixed outer bars;
4: bottom platen fixating other bars;
5: idem, top platen;
6: roller bearings reducing friction of the middle bar and constraining its movement to vertical;
7: furnace windings in ceramic material;
8: insulating mica sheets;
9: ceramic fibre insulation;
10: sample thermocouple;
11: controller thermocouple;
12: spherical seat;
13: water-cooling access;
14: spacers;
15: furnace support;
16: Instron loading ram.

4.1 INTRODUCTION

It is widely accepted that most natural rock deformation phenomena of interest in structural geology and geophysics are non-coaxial (e.g. flow within shear zones, diapiric flow and mantle convection). Despite this, most rock deformation experiments have focused on coaxial configurations, and relatively few non-coaxial deformation experiments have been reported (examples include Bouchez and Duval, 1982; Kern and Wenk, 1983; Shimamoto and Logan, 1986; Schmid et al., 1987; Borradaile and Alford, 1988; Price and Torok, 1989; Williams and Price, 1990). This discrepancy is mainly due to experimental difficulties in achieving a well-constrained non-coaxial deformation path while still being able to measure and/or control experimental variables such as the state of stress in the sample. For these reasons, almost all *quantitative* rheological data for rocks have been obtained from axi-symmetric compression experiments.

To predict the behaviour of a body of rock under a given stress state or given boundary conditions, it is necessary to generalize the axi-symmetrically derived flow law, in which stress and strain rate are treated as scalars, to three dimensions, in which stress and strain rate are treated as tensors (see for example Stocker and Ashby, 1973). This is usually done using the theory of perfect isotropic plasticity to relate stress and strain-rate components (Nye, 1953a; Paterson, 1976). The assumptions underlying this method of generalization (often referred to as the associated flow rule) are that the material is isotropic and stays isotropic during deformation, the material has no other "memory" for incremental strain history, and that deformation is isovolumetric. However, there is no *a priori* justification that flow laws derived from coaxial experiments can be generalized in this way (Ferguson, 1979). Indeed, axi-symmetric experiments on most materials with "memory" are insufficient to fully characterize the material behaviour (see Hobbs, 1972). Thus, the generalization of coaxial flow laws is not straight-forward, and the validity of the associated flow rule approach

(assuming perfect isotropic plasticity) is not known for most geological materials.

An understanding of the effect of deformation mode on flow behaviour and an adequate 3-D flow law are of crucial importance in considering (or modelling) deformation localization phenomena. Mechanical weakening, thought to greatly enhance the development of localized shear zones, can be caused by the development of crystallographic preferred orientations within a deforming material (as suggested by texture simulations - see Tomé et al., 1984; Wenk et al., 1986, 1987) or by microstructural changes such as dynamic recrystallization or grain boundary alignment (White et al., 1980). Rotational and irrotational deformation paths have different effects on the development of textures and on microstructural evolution (White et al., 1980; Tomé et al., 1984; Wenk et al., 1986). Hence, deformation path (or geometry) can be expected to have a significant influence on the mechanical anisotropy and response of deforming materials.

In this paper we report deformation experiments on polycrystalline NaCl deformed in uniaxial compression and in "simple shear" at intermediate temperatures (T/T_m between 0.5 and 0.6). The aim of the study was to gain insight into the influence of deformation mode on the development of crystallographic preferred orientation (or texture), on microstructural evolution and on the mechanical behaviour (flow strength) of the material. Polycrystalline NaCl was chosen as a suitable material to investigate for the following reasons. Firstly, polycrystalline salt is ductile and relatively weak at temperatures as low as 200 °C. This allows simple shear to be carried out without confining pressure, using relatively simple deformation apparatus. Secondly, NaCl exhibits well understood dislocation creep behaviour at intermediate temperatures and is a useful mineral analogue in a general sense (see Guillopé & Poirier, 1979; Banerdt and Sammis, 1985; Shimamoto and Logan, 1986). Lastly, NaCl is extremely suitable for microstructural and textural studies since dislocation substructures are readily made visible and texture measurements can be carried out relatively easily.

4.2 EXPERIMENTAL METHODS

In this study, synthetic polycrystalline NaCl samples were used. These were prepared as follows. First, analytical grade NaCl powder, jacketed in rubber tubes, was hydrostatically cold-pressed into irregular billets. From these billets, right cylindrical samples were machined. For

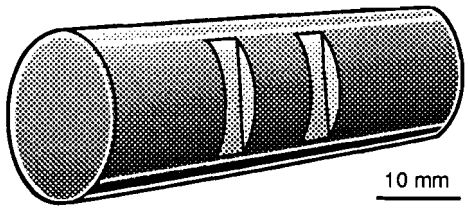

Figure 4.1a:
Perspective view of cylindrical sample with reduced sections used for shear experiments. This sketch illustrates the final sample geometry.

the compression experiments, the samples produced measured 20 mm in length by 10 mm in diameter. For the shear experiments, cylindrical samples with reduced sections were prepared. These samples were 75 mm long and two diameters were used, namely 25 and 15 mm. The reduced sections were cut using a file plus slotted template. Fig. 4.1a illustrates the final geometry. After machining, all samples were annealed for 12 - 14 hrs in an argon atmosphere at 720 - 725 °C (i.e. *c.* 0.9 T_m). The material obtained possessed a recrystallized polygonal "foam" microstructure with a grainsize 100 to 400 μm. Grain boundaries contained gas-filled tubular and spherical inclusions of about 10 μm in diameter. The grains contained no optically visible substructure. The porosity of the starting material ranged from 2% to 2.5%. Neutron diffraction analysis showed that no significant texture was developed.

The uniaxial compression experiments were carried out in an Instron 1193 constant displacement rate apparatus equipped with a high temperature furnace and superalloy loading pistons (see De Bresser and Spiers, 1990). The axial force applied to the sample was measured using a 5kN load cell, with an absolute accuracy better than 0.5%. The maximum strains attained were *c.* 20%.

The shear experiments were carried out in the deformation apparatus shown in Fig. 4.1b, mounted in an Instron 1362 loading frame. Basically, the shear rig consists of three parallel loading bars. The two outer bars are fixed to end-platens and are immobile. The middle bar is free to move in the vertical direction only, i.e. parallel to the fixed outer bars. The sample (Fig. 4.1a) is fitted lengthwise through aligned holes in the three loading bars. Advancing the middle bar downwards imposes a shear deformation on the reduced sections of the sample. The shear load and hence the total shear stress supported by the sample were measured using a 10 kN load cell with an absolute accuracy better

Table 4.1. *Summary of experimental conditions.*

Uniaxial compression experiments.				
Test number	Temperature (°C)	Strain rate (s^{-1})	Final stress (MPa)	strain (%)
C35	250	$2.9*10^{-7}$	9.8	6.6
C6	300	$3.6*10^{-6}$	9.4	24.0
C53	300	$1.8*10^{-6}$	7.7	14.2
C42	350	$1.8*10^{-6}$	7.3	13.9
C46	350	$1.8*10^{-6}$	6.9	14.6
C45	350	$1.8*10^{-7}$	5.0	8.9
Shear experiments				
120s	250	$5.8*10^{-7}$	4.0	0.66
118s	300	$3.6*10^{-6}$	2.9	1.22
123	300	$3.6*10^{-6}$	3.5	0.56
124	365	$7.2*10^{-6}$	2.2	0.99
121	365	$3.6*10^{-6}$	2.5	0.34

than 0.5% and a resolution better than 0.01%. Normal stresses acting parallel to the length of the sample could not be measured. Displacement (hence shear strain γ) was measured using the linear variable differential transformer (LVDT) located in the drive unit of the Instron 1362.

Both the uniaxial and shear experiments were carried out at constant displacement rate in the temperature range 250 to 350 °C under unconfined (i.e. atmospheric pressure) conditions. Axial and shear strain rates varied from test to test between 10^{-5} s^{-1} and 10^{-7} s^{-1}. The shear strain rates were chosen to be comparable with the compression strain rates according to the equivalent strain rate concept introduced later.

Stress-strain curves were calculated from strip-chart records of force and displacement vs. time (shear tests) or of force vs. time alone (uniaxial tests). The stresses were corrected for dimensional changes of the sample and, in case of shear, for the weight of the middle bar. Displacement measurements were corrected for apparatus stiffness and

for thermal expansion of the sample. Strain and strain rates were calculated with respect to the starting dimensions of the sample.

The microstructures of both the deformed and undeformed samples were studied by means of reflected light microscopy carried out on polished sections. Grain boundaries and dislocation substructures were made visible by etching the polished sections. Details of section preparation techniques and etching procedures are given in Spiers et al. (1986). All micrographs presented here were obtained from polished and etched sections.

4.3 EXPERIMENTAL RESULTS

4.3.1 *Mechanical data*

Table 4.1 shows details of the experiments reported in the present study. The corresponding applied stress vs. axial strain curves for the uniaxial experiments are shown in Fig. 4.2. All of these curves show considerable work hardening during the first 10% shortening, reaching stress levels between *c.* 5 and 10 MPa at 10 - 20% strain. With in creasing temperature and decreasing strain rate, the flow stresses decrease. Above 300 °C, steady state behaviour is closely approached, particularly at low strain rates.

The applied shear stress vs. shear strain curves obtained from the shear tests are shown in Fig. 4.3 (refer Table 4.1 for details). These curves show some work hardening during the first 0.2 shear strain,

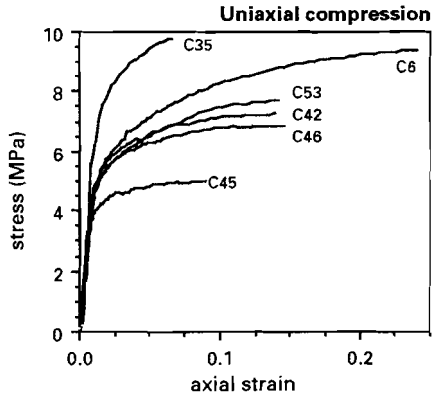

Figure 4.2:
Plots of applied uniaxial stress ($\sigma_{applied}$) versus axial strain for the present uniaxial compression tests on polycrystalline salt.

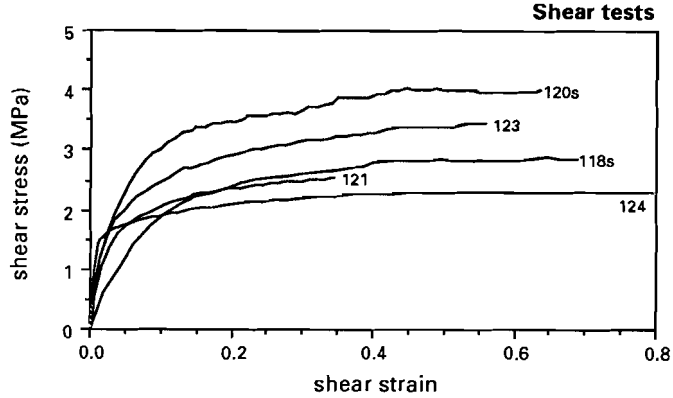

Figure 4.3:
Applied shear stress ($\tau_{applied}$) versus shear strain plots for the polycrystalline halite samples deformed in shear. The shear stress is determined by the vertical load transmitted through the sample (see text).

then attaining more or less steady state flow at shear stresses in the range 2 - 4 MPa. As in the compression tests, the flow stresses in shear decrease substantially towards higher temperatures.

4.3.2 *Optical microstructures*

The microstructures developed during the uniaxial compression tests are illustrated in Figs. 4.4 and 4.5. The samples showed a well-defined grain flattening fabric, with clear dislocation substructures. At low strains (ε<10%), an irregular pattern of subgrains develops with incomplete boundaries, indicating incipient polygonization involving climb (Friedman et al., 1981). With increasing strain, a well-defined cellular network of subgrains forms, and the flattening fabric becomes more intense. Additionally, in the samples deformed at strain rates above 10^{-6} s^{-1}, characteristic linear arrangements of rhomboidal subgrains are developed (Fig. 4.4). These linear substructures are oriented at 30 - 60° to the compression direction. A marked change in grain boundary morphology is linked with the development of subgrains. The straight grain boundaries observed in the undeformed material become bulged where intersected by subgrains (Fig. 4.5). However, extensive migration of these bulged grain boundaries was not observed.

The microstructures typical of shear deformation are presented in Figs. 4.6 and 4.7. The transition from undeformed "wall rock" into the shear zone is illustrated in Fig. 4.6. The lower part of the micrograph

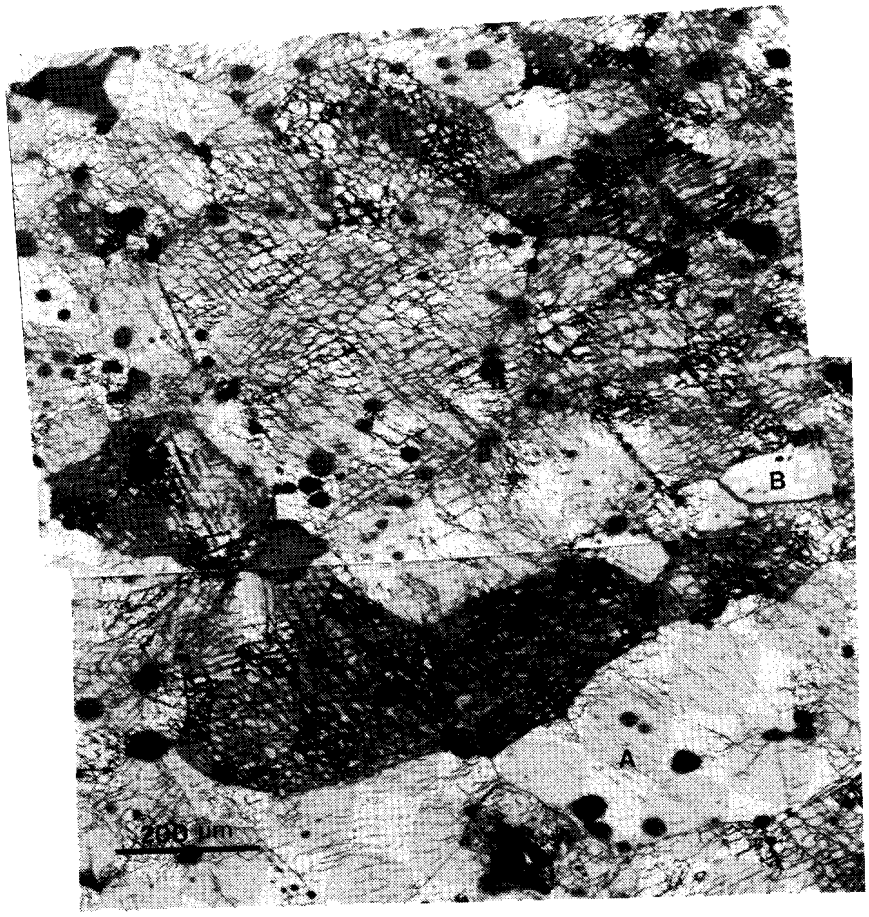

Figure 4.4:
Optical micrograph illustrating the development of linear arrangements of subgrains typical for uniaxial deformation at 250°C. In the two dark grains, just below the centre of the micrograph, two intersecting sets of linear substructures give rise to the formation of rhomboidal subgrains. Thin etch lines present in grain A resemble wavy slip lines. Incipient recovery leads to the development of incomplete subgrains. Close inspection of grain B, which is relatively unaffected by the etching procedure, reveals the presence of a very faint network of subgrains (Sample C15, 250°C)

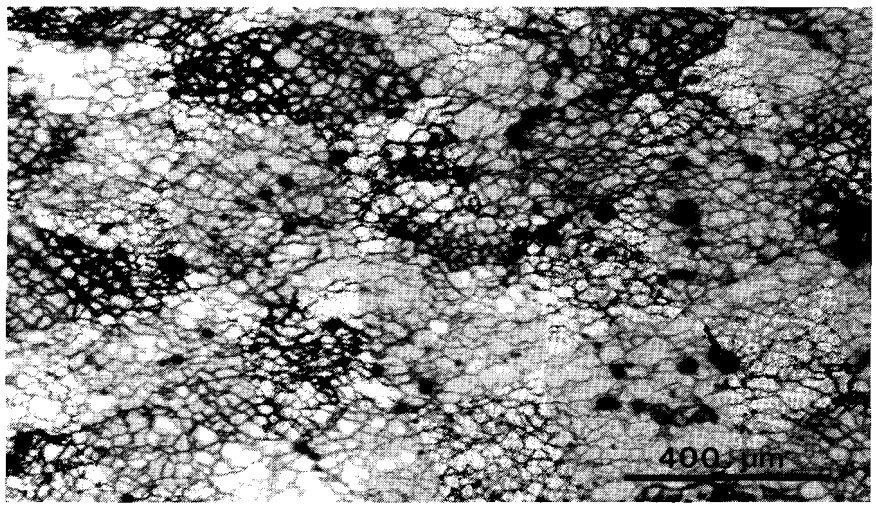

Figure 4.5:
Optical micrograph of a sample shortened 39% in uniaxial compression revealing the development of a cellular network of subgrains in all grains. The grains are strongly flattened. The subgrains also show a dimensional fabric. Note the scalloped grain boundaries visible even at this low magnification. (Sample C52, 350°C, ε =39%, compression direction vertical).

reveals the undeformed part of the sample. The upper half of the micrograph shows the dextral shear zone, containing strongly deformed grains. The transition zone between the "wall rock" and the shear zone is less than 400 µm (less than one grain diameter). Within typical shear zones, flattened and elongated grains define a clear foliation (Fig. 4.7). The orientation of the foliation was found to be constant across the width of the shear zone in all samples examined, and corresponded closely to the orientation of the plane of finite flattening of the strain ellipse calculated for simple shear (i.e. a simple shear deformation corresponding to the imposed displacement). Good agreement was also obtained between the strain ellipse calculated from grain boundary configurations and that expected for simple shear. These observations indicate that the deformation was close to simple shear. Turning now to the dislocation substructure, the sheared grains within the shear zones show cellular networks of subgrains (Figs. 4.6 and 4.7). The subgrain walls are preferentially oriented parallel and subnormal to the shear plane. Once again, grain boundaries tend to be irregular due to

Figure 4.6:
Photomicrograph revealing the transition from the undeformed wall rock to the shear zone in the reduced section of a sheared sample. The lower half shows the wall rock containing undeformed substructure-free grains. The upper half of the micrograph is well within the shear zone and contains sheared grains with a cellular network of subgrains. The shear zone boundary is less then 400 µm wide (i.e. the average grain size of the staring material). (Sample 118s, 300°C, γ=1.2, right lateral shear zone).

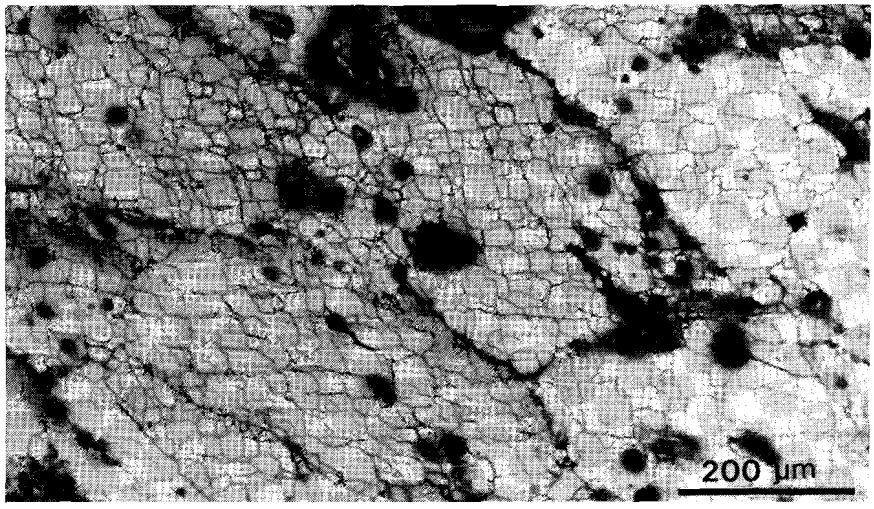

Figure 4.7:
Sheared sample containing a clear grain shape fabric defining the foliation apparent in this micrograph. The orientation of the foliation, as calculated from the grain boundary markers, corresponds closely to the orientation of the long axis of the strain ellipse. Note the scalloping of grain boundaries developed from small bulges at subgrains. (Sample 123, 300°C, γ=0.6, left lateral shear zone).

small bulges developing where subgrains intersect grain boundaries. Grain flattening and polygonization dominate the microstructure. However, evidence for grain boundary migration on the grain scale was observed locally.

In Fig. 4.8, subgrain size data obtained from both the compression and shear tests are plotted against applied stress ($\sigma_{applied}$, $\tau_{applied}$). In most materials, subgrain size is empirically found to be an inverse function of stress (Servi and Grant, 1951), and for salt various relationships have been obtained. The subgrain size vs. stress relationship for natural polycrystalline salt is given by $d(\mu m) = 190\ \sigma^{-1}$ (MPa) (Carter et al., 1982). For synthetic polycrystalline salt, Burke et al. (1981) obtained $d(\mu m) = 75\ \sigma^{-0.9}$ (MPa). Both relationships are shown in Fig. 4.8. All previously reported data for salt fall between these two lines (see Carter et al., 1982). Thus the present subgrain size vs. applied stress data seem reasonably consistent with previous findings although the significance of plotting $\tau_{applied}$ is not yet clear.

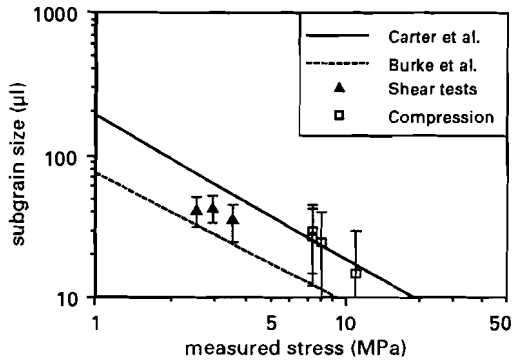

Figure 4.8:
Subgrain size versus applied ($\sigma_{applied}$, $\tau_{applied}$) stress for synthetic rocksalt experimentally deformed in compression (squares) and shear (triangles). The solid lines represent the empirical relationships obtained by Carter et al. (1982) and by Burke et al. (1981).

Figure 4.9:
Inverse pole figure for compression direction obtained from a uni-axially deformed sample (C15) shortened 18% at 250°C. Contour intervals are 0.2 times uniform. The area with an intensity greater than 1 is shaded. Maximum intensity observed is 1.4 times uniform at <110>.

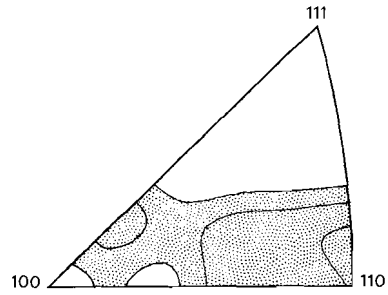

4.3.3 *Textures*

Pole figures have been determined for samples deformed in both deformation modes. The pole figures were measured using neutron diffraction goniometry at the GKSS Research Centre, Geesthacht, F.R.G. From the {220} and the {200} pole figures obtained for each sample, the orientation distribution function was calculated. From this, inverse pole figures were determined (Bunge, 1969; Dahms, 1987). The results presented here have been found to be representative of the two test types, for all temperatures in the range 250-550 °C.

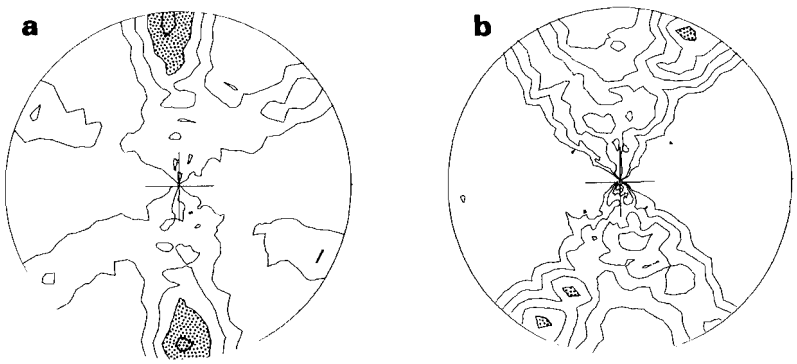

Figure 4.10:
Pole figures for the (a) {220} and the (b) (200) crystallographic directions for sample 123, deformed in shear at 300°C to a shear strain of 0.6. Contour interval for (a) is 0.25 and for (b) 0.125 times uniform. Areas with intensities greater than 1.5 times uniform are shaded. The orientation of the shear plane is E - W and the sense of shear is sinistral.

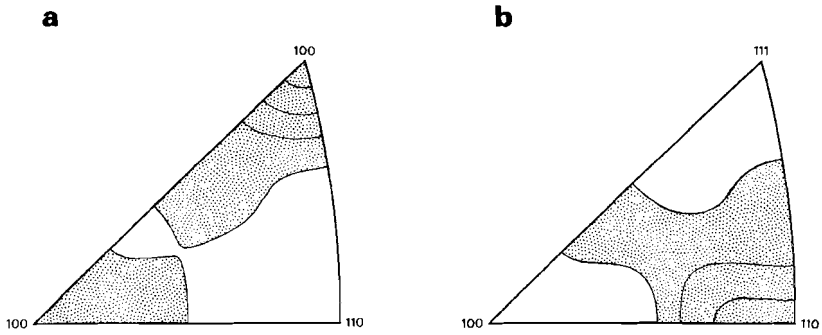

Figure 4.11:
Inverse pole figures for (a) the shear direction and (b) the shear plane normal, derived from the pole figures shown in Fig. 4.10. Contours intervals are 0.2 times uniform. Areas with intensities greater than 1 time uniform are shaded. Sample 123.

Fig. 4.9 shows an inverse pole figure for the compression direction of a uniaxially shortened sample deformed at 250 °C to 18% strain (C15). This texture consists of a maximum around the <110> direction spreading towards the <100> and <115> directions. The maximum around <110> is about 1.5 times uniform.

Fig. 4.10 shows the {220} and the {200} pole figures for sample 123 deformed in shear (at 300 °C) to a shear strain of 0.6. The {220} pole figure (Fig. 4.10a) exhibits a maximum perpendicular to the shear plane. In contrast, the {200} pole figure (Fig. 4.10b) shows a crossed girdle distribution with less intense maxima. Taking into account observations from other samples (Chapter 3), no consistent relationship between the sense of shear and the symmetry of the pole figures could be determined. With regard to the inverse pole figures for sample 123, that for the shear direction (Fig. 4.11a) shows a maximum around the <111> direction and a submaximum around <100>. The inverse pole figure for the shear plane normal (Fig. 4.11b) shows a maximum around the <110> direction (cf. Fig. 4.10a).

4.4 DISCUSSION

4.4.1 *Deformation mechanisms and microstructure*

The observed subgrain microstructures plus the presence of crystallographic and shape preferred orientation in compression and in shear are consistent with a climb-controlled dislocation creep mechanism. Furthermore, additional experimental data (Chapters 2 and 3) demonstrate power law creep behaviour in both deformation modes under the present conditions, with the power law exponent *(n)* ranging between 4 and 6 and the activation energy for creep (ΔH) ranging from 90 to 129 kJ/mol. These creep parameters are fully consistent with previous data on diffusion and on dislocation creep in dry salt (Heard, 1972; Arieli et al., 1982; Heard and Ryerson, 1986). It is concluded that deformation occurred by climb-controlled dislocation creep in both deformation geometries. The observation that grain boundary migration is more extensive in shear than in compression is thought to reflect the fact that higher strains are achieved in the shear experiments (Table 4.1).

4.4.2 *Textures*

The present texture data for uniaxial compression closely resemble the results obtained by Kern & Braun (1973) for salt deformed in axisymmetric compression under comparable conditions. We are not awa-

re of any previous experimental data on textures development in salt during simple shear under the present conditions. Recently, however, the Taylor theory and the self-consistent viscoplastic theory were applied to texture development in polycrystalline halite by Wenk et al. (1989a). Modelling was carried out for uniaxial compression and for simple shear assuming easy $\{110\}\langle 1\bar{1}0\rangle$ slip in accordance with the low/intermediate temperature single crystal yield data of Carter & Heard (1970). The Taylor simulation for uniaxial compression yields inverse pole figures which correspond closely with the present inverse pole figures for compression. The self-consistent simulation gives inverse pole figures with a maximum around <100>. Both the Taylor and the self-consistent texture simulations for shear deformation yield pole figures for {220} which are very similar to our results (Fig. 4.10), allowing for typical experimental errors. This broad agreement between our tests and the simulations supports the idea that texture development was dominated by the weaker $\{110\}\langle 1\bar{1}0\rangle$ systems in the present experiments. Since our data show a tendency for the {110} planes to align parallel to the shear plane in the shear tests, and normal to the compression direction in the uniaxial tests, at least some difference in mechanical behaviour can be expected in the two modes. Note, however, that our inverse pole figure for shear direction (Fig. 4.11a) shows a maximum parallel to <111>. Thus in shear, the slip direction of the weakest slip system is not aligned with the macroscopic shear direction.

4.4.3 *Mechanical behaviour*

An attempt is now made to compare the mechanical behaviour (strength) obtained in compression and shear in the framework of the von Mises theory of isotropic plasticity or the associated flow rule discussed in the introduction. In order to do this, we must first define a number of quantities required for such a comparison (see also Schmid et al., 1987).

Definitions

We start by introducing a quantity known as the equivalent stress, σ_{eq} (see McClintock & Argon, 1966). This is defined as

$$\sigma_{eq} = \sqrt{\tfrac{3}{2}\,\sigma_{ij}^{*}\,\sigma_{ij}^{*}} = \sqrt{3J_2^{*}} \qquad (4.1)$$

(where σ_{ij}^{*} is the deviatoric stress tensor and J_2^{*} is its second invariant) and represents a shear stress component equal to the octahedral shear stress of Nadai (1963) multiplied by a factor $\sqrt{\frac{3}{2}}$ (see Schmid at

al., 1987). Now, the von Mises yield criterion states that flow in an isotropic, perfectly plastic solid occurs when σ_{eq} attains a value equal to the yield (i.e. flow) strength in uniaxial compression (see McClintock & Argon, 1966). This holds for all stress states (σ_{ij}*) causing flow in such materials. For the case of an isotropic, perfectly plastic material undergoing flow, σ_{eq} can thus be regarded as a measure of flow strength, or flow stress, taking the same value independently of deformation geometry. Hence σ_{eq} forms a useful quantity for comparing the flow strength of real materials in different deformation modes. Note that for uniaxial stress ($\sigma_{11} = \sigma_{applied}$) equation (4.1) yields $\sigma_{eq} = \sigma_{11}$, whereas for a pure shear stress of magnitude τ, $\sigma_{eq} = \sqrt{3}.\tau$.

In order to compare strain rates in different deformation modes, we follow Schmid et al. (1987) in using a quantity generally referred to as the equivalent strain rate (see also Stocker & Ashby, 1973). For constant volume deformation, this is defined as

$$Seq = \sqrt{\frac{2}{3} SijSij} = \sqrt{\frac{4}{3} I_2} \qquad (4.2)$$

where S_{ij} is the strain rate tensor and I_2 is the second invariant of S_{ij}. It can be viewed as an octahedral shear strain rate in which the numerical factor is chosen such that the product $\sigma_{eq}S_{eq}$ equals the mechanical work rate $\sigma_{ij}S_{ij}$. In uniaxial shortening, S_{eq} is equal to the shortening strain rate (S_{11}). In simple shear at a shearing rate $\dot{\gamma}$, $S_{eq}=\dot{\gamma}/\sqrt{3}$.

To compare finite strains in different deformation geometries, we use the equivalent logarithmic strain. This is equal to the Nadai measure of octahedral strain magnitude (used by Schmid et al., 1987) multiplied by the factor $\sqrt{\frac{2}{3}}$. For deformation at constant volume it is defined as

$$\varepsilon eq = \sqrt{\frac{2}{3} \varepsilon ij \varepsilon ij} \qquad (4.3)$$

where ε_{ij} is the logarithmic strain tensor (Hill, 1950). This gives $\varepsilon_{eq} = \varepsilon_{11}$ in uniaxial compression and $\varepsilon_{eq} = \sqrt{4/3} \ln [\frac{1}{2} (\gamma+\sqrt{\gamma^2+4})]$ in simple shear. Note, however, that the physical significance of eeq is not clear.

4.4.4 *Comparison*

We begin our comparison of the mechanical behaviour observed in the uniaxial and shear tests by obtaining expressions for the state of deviatoric stress (σ_{ij}*) in the samples assuming isotropic, perfectly plastic behaviour. We make the additional assumptions (a) that the applied stresses are uniformally transmitted throughout the samples, and (b)

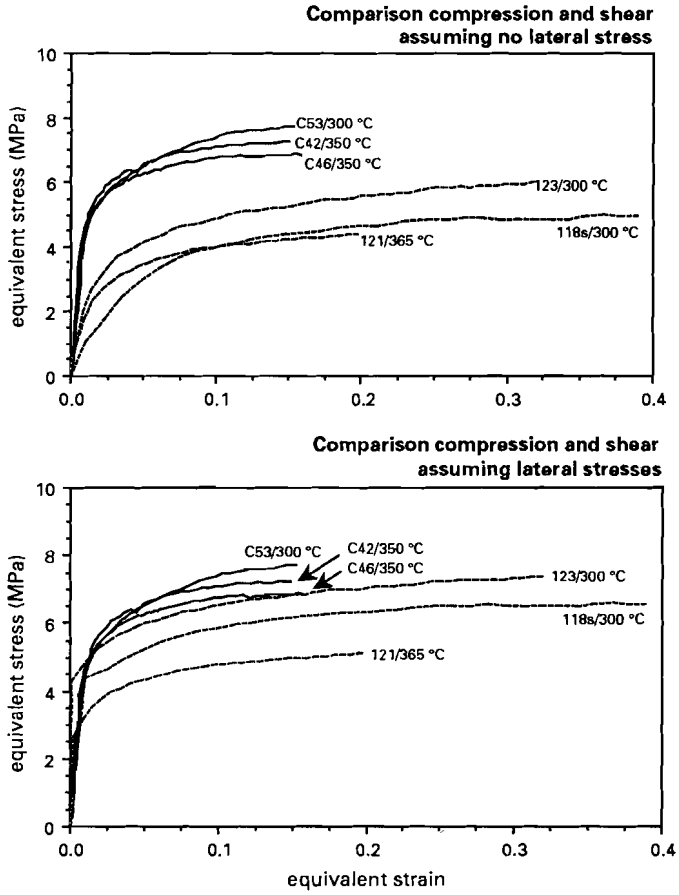

Figure 4.12:
Comparison of mechanical data from the compression tests (solid lines) and the shear tests (dashed lines) in terms of σ_{eq} and ε_{eq}. In (a), σ_{eq} is calculated directly from the applied stress ($\sigma_{applied}$ $\tau_{applied}$). In (b) lateral stresses of 3.5 MPa for 300°C and 2.15 MPa for 365°C are superposed for the calculation of the equivalent stress in shear. See text for discussion.

that the samples can be considered to be in static equilibrium with no couple stresses. For the uniaxial case, the results obtained for the non-zero components of σ_{ij}^* are $\sigma_{11}^* = (\frac{2}{3})\sigma_{applied}$ and $\sigma_{22}^* = \sigma_{33}^* = (\frac{1}{3})\sigma_{applied}$, whereas in shear we have $\sigma_{12}^* = \sigma_{21}^* = \tau_{applied}$. Using these results and assuming true uniaxial compression and simple shear deformations (at constant volume), equations (4.1) and (4.3) can be applied to derive σ_{eq} vs. ε_{eq} curves for the samples tested. This has been done for all experiments performed at comparable strain rates, i.e. at similar equivalent strain rates ($S_{eq} \approx 2x10^{-6}$ s^{-1}, refer to Table 4.1 and equation 4.2). The curves obtained are shown in Fig. 4.12a. From these, it appears that at constant temperature the uniaxially deformed samples support substantially higher equivalent stresses (σ_{eq}) than the sheared samples, for all values of ε_{eq}. Because of ambiguity in the physical meaning of ε_{eq}, however, the most significant observation is that the (near) *steady state* values of σ_{eq} are 1.5 times larger in compression than in shear (under comparable conditions). This behaviour is clearly not consistent with that expected for an isotropic, perfectly plastic material under the assumptions made above. The implication is:

(a) that the samples (though initially free of crystallographic or dimensional preferred orientation) become mechanically anisotropic during deformation, exhibiting truly lower strength in shear than in compression; or

(b) if the samples remain more or less mechanically isotropic, that the calculated values of σ_{ij}^* and σ_{eq} are in serious error because of imperfectly imposed boundary conditions or effects such as volume changes occurring within the samples.

Now, taking into account the lack of texture in the starting material and the symmetry of deformation, the state of deviatoric stress (and hence σ_{eq}) in the compression tests can be considered reasonably well determined $\sigma_{11}^* = \frac{2}{3}\sigma_{applied}$, $\sigma_{22}^* = \sigma_{33}^* = \frac{-\sigma_{11}}{2}$). In shear deformation, however, the full state of deviatoric stress in the samples is not known, since only vertical stresses are measured. Thus, errors may arise in calculating σ_{eq} in shear. Nonetheless, *for the case that the samples remain roughly isotropic during deformation* (see (b) above), the range in magnitude of σ_{eq} can be constrained. Two extreme constraints can be envisaged:

(1) If the sample in the shear zone dilates during deformation, compressive stresses will be generated in the "wall rock" of the sample. Density measurements on the deformed samples show dilation during shear was less than 0.2%. If this volume change is translated

into "virtual displacements" occurring perpendicular to the shear plane at a constant rate throughout deformation, then the maximum compressive stress generated normal to the shear zone can be estimated (in a time-averaged sense) from the creep law derived from uniaxial tests. From these calculations, it has been found that the maximum normal stresses induced by dilatancy during the shear experiments take average values between 2.15 and 3.5 MPa, depending on temperature. The σ_{eq} - ε_{eq} curves for shear have been recalculated using these values of normal stress superposed on the measured stresses. The result is shown in Fig. 4.12b. Still the salt appears weaker in shear than in the compression experiments.

2) In the present shear apparatus tensile stresses may develop in the sample due to imperfectly imposed boundary conditions as the middle bar is displaced downwards. However, no evidence of tensile or extensional failure was observed in the sheared samples. It follows that the tensile stresses acting in the shear samples were almost certainly less than the room temperature tensile strength of 1-3 MPa (Gessler, 1983). Introducing tensile stresses of 3 MPa; perpendicular or parallel to the shear zone, into the equivalent stress calculation yields closely similar curves to those shown in Fig. 4.12b.

On the basis of the above, it seems that the "weak" behaviour observed in shear cannot be accounted for by isotropic behaviour of the samples coupled with errors in determining stress. We therefore infer that the samples became *mechanically anisotropic* during deformation, leading to truly weaker behaviour in shear than in compression when viewed in the framework of the von Mises theory. Thus the assumptions underlying the theory of perfect isotropic plasticity and the associated flow rule (for generalizing creep laws to 3-D) do not seem to be applicable to the present experiments. Since the volume changes are smaller than 0.2% in both shear and compression, and since the same deformation mechanisms (dislocation creep) and microstructural processes are operative, we infer that the observed differences in mechanical behaviour between shear and compression are largely due to the textures developed in the two modes. In future, this explanation should be tested by means of Taylor or self-consistent simulations including the single cystal yield parameters and creep properties appropriate to the present experimental conditions (see Wenk et al., 1989). Finally, we note that the 'texture weakening' effect inferred here is quite different from the weakening reported by Burrows et al. (1979) and Drury et al. (1985). Their weakening was associated with grain-scale shear lo-

calization, recrystallization and internal strain softening. The present effect involves no grain-scale localization process.

4.5 CONCLUSIONS

Dry polycrystalline salt has been deformed in compression and in near simple shear, at temperatures in the range 250 - 350 °C. The microstructure developed in compression and in shear is characterized by strongly deformed grains containing cellular networks of subgrains produced by polygonization. The deformation mechanism is of a climb-controlled dislocation creep type. The textures developed in compression are characterized by a tendency for the {110} planes of the relatively weak $\{110\}\langle 1\bar{1}0\rangle$ slip systems to rotate perpendicular to the compression direction. In shear the {110} planes tend to align with the flow plane, but the $\langle 1\bar{1}0\rangle$ direction does not align with the flow direction. Instead the <111> direction tends to lie parallel to the shear direction. A difference in mechanical behaviour has been observed between shear and compression. In terms of equivalent stress (calculated assuming isotropic behaviour), significantly lower flow stresses were obtained in shear than in compression. It is inferred that this difference in flow strength is largely due to anisotropy, i.e. to the development of the observed textures. Our results suggest that the associated flow rule does not offer an accurate method of generalizing creep laws for salt to 3-D (under the deformation conditions investigated here).

INFLUENCE OF DEFORMATION GEOMETRY on the flow behaviour of polycrystalline halite at temperatures in the range 250-600 °C*

ABSTRACT

In almost all geological modelling studies of large scale deformation, experimentally obtained axisymmetric flow laws, have been generalized using the associated flow rule known from the theory of perfect isotropic plasticity. The present study aims at a verification of the validity of this approach using an extensive experimental data set for synthetic polycrystalline halite, deformed in uniaxial compression and simple shear in the temperature field 250-600 °C. Climb-controlled dislocation creep models describe the flow behaviour, and at temperatures below 450 °C climb is controlled by pipe diffusion, whereas at higher temperatures climb is controlled by lattice diffusion.

The mechanical behaviour seen in uniaxial compression and shear is compared in terms of equivalent stress and strain and strain rate, as defined in the theory of perfect isotropic plasticity. Below 400 °C, the equivalent stresses supported in shear are smaller than those in compression (at similar equivalent strain rate and temperatures) for all strains, from the initial work-hardening stage of deformation through into the steady state. However, at temperatures above 400-45°C, the work hardening and steady-state behaviour obtained from both test geometries is similar. It is argued that the hardening behaviour of salt depends on the number and combination of activated slip systems (with differing critical resolved shear stresses), which in turn depends on the deformation geometry. The flow laws obtained in compression and shear have been compared using the associated flow rule. In the temperature range 250-450 °C, the flow law for compression is characterized by a significantly higher activation energy (by 35 kJ/mol) than the flow law for shear. The difference in activation energy in the

* *This chapter has been submitted to Journal of Geophysical Research as: Franssen, R.C.M.W. and Spiers, C.J. Influence of deformation geometry on the flow behaviour of polycrystalline rocksalt at temperatures in the range 250 - 600 °C.*

pipe diffusion field may be caused by variations in dislocation substructure developed in shear and compression as a result of differences in activated slip systems.

The associated flow rule does not offer an adequate method of generalizing the flow law for salt in the pipe-diffusion field. However, dislocation creep laws reflecting lattice diffusion control can be generalized by the associated flow rule. Under geologically relevant conditions ($T < 250$ °C), the generalization of the flow law for rocksalt, using the associated flow rule, may lead to errors in strain rate up to 2 orders of magnitude. Similar effects may occur in other rock forming minerals in the low temperature dislocation creep field when slip systems have very different strengths and when recovery and migration recrystallization are limited, or when pipe diffusion controls the dislocation creep rate.

5.1 INTRODUCTION

To numerically model the mechanical behaviour of a rock body under given boundary conditions, it is necessary to generalize experimentally obtained flow laws, in which stress and strain rate are generally treated as scalars, to a general three dimensional description wherein these quantities are treated as tensors (McClintock and Argon, 1966; Stocker and Ashby, 1973; Ranalli, 1987; Twiss and Moores, 1992). For example, almost all flow laws available for olivine rocks have been obtained from axially symmetric experiments and relate axial strain-rate to axial differential stress; in order to model large-scale mantle flow processes in 2-D or 3-D, these have to be generalized into relations linking the strain rate tensor $\dot{\varepsilon}_{ij}$ to the stress state σ_{ij} (Stocker and Ashby, 1973; Ranalli, 1987; Van Keken, 1993). The same type of generalization procedure must also be applied to axi-symmetric data on rocksalt in order to model tectonic processes as well as the (thermo)mechanical response of salt formations to the construction of waste repositories and/or storage caverns (Prij, 1983; Janssen et al. 1984; Van Sambeek, 1987; Spiers et al., 1986; Van Keken et al., 1993). This type of generalization is usually done using the theory of perfect isotropic plasticity known from metallurgy (applied to incompressible media in a form often referred to as the associated flow rule). This theory implies that the principal axes of stress coincide with the principal axes of strain rate (Nye, 1953a; Paterson, 1976; Hobbs et al., 1990). In other words, the plastic strain rate vector is always normal to the yield surface ('normality rule' of Drucker, 1951, 1956).

The assumptions underlying this method of generalization are that i) the material is isotropic, remains isotropic during deformation and has no memory for incremental strain history (i.e. the behaviour is path independent), ii) deformation is isovolumetric and iii) the material response is independent of the third invariant of the deviatoric stress tensor (Nye, 1953ab; Ranalli, 1987; Schmid et al., 1987).

While the above method of generalization is widely applied in almost all modelling studies of large scale deformation phenomena, it is well-known that most plastically deforming materials have some microstructural memory for incremental strain history (for example Schmid et al., 1987), and it may be expected and occasionally has been observed that the incremental deformation history influences the mechanical behaviour to some extent (for example: Ghosh and Backofen, 1973; Tomé et al., 1984). Furthermore, it has been clearly demonstrated from theory that axi-symmetric deformation experiments on materials with 'memory' are insufficient to fully characterize the material behaviour (Hobbs, 1972; Ferguson, 1979). Since most flow laws for rocks are obtained from axi-symmetric compression experiments, there is no *a priori* justification for generalizing these flow laws using the associated flow rule, and experimentally based information on the validity of the associated flow rule for individual materials is clearly needed.

Limited experimental data for calcite rocks suggest that flow laws derived from axi-symmetric experiments may be generalized using the associated flow rule approach (Schmid et al, 1987). Schmid et al. (1987) compared mechanical data from simple shear experiments with flow law predictions based on conventional axially symmetric experiments. In the case of Carrara marble deformed in the dislocation creep regime, a good agreement was observed between the shear data and flow laws obtained from axi-symmetric experiments, though, the mechanical data from Solnhofen limestone deformed in shear and compression show a less favourable agreement. On the other hand, in a simple comparison of the flow stresses obtained in polycrystalline halite in compression and shear at 250-350 °C at fixed strain rate, Franssen and Spiers (1990) (Chapter 4) found that the associated flow rule can introduce very significant errors. For example, assuming isotropic plasticity, it has been shown that the near steady state flow stresses are c. 1.5 times larger in compression than in shear (under comparable conditions). In the present paper we extend this earlier work by conducting a comparison of the extensive bodies of σ-$\dot{\varepsilon}$-T data reported in Chapters 2 and 3 for salt deformed in compression and shear. The comparison is carried out in the framework of perfect plasticity theory with the aims of i) testing the validity of the associated flow rule for deformation of salt in the dislocation creep field, and ii) of interpreting any differences in flow behaviour between the two deformation geometries in terms of the underlying microphysical processes operating in the material. The motivation for the present study was to gain insight into the influence of deformation geometry on flow behaviour, not only for salt in its own

right, but also from the viewpoint of shedding light on effects that might occur in silicate minerals. The results show that the deformation geometry has a clear effect in salt at conditions favouring pipe-diffusion controlled dislocation creep. A similar effect can also be expected in other minerals, for example quartz and olivine, under conditions of favouring dislocation glide or creep.

5.2 EXPERIMENTAL DATA FOR POLYCRYSTALLINE HALITE DEFORMED IN COMPRESSION AND SHEAR

As mentioned above, a large body of experimental data on the deformation behaviour of synthetic polycrystalline salt in uniaxial compression and in shear has been reported in Chapters 2 and 3.

The uniaxial compression experiments were carried out in an Instron 1193 constant displacement apparatus equipped with a high temperature furnace and superalloy loading pistons. The shear experiments were carried out in a shear rig consisting of three parallel bars (Franssen and Spiers, 1990). The two outer bars were fixed to end-platens and are immobile whereas the middle bar is free to move in the vertical direction only, i.e. parallel to the fixed outer bars. A sample with reduced sections was fitted length-wise through aligned holes in the three loading bars. Advancing the middle bar downwards imposed a deformation close to simple shear on the reduced sections of the sample. The experiments were carried out in the temperature range 250 - 600 °C with strain rates between 10^{-3} - 10^{-7} s^{-1}. The shear strain-rates were chosen to be comparable with the compression strain-rates according to the equivalent strain-rate concept (Franssen and Spiers, 1990). Constant strain-rate, strain-rate stepping tests and creep tests were carried out, the data set consists of $\sigma - \varepsilon$ and σ-$\dot{\varepsilon}$-T data.

Mechanical data

Table 5.1 summarizes the details of the experiments reported in the present study. Typical applied stress vs. axial strain curves for uniaxial compression experiments are shown in Fig. 5.1. Below 400-450 °C, these curves show considerable work-hardening during the 5 - 10% shortening. At higher temperatures, steady state is attained within c.2% strain. The steady state flow stress decreases from c. 5 - 10 MPa at low temperatures to c. 0.5 - 1 MPa at 600 °C. Typical applied shear stress vs. shear strain data obtained from shear experiments are shown in Fig. 5.2 (see Table 5.1 for details). All curves show work hardening during the first 0.1 - 0.2 shear strain, then steady state flow is attained.

Table 5.1 *Summary of mechanical data of uniaxial compression and shear experiments used in this study.*

Test number	T (°C)	Strain rate (s^{-1})	Stress (MPa) at 10% strain or	Final strain	Equivalent stress at end of test or step
Uniaxial compression experiments					
C53	300	$1.8*10^{-6}$	7.5	14.2%	7.7
C6	300	$3.6*10^{-6}$	8.3	24.0%	9.4
C42	350	$1.8*10^{-6}$	7.1	13.9%	7.3
C46	350	$1.8*10^{-6}$	6.7	14.6%	6.9
C5	350	$3.6*10^{-6}$	6.4	23.0%	7.1
C8	400	$1.8*10^{-6}$	4.2	14.0%	4.2
C27	400	$1.8*10^{-6}$	3.7	14.3%	3.8
C2	400	$3.6*10^{-6}$	5.2	19.9%	5.7
C3	450	$3.6*10^{-6}$	3.6	20.2%	4.0
C44st1	*450*	*$3.6*10^{-7}$*	*2.3 at*	*9.0%*	*2.3*
C44st2	*450*	*$1.8*10^{-6}$*	*3.0 at*	*12.0%*	*3.0*
C44st3	450	$3.6*10^{-6}$	3.4 at	14.8%	3.4
C4	500	$3.6*10^{-6}$	2.8	20.6%	3.0
C54st1	*500*	*$1.8*10^{-6}$*	*3.4*	*11.2%*	*3.4*
C54st2	500	$3.6*10^{-6}$	3.9	14.9%	3.9
C19	550	$1.8*10^{-6}$	1.5	15.2%	1.5
C24	550	$3.6*10^{-6}$	1.7	19.1%	1.8
C40	600	$3.6*10^{-6}$	1.2	19.3%	1.2
C41st1	*600*	*$3.6*10^{-7}$*	*0.6 at*	*11.6%*	*0.6*
C41st2	600	$1.8*10^{-6}$	0.8 at	14.4%	0.8
C41st3	600	$3.6*10^{-6}$	1.0 at	17.9%	1.0
C41st4	600	$1.8*10^{-5}$	1.5 at	22.0%	1.5
			Final shear stress (MPa)	Final shear strain	
Shear experiments					
123	300	$3.6*10^{-6}$	3.46	0.56	6.0
118s	300	$3.6*10^{-6}$	2.85	1.22	5.0
121	365	$3.6*10^{-6}$	2.54	0.34	4.4
124	365	$7.2*10^{-6}$	2.23	0.99	3.9
122	400	$3.6*10^{-6}$	2.27	0.96	3.9
114s	400	$3.6*10^{-6}$	2.67	1.58	4.6
117s	400	$7.2*10^{-6}$	2.22	1.19	3.8
112s	450	$7.2*10^{-6}$	2.20	1.80	3.8
101	500	$7.2*10^{-6}$	1.41	0.55	2.4
110s	500	$7.2*10^{-6}$	1.43	0.66	2.5
111s	500	$7.2*10^{-6}$	1.5	1.95	2.6
108	550	$3.6*10^{-6}$	0.75	0.96	1.3
116s	550	$7.2*10^{-6}$	1.3	1.18	2.2
109	550	$7.2*10^{-6}$	1.12	1.38	1.9
126st1	600	$3.6*10^{-6}$	0.52	0.32	0.9
126st2	600	$7.2*10^{-6}$	0.58	0.58	1.0
126st3	600	$3.6*10^{-5}$	0.8	1.0	1.4

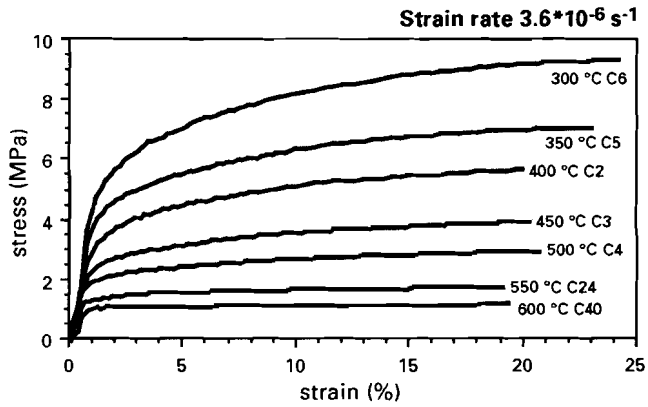

Figure 5.1:
Typical stress-strain curves for uniaxially compressed polycrystalline halite deformed at a constant strain rate of $3.6*10^{-6}$ s^{-1} between 300 and 600°C. Each curve is labelled with test temperature and test number (italics).

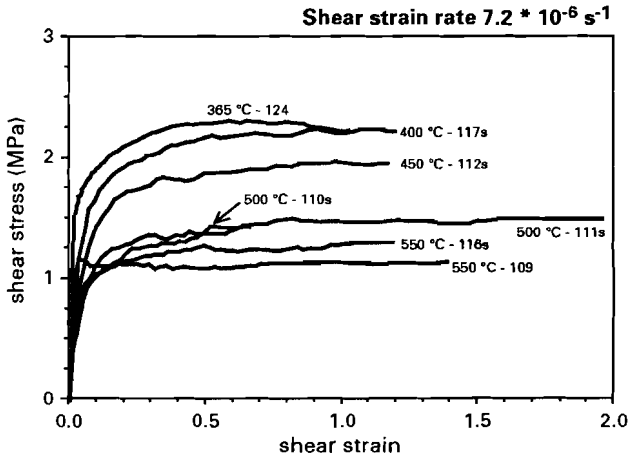

Figure 5.2:
Applied shear stress ($\tau_{applied}$) versus shear strain plots for polycrystalline halite deformed in shear for temperatures between 365 and 550°C and an applied shear strain rate of $7.2*10^{-6}$ s^{-1}. Each curve is labelled with test temperature and test number (italics).

Table 5.2
Flow law parameters derived from uniaxial compression and simple shear experiments (see Chapters 2 and 3). The mechanical data have been fitted to a general power law creep equation (Frost & Ashby, 1982):

$\dot{\varepsilon} = A\exp(-\Delta H/RT)(\sigma_{applied})^n$ for uniaxial compression and

$\dot{\gamma} = A\exp(-\Delta H/RT)(\tau_{applied})^n$ for shear deformation

Temperature interval (°C)	Deformation mode	n-value	ΔH (kJ/mol)	lnA ($MPa^{-n}s^{-1}$)
250 - 450	shear deformation	5.2±0.20	92.7±7	-0.33±3.0
	uniaxial compression	5.7±0.33	129±8	1.75±4.0
500 - 600	shear deformation	4.3±0.28	209±18	19.5±2.7
500 - 780	uniaxial compression	4.4±0.22	227±10	18±2.3

Meaning of symbols: $\dot{\varepsilon}$ the strain rate (s^{-1}); σ: the applied stress (MPa); $\dot{\gamma}$: the shear strain rate (s^{-1}); τ: the applied shear stress (MPa); n: the power-law exponent; ΔH: apparent activation energy for creep (kJ/mol); A is a constant ($MPa^{-n}s^{-1}$); R: the gas constant (kJ/Kmol); T: temperature (K); ln: natural logarithm.

The steady state flow stress ranges from c. 3.5 MPa at 300 °C to c. 0.5-1 MPa at 600 °C. Accurate density measurements on the deformed samples showed that dilation during shear was less then 0.2%.

Flow behaviour and rate-controlling processes

In compression and simple shear, climb-controlled dislocation creep models describe the flow behaviour across the entire range of conditions investigated. At temperatures from 250 to 450 °C, the dominant mechanism is inferred to be climb controlled by diffusion through dislocation cores (pipe diffusion). The flow law for *uniaxial* compression, in this temperature regime, is given by (see also Table 5.2):

$$\dot{\varepsilon} = 5.75\exp(-129 \pm 8/RT)\sigma^{5.7\pm0.33} \qquad (5.1)$$

where $\dot{\varepsilon}$ is the compression strain rate (in s^{-1}); the activation energy for creep is expressed in kJ/mol and the applied stress σ in MPa.

The flow law obtained from *shear* experiments, at temperature, in the range from 250 to 450 °C, is given by:

$$\dot{\gamma} = 0.72\exp(-93 \pm 7/RT)\tau^{5.2\pm0.2} \qquad (5.2)$$

and $\dot{\gamma}$ is the shear strain rate, τ is the shear stress.

In the temperature range 500-600 °C, the flow behaviour is inferred to be dominated by lattice diffusion controlled dislocation creep. The flow law for uniaxial compression is given by the empirical equation:

$$\dot{\varepsilon} = 6.57\times10^{7}\exp(-227 \pm 10/RT)\sigma^{4.4\pm0.2} \qquad (5.3)$$

and the flow law for shear deformation is given by:

$$\dot{\gamma} = 2.65\times10^{8}\exp(-209 \pm 18/RT)\tau^{4.3\pm0.3} \qquad (5.4)$$

Pipe diffusion and lattice diffusion controlled dislocation creep are parallel-concurrent processes, which act simultaneous and each contribute to the total strain-rate. The total strain-rate therefore can be described as the sum of the strain rates of the two creep mechanisms (Poirier, 1985). Consequently, the total strain rate in compression is given by:

$$\dot{\varepsilon}_{tot} = 6.57\times10^{7}\exp(-227 \pm 10/RT)\sigma^{4.4\pm0.2} + 5.75\exp(-129\pm8/RT).\sigma^{5.7\pm0.33} \qquad (5.5)$$

and the total strain rate in shear is given by:

$$\dot{\gamma}_{tot} = 2.65\times10^{8}\exp(-209 \pm 18/RT)\tau^{4.3\pm0.3} + 0.72\exp(-93 \pm 7/RT)\tau^{5.2\pm0.2} \qquad (5.6)$$

The empirical equations 5.5 and 5.6 agree favorably with the mechanical data obtained in compression and in shear respectively (Chapters 2 and 3). In general, the process with the lowest activation energy gives the largest contribution to the total strain rate at low temperatures, whereas the process with the highest activation energy dominates the deformation rate at high temperatures. In the temperature range 450-500 °C, both pipe diffusion and lattice-diffusion controlled dislocation creep contribute approximately equally to the total strain rate (Chapters 2 and 3).

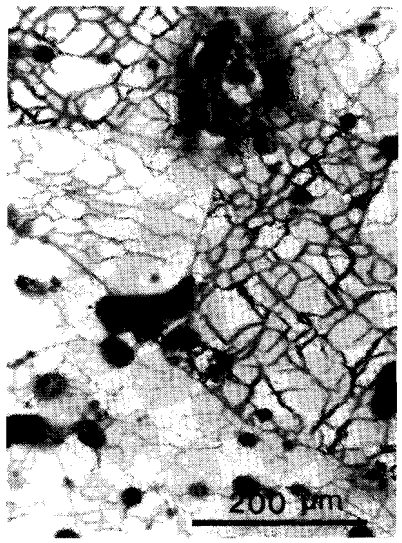

a

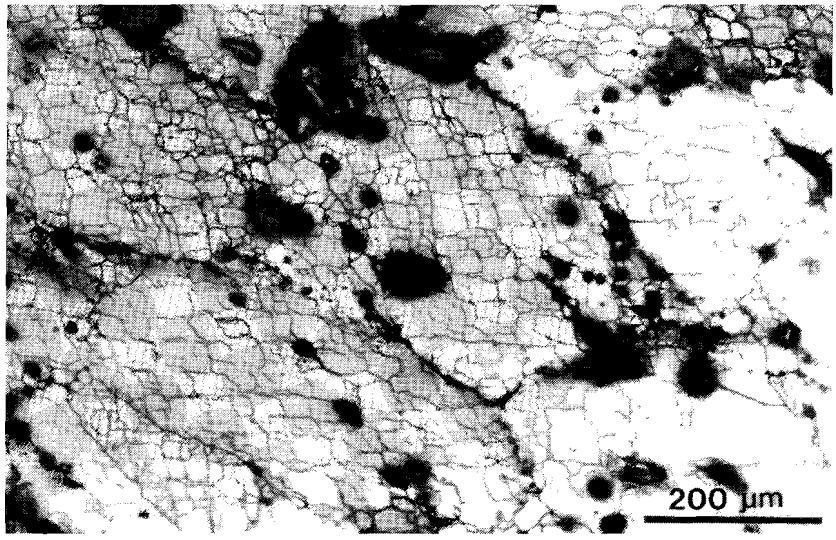

b

Figure 5.3:
Typical microstructures developed in compression and shear experiments at 250-350°C.

(a) Cellular subgrains develop in uniaxial compression (sample C42, 350°C, ε = 13.9%)

(b) Blocky subgrains, with the sides approximately parallel and subnormal to the shear plane, are often observed in sheared samples. The deformed grain shape fabric defines a foliation. (sample 123, 300°C, final shear strain 0.56).

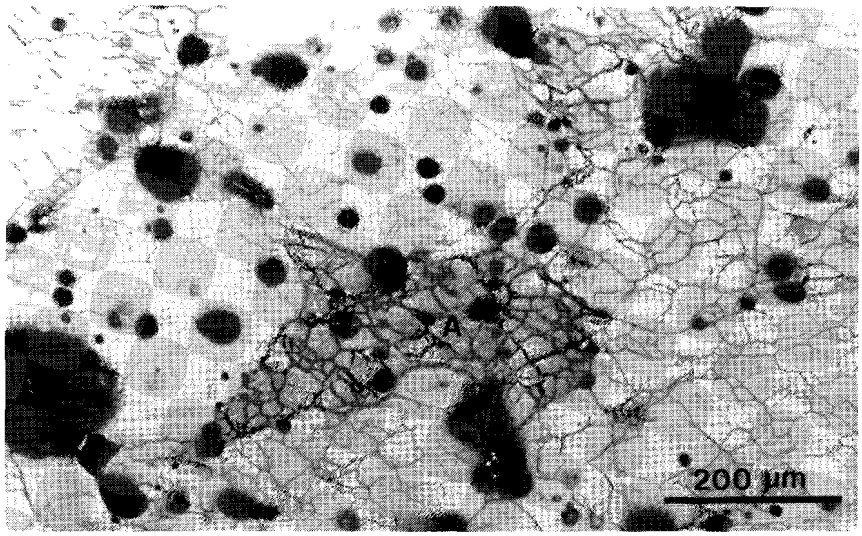

a

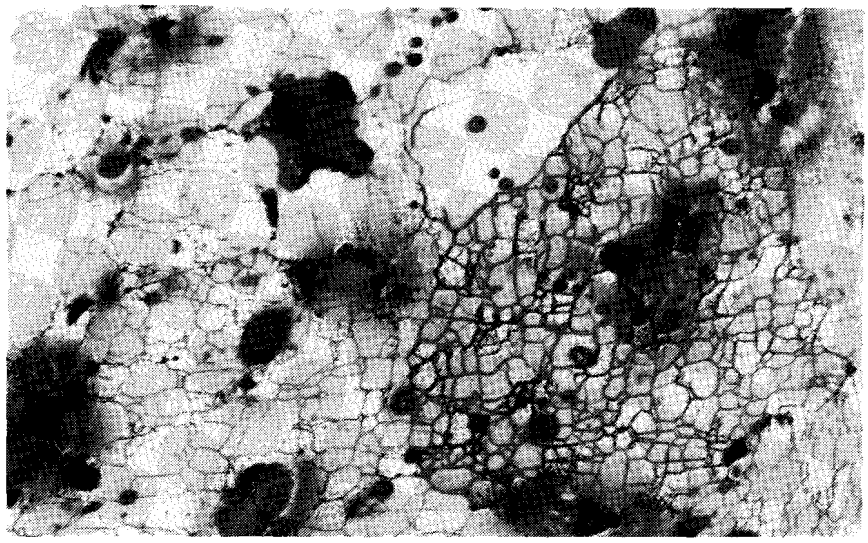

b

Figure 5.4:
Microstructures observed in uniaxially and sheared samples deformed at 400-500 °C. Grains have concavo-convex contacts due the development of grain boundary bulges which indicates limited activity of migration recrystallization. Deformed and recrystallized grains contain well developed cellular subgrains. (a) Compression, sample C8, 400 °C, 14% shortening, (b) Sheared sample 122, 400 °C, final shear strain 1.2. Same scale bar as in a) applies.

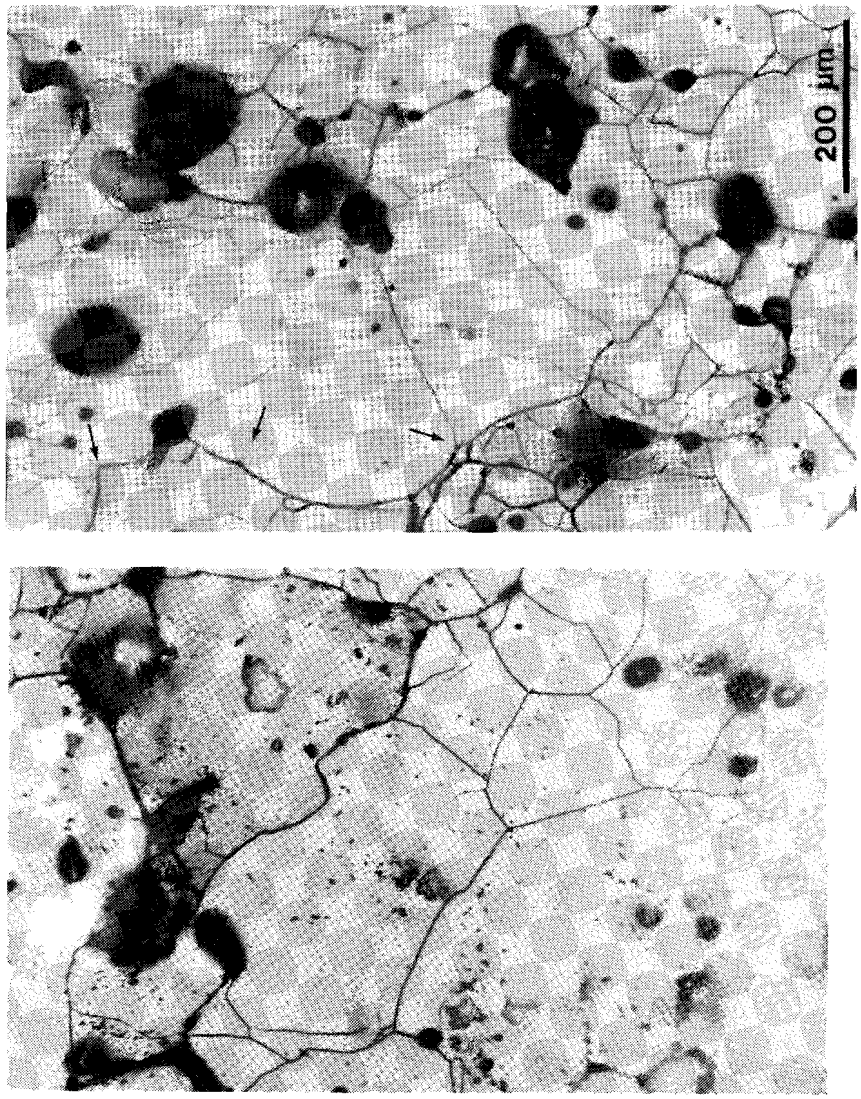

Figure 5.5:
At temperatures above 500 °C the microstructural development is controlled by grain boundary migration recrystallization. (a) Sample shortened 15.2% at 550°C. The dark-etched grain (left of centre) is a deformed grain which being consumed by the light-etched grain in the centre. Subgrain boundaries in the recrystallizing grain appear to pin the migrating boundary. (b) Sheared sample 110s deformed at 500 °C to $\gamma = 0.66$. Similar observations as in (a) can be made. For micrograph in b): scale bar shown in (a) should read 100 µm.

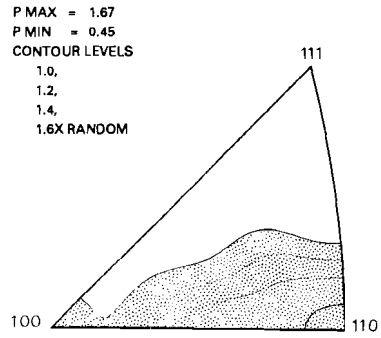

Figure 5.6:
Inverse pole figure for the compression direction of sample C4 shortened 21% at 500 °C. Contour intervals in 0.2 times uniform, area with intensities greater than 1 is shaded. The maximum intensity at <110> is characteristic for the temperature range 250-550 °C.

Microstructural processes

In the temperature range 250 - 350 °C, the microstructural development in both deformation geometries is characterized by polygonization and rotation recrystallization (Fig. 5.3). At higher temperatures, grain boundary migration becomes more important (Fig. 5.4). The development of concavo-convex grain contacts and cuspate grain boundaries is inferred to be consistent with strain-induced grain boundary migration (Nicolas and Poirier, 1976; Karato, 1988, Derby, 1990; Drury and Urai, 1990). At temperatures in the range 500-600 °C, grain boundary migration is the dominant microstructural processes. The transition to migration recrystallization dominated microstructures coincides with a change in the dominant deformation mechanism from pipe- to lattice-diffusion controlled creep (Fig. 5.5) (Chapters 2 and 3). This can be explained as due to relative changes of grain boundary mobility, nucleation rate and driving force in relation to Derby's (1992) dynamic recrystallization model (see Chapter 2).

Crystallographic preferred orientations

For all temperatures investigated, the crystallographic preferred orientations developed in compression are characterized by rotation of the {110} poles towards the shortening direction (Fig. 5.6). In shear, the crystallographic preferred orientation is characterized by rotation of {110} planes parallel to the shear plane. The inverse pole figures of the shear direction show a maximum around <111> (Fig. 5.7). The experimentally obtained textures resemble the results obtained by Wenk et al. (1989a), who modelled texture development in halite simulating compression and shear deformation at room temperature.

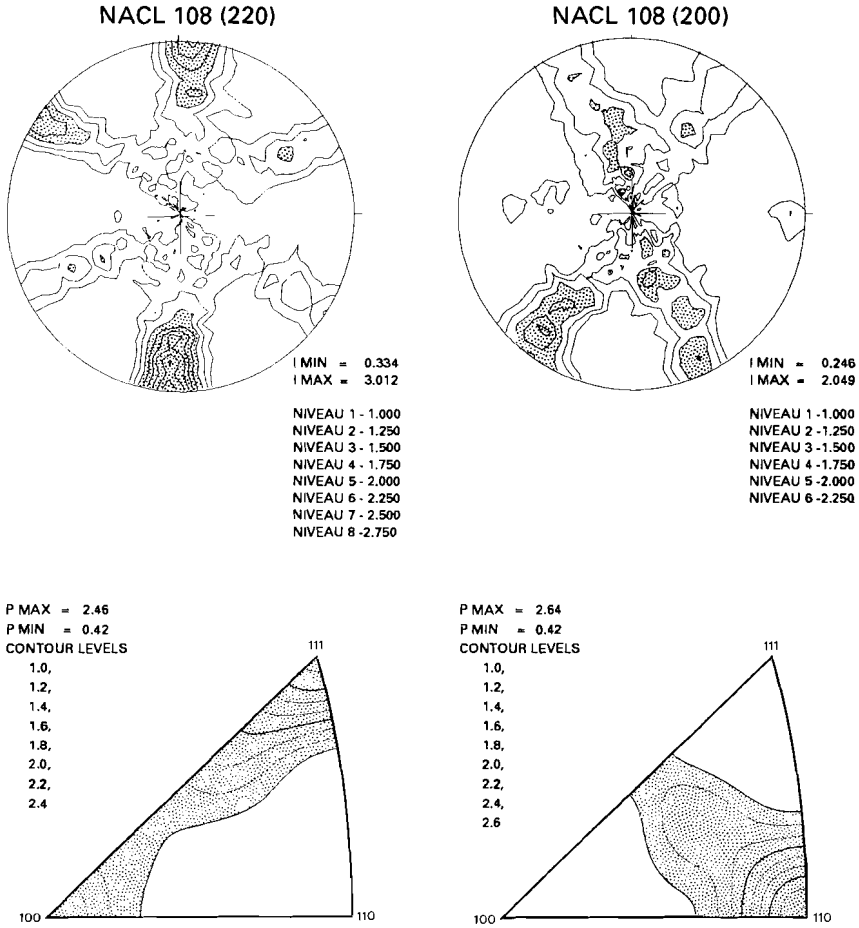

Figure 5.7:
Top: pole figure for the {220} and {200} crystallographic directions and bottom: inverse pole figure for the shear direction (left) and the shear plane normal (right) of sample 108 deformed at 550 °C (γ = 1). Contour levels in times uniform are indicated. Similar (inverse) pole figures are obtained from samples deformed in the temperature range 300 - 550 °C.

5.3 COMPARISON OF THE MECHANICAL BEHAVIOUR IN COMPRESSION AND SHEAR

5.3.1 *Definition of quantities*

An attempt is now made to compare the mechanical behaviour (flow strength) and the flow laws obtained in compression and shear. This comparison is done within the framework of the von Mises theory of isotropic plasticity. This theory states that yielding (flow) in an isotropic incompressible material occurs when the state of stress satisfies a particular condition c.q. the yield criterion. The flow behaviour reflects physical properties of the material and the von Mises criterion must be valid under any coordinate transformation. It is therefore natural to express a number of quantities in terms of invariants (McClintock and Argon, 1966; Ranalli, 1987).

Definitions

We start by introducing a quantity known as the equivalent stress, (see Hill, 1950; McClintock & Argon, 1966). This is defined as

$$\sigma_{eq} = \sqrt{\tfrac{3}{2}\ \sigma_{ij}{}^{*}\sigma_{ij}{}^{*}} = \sqrt{3J_2{}^{*}} \qquad (5.7)$$

where $\sigma_{ij}{}^{*}$ is the deviatoric stress tensor and $J_2{}^{*}$) is its second invariant. The von Mises yield criterion states that flow in a homogeneous isotropic, incompressible, perfectly plastic solid occurs when σ_{eq} reaches a critical value equal to the yield strength in uniaxial compression. This holds for all stress states ($\sigma_{ij}{}^{*}$) causing flow in such materials (Hill, 1950; McClintock & Argon, 1966). In case of an isotropic, perfectly plastic material undergoing flow, σ_{eq} can thus be regarded as a measure of flow strength, or flow stress, taking the same value independently of deformation geometry. Hence σ_{eq} forms a useful quantity for comparing the flow strength of real materials in different deformation modes. For uniaxial stress ($\sigma_{11}=\sigma_{applied}$) equation (Eq. 5.7) yields $\sigma_{eq} = \sigma_{11}$, whereas for a pure shear stress of magnitude τ, $\sigma_{eq} = \sqrt{3}.\tau$.

In order to compare strain rates in different deformation modes, we follow Schmid et al. (1987) in using a quantity generally referred to as the equivalent strain rate (see also Stocker & Ashby, 1973). For constant volume deformation, this is defined as

$$S_{eq} = \sqrt{\tfrac{2}{3}\ S_{ij}S_{ij}} = \sqrt{\tfrac{4}{3}\ I_2} \qquad (5.8)$$

where S_{ij} is the strain rate tensor and I_2 is the second invariant of S_{ij}. It can be viewed as an octahedral shear strain-rate in which the numerical factor is chosen such that the product $\sigma_{eq}S_{eq}$ equals the mechanical work rate $\sigma_{ij}S_{ij}$. In uniaxial shortening, S_{eq} is equal to the shortening strain rate (S_{11}). In simple shear at a shearing rate $\dot{\gamma}$, $S_{eq}=\dot{\gamma}/\sqrt{3}$.

To compare finite strains in different deformation geometries, we use the equivalent logarithmic strain (Hill, 1950; McClintock and Argon, 1966). For deformation at constant volume it is defined as

$$\varepsilon_{eq}=\sqrt{\tfrac{2}{3}\varepsilon_{ij}\varepsilon_{ij}} \qquad (5.9)$$

where ε_{ij} is the logarithmic strain tensor. This gives $\varepsilon_{eq}=\varepsilon_{11}$ in uniaxial compression and $\varepsilon_{eq}=\sqrt{4/3}.\ln\left[\frac{1}{2}\gamma+\sqrt{\gamma^2+4}\right]$ in simple shear. Note, however, that the physical significance of ε_{eq} is not clear. Assuming isotropy, the stress-strain curve in uniaxial compression is the equivalent stress-equivalent strain curve.

In case of steady state deformation, the von Mises theory of perfect plasticity relates equivalent stress to equivalent strain for a given equivalent strain-rate. Hence, the theory assumes the existence of a universal stress-strain curve whose form can be determined by a single uniaxial test (Malvern, 1969; Tomé et al., 1984).

Generalized flow law

First, we derive a general tensor form of a power-law creep equation following Ranalli (1987, p. 75-78), and then we will derive expressions allowing the flow law, established from uniaxial compression experiments (Eq. 5.5), to be compared to the flow law obtained from simple shear experiments (Eq. 5.6).

Suppose a steady state flow law, relating S_{11} to σ_{11}, obtained from laboratory compression experiments has the general power-law form:

$$S_{11} = A(\sigma_{11})^n \qquad (5.10)$$

where A is a function of temperature and material parameters. Expressing the power-law creep equation 5.10 in tensor form allows extensions of the experimental results to a general state of stress. According to the theory of isotropic plasticity, the flow properties are material properties valid under any stress state, therefore we express Eq. 5.10 in terms of the σ_{eq} and S_{eq} as defined above. For a homogeneous, isotropic, incompressible material with a flow law as expressed in Eq. 5.10, it can be postulated that the general flow law expresses a

relation between σ_{eq} and S_{eq} of the form (Nye, 1953a; Ranalli, 1987):

$$S_{eq} = A(\sigma_{eq})^n \tag{5.11}$$

This equation describes the power-law creep equation in terms of invariants I_2 and J_2*. If the material *remains* isotropic and homogeneous during flow, then the principal axes of S_{ij} must be parallel and proportional to σ_{ij}* (Nye, 1953a; Malvern, 1969):

$$S_{ij} = \lambda\sigma_{ij}^* \tag{5.12}$$

where λ is a positive scalar that depends on position and time (for example due to strain hardening). Equations 5.12 are analogues to the Lévy-Mises relations in the theory of plasticity (Hill, 1950; Malvern, 1969) and are often referred to as the associated flow rule. Equations 5.11 and 5.12, combined with Eqs. 5.7 and 5.8, imply that (Nye, 1953ab):

$$S_{eq} = \lambda\, \sigma_{eq} \tag{5.13}$$

Combining Eqs. 5.11 with 5.13 yields:

$$\lambda = A\,(\sigma_{eq})^{n-1} \tag{5.14}$$

and hence, Eq. 5.12 can be written as:

$$S_{ij} = A\,(\sigma_{eq})^{n-1}\sigma_{ij}^* \tag{5.15}$$

Equation 5.15 is a generalized power-law creep equation in tensor form. In case of compression, $\sigma_{eq} = \sigma_{11}$ and $S_{ij} = S_{11}$ (Eqs 5.7 and 5.8) and therefore

$$S_{11} = A(\sigma_{11})^n$$

which is identical to Eq. 5.10, that was obtained experimentally.

The generalized uniaxially derived flow law (Eq. 5.15) can be expressed in terms of shear deformation. The only non-zero stress components of the deviatoric stress tensor are $\sigma_{12}^* = \sigma_{21}^* = \tau_{applied}$ and the strain rate $S_{ij} = \dot{\gamma}/\sqrt{3} = 2S_{12}/\sqrt{3}$. Insertion into 5.15 yields

$$\dot{\gamma} = (\sqrt{3})^{n+1}\, A\tau^n \tag{5.16}$$

If a power-law creep equation is determined from uniaxial deformation experiments, the general expression of the flow law in tensor form is given by:

$$S_{ij} = \frac{(\sqrt{3})^{n+1}}{2} A \exp(-\Delta H/RT)(\sigma_{eq})^{n-1}\sigma_{ij}^* \quad (5.17)$$

Similar expressions have been derived by Stocker and Ashby (1973), Schmid et al. (1987) and Ranalli (1987). If n -> ∞ and S_{eq} -> ∞ , Eqs 5.12 are the usual Lévy-Mises relations for an isotropic incompressible plastic-rigid material with a constant yield stress (Nye, 1953a; Malvern, 1969).

5.3.2 *Comparison of stress - strain behaviour*

The mechanical behaviour observed in the uniaxial compression and shear experiments can be compared assuming isotropic, perfectly plastic behaviour. Expressions for the state of deviatoric stress (σ_{ij}^*) in the samples can then be obtained, if the following additional assumptions are made (Franssen and Spiers, 1990): (a) that the applied stresses are uniformly transmitted throughout the samples, and (b) that the samples can be considered to be in static equilibrium with no couple stresses. For uniaxial deformation, the results obtained for the non-zero components of σ_{ij}^* are $\sigma_{11}^* = (\frac{2}{3})\sigma_{applied}$ and $\sigma_{22}^* = \sigma_{33}^* = (\frac{-1}{3})\sigma_{applied}$, whereas in shear we have $\sigma_{12}^* = \sigma_{21}^* = \tau_{applied}$. Using these results and assuming isovolumetric true uniaxial compression and true simple shear deformations, Equations (5.7) and (5.9) can be applied to derive σ_{eq} vs. ε_{eq} curves for the samples tested. In the following section, the σ_{eq} vs. ε_{eq} behaviour is compared as a function of comparable strain rates S_{eq} and temperature (refer to Table 5.1).

250-350 °C

Representative σ_{eq} vs. ε_{eq} curves for shear and compression tests deformed at comparable rates are shown in Fig. 5.8 (see also Franssen and Spiers, 1990). At constant temperature, the uniaxially deformed samples support significantly higher equivalent stresses than the sheared samples, for *all* values of ε_{eq}. Leaving the physical meaning of ε_{eq} undiscussed, the most significant observation is that in compression the (near) steady state σ_{eq} is c. 1.5 times larger than in shear. This behaviour is inconsistent with that expected for an isotropic perfectly plastic material under the assumptions made above.

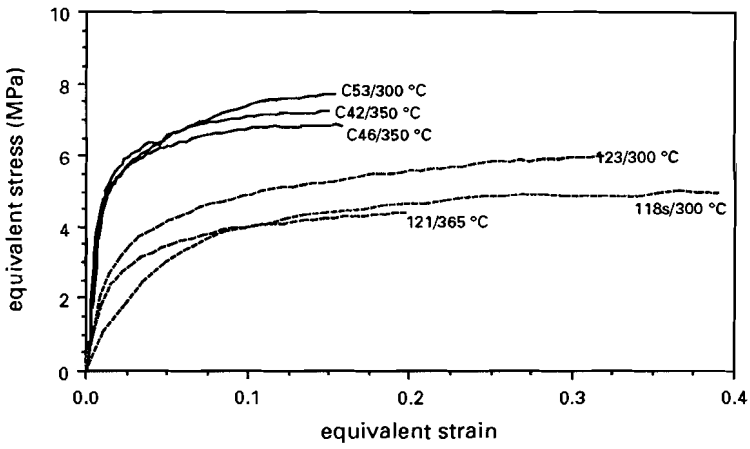

Figure 5.8:
Comparison of mechanical data from the compression tests (bold lines) and shear tests (dashed lines) in terms of σ_{eq} and ε_{eq} for the temperature range 250 - 350°C. In compression the steady state values of σ_{eq} supported are c. 1.5 times larger than in shear, under comparable conditions.

400-600 °C

In this temperature range, the σ_{eq} vs. ε_{eq} curves obtained for shear and compression agree rather well (Figs. 5.9 and 5.10). The values of σ_{eq} of the compression and shear tests agree within 0.5 MPa. This is similar to the reproducibility of the tests. Strain-rate stepping tests yield similar results as constant strain-rate tests. The most notable differences between the shear and compression experiments are the higher strains attained in the latter tests.

5.3.3. *Comparison of flow behaviour in compression and shear*

The comparison of the flow laws obtained from uniaxial compression and shear experiments (Eqs. 5.5 and 5.6 respectively) is carried out using Eq. 5.16 in order to express the uniaxially-derived flow law in terms of shear deformation. Inserting the combined flow law of Eq. 5.5 into Eq. 5.16 yields

$$\dot{\gamma}_{tot} = (\sqrt{3})^{5.4}\,(6.57 \times 10^{7}\,\exp(-227/RT)\sigma^{4.4}) + (\sqrt{3})^{6.7}\,(5.75\,\exp(-129/RT)\sigma^{5.7}) \qquad (5.18)$$

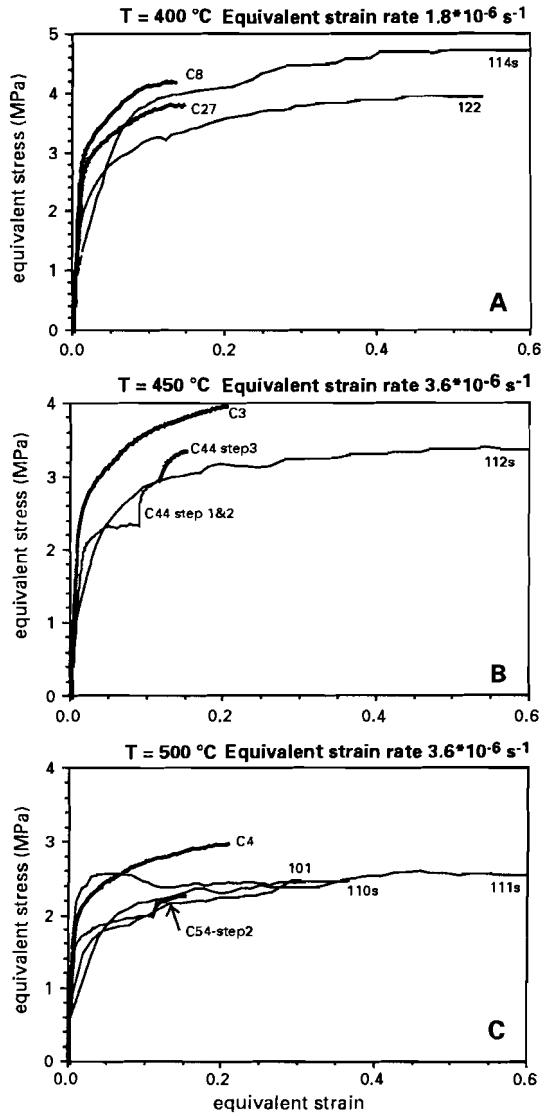

Figure 5.9:
Comparison of mechanical data from the compression tests (bold lines) and shear tests (thin lines) in terms of σ_{eq} and ε_{eq}. In (a) experiments carried out at 400 °C; (b) at 450 °C and (c) at 500 °C are shown. Equivalent strain rates are indicated. The steady state values of σ_{eq}supported in compression and in shear are approximately similar. The strain-rates of the uniaxial stepping tests (C44 in (b)) and (C54 in (c)) which do not correspond to the equivalent strain rates as indicated, are shown as thin lines.

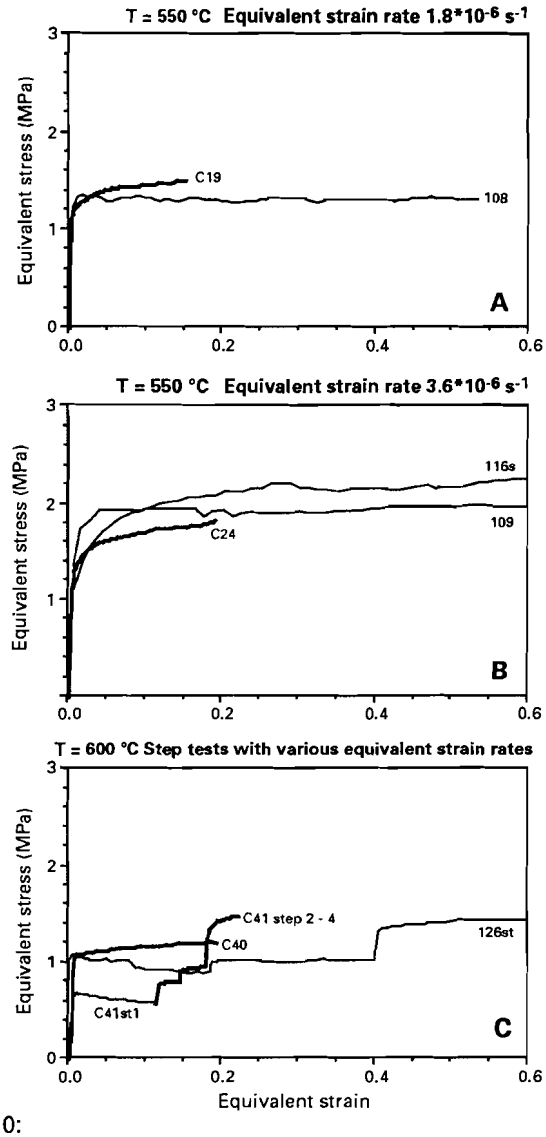

Figure 5.10:
Comparison of mechanical data from the compression tests (bold lines) and shear tests (thin lines) in terms of σ_{eq} and ε_{eq}. The temperatures and equivalent strain rates are indicated, the strain rates of step test 126st are shown in Table 5.2. The steady state values of σ_{eq} supported compression and shear are approximately similar. The strain rates of uniaxial strain-rate step test C41 (in c) which do not correspond to the equivalent strain-rate are shown as thin lines.

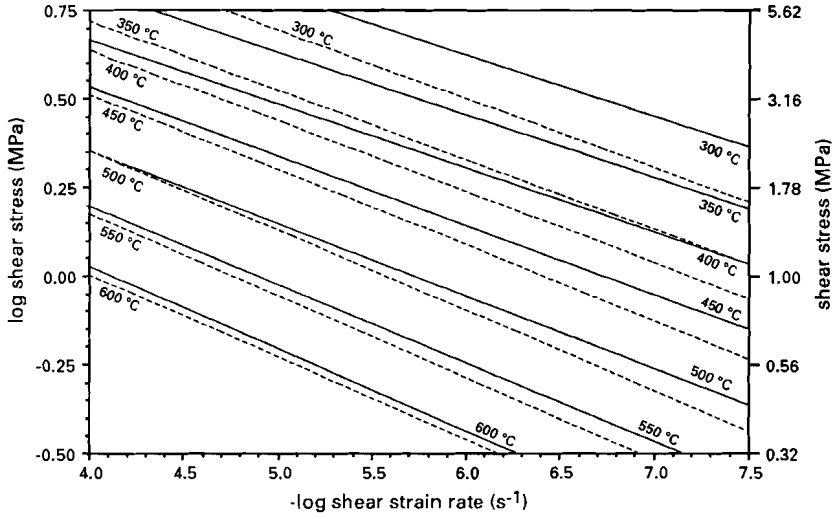

Figure 5.11:
Comparison between the shear strain rate - shear stress relations predicted by Eq. 5.18, based on uniaxial creep data (solid lines) and Eq. 5.6, based on simple shear creep data (dashed lines). The uniaxially-derived flow law predicts significantly lower shear strain rates than the simple shear flow law for temperatures below c. 450°C. For higher temperatures a favourable agreement between the two flow laws is obtained.

This uniaxially-derived flow law can be compared directly with the flow law obtained from the shear experiments (Fig. 5.11). If the theory of perfect isotropic plasticity, under the assumptions made in the introduction, is correct the isotherms describing the shear stress - shear strain-rate relations given by Eqs. 5.6 and 5.18 should coincide. Note that the estimated error in shear stress is less than 20% of the calculated value and that the strain rate is estimated to be within half order of magnitude accuracy.

Fig. 5.11 shows isotherms described by Eqs. 5.6 and 5.18 in temperature range from 300 to 600 °C. *Below* 400-450 °C, the uniaxially-derived flow law (Eq. 5.18) yields significantly higher shear stresses for a given shear strain-rate than the shear-derived flow law. For example, at 300 °C, the generalized uniaxial flow law (Eq. 5.18) yields shear stresses which are c. 1.5 times larger than those obtained from the shear experiments. In other words, over the experimental range in-

vestigated, the generalized uniaxial flow law predicts lower shear strain rates than the shear flow law. With increasing temperature the difference between Eq. 5.6 and Eq. 5.18 decreases and at temperatures above 400-450 °C, a fairly good agreement is obtained between the two flow laws (within approximately 10 - 20% of the shear stress for a given shear strain-rate).

5.4 DISCUSSION

The results obtained from a comparison of the deformation behaviour seen in compression and in shear using the perfect isotropic plasticity theory can be summarized as follows:

1) at temperatures above c. 400, °C similar (near) steady state values of σ_{eq} are obtained in compression and in shear at constant S_{eq};
2) above 400-450 °C, the uniaxially-derived flow law and the flow law obtained from the shear experiments describe similar behaviour;
3) at constant S_{eq}, significantly higher values of σ_{eq} are obtained in compression than in shear at temperatures below 400 °C;
4) and finally, at temperatures below 400 °C, the generalized uniaxially derived flow law fails to predict the shear strain rates obtained from the shear experiments by almost one order of magnitude.

It has been shown above that at temperatures above 400-450 °C possible deviations from the theory of isotropic plasticity are small. On the basis of these findings, it can be stated that at temperatures above 400-450 °C, the associated flow rule provides an adequate method to generalize the flow laws.

At temperatures below 400 °C, however, the associated flow law derived from the theory of perfect isotropic plasticity is clearly not valid and the generalization of the flow laws in this temperature regime will introduce significant errors. The associated flow rule is based on the assumptions that i) deforming material is and remains isotropic, ii) the material response is independent of the third invariant of the deviatoric stress tensor and, iii) deformation does not involve any volume changes in the sample. These results imply that below 400 °C (a) the samples become mechanically anisotropic during deformation (though initially free of any crystallographic or shape preferred orientation), thus exhibiting truly lower strength in shear than in compression; or (b) the samples remain more or less mechanically isotropic and that the

calculated values in σ_{ij}* and σ_{eq} are in serious error because of imperfectly imposed boundary conditions. Especially in case of shear deformation, the full state of deviatoric stress in the sample may not be fully known, since only vertical stresses are measured. Franssen and Spiers (1990) have shown by a careful analysis that possible compressive stresses due to dilation of the sample or possible tensile stresses due to imperfectly imposed boundary conditions cannot account for the observed differences and implication (b) can be ruled out.

In the following, we will discuss possible microphysical reasons for the inferred development of mechanical anisotropy and the associated differences in the shear and compression flow laws observed at low temperatures.

5.4.1 *Development of mechanical anisotropy*

It is apparent from the σ_{eq} vs. ε_{eq} data and from the comparison of the flow laws presented above that, at T<400 °C, the equivalent stresses σ_{eq} supported in shear are smaller than those supported in compression (at similar S_{eq} and T) *for all strains*, i.e. from the initial work hardening stage of deformation through into the steady state stage. However, at temperatures above 400 °C, the strain hardening and steady state behaviour obtained from both deformation geometries are similar.

The microstructural and microphysical processes identified in the salt deformed in shear and compression are virtually identical (Chapters 2 and 3) and thus do not offer an explanation for the different mechanical behaviour seen at lower temperatures. Now, the average Taylor factors for compression and shear of aggregates with no crystallographic preferred orientation are approximately equal, for the first increment of deformation (e.g. Tomé et al., 1984; Takeshita and Wenk, 1988; Takeshita, 1989). On the other hand, polycrystal plasticity modelling studies show that deformation in (pure) simple shear and compression leads to the activation of different combinations of slip systems integrated over the entire grain population, and to the associated development of distinct crystallographic preferred orientations (e.g. Tomé et al., 1984; Wenk et al., 1986, 1989ab). Thus, the difference in mechanical behaviour seen at lower temperatures (<400 °C) may be due to the development of different preferred orientations (as suggested by Franssen and Spiers, 1990) or due to differences in number and combinations of activated slip systems and coupled differences in dislocation interaction and hardening (Tomé et al., 1984). These two possibilities are considered further below.

Effect of texture development

Texture modelling studies for various rock forming minerals have shown that the imposed deformation geometry determines the activated slip systems, and hence the texture evolution (Takeshita and Wenk, 1988; Takeshita, 1989; Takeshita et al., 1990; Wenk et al., 1986; 1989ab). Lattice rotations create crystallographic preferred orientations and the associated mechanical anisotropy (geometrical softening or hardening, cf. White et al., 1980) will depend on the deformation geometry. Texture simulations have shown that materials, in which the critical resolved shear stresses (CRSS) of the slip systems vary, become stronger with increasing number of significant slip systems, probably because this requires activation of harder slip systems (Wenk et al., 1986; Takeshita, 1989). In addition, texture simulations have shown that in general fewer slip systems are needed to accommodate an increment of simple shear compared to an increment of uniaxial compression. For Cu, Tomé et al. (1984) have shown that this gives rise to weaker behaviour in torsion/shear than in compression. However, in most cases, the effects are slight (<10%) and only significant at relative large strains.

In the present study, the crystallographic preferred orientations developed in shear and compression were approximately similar at low temperatures (250-400 °C), compared to those obtained at high temperatures (450-600 °C). The development of crystallographic preferred orientation, coupled with varying CRSS of the active slip systems, cannot explain the large differences in σ_{eq}, because these are apparent from the initial work hardening stage at $T < 400$ °C .

Effects of dislocation activation and interaction

From above, it is clear that crystallographic preferred orientation development cannot fully explain the present results. The work-hardening rate of polycrystalline halite is not unique (loading path dependent) and may depend on the deformation geometry. First, the effects of the activation of 'harder' slip systems on the mechanical behaviour will be addressed, followed by a brief discussion on the relation between work-hardening rate and deformation mode.

The effect of the activation of different (combination of) slip systems on the mechanical behaviour can best be illustrated by the analogy with NaCl single crystals deformed along different crystallographic directions (Carter and Heard, 1970; Van Alsem et al., 1982). Single crystals shortened along the <100> direction favour slip on the 'softer' $\{110\}\langle 1\bar{1}0\rangle$ system. If glide on this slip system is impeded, for ex-

ample by loading along the <111> direction, *subsidiary* glide on {100} and {111} planes, which have higher CRSS and higher hardening rates, result in deformation at significantly higher stresses. This difference in flow stress will be most pronounced at temperatures below 400 °C, where the CRSS of the three principal types of slip systems in halite differ most (by a factor 2 - 3 at 250 °C). At higher temperatures, all slip systems have comparable CRSS (Carter and Heard, 1970) and this effect is less significant.

The effect of the activation of subsidiary glide on the hardening behaviour of NaCl poycrystals is investigated by Bulatova & Nadgornyi (1982) and Nadgornyi & Strunk (1987). These authors showed that the strain hardening behaviour in NaCl polycrystals is fully determined by internal stresses produced by arising dislocations, and the magnitude of the internal stresses depends on the number of activated slip systems. TEM studies by Nadgornyi and Strunk (1987) revealed that the dislocation substructure of NaCl polycrystals, deformed in compression at room temperature, is characterized by a 3-dimensional cellular network with no evidence of macroscopic single glide. The high stresses obtained in the uniaxially compressed polycrystals (relative to single crystal values compressed along <100>) result from *considerable* glide on the subsidiary {111} and {100} planes and from strong dislocation interaction (Nadgornyi and Strunk, 1987). This effect is significant even in the micro-plastic range ($\varepsilon < 0.2\%$) (Bulatova and Nadgornyi, 1982).

Similar effects, such as glide on subsidiary slip systems, may occur in the uniaxially shortened samples of the present study. Unfortunately, no TEM data are available for the samples used in the present study and a comparison between the dislocation structures obtained in shear and compression cannot be made. As has been mentioned above, texture simulation showed that for an increment of simple shear fewer slip systems are needed, compared to an increment of uniaxial compression. At the same time, the systems activated in shear tend to be 'softer' slip systems, with the result that the flow stresses in shear are lower than in compression (Takeshita, 1989). This effect will be strongest at temperatures below 400 °C, where the slip systems have very different CRSS (so that the single crystal yield surface is highly anisotropic) and different hardening rates. Note that some additional support for subsidiary glide in uniaxial compression can be drawn from the halite texture simulations carried out by Wenk et al. (1989a). The experimental textures of compressed polycrystalline NaCl resemble most the results of the simulations in which hardening of the slip systems was included (see also Chapter 2). The simulations showed that in those cases, hardening gave rise to a higher average number of slip systems

and, consequently, subsidiary glide was important in the case of uniaxial compression. Unfortunately, no detailed texture simulation results were presented by Wenk et al. (1989a) for deformation of halite in simple shear, prohibiting a comparison with the experimental results.

The following point to be discussed in some more detail is how the work-hardening rate may depend on the deformation mode. The work-hardening rate of polycrystalline halite has been shown to depend on deformation mode and this may be due to differences in number and combinations of the slip systems activated. Such behaviour has been observed for Cu polycrystals (Tomé et al., 1984) and since neither the dislocation substructure nor the number of active slip systems of the experimentally deformed polycrystalline halite are known, we have to rely on results obtained for other materials.

Based on mechanical data of Cu polycrystals deformed in compression, tension and torsion, together with texture simulation investigations, Tomé et al. (1984) showed that the strain hardening behaviour of polycrystalline Cu depends on the deformation mode. After accounting for the mechanical effects of the development of crystallographic preferred orientation, the shear stresses for Cu deformed in torsion remained lower than the uniaxial curves even for very small equivalent strain (ε_{eq} <0.1) (Fig. 5.12a) and a single unique hardening law for Cu was not obtained (Tomé et al., 1984). The rate of work-hardening was shown to increase with the number of significant slip systems (a slip system was defined to be significant, if it accommodates at least 10% shear associated with the most active system (Tomé et al., 1984)), which in turn was shown to depend on the deformation mode. In case of Cu, the average number of significant slip systems for torsion/shear, decreases from initially 4 to 2.5, whereas compression and extension initially employ on average 4.5 slip system decreasing to approximately 3.5 to 4 (Fig, 5.12b). The lowest hardening rates were obtained in deformation modes which employed the smallest average number of significant slip systems.

Again, similar processes may operate in the polycrystalline halite deformed in shear and compression. The hardening rate may depend on the number of signficant slip systems, which in turn may depend on the deformation mode. By analogy with texture simulation studies, this would imply that in simple shear fewer slip systems contribute significantly to the deformation than in compression. In the work-hardening stage, this will result in fewer dislocation interactions, and hence lower work hardening rates. Again, these effects are most pronounced at temperatures below 400 °C, where the CRSS's and the hardening rates of

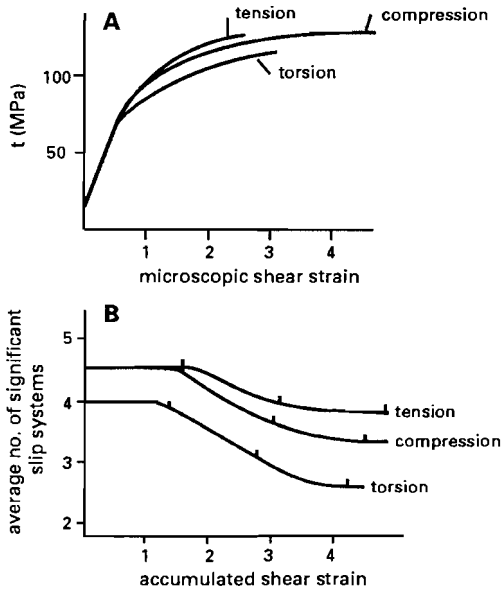

Figure 5.12:

(a) Shear stress - microscopic shear strain curves for Cu as function of deformation mode. The curves represent the average hardening of the slip systems associated with a particular kind of poly-slip occurring in the deforming grains. The shear stresses have been accounted for changes in crystalllographic orientation (geometrical effects).

(b) Average number of significant slip systems per grain as a function of increasing shear strain for different deformation modes. The equivalent rate of work hardening increases with the number of significant slip systems.

After Tomé et al. (1984). The markers correspond equivalent strain of ε_{eq} = 0.5, 1.0 and 1.5.

the subsidiary slip systems are significantly higher than those of the easy $\{110\}\langle 1\bar{1}0\rangle$ slip system. At higher temperatures, all slip systems have similar CRSS values and hardening rates and the effect of subsidiary glide on the hardening behaviour is less strong. In addition, recovery processes and migration recrystallization are more effective above 400 °C, and the internal stresses produced from dislocations and hardening of slip systems are more efficiently reduced. Note, however, that for a given number of slip systems the hardening rate may also depend on the detailed crystallographic configuration of the active slip systems.

5.4.2 *Flow laws in shear and compression*

Steady state flow of polycrystalline halite has been shown to be of the climb-controlled dislocation creep type. The creep rate is believed to be controlled by the diffusion of cations and anions to and from dislocation cores.

Above 500 °C, in the lattice diffusion creep field, the flow law parameters obtained for shear and compression agree to within 1 standard deviations of each other (Table 5.2). Because the ions, diffusing through the lattice control the creep rate, neither the type of dislocations nor the dislocation substructure are expected to have an influence on the diffusion kinetics, and therefore the creep activation energies for shear and compression are expected to be similar.

In the temperature range 250-450 °C, i.e. in the pipe diffusion field, diffusion through dislocation cores is the rate-controlling process (Chapters 2 and 3). In this temperature range, the activation energy for shear deformation (93 ± 9 kJ/mol) is significantly lower compared to the activation energy for uniaxial compression (129 ± 8 kJ/mol).

The kinetics for diffusion through the core of an edge dislocation depend on the exact structure of that dislocation, such as the effective cross sectional area, vacancy concentration and atomic structure around the dislocations (see Verall et al., 1977; Frost and Ashby, 1982; Poirier, 1985). We assume that these dislocation properties do not vary, since the samples used in the compression and shear experiments are prepared from exactly the same starting material. However, the rate of pipe diffusion also depends on the type dislocation through which the ions travel. For example, diffusion through edge dislocations is significantly faster than diffusion through screw or mixed dislocations (being perhaps 10 times faster for edges than for screws), because the stress field around edge dislocation has dilational and shear components, whereas the stress field around screw dislocation has only shear components (Hull, 1975; Frost and Ashby, 1982). In addition, in the temperature range 250-450 °C, the activation energies for climb-controlled dislocation creep of NaCl single crystals is shown to depend on the slip system activated (Carter and Heard, 1970). For these reasons, it is plausible that the variations in dislocation substructure (such as dislocation density,- type, - networks) may also influence the diffusion kinetics. Thus, the difference in activation energy for pipe-diffusion controlled dislocation creep in simple shear and compression may reflect variations in dislocation substructure as a result of the above mentioned differences in activated slip systems. This implies that, in general, the activation energy for pipe-diffusion may depend on the number and combination of slip systems activated, which in turn depends on the deformation mode imposed.

5.5 IMPLICATIONS

The associated flow rule is found not to work for polycrystalline salt at temperatures below 400 - 450 °C, i.e. when slip systems are different in strength, and the rate-of-deformation is controlled by pipe-diffusion through dislocation cores. In this temperature regime, salt becomes mechanically anisotropic during deformation, exhibiting truly lower strength in shear than in compression. The deformation geometry does not affect the mechanical behaviour at temperatures above 400-450 °C, where the slip systems have similar strengths and where the rate-controlling process is controlled by lattice diffusion. These findings have the following implications.

Salt deformation

It is shown above that, in case of polycrystalline halite, the associated flow rule gives a poor generalization of flow laws derived from axi-symmetric experiments for temperatures in the range 250 to 450 °C. Under natural conditions, the deformation of rocksalt occurs by dislocation creep or by a combination of dislocation and solution-precipitation creep (Carter and Hansen, 1983; Urai et al., 1987; Spiers et al., 1990; Carter et al., 1993). Therefore, generalization of laboratory flow laws, using the associated flow rule, for modelling salt tectonic processes (Van Keken et al., 1993) as well as the (thermo)mechanical response of salt formations to the construction of (waste) repositories (Janssen et al., 1984) may lead to serious errors. The present results indicate that, under geologically relevant stresses (1 - 10 MPa) and temperatures (below 250 °C), converting the uniaxial flow law for salt to simple shear deformation may result in errors in strain rate of up to 2 orders of magnitude. Errors with similar magnitudes may arise from generalizations of flow laws obtained from axi-symmetric laboratory experiments on *natural* rocksalt.

Other geological materials

The results of the present study suggest that the associated flow rule may not apply to other geological materials which have slip systems with very different strengths, that deform in the low temperature dislocation creep field when recovery and migration recrystallization are limited, or when pipe diffusion controls the dislocation creep-rate. At higher temperatures, when lattice diffusion or other deformation mechanisms control the deformation rate (such as grain-size sensitive diffusional creep), the associated flow rule may offer a reliable formalism for generalization of laboratory flows laws.

Models for mantle flow rely on the flow laws for olivine, which is believed to be the major constituent of the upper mantle. The possible range of deformation conditions in the upper mantle covers both dislocation and diffusion creep regimes where dislocation creep is favoured at relatively high stresses, coarse grain sizes and high temperatures (Ashby and Verral, 1977; Karato et al., 1986; Karato, 1989). The exact creep-controlling mechanism is not known, although, some mechanism of diffusion-related climb of dislocations controls the creep rate (Ranalli, 1987) and power-laws adequately describe the deformation behaviour obtained from axially symmetric compression experiments (for example Karato, 1989). Field data suggest that olivine in the mantle deforms in a regime of steady state creep in which dislocation slip and climb occurs (e.g. Nicolas et al., 1971).

Major uncertainties in estimates of the creep properties of the mantle result from the (not fully understood) dependency of the flow behaviour on pressure and on chemical environment (Ranalli, 1987; Karato, 1989). Another uncertainty may arise if the mechanical behaviour of olivine depends on the deformation geometry. The latter may be important in the flow behaviour of olivine polycrystals since the CRSS's of the slip systems in olivine vary significantly under all temperature conditions (Takeshita et al., 1990), and because diffusion through dislocation cores may be the rate-controlling mechanism in the dislocation creep regime. Under these conditions, the mechanical behaviour of olivine may depend on the deformation geometry in a manner similar to that described here for polycrystalline halite. The effects of variations in the rheological behaviour on mantle dynamics is illustrated by numerical simulations of Van den Berg et al. (1991) and Van Keken (1993). The present experimental results merely illustrate the need for simple shear experiments on olivine polycrystals (or analogue materials) under well-controlled experimental conditions in order to asses possible inaccuracies, arising when olivine flow laws, derived from axi-symmetric deformation experiments, are generalized using the associated flow rule (Stocker and Ashby, 1973; Ranalli, 1987).

5.6 CONCLUSIONS

The mechanical behaviour of dry synthetic polycrystalline halite deformed in uniaxial compression and in simple shear has been compared. Deformation was inferred to be climb-controlled dislocation creep and at temperatures in the range from 250 to 450 °C, climb is controlled by pipe diffusion through dislocation cores, whereas at temperatures from 500 to 600 °C, anion lattice diffusion is the rate-controlling process.

The stress-strain behaviour has been compared in terms of equivalent stress (σ_{eq}) and equivalent strain (ε_{eq}) and equivalent strain rate (S_{eq}) using the associated flow rule known from the theory of perfect isotropic plasticity. At temperatures below 400 °C, the equivalent stresses supported in compression (at similar equivalent strain rate, S_{eq}, and temperature) are significantly higher for *all* strains, from the initial work hardening stage through into the steady state stage. At temperatures above 400-450 °C, the strain hardening and steady state behaviour obtained in both deformation geometries are approximately similar.

The mechanical anisotropy, which the samples develop below 400 °C, cannot be fully explained by the development of crystallographic preferred orientations, because the mechanical anisotropy is apparent from the beginning of deformation. By analogy with texture simulations and other experimental data, it has been argued that the hardening behaviour depends on the deformation mode through the number and combination of the slip systems activated. In the work-hardening stage, this would imply that fewer slip systems are activated in simple shear than in compression. This gives rise to fewer dislocation interactions and smaller contributions of the harder subsidiary slip systems, and hence to lower work-hardening rates and lower flow stresses. This effect is most pronounced at temperatures below 400 °C, where the single crystal yield surface of halite is highly anisotropic. At higher temperatures, all slip systems have comparable CRSS and the effect of subsidiary glide on the hardening behaviour is less significant. In addition, above 400 °C, recovery processes and migration recrystallization are more effective and the internal stresses produced from the dislocations and hardening of slip systems are more efficiently reduced.

The flow law based on the uniaxial compression experiments is rederived, using the associated flow rule, to obtain an expression for shear deformation. Comparison of the flow laws shows that, in the temperature range 250-450 °C, the shear strain rates predicted by the

flow law based on the compression tests are significantly lower than the shear strain rates predicted by the flow law based on the shear experiments. At higher temperatures, a good agreement between the two flow laws is obtained. In the temperature range 250-450 °C, the flow law for compression is characterized by a significantly higher activation energy (by 129 kJ/mol) than the flow law for shear (93 kJ/mol). The difference in activation energy for pipe diffusion may reflect variations in dislocation substructure developed in simple shear and compression as a result of the above mentioned differences in activated slip systems.

The associated flow rule is found not to work for polycrystalline salt at temperatures below 400-450 °C. Under geologically relevant conditions, the generalization of flow laws for rocksalt, using the associated flow rule, may lead to errors in strain rate of up to 2 orders of magnitude. Similar effects may occur in other geological materials deforming in the low temperature dislocation creep field. In other words, the theory of perfect isotropic plasticity may not offer a reliable method of generalization of axisymmetric flow laws, when the slip systems have very different strengths and when recovery and migration recrystallization are limited, or when pipe diffusion controls the dislocation creep rate. Under conditions when lattice diffusion or grain-size sensitive diffusional creep mechanisms control the creep rate, the associated flow rule may offer a reliable formalism for generalization of flow laws. The results indicate the need for (a) simple shear experiments on other rock-forming minerals in order to assess inaccuracies which may arise from using the associated rule and (b) the development of constitutive relations including the development of mechanical anisotropy as function strain and deformation path.

GENERAL CONCLUSIONS
Suggestions for further work

This thesis has investigated the mechanical behaviour, microstructural evolution and crystallographic preferred orientation development in synthetic rocksalt deformed in uniaxial compression and in simple shear. The purpose of the present final chapter is to draw together general conclusions, based on the findings presented in the preceding chapters (i.e. Chapters 2 to 5). In addition, questions which remain unanswered are identified and suggestions are made for further research.

6.1 DEFORMATION BEHAVIOUR OF SYNTHETIC ROCKSALT

6.1.1 *Deformation mechanisms and rate-controlling processes*

The present experiments on synthetic polycrystalline halite consisted of

1) uniaxial compression tests performed at temperatures of 250-780 °C ($0.5< T/T_m< 0.98$) and strain rates of $10^{-3}< \dot{\varepsilon} < 10^{-7}$ s^{-1} using constant strain-rate and strain-rate stepping/cycling methods;
2) simple shear deformation tests carried out in the temperature range 250-600 °C ($0.5< T/T_m< 0.8$) at strain rates between 10^{-5} and 10^{-7} s^{-1}, reaching finite shear strains of up to 1.4.

Under these conditions, deformation proceeds by steady-state flow ($T > 450$ °C) or near steady-state flow ($T < 450$ °C), without major macroscopic softening or hardening in either deformation mode. The observed flow behaviour and microstructures are consistent with climb-controlled dislocation creep models. Further, in the temperature range from 450 to 600 (780)°C, the data obtained indicate that the creep rate is controlled by anion lattice-diffusion, whereas in the temperature range 250-450 °C, the rate-controlling process is anion diffusion through dislocation cores (pipe diffusion).

6.1.2 *Microstructural processes*

At temperatures between 250 and 450 °C, the microstructural development in both deformation geometries investigated is characterized by polygonization, rotation recrystallization and limited grain-boundary migration. The development of concavo-convex grain boundaries in this low temperature field is consistent with strain-induced migration recrystallization processes. At higher temperatures, grain-boundary migration recrystallization becomes more important, and at temperatures above 500 °C, migration recrystallization, apparently driven by a combination of both lattice stored energy and grain-boundary energy, is the dominant microstructural process.

The transition to a migration recrystallization dominated microstructure clearly coincides with the above mentioned change in creep mechanism. The present results, in relation to Derby's (1990, 1991, 1992) model for dynamic recrystallization by grain boundary migration, show that the change in creep mechanism affects the driving force for recrystallization and the nucleation rate differently than the grain boundary mobility. The increase in grain boundary mobility, associated with the temperature increase over which the change in creep mechanism occurs, is strong enough to compensate the decrease in driving force and the increase in equilibrium recrystallized grain-size. These relative changes in the lattice-diffusion controlled creep field allow a dynamic balance to be established between nucleation rate of new grains and the migration rate of nucleated grains. However, in the pipe-diffusion controlled creep field, such a balance cannot be established and the volume swept by a migrating grain boundary during the unit time for one nucleation event to occur is smaller than the volume equivalent to the steady state grain size and consequently migration recrystallization is not the dominant process.

6.1.3 *Crystallographic preferred orientations*

Regardless of temperature, during uniaxial compression experiments, the <110> crystallographic directions rotate towards the compression direction. During simple shear deformation, the {110} slip planes rotate into an orientation parallel to the shear plane, while the <111> direction tends to align parallel to the shear direction. Notably, the <110> slip direction does not orient itself parallel to the shear direction. Crystallographic preferred orientation patterns thus appear to be independent of temperature, though in simple shear deformation the intensity of the <110> texture component appears to increase slightly with temperature.

The crystallographic preferred orientations, which develop in both compression and shear, agree favourably with viscoplastic Taylor and self-consistent texture simulations (Wenk et al., 1989a). However, the results do not allow any discrimination as to which model might apply most effectively to polycrystalline halite.

6.1.4 *Strain-rate history effects*

At temperatures between 250 and 450 °C, i.e. in the pipe diffusion controlled creep field, the mechanical behaviour and the microstructural evolution of uniaxially deformed polycrystalline halite has been shown to be influenced by strain-rate history. The subgrains, which develop in this temperature range, do not grow to the expected "steady state size" upon a lowering of strain-rate, even after 10% of subsequent strain. Deviations of up to c. 40% from the "steady state size" have been observed. This results in a relative hardening effect (by a factor up to 1.4) and in an increase of the stress sensitivity of strain rate from c. 6 to 7 - 10. In the low temperature range, the nature and amplitude of a decrease in strain rate and the microstructural characteristics of the material before that change both determine the mechanical response (memory effect). The transient response to varying strain rate, described here, should be accounted for in studies modelling the mechanical response of geotechnical structures (e.g. Aubertin et al., 1991).

Above 450 °C, i.e. in the lattice-diffusion controlled creep field, recovery processes and especially migration recrystallization are sufficiently efficient to quickly establish new steady state subgrain sizes, and the microstructures re-adjust to the newly imposed conditions within c. 1% strain. The microstructures observed in this temperature range suggest that migration recrystallization occurs continual, obliterating strongly deformed relative 'old' grains and renewing the internal grain substructures. Thus, the transient and steady state behaviour and the microstructural development above c. 450 °C are no longer significantly strain-rate history dependent (no memory effects).

By analogy with the behaviour of polycrystalline halite, other rock-forming minerals deforming by dislocation creep can also be expected to be sensitive to deformation-history. In other words, if the dislocation creep rate is controlled by pipe-diffusion, recovery is limited and migration recrystallization is not operating continually, and a decrease in strain rate may give rise to higher than expected flow stresses and an increase of the stress exponent in the flow law, relative to true steady state condition. Accordingly, such effects are not to be

expected in materials deforming under conditions promoting dynamic recrystallization by grain boundary migration or diffusional creep processes.

6.2 VALIDITY OF THE ASSOCIATED FLOW RULE AND GENERALIZATION OF LABORATORY CREEP LAWS

In this study, the influence of deformation geometry on mechanical behaviour has been investigated using the extensive experimental data sets obtained for synthetic polycrystalline halite, deformed in uniaxial compression and simple shear (Chapters 2 and 3). The experimental results have been compared with the aim of testing the applicability of the assumptions underlying the associated flow rule to polycrystalline halite. This rule is commonly used to generalize experimentally obtained flow laws to a 3-D description.

The stress - strain data obtained in compression and shear have been compared in terms of equivalent stress (σ_{eq}), equivalent strain (ε_{eq}) and equivalent strain-rate (S_{eq}), within the framework of the theory of perfect isotropic plasticity upon which the associated flow rule is based.

Below 400 °C, the equivalent stresses supported in compression, at similar equivalent strain rate and temperature, are significantly higher for *all* strains, i.e. from the initial work hardening stage through into the steady state stage. The (near) steady state values of σ_{eq} are c. 1.5 times larger in compression than in shear (under comparable conditions). However, at temperatures above 400 °C, the strain hardening and steady state behaviour obtained in compression and shear are approximately similar. Now, the flow laws obtained from uniaxial compression and simple shear experiments can also be compared using the associated flow rule. At temperatures below 400-450 °C, the flow law thus obtained from the uniaxial experiments, expressed in terms of shear deformation, underestimates the shear strain rate (for a given shear stress) by 1 - 2 orders of magnitude. At higher temperatures, however, a good agreement between the flow laws is obtained.

This information implies that the assumptions of "isotropy" and "no memory" in the theory of perfect isotropic plasticity are not applicable at temperatures below 400 °C, whereas they are at higher temperatures. Thus, it seems that the differences in flow stress seen in compression and shear at $T < 400$ °C can be attributed to anisotropy developed during deformation. In other words, flow is non-associated at

these temperatures, but this is not seen at higher temperatures. However, the mechanical anisotropy developed below 400 °C cannot fully be explained by the development of the observed crystallographic preferred orientations, because the difference in strength is apparent from the beginning, i.e. from the initial work hardening stage of deformation.

The work hardening rate of polycrystalline material is not necessarily unique and may depend on the number and combination of slip systems activated, which may in turn depend on the deformation mode imposed. Such behaviour has been observed in Cu polycrystals (Tomé et al., 1984) and this may also apply to polycrystalline halite. Texture simulations for other rock-forming minerals show that, in general, fewer slip systems are needed to accommodate an increment of simple shear compared to an increment of uniaxial compression (for example Wenk et al., 1986; Takeshita, 1989). In the work hardening stage, this would imply fewer dislocation interactions in shear than in compression, and hence lower rates of workhardening. At the same time the systems activated in shear preferentially tend to be 'softer' slip systems with the result that the flow stresses in shear will tend to be lower than in compression. This effect is most pronounced at temperatures below 400 °C, where the differences in the critical resolved shear stress (CRSS) of the slip systems of halite are most prominent and the slip systems have different hardening rates (Carter and Heard, 1970). At higher temperatures, all slip systems have comparable CRSS and hardening rates and the effect of 'softer' slip systems on the hardening behaviour is less significant.

In addition, at temperatures of 250-450 °C, the flow law for compression is characterized by a significantly higher activation energy (129 ± 8 kJ/mol) than the flow law for shear deformation (93 ± 7 kJ/mol). The difference in activation energy in the pipe-diffusion field, controlled creep may be caused by variations in dislocation substructure developed in simple shear and compression as a result of the above mentioned differences in activated slip systems.

In summary, it is evident that the associated flow rule does not offer an adequate method of generalizing flow laws for rocksalt at temperatures below 400-450 °C, i.e. when slip systems are different in strength, and the rate-of-deformation is controlled by pipe-diffusion through dislocation cores. Application of the associated flow rule to model the behaviour of rocksalt in tectonic processes or in geotechnical applications ($T < 250$ °C, strain rates 10^{-15} - 10^{-10} s^{-1}) may thus lead to serious errors. For example, under geologically relevant conditions, the generalization of flow laws for rocksalt, using the associated flow rule,

may lead to errors in strain rate up to 2 orders of magnitude for a given applied stress.

Again, viewing rocksalt as an analogue material, similar effects may occur in other rock-forming minerals deforming in the low temperature dislocation creep field. In other words, the associated flow rule may not offer a reliable method of generalizing laboratory-derived flow laws for minerals with slip systems which have very different strengths that deform under conditions when recovery is limited and migration rerystallization is not operating, or when pipe diffusion controls the dislocation creep rate. Under conditions when lattice diffusion or grain-size sensitive diffusional creep processes control the deformation rate, the associated flow rule may offer a reliable formalism for generalization.

6.3 MECHANICAL ANISOTROPY AND SHEAR LOCALIZATION

As has been described above, non-associated flow behaviour has been shown to occur in polycrystalline halite, at low temperatures due to the development of mechanical anisotropy, giving rise to different flow strengths depending on deformation geometry. Since shear localization may arise from non-associated flow behaviour (Rice, 1976; Leroy and Ortiz, 1990; Hobbs et al., 1990), this has important implications. In materials characterized by non-associated flow behaviour, shear localization may occur without the operation of strain softening mechanisms, though these are commonly taken as a requirement for localization in natural shear zones (White et al., 1980; Kirby, 1985; Evans and Wong, 1985). Hence, if in natural deformation heterogeneous deformation is allowed to some degree, the most economical deformation mode by which the current flow strength is minimized (or the bulk dissipation rate maximized) will be preferred to the externally imposed homogenous deformation modes (Takeshita, 1989; Wenk et al., 1989b). The results of the present study indicate that the lowest yield or flow strength for salt is obtained in shear deformation. Thus, in salt, localization into a ductile shear zone can in principle result from "loose" boundary conditions coupled with non-associated flow behaviour. Once again, this should be bourne in mind in numerical modelling studies of (large scale) salt deformation, for example in modelling salt diapirism or the creep closure of cavities.

Now, similar processes may also occur in other rock-forming minerals in which non-associated flow behaviour can be expected. For example, minerals with slip systems with very different CRSS (i.e. strongly anisotropic single crystal yield surfaces) that deform under conditions favouring low recovery rates and suppressing migration recrystallization can be expected to show non-associated flow behaviour. Thus, the onset of localization in some rocks may be due to the non-associated behaviour of the rock-forming minerals. Processes leading to typical mylonitic microstructures and textures, such as grain-size reduction, lattice rotations, and recrystallization, often have been taken as indicative of strain softening and of localization via strain softening (e.g. White et al., 1980). However, it is clear from the experiments that these processes become important only after significant amounts of strain have been accommodated (see for a field example Michibayashi, 1993). It is therefore postulated that in some cases these processes may operate during the evolution of a ductile shear zone but after initial localization has occurred. Thus, lattice rotations, recrystallization and grain-size reduction may enhance further localization, but alternatively, they could in some cases be considered as a *result* and not as the *cause* of localization.

6.4 SUGGESTIONS FOR FURTHER WORK

While the present study has addressed a substantial number of the questions posed in the introduction, it will be apparent to the reader that many have remained unanswered or only partly have been answered, and that some new questions have been raised. In the following, suggestions for further work are proposed.

(i) In polycrystalline rocksalt, two recrystallization processes have been identified. At low temperatures, rotation recrystallization was inferred to play an important role in the microstructural evolution (Chapters 2 and 3). At high temperatures grain boundary migration recrystallization dominated the microstructural evolution. However, due to the optical isotropic nature of halite, the presence of high angle grain boundaries within strongly deformed grains (diagnostic for rotation recrystallization) could not be identified. Furthermore, it is clear from the data presented in Chapters 2 and 3 that the influence of migration recrystallization on the development of crystallographic preferred orientations is only poorly understood.

For a better understanding of the interplay between rotation and migration recrystallization and lattice re-orientation in rocksalt, electron channelling techniques (for example Davidson, 1984; Lloyd et al., 1987) should be used. This technique allows the determination of the orientation of particular grains and subgrains in their microstructural position. This information may provide a basis for a better understanding of the interplay between dynamic recrystallization processes and crystallographic preferred orientation development (see for example Jessel, 1986; Wilson, 1986) and ultimately of the role of microstructural processes on the development of mechanical anisotropy.

(ii) It will be recalled from Chapters 2 and 3 that Wenk et al. (1989a) have applied Taylor and visco-plastic self-consistent (SC) texture simulation models to the development of crystallographic preferred orientations in halite. However, comparison of their results with the experimental data presented in this study should be viewed as preliminary, since Wenk et al. simulated deformation experiments at room temperature. Under these conditions, the three principal types of slip systems in halite have widely differing strengths, so that the single crystal yield surface is highly anisotropic (Carter and Heard, 1970). Texture simulations using mechanical data (i.e. CRSS and hardening rates) more directly relevant to the present study are needed, if simulation results are to be compared in detail, with the experimentally-obtained textures. Such comparisons would provide a useful means of testing the explanation put forward in this thesis that the non-associated behaviour in halite is a result of different numbers and combinations of slip systems activated in shear and compression and due to the associated texture development.

(iii) The mechanical behaviour (hardening and steady state) of salt has been shown to depend on the deformation geometry. Not only the development of crystallographic preferred orientation, but also the activation of particular slip systems appears to depend on the deformation geometry. Furthermore, in the pipe-diffusion controlled creep field the activation energy for creep in compression is significantly higher than the activation energy for creep in shear deformation. This has been explained tentatively by variations in dislocation substructures developed in simple shear and compression through the activation of different combinations of slip systems. Transmission electron microscopy (TEM) work (for example Strunk, 1975; Nadgornyi and Strunk, 1987) is clearly needed to

verify a) whether less slip systems contribute to strain in simple shear deformation compared to uniaxial compression (considerable glide on subsidiary systems vs. dominantly single glide?) and b) whether the dislocation networks developed in uniaxial compression and in simple shear differ significantly (3-dimensional cellular networks vs. blocky subgrains comprising tilt walls of {110}<1$\bar{1}$0> dislocations?).

(iv) Lastly, the present results have shown that generalization of experimentally derived flow laws, using the associated flow rule (see for example Ranalli, 1987), with the aim of numerically modelling the mechanical behaviour of a rock body under given boundary conditions, may lead to serious errors under low temperature conditions when slip systems have greatly varying strengths and recovery and migration recrystallization is limited. There therefore is a clear need for well-constrained simple shear and uniaxial experiments on silicate polycrystals, such as quartz and olivine under conditions favouring low temperature dislocation creep. Not only accurate measurements of experimental parameters, such as stress state, displacement and volumetric strain are a prerequisite, but also a well-constrained and simple deformation path allowing homogeneous deformation. From these experiments insight will be obtained with regard to the inaccuracies that may arise from application of the associated flow rule. As a first step, experiments can be carried out on other "soft" plastically anisotropic mineral analogues (such as $NaNO_3$, octochloropropane) that allow the use of relatively large samples deformed in a relatively simple deformation apparatus. Such results for analogue and rock-forming minerals could ultimately assist in the development of constitutive relations, which include the development of mechanical anisotropy as function of deformation path.

Nonlinear inversion method applied to processing uniaxial creep data

Previous studies (Heard 1970; Burke 1981; Arieli et al., 1982; Frost and Ashby, 1982) suggest that the relationship between stress, strain rate and temperature for polycrystalline salt, deformed above $0.5T_m$ can be described by a power-law equation:

$$\dot{\varepsilon} = A\exp(-\Delta H/RT)(\sigma/\mu)^n \qquad (A.1)$$

where $\dot{\varepsilon}$ is the strain rate (s^{-1}), A is a pre-exponential constant ($MPa^{-n}s^{-1}$), ΔH is the activation energy for creep (kJ/mol), R is the gas constant (kJ/Kmol), T is the temperature (K), σ the stress (MPa), μ is the temperature-compensated shear modulus (MPa) and n is the power-law exponent. The flow behaviour can be described empirically by a surface defined by:

$$f(\ln\dot{\varepsilon}, \ln\sigma, 1/T) = 0 \qquad (A.2)$$

(Poirier, 1985). In order to derive values for the flow law parameters A, ΔH and n, the experimental data (Chapter 2) were fitted to Eq. A.1, using a global inversion method (Tarantola and Valette, 1982) adapted by Sotin and Poirier (1984) for processing creep data. The inversion method aims at finding the best-fit solution of the data to the equation defining the creep surface (Eq. A.2), using an iterative least squares minimisation method. The iteration is stopped when a convergence test indicates $f_i(X) \leq 10^{-6}$. The least square fitting technique assumes that the experimental data follow a normal distribution (strain rate follows a lognormal distribution). The standard deviation in temperature was assumed to be 10 °C (in practice it was <4°C). The relative uncertainty in flow stress was assumed to be 10% of the measured value, thereby underestimating the experimental accuracy. The variation in $\ln\dot{\varepsilon}$ was $\ln 2$; i.e. $\ln\dot{\varepsilon} \pm \ln 2$. The (log) normal distributions of the experimental data are checked a posteriori by comparing the distributions of the residuals with a Gaussian distribution. The initial values

and standard deviations for the flow law parameters were: lnA = -20±100, n = 5±5 and ΔH = 250±250 kJ/mol.

The data from the uniaxial compression experiments shown in Fig. 2.10 have been fitted to Eq. A.1. Separate solutions to Eq. A.1 were sought for the temperature range 250-450 °C and 500-780 °C (see Chapter 2). This subdivision yields an optimal fit of the data to Eq. A.1.

For the experimental data in the *250-450 °C* temperature range the inversion yielded:

$$\ln A \text{ (in } MPa^{-n}s^{-1}) = 1.75 \pm 4.0$$
$$n = 5.7 \pm 0.33$$
$$\Delta H = 129 \pm 7.9 \text{ kJ/mol}$$

Only 5 iterations were needed and the residuals match a Gaussian distribution (Fig. A.1a). The ratio between the sum of the squares of the residuals and the number of equations solved ($\Sigma(res)^2/n$) is 1.85.

The data obtained in the *500-780 °C* temperature range yielded after only 4 iterations:

$$\ln A \text{ (in } MPa^{-n}s^{-1}) = 18.0 \pm 2.3$$
$$n = 4.4 \pm 0.22$$
$$\Delta H = 227 \pm 10 \text{ kJ/mol}$$

The residuals compare favourably with the expected Gaussian curve (Fig. A.1b). The ratio between the sum of the residuals squared and the number of equations is 0.9.

The data have also been fit to other temperature intervals which always yielded poorer fits. For example, if the mechanical data are used to determine a single creep law (for the temperature range 250-780 °C) then convergence occurred after 10 iterations. The residuals are relatively large ($\Sigma(res)^2/n$ = 4.3) and they do not match a Gaussian distribution (Fig. A.1c).

At low temperatures and relatively high stress levels, the power law relation is generally expected to break down (see e.g. Frost and Ashby, 1982; Tsenn and Carter, 1987). An exponential dependence of strain rate upon stress describes then the flow behaviour:

$$\dot{\varepsilon} = B\exp(\Delta H/RT)\exp(\beta\sigma) \qquad (A.3)$$

where B and β are constants. Fitting the present low temperature data to Eq. A.3, yielded

$\ln B = -11.3 \pm 0.873$
$\beta = (6.86 \times 10^{-2}) \pm 0.000315$
$\Delta H = 87.8 \pm 13.8$ kJ/mol

with convergence after 8 iterations. The distribution of the residuals does not match a Gaussian distribution (Fig. A.1d) and the ratio between the sum of the squares of the residuals and the number of equations is relatively high ($\Sigma(res)^2/n=8.5$) compared to the power-law inversions.

The best rheological description is the one which leads to the quickest inversion with the smallest residuals and standard deviations (Poirier et al., 1990). The results of the most optimal inversions, i.e. the best rheological descriptions are summarized in Table 2.5.

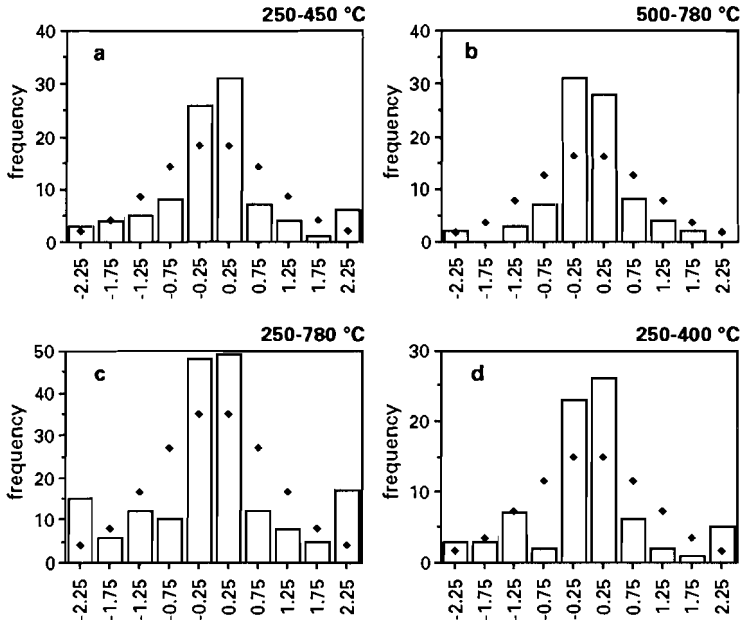

Figure A1. *Histograms of the residuals of the input parameters (lnA, ΔH, n and the mechanical data) after recalculation using the rheological laws derived and the theoretical normal distributions (diamonts) whose mean value and standard deviation are 0 and 1, respectively. Horizontal axis is the number of standard deviayions abuod the mean. (a) power-law fit in the range 250-450 °C; (b) idem for 500-780 °C; (c) idem for 250-780 °C; (d) exponential fit for 250-400 °C.*

Results nonlinear inversion method applied to simple shear data

For shear deformation, the relationship between shear stress, shear strain-rate and temperature for polycrystalline salt, deformed above $0.5T_m$ can be described by a power-law equation (see for example Frost & Ashby, 1982):

$$\dot{\gamma} = A\exp(-\Delta H/RT)(\tau/\mu)^n \qquad (B.1)$$

where $\dot{\gamma}$ is the shear strain rate (s^{-1}), A is a pre-exponential constant ($MPa^{-n}s^{-1}$), ΔH is the activation energy for creep (kJ/mol), R is the gas constant (kJ/Kmol), T is the temperature (K), τ the applied stress (MPa), μ is the temperature-compensated shear modulus (MPa) and n is the power- law exponent.

The mechanical data of Chapter 3 have been fitted to Eq. B.1 in order to obtain values for A, ΔH and n. The global inversion method (Sotin and Poirier, 1984; Poirier et al., 1990) described in Appendix A was used to obtain values for the flow law parameters. Separate solutions were sought for the temperature range 250 - 450 °C and for 500 - 600 °C (see Chapter 3).

In a first attempt, the initial values and standard deviations used for the inversion were $\ln A = -20 \pm 100$ $MPa^{-n}s^{-1}$, $n = 5\pm5$ and $\Delta H = 250 \pm 250$ kJ/mol. For the *250-450 °C* temperature range the results of the inversion are :

$\ln A$ (in $MPa^{-n}s^{-1}$) = -2.1±7.2
n = 3.42±0.58
ΔH = 72±9.4 kJ/mol

obtained after 6 iterations for the 15 equations. Figure B.1a shows the distribution of the residuals (histogram) compared with a Gaussian distribution (diamonds).

The flow law parameters obtained from tests in the temperature range *500-600 °C* yield the following values after 6 iterations:

$$\ln A \text{ (in } MPa^{-n}s^{-1}) = 14.5 \pm 5.0$$
$$n = 3.49 \pm 0.53$$
$$\Delta H = 179 \pm 28.3 \text{ kJ/mol}$$

The residuals (Fig. B.1b) show a slightly skewed distribution. The inversion scheme has also been applied to other temperature ranges, but always yielded poorer fits. For example the data from temperature range 450-600 °C converged after only 8 iterations with marginally smaller standard deviations as found for the 500-600 °C temperature range above. Inversion of the 250-400 °C dataset yielded higher standard deviations and higher residual values.

In an attempt to optimize the quality of the data fit, the range of the estimated initial values has been constrained. This optimization was inspired by the quality of fit obtained for the well-constrained data set of the uniaxial compression experiments (Appendix A). In order to see whether a better fit could be obtained, whilst still using physical significant parameter values, the flow law parameters derived from the uniaxial datasets were used as initial values. For both temperature regimes, flow laws were obtained after a smaller number of iterations with smaller residuals and standard deviations. The *250-450 °C* dataset yielded, after only 5 iterations:

$$\ln A \text{ (in } MPa^{-n}s^{-1}) = -0.33 \pm 3.0$$
$$n = 5.17 \pm 0.2$$
$$\Delta H = 92.7 \pm 7.0 \text{ kJ/mol}$$

The residuals calculated for this inversion (Fig. B.1c) match a normal distribution better than in previous case (Fig. B.1a).

Using the high temperature uniaxial flow parameters as initial values, the *500-600 °C* dataset yielded, after 5 iterations:

$$\ln A \text{ (in } MPa^{-n}s^{-1}) = 19.5 \pm 2.7$$
$$n = 4.3 \pm 0.28$$
$$\Delta H = 209 \pm 18.3 \text{ kJ/mol}$$

Again, the residuals show a slightly skewed distribution (compare Fig. B.1d with B.1b). The results of these inversions are summarized in Table 3.4.

The best rheological description is, according to Poirier et al. (1990), the one which leads to the quickest inversion with the smallest residuals and standard deviations. The second attempt, using the flow law parameters obtained from the uniaxial compression tests as initial values, yielded quicker inversions with significantly smaller standard deviations. The flow law parameters obtained during the second attempt are inferred to represent a better description of the rheological behaviour of polycrystalline salt in shear than the flow laws obtained in the first inversion attempt (see for discussion Chapter 3).

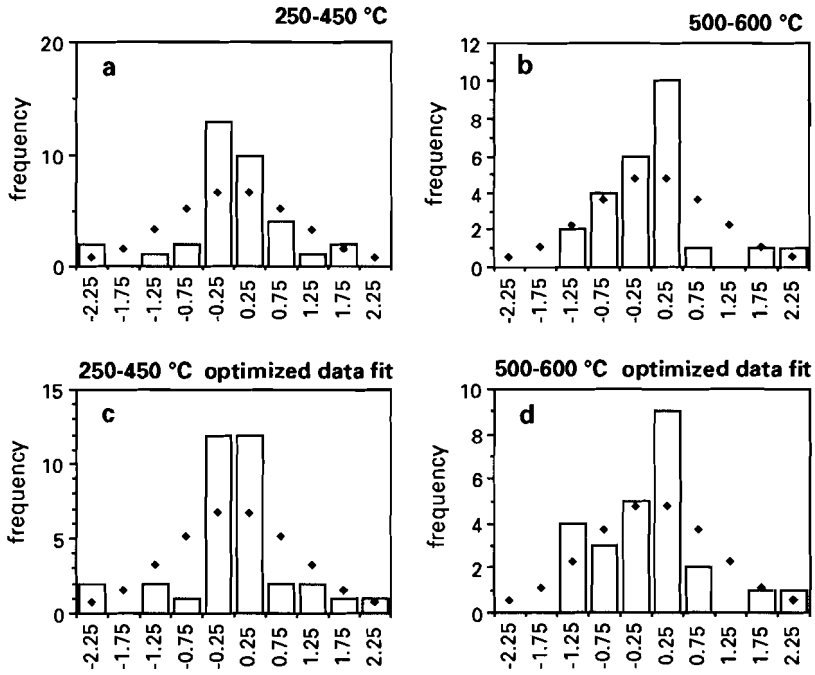

Figure B1. *Histograms of the residuals of the input parameters (lnA, ΔH, n and the mechanical data) after recalculation using the rheological laws derived and the theoretical normal distributions (diamonts) whose mean value and standard deviation are 0 and 1, respectively. Horizontal axis is the number of standard deviayions abuod the mean. (a) power-law fit in the range 250-450 °C, firts attempt using a wide range of initial values; (b) idem for 500-600 °C; (c) power-law fit in the range 250-450 °C, using a narrow range of initial values;(d) idem for 500-600 °C.*

REFERENCES

Alsem, W.H.M. van, De Hosson, J.Th.M., Tamler, H. and Kanert, O. 1982. The orientation dependence of dislocation slip in NaCl single crystals. Philos. Mag. A, 46: 451-468.

Anand, L., Kim, K.H. and Shawki, T.G. 1987. Onset of shear localization in viscoplastic solids. J. Mech. Phys. Solids., 35: 407-429.

Arieli, A., Heard, H. C. & Mukherjee, A.K. 1982. Deformation modelling in sodium chloride at intermediate and elevated temperatures. In: R.W. Rohde and J.C. Swearengen (Editors), Mechanical testing for deformation model development. American Society for Testing of Material Special Technical Publication, 765: 342-365.

Asaro, R.J. and Needleman, A. 1985. Texture development and strain hardening in rate dependent polycrystals. Acta metall., 33: 923-953.

Ashby, M.F. and Verall, R.A. 1977. Micromechanisms of flow and fracture, and their relevance to the rheology of the upper mantle. Philos. Trans. R. Soc. Lond. A., 288: 59-95.

Aubertin, M., Gill, D. E. and Ladanyi, B. 1991. A unified model for the inelastic flow of alkali halides. Mech. Mater., 11: 63-82.

Banerdt, W. B. & Sammis, C. G. 1985. Low stress high temperature creep in single crystal NaCl. Phys. Earth and Planet. Inter., 41: 108-124.

Barr, L.W., Morisson, J.A. and Schroeder, P.A., 1965. Anion diffusion in crystals of NaCl. J. Appl. Physics, 36: 624-631.

Barr, L.W., Hoodless, I.M., Morrison, J.A. and Rudham, R. 1960. Effects of gross imperfections on chloride ion diffusion in crystals of sodium and potassium chloride. Trans. Faraday Soc., 56: 697-708.

Beeman, M.L. and Kohlstedt, D.L., 1988. Dislocation density: stress relationships in natural and synthetic sodium chloride. Tectonophysics, 149: 147-161.

Benière, F., Benière, M. and Chemla, M. 1968. Auto-diffussion des ions Cl^- dans des cristaux de NaCl dopés par Sr^{++}. C.R. Acad. Sci. Serie C, 267: 633-636.

Borradaile, G.J. and Alford. C. 1988. Experimental shear zones and magnetic fabrics. J. Struct. geol., 10: 895-904.

Bouchez, J.L. and Duval, P. 1982. The fabric of polycrystalline ice in simple shear: experiments in torsion, natural deformation and geometrical intepretation. Textures and Microstructures, 5:171-190.

Brokmeier, H. G., Böcker, W, and Bunge, H.J., 1988. Neutron diffraction texture analysis in extruded Al-Pb composites. Textures and Microstructures, 8&9: 429-441.

Bulatova, T.M. and Nadgornyi, E.M., 1982. Effect of the polycrystalline structure on the relaxation processes and dislocation motion in NaCl crystals. Phys. Stat. Sol. (a), 69: 527-533.

Bunge, H. J. 1969. Mathematische Methoden der Texturanalyse. Akademie- Verlag Berlin.

Bunge, H.J., 1982. Texture Analysis in Material Science (P.R. Morris, trans.), Butterworth, London.

Burke, P.M., Cannon, R.W. and Sherby, O.D., 1981. Intermediate and high temperature creep of polycrystalline sodium chloride. Workshop on Structural Behavior of Repository Materials, Sandia National Laboratories, Albuquerque, N.M., April 29.

Burrows, S. E., Humphreys, F. J. & White, S. H. 1979. Dynamic recrystallization. A comparison between magnesium and quartz. Bull. Mineral., 102: 70-75.

Butler, R.W.H., Coward, M.P., Harwood, G.M. and Knipe, R.J. 1987. Salt control on thrust geometry, structural style and gravitational collapse along the Himalayan mountain front in the Salt range of Northern Pakistan. In: Lerche, I. and O'Brien, J.J. (Editors), Dynamical geology of salt and related structures: 339-418.

Cannon, W.R. and Langdon, T.G., 1983. Creep of ceramics. Part 1 Mechanical characteristics. J. Mat. Sci., 18: 1 - 50.

Cannon, W.R. and Langdon, T.G., 1988. Creep of ceramics. Part 2 An examination of flow mechanisms. J. Mat. Sci., 23: 1-20.

Carter, N. L. & Heard, H. C., 1970. Temperature and rate dependent deformation of halite. Am. J. Science, 26: 193-249.

Carter, N.L. and Kirby, S.H., 1978. Transient creep and semibrittle behaviour of crystalline rocks. Pageoph., 116: 807-839.

Carter, N.L. and Hansen, F.D., 1983. Creep of rocksalt. Tectonophysics, 92: 275-333.

Carter, N. L., Hansen, F. D. & Senseny, P. E., 1982. Stress magnitudes in natural rocksalt. J. Geophys. Res., B 87: 9289-9300.

Carter, N.L., Handin, J. and Russel, J.E., 1984. Equilibrium subgrain size in deformed rocksalt. Trans. Am. Geophys. Union EOS, 65: 280.

Carter, N.L., Handin, J., Russel, J.E. and Horseman, S.T., 1993. Rheology of rocksalt. J. Struct. geol., in press.

Chester, F.M. 1989. Dynamic recrystallization in semi-brittle faults. J. Struct. geol., 7: 847-858.

Chester, F.M. and Logan, J.M., 1990. Frictional faulting in polycrystalline halite: correlation of microstructure, mechanism of slip, and constitutive behavior. In: A.G. Duba, W.B. Durham. J.W. Handin and H.F. Wang (Editors), The Brittle-Ductile Transition in Rocks. Geophys. Monogr., 56: 49-65.

Cobbold, P.R. and Szatmari, P., 1991. Radial gravitational gliding on passive margins. Tectonophysics, 188: 249-289.

Cogné, J.P. and Canot-Laurent, S., 1992. Simple shear experiments on magnetized wax-hematite samples. Earth and Planet. Sci. Lett., 112: 147-159.

Dahms, M. 1987. Spezielle mathematische Methoden der Texturanalyse und ihre Anwendungen unter Berücksichtigung der intermetallischen Phasen. Ph.D. Thesis, T. U. Clausthal.

Dahms, M. 1992. The intervative series expansion method for quantitative texture analysis - Part II: Applications. J. Appl. Cryst., 25: 258-267.

Dahms, M. and Bunge, H.J. 1989. The iterative series-expansion method for quantitative texture analysis - Part I: General outline. J. Appl. Cryst., 22: 439-447.

Davidson, D.L. 1984. Uses of electron channelling in studying material deformation. Int. Metals Revs., 29: 75-95.

Davis, D.M. and Engelder, T. 1985. The role of salt in fold-and-thrust belts. Tectonophysics, 119: 67-88.

Davis, D.M. and Engelder, T. 1987. Thin-skinned deformation over salt. In: Lerche, I. and O'Brien, J.J. (Editors), Dynamical geology of salt and related structures: 301-337.

De Bresser, J.H.P. and Spiers, C. J. 1990. High temperature deformation of calcite single crystals by r^+ and f^+ slip. In: R.J. Knipe and E.H. Rutter (Editors), Deformation Mechanisms, Rheology and Tectonics. Geol. Soc. Spec. Publ., 54: 285-295.

Dell'Angelo, L.N. and Tullis, J.,1989. Fabric development in experimentally sheared quartzites. Tectonophysics, 169: 1-21.

Derby, B. 1990. Dynamic recrystallization and grain size. In: D.J. Barber and P.D. Meredith (Editors), Deformation Processes in Minerals, Ceramics and Rocks. Unwin Hyman, London, pp.354-364.

Derby, B. 1991. The dependence of grain size on stress during dynamic recrystallization. Acta metall. mater., 39: 955-962.

Derby, B. 1992. Dynamic recrystallization: the steady state grain size. Scripta Metall., 27: 1581-1586.

Dorn, J.E., 1954. Some fundamental experiments on high temperature creep. J. Mech. Phys. Solids, 3: 85-116.

Drucker, D.C. 1951. A more fundamental approach to plastic stress-strain relations. Proc. 1st US Nat. Congress Appl. Mech. ASME: 487-491.

Drucker, D.C. 1956. On uniqueness in the theory of plasticity. Quart. of Appl. Math., 14: 35-42.

Drucker, D.C. 1959. A definition of stable inelastic material. J. Appl. Mech. Trans. ASME, 26: 101-106.

Drury, M.R. and Urai, J.L., 1990. Deformation-related recrystallization processes. Tectonophysics, 172: 235-253.

Drury, M. R., Humphreys, F. J. & White, S. H. 1985. Large strain deformation studies using polycrystalline magnesium as a rock analogue. Part II: dynamic recrystallization mechanisms at high temperatures. Phys. Earth and Planet. Interiors, 40: 208-222.

Drury, M.R., Vissers, R.L.M., van der Wal, D. and Hoogerduin Strating, E.H. 1991. Shear localization in upper mantle peridotites. PAGEOPH., 137: 439-460.

Duval, B., Cramez, C. and Jackson, M.P.A. 1992. Raft tectonics in the Kwanza Basin, Angola. Marine and Petrol. Geol., 9: 389-404.

Evans, B. and Wong, T.-f. 1985. Shear localization in rocks induced by tectonic deformation. In: Bazant, Z.P. (Editor), Mechanics of geomaterials. Rocks, concretes and soils. John Wiley and Sons, Chichester. pp. 189-210.

Ferguson, C. C. 1979. The simple fluid with fading memory as a rheological model for steady-state flow of rocks. In: Easterling, K. E. (Editor), Proc. Int. Conf. Mech. Deformation and Fracture. Luleå, Sweden. pp. 371-383.

Franssen, R.C.M.W. and Spiers, C.J., 1990. Deformation of polycrystalline salt in compression and in shear at 250 - 350 °C. In: R.J. Knipe and E.H. Rutter (Editors), Deformation Mechanisms, Rheology and Tectonics. Geol. Soc. Spec. Publ., 54: 201-212.

Friedman, M., Dula, W. F., Gangi, A. F. and Gazonas, G. A., 1981. Structural petrology of experimentally deformed synthetic rocksalt. In: M. Langer and R. Hardy (Editors), First Conference on the Mechanical Behaviour of Rocksalt. Transtech, Claustal-Zellerfeld, pp. 19-36.

Frost, H.J. and Ashby, M.F., 1982. Deformation-mechanism Maps. The Plasticity and Creep of Metals and Ceramics, Pergamon Press.

Gessler, K. 1983. Vergleich der einaxialen Zugfestigkeit mit der Drei-Punkt-Biege Zugfestigkeit und unterschiedlichen Spaltzugfestigkeiten. Kali und Steinsalz, 8: 416-423.

Ghosh, A.K. and Backofen, W.A. 1973. Strain hardening and instability in biaxially stretched sheets. Metall. Trans., 4: 1113-1123.

Gjostein, N.A., 1972. Short circuit diffusion. In: H.I. Aaronson (Editor), Diffusion. Am. Soc. for Metals, Metals park, Ohio, pp. 241-274.

Guillopé, M and Poirier, J.P., 1979. Dynamic recrystallization during creep of single crystalline halite: an experimental study. J. Geoph. Res., B 84: 5557-5567.

Guillopé, M. and Poirier, J.P., 1980. A model for stress-induced migration of tilt grain boundaries in crystals of NaCl structure. Acta metall., 28: 163-167.

Handin, J., Russel, J.E. and Carter, N.L. 1986. Experimental deformation of rocksalt. In: B.E. Hobbs and H.C. Heard (Editors), Mineral and Rock Deformation: Laboratory Studies. Geophys. Monogr., 36: 117-160.

Harren, S.V., Dève, H.E. and Asaro, R.J. 1988. Shear band formation in plane strain compression. Acta metall., 36: 2435-2480.

Heard, H.C., 1972. Steady-state flow in polycrystalline halite at pressure of 2 Kilobars. In: H.C. Heard, I.Y. Borg, N.L. Carter and C.B. Raleigh (Editors), Flow and Fracture of Rocks. Geophys. Monogr., 16: 191-209.

Heard, H.C. and Ryerson, F.J. 1986. Effect of impurities on steady-state flow of salt. In: B.E. Hobbs and H.C. Heard (Editors), Mineral and Rock Deformation: Laboratory Studies. Geophys. Monogr., 36: 99-115.

Hill, R. 1950. The mathematical theory of plasticity. Oxford University Press, Oxford, 355 pp.

Hiraga, H. and Shimamoto, T. 1987. Textures of sheared halite and their impications for the seismogenic slip of deep faults. Tectonophysics, 144: 69-86.

Hirth, J.P. 1972. The influence of grain boundaries on mechanical properties. Metall. Trans., 3: 3047-3067.

Hobbs, B. E. 1972. Deformation of non-newtonian fluids in simple shear. In: Heard, H. C., Borg, I. Y., Carter, N. L. & Raleigh, C. B. (Editors), Flow and fracture of rocks. Geophys. Monogr., 16: 243-258.

Hobbs, B.E., Mühlhaus, H.-B. and Ord, A. 1990. Instability, softening and localization of deformation. In: R.J. Knipe and E.H. Rutter (Editors), Deformation Mechanisms, Rheology and Tectonics. Geol. Soc. Spec. Publ., 54: 143-165.

Horseman, S. T. and Handin, J., 1990. Triaxial-compression tests on rocksalt at temperatures from 50° to 200 °C and strain rates from 10^{-4} to 10^{-9}/s. In: A.G. Duba, W.B. Durham. J.W. Handin and H.F. Wang (Editors), The Brittle-Ductile Transition in Rocks. Geophys. Monogr., 56: 103-110.

Horseman, S.T., Russel, J.E., Handin, J. and Carter, N.L. 1992. Slow experimental deformation of Avery Island salt. 7th Int. Symp. on Salt, April 6-9, Kyoto, Japan.

Hull, D. 1975. Introduction to dislocations. Pergamon Press, Oxford, 271 pp.

Jackson, M.P.A. and Talbot, C.J. 1991. A glossary of salt tectonics. In: Geological Circular 91-14, Bureau of Economic Geology, University of Texas at Austin, 44 pp.

Janssen, L.G.J., Prij, J., Kevenaar, J.W.A.M., Jong, C.J.T., Klok, J. and Beemsterboer, C. 1984. The thermo-mechanical behaviour of a salt dome with a heat generating waste repository. European Communities Commission, Nuclear Science and Technology Series. EUR-9205.

Jessel, M.W. 1986. Grain boundary migration and fabric development in experimentally deformed octochloropropane. J. Struct. geol., 8: 527-542

Jessel, M.W. and Lister, G.S., 1991. Strain localization behaviour in experimental shear zones. Pageoph., 137: 421-438.

Karato, S.-i., 1988. The role of recrystallization in the preferred orientation of olivine. Phys. Earth Planet. Interiors, 51: 107-122.

Karato, S.-i., 1989. Defects and plastic deformation in olivine. In: Karato, S.-i. and Toriumi (edidtors), Rheology of solids and of the Earth. pp. 176-208.

Karato, S.-i., Paterson, M.S. and FitzGerald, J.D. 1986. Rheology of synthetic olivine aggregates: influence of grain size and water. J. Geophys. Res., 91: 8151-8176.

Kern, H., 1977. Prefferred orientation of experimentally deformed limestone marble, quartzites and rock salt at different temperatures and states of strain. Tectonophysics, 39: 103-120.

Kern, H. and Braun, G., 1973. Deformation und Gefügeregelung von Steinsalz im Temperaturbereich 20-200 °C. Contrib. Miner. Petrol., 40: 169-181.

Kern, H. and Wenk, H.R. 1983. Calcite texture development in experimentally induced ductile shear zones. Contrib. Mineral. Petrol., 83: 231-236.

Kern, H. and Richter, A., 1985. Microstructures and textures in evaporites. In: H.R. Wenk (Editor), Preferred Orientation in Deformed Metals and Rocks: An Introduction to Modern Texture Analysis. Academic Press, Orlando, pp. 317-333.

Kirby, S.H. 1985. Rock mechanics observations pertinent to the rheology of the continental lithosphere and localization of strain along shear zones. Tectonophysics, 119: 1-27.

Knapp, S.T., Friedman, M. and Logan, J.M. 1987. Slip and recrystallization of halite gouge in experimental shear zones. Tectonophysics, 187: 171-183.

Kopetskii, Ch. V., Nadgornaya, N. M. and Nadgornyi, E.M., 1982. Structure and properties of sodium chloride single crystals deformed under dynamic recrystallization conditions. Sov. Phys. Solid State, 24: 427-431.

Krieg, R.D. 1982. A unified creep plasticity model for halite. In: R.W. Rohde and J.C. Swearengen (Editors), Mechanical testing for deformation model development. American Society for Testing of Material Special Technical Publication, 765: 139-147.

Kunze, F.R. and Avé Lallement, H. G. 1981. Non-coaxial experimental deformation of olivine. Tectonophysics, 74: T1-T13.

Langdon, T. 1985. Regimes of plastic deformation. In: Wenk, H.P. (Editor): Preferred orientation in deformed metals and rocks, an introduction to modern texture analysis. Academic Press. pp. 219-232.

Laurance, N. 1960. Self-diffusion of the Chloride ion in sodium chloride. Phys. rev., 120: 57-62.

Laurent, J.F. and Bénard, J., 1957. Autodiffusion des ions dans les cristaux uniques des halogenures de potassium et des chlorures alcalins. J. Phys. Chem. Solids, 3: 7-19.

Laurent, J.F. and Bénard, J., 1958. Autodiffusion des ions dans les halogenures alcalins polycrystallins. J. Phys. Chem. Solids, 7: 218-227.

Lerche, I. and O'Brien, J.J. 1987. Modelling of buoyant salt diaprism. In: Lerche, I. and O'Brien, J.J. (Editors): Dynamical geology of salt and related structures. Academic Press, pp. 129-162.

Leroy, Y. and Ortiz, M. 1990. Finite element analysis of transient strain localization phenomena in frictional solids. Int. j. numer. anal. methods. geomech., 14: 93-124.

Lloyd, G.E. , Ferguson, C.C. and Law, R.D.1987. Discriminatory petrofabric analysis of quartz rocks using SEM electron channelling. Tectonophysics, 135: 243-249.

Lundin. E.R. 1992. Thin-skinned extensional tectonics on a salt detachment, northern Kwanza Basin, Angola. Marine and Petrol., 9: 405-411.

Malvern, L.E. 1969. Introduction to the mechanics of a continuous medium. Prentice-Hall, Englewood Cliffs, U.S.A. 713 pp.

Mapother, D., Crooks, H.N. and Maurer, R., 1950. Self-diffusion of Sodium in Sodium Chloride and Sodium Bromide. J. Chem. Phys., 18: 1231-1236.

Masuda, T. 1989. Shear zone experiment on quartz aggregate: a preliminary result. In: Karato, S.-i. and Toriumi (Editors). Rheology of solids and of the Earth. pp. 308-316.

McClintock, F. A. & Argon, A. S. 1966. Mechanical behaviour of materials. Addison-Wesley, Reading Massachusetts, U.S.A.

Means, W.D. and Ree, J.H., 1988. Seven types of subgrain boundaries in octachloropropane. J.Struct. geol., 10: 765-770.

Michibayashi, K. 1993. Syntectonic development of a strain-independent steady-state grain size during mylonitization. Tectonophysics, 222: 151-164.

Miller, A.K., Robinson, S.L. and Sherby, O.D. 1977. On the importance of subgrain size to the creep rate. Philos. Mag., 36: 757-760.

Molinari, A., Canova, G.R. and Ahzi, S. 1987. A self consistent approach of the large deformation polycrystal viscoplasticity. Acta metall., 35: 2983-2994.

Nadai, A. 1963. Theory of flow and fracture of solids. McGraw-Hill, New York.

Nadgornyi, E.M. and Strunk, H.P., 1987. Dislocation structure of plastically deformed NaCl polycrystals. Phys. Stat. Sol. (a), 104: 193-202.

Nicolas, A. and Piorier, J.P., 1976. Crystalline plasticity and solid-state flow in metamorphic rocks. Wiley, Chichester, 444 pp.

Nicolas, A., Bouchez, J.L., Boudier, F. and Mercier, J.-C.C. 1971. Textures, structures and fabrics due to solid state flow in some European lherzolites. Tectonophysics, 12: 55-86.

Nye, J.F. 1953a. The flow law of ice from measurements in glacier tunnels, laboratory experiments and the Jungfraufirn borehole experiment. Proc. Roy. Soc. London. Series A., 219: 477-489.

Nye, J. F. 1953b. The mechanics of glacier flow. Journal of Glaciology, 2: 82-93.

Olgaard, D.L. and FitzGerald, J.D. 1993. Evolution of pore microstructures during healing of grain boundaries in synthetic calcite rocks. Contrib. Mineral. Petrol., in press.

Ord, A. 1991. Deformation of rock: a pressure-sensitive, dilatant material. PAGEOPH., 137: 337-366.

Ord, A. and Hobbs, B.E. 1989. The strength of the continental crust, detachment zones and the development of plastic instabilities. Tectonophysics, 158: 269-289.

Paterson, W. S. B. 1976. The physics of glaciers. Pergamon press, Oxford.

Peach, C.J. 1991. Influence of deformation on the fluid transport properties of salt rocks. PhD Thesis University of Utrecht, Geologica Ultraiectina, 77: 238 pp.

Poirier, J.P. 1980. Shear localization and shear instability in materials in the ductile field. J. Struct. geol., 2: 134-142.

Poirier, J.P., 1985. Creep of Crystals. Cambridge University Press. 260 pp.

Poirier, J.P. and Guillopé, M. 1979. Deformation induced recrystallization of minerals. Bull. Minéral., 102: 67-74.

Poirier, J.P., Sotin, C. and Beauchesne, S. 1990. Experimental deformation and data processing. In: D.J. Barber and P.D. Meredith (Editors), Deformation Processes in Minerals, Ceramics and Rocks. Unwin Hyman, London, pp.179-189.

Pontikis, V. and Poirier, J.P., 1975. Phenomenological and structural analysis of recovery-controlled creep, with special reference to the creep of single-crystal silver chloride. Philos. Mag., 32: 577-592.

Price, G.P. and Torok, P.A. 1989. A new simple shear deformation apparatus for rocks and soils. Tectonophysics., 158: 291-309.

Prij, J. 1983. Creep behaviour of a salt dome with a repository. Stichting Energieonderzoek Centrum Nederland (ECN), Petten. ECN83-063.

Ralser, S 1989. Shear zones developed in an experimentally deformed quartz mylonite. J. Struct. geol., 8: 1033-1045.

Ramsay, J.G. and Graham, R.H. 1970. Strain variations in shear belts. Can. J. Earth Sci., 7: 786-813.

Ramsay, J.G.1980. Shear zone geometry: a review. J. Struct. geol., 2: 83-99.

Ranalli, G. 1987. Rheology of the Earth - deformation and flow processes in geophysics and geodynamics. Allen and Unwin. 366 pp.

Rice, J.R. 1976. The localization of plastic deformation. In: Theoretical and Applied Mechanics (Editor: Koiter, W.T.). North Holland Publishing Co. pp. 207-220.

Robinson, S.L., Burke, P.M. and Sherby, O.D., 1974. Activation energy and subgrain size-creep rate relations in sodium chloride. Philos. Mag., 24: 423-427.

Ross, J.V., Ave Lallement, H.G. and Carter, N.L., 1980. Stress dependence of recrystallized-grain and subgrain size in olivine. Tectonophysics, 70: 39-61.

Rudnicki, J.W. and Rice, J.R. Conditions for the localization of deformation in pressure-sensitive dilatant materials. J. Mech. Phys. Solids, 23: 371-394.

Rutter, E.H. and Brodie, K.H., 1992. Rheology of the lower crust. In: Fountian, D.M., Arculus, R. and Kay, R.W. (Editors). Continental lower crust. Developments in Geotectonics 23. Elsevier, Amsterdam, pp. 201-267.

Rutter, E.H., Atkinson, B.K. and Mainprice, D.H., 1978. On the use of the stress relaxation testing method in studies of the mechanical behaviour of geological materials. Geophys. J. R. astr. Soc., 55: 155-170.

Russel, J.E., Carter, N.L. and Walker, S.C., 1990. A material model for Avery Island rocksalt. In: A.G. Duba, W.B. Durham. J.W. Handin and H.F. Wang (Editors), The Brittle-Ductile Transition in Rocks. Geophys. Monogr., 56: 111-118.

Schuh, F., Blum, W. and Ilschner, B. Steady-state creep rate, impurities and diffusion in the rock-salt structure. 1970. Proc. Br. Ceram. Soc., 15: 143-156.

Schmid, S., Paterson, M.S. and Boland, J.N. 1980. High temperature flow and dynamic recrystallization in Carrara marble. Tectonophysics, 65: 245-280.

Schmid, S.M., Panozzo, R. and Bauer, S. 1987. Simple shear experiments on calcite rocks: rheology and microfabric. J. Struct. geol.,9: 747-778.

Senseny, P.E., Hansen, F.D., Russel, J.E., Carter, N.L. and Handin, J.W. 1992. Mechanical behaviour of rocksalt: phenomenology and micro-mechanisms. Int. J. Rock Mech. Min. Sci. & Geomech. Abstr., 29: 363-378.

Servi, I.S. and Grant, N.J., 1951. Creep and stress behavior of alluminium as a function of purity. Trans. AIME, 191: 909-916.

Sherby, O.D. and Burke, P.M., 1967. Mechanical behaviour of crystalline solids at elevated temperature. Progr. Mat. Sci, 13: 325-390.

Sherby, O.D. and Weertman, J., 1979. Diffusion-controlled dislocation creep: a defense. Acta Metall., 27: 387-400.

Sherby, O.D., Klundt, R.H. and Miller, A.K. 1977. Flow stress, subgrain size, and subgrain stability at elevated temperatures. Metall. Trans. 8A: 843-850.

Shimamoto, T. 1986. Transition between frictional slip and ductile flow for halite shear zones at room temperature. Science, 231: 711-714.

Shimamoto, T. 1989a. Mechanical behaviours of simulated halite shear zones: implications for the seismicity along subducting plate-boundaries. In: Karato, S.-i. and Toriumi(Editors). Rheology of solids and of the Earth. pp. 351-373.

Shimamoto, T. 1989b. The origin of S-C mylonites and a new fault-zone model. J. Struct. geol., 11: 51-64.

Shimamoto, T. and Logan, J.M. 1986. Velocity-dependent behavior of simulated halite shear zones: an analog for silicates. In: Das, J., Boatwright, J. and Scholze, C.H. (Editors) Earthquake source mechanics. Geophys. Monogr., 37: 49-63.

Skrotzki, W. and Welch, P., 1983. Development of texture and microstructure in extruded ionic polycrystalline aggregates. Tectonophysics, 99: 47-62.

Skrotzki, W. and Haasen, P., 1984. The role of cross slip in the steady state creep of salt. In: M. Langer and R. Hardy (Editors), First Conference on the Mechanical Behaviour of Rocksalt. Trans Tech, Claustal-Zellerfeld, pp. 69-81.

Skrotzki, W. and Haasen, P. 1988. The influence of texture on the creep rate of salt. In: Second Conf. on the Mech. Behavior of Salt. Trans Tech FRG. pp. 83-88.

Sotin, C. and Poirier, J.P., 1984. Analysis of high-temperature creep experiments by generalized nonlinear inversion. Mech. Mat., 3: 311-317.

Spiers C.J., Urai, J.L., Lister, G.S., Boland, J.N. and Zwart, H.J., 1986. The influence of fluid-rock interaction on the rheology of salt rock. European Communities Commission, Nuclear Science and Technology Series. EUR-10399.

Spiers, C.J., Schutjens, P.M.T.M., Brzesowsky, R.H., Peach, C.J., Liezenberg, J.L. and Zwart, H.J. 1990. Experimental determination of constitutive parameters governing creep of rocksalt by pressure solution. In: R.J. Knipe and E.H. Rutter (Editors), Deformation Mechanisms, Rheology and Tectonics. Geol. Soc. Spec. Publ., 54: 215-227.

Stocker, R. L. & Ashby, M. F. 1973. On the rheology of the upper mantle. Rev. in Geoph. and Space Phys., 11: 391-426.

Strunk, H. 1975. Investigation of cross-slip in NaCl crystals by transmission electron microscope. Phys. Stat. Sol. (a), 28: 119-126.

Sun, R.C. and Bauer, C.L., 1970. Tilt boundary migration in NaCl bicrystals. Acta metall., 18: 639-647.

Takeshita, T. 1989. Plastic anisotropy in textures mineral aggregates: theories and geological implications. In: Karato, S.-i. and Toriumi (Editors). Rheology of solids and of the Earth. pp. 237-262.

Takeshita, T. and Wenk, H.R. 1988. Plastic anisotropy and geometrical hardening in quartzites. Tectonophysics, 149: 345-361.

Takeshita, T., Wenk, H.R., Canova, G.R. and Molinari, A. 1990. Simulation of dislocation-assisted plastic deformation in olivine polycrystals. In: D.J. Barber and P.D. Meredith (Editors), Deformation Processes in Minerals, Ceramics and Rocks. Unwin Hyman, London, pp. 365-376.

Tarantola, A. and Valette, B. 1982. Generalized nonlinear inverse problems solved in using least-squares criterion. Rev. Geophys. Space Phys., 20: 219-232.

Tomé, C., Canova, G.R., Kocks, U.F., Christodoulou, N. and Jonas, J.J. 1984. The relation between macroscopic and microscopic strain hardening in F.C.C. polycrystals. Acta metall., 32: 1637-1653.

Tsenn, R.J. amd Carter, N.L. 1987. Upper limits of power law creep of rocks. Tectonophysics, 136: 1-26.

Twiss, R.J. and Moores, E.M. 1992. Structural geology. W.H. Freeman and Company, New York, 532 pp.

Urai, J.L., 1983. Deformation of wet salt rocks. Ph.D thesis, University of Utrecht, 221 pp.

Urai, J.L., Means W.D., and Lister, G.S., 1986a. Dynamic recrystallization of minerals. In: B.E. Hobbs and H.C. Heard (Editors), Mineral and Rock Deformation: Laboratory Studies. Geophys. Monogr., 36: 161-199.

Urai, J.L., Spiers, C.J., Zwart, H.J. and Lister, G.S. 1986b. Weakening of rocksalt by water during long-term creep. Nature, 324: 554-557.

Urai, J.L., Spiers, C.J., Peach, C.J., Franssen, R.C.M.W. and Liezenberg, J.L., 1987. Deformation mechanisms operating in naturally deformed halite rocks as deduced from microstructural investigations. Geol. and Mijnb., 66: 165-176.

Van den Berg, A., Yuen, D.A. and Keken, P.E. van, 1991. Effects of depth-variations in creep laws on the formation of plates in mantle dynamics. Geophys. Res. Lett., 18: 2197-2200.

Van Keken, P.E. 1993. Numerical modelling of thermochemically driven fluid flow with non-newtonian rheology- applied to the Earth's lithosphere and mantle. PhD Thesis University of Utrecht, Geologica Ultraiectina, 107: 159 pp.

Van Keken, P.E., Spiers, C.J., van den Berg, A.P. and Muyzert, E.J. 1993. The effective viscosity of rocksalt: implementation of steady state creep laws in numerical models of salt diapirsm. Tectonophysics, in press.

Van Sambeek, L.L. 1987. Three-dimensional generalization of creep laws. RSI presentation 87-20, 7 pp.

Vendeville, B.C. and Jackson. M.P.A. 1992a, The rise of diapirs during thin-skinned extension. Marine and Petrol. Geol., 9: 331-353.

Vendeville, B.C. and Jackson. M.P.A. 1992b, The fall of diapirs during thin-skinned extension. Marine and Petrol. Geol., 9: 354-371.

Vernon., R.H. 1976. Metamorphic processes. Reactions and microstructure development. Allen & Unwin. 247 pp.

Verrall, R.A., Fields, R.J. and Ashby, M.F., 1977. Deformation-mechanism maps for LiF and NaCl. J. Am. Ceram. Soc., 60: 211-216.

Vissers, R.L.M., Drury, M.R., Hoogerduijn Strating, E.H. and Van der Wal, D. 1991. Shear zones in the upper mantle: a case study in an Alpine lherzolite massif. Geology, 19: 990-993.

Wawersik, W.R. 1988. Alternatives to a power-law creep model for rocksalt at temperatures below 160 °C. In: Hardy, H.R. and Langer, M. (Editors): Proc. Second Conf. on Mechanical behaviour of salt. Trans tech Publ. Hannover. pp. 103-128.

Wawersik, W.R. and Zeuch, D.H., 1986. Modelling and mechanistic interpretation of creep of rock salt below 200 °C. Tectonophysics, 121: 125-152.

Weertman J.R. 1968. Dislocation climb theory of steady state creep. Trans. Am. Soc. of Metals., 81: 681-694.

Weijermars, R., Jackson, M.P.A. and Vendeville, B. 1993. Rheological and tectonic modelling of salt provinces. Tectonophysics, 217: 143-174.

Wenk, H. R. and Kocks, U.F. 1987. The representation of orientation distributions. Metall. Trans., 18A: 1083-1092.

Wenk, H. R. and Christie, J.M. 1991. Comments on the interpretation of deformation textures in rocks. J.Struct. geol., 13: 1091-1110.

Wenk, H. R., Takeshita, T., Van Houtte, P. and Wagner, F. 1986. Plastic anisotropy and texture development in calcite polycrystals. J. Geophys. res., B91: 3861-3869.

Wenk, H.R., Canova, G.R., Molinari, A. and Mecking, H.,1989a. Texture development in halite: comparison of Taylor model and self-consistent theory. Acta metall, 37: 2017-2029.

Wenk, H.R., Canova, G.R., Molinari, A. and Kocks, U.F.,1989b. Viscoplastic modelling of texture development in quartzite. J. Geophys. res., B94: 17895-17906.

Wenk, H. R., Takeshita, T., Bechler, E., Erskine, B. G. & Matthies, S. 1987. Pure shear and simple shear calcite textures. Comparison of experimental, theoretical and natural data. J. Struct. geol, 9: 31-745.

Wernicke, B. 1985. Uniform sense normal simple shear of the continental lithosphere. Canad. J. Earth Sci., 22: 108-125.

White, S.H., Burrow, S.E., Carreras, J. and Shaw, N.D. 1980. On mylonites in ductile shear zones. J. Struct. geol., 2: 175-187.

Williams, R.O. 1962. Shear textures in copper, brass, aluminium, iron and zirconium. Trans. Metall. Soc. of AIME., 224: 129-225.

Williams, P.F. and Price, G.P. 1990. Origin of kinkbands and shear band cleavage in shear zones: an experimental study. J. Struct. geol., 12: 145-164.

Wilson, C.J.L. 1986. Deformation induced recrystallization of ice: the application of in situ experiments. In: Hobbs, B.E. and Heard, H.C. (Editors). Mineral and rock deformation: laboratory studies. Geophys. Monogr., 56: 213-232.

Worall, D.M. and Snelson, S. 1989. Evolution of the northern Gulf of Mexico, with emphasis on Cenozoic growth faulting and the role of salt. In: The geology of North America - An overview (Editors: Bally, A.W. and Palmer, A.R.). Vol. A. Geol. Soc. Am. Boulder, CO, pp. 97-138.

Wu, S., Bally, A.W. and Cramez, C. 1990. Allochtonous salt, structure and stratigraphy of the north-eastern Gulf of Mexico. Part II: Structure. Marine and Petrol., 7: 334-370.

Yan, M.F., Cannon, R.M., Bowen, H.K. and Coble, R.L., 1975. Grain boundaries and grain boundary mobility in hot-forged alkali halides. In: R.J. Bards and R.E. Tressler (Editors), Deformation of Ceramic Materials. Plenum, New York, pp. 549-569.

NEDERLANDSE SAMENVATTING

Steenzout (haliet) vormt het belangrijkste bestanddeel van zoutafzettingen. Ondanks het feit dat steenzout ten opzichte van andere mineralen in de aardkorst relatief weinig voorkomt, kunnen zoutafzettingen een zeer belangrijke rol spelen in tektonische processen. Dit komt met name door de relatief lage dichtheid van steenzout en doordat plastische vervorming zonder breukvorming kan plaatsvinden onder relatief lage spanningen. Bijvoorbeeld, gelaagde zoutformaties kunnen dienen als schuifzones waarover enorme massa's gesteenten kunnen bewegen gedurende gebergtevorming (zoals in het Jura-gebergte in Zwitserland, de 'Salt Range' in Pakistan) of gedurende extensie op passieve continentale marges (zoals in het Kwanza bekken in Angola of in de Santos en Campos bekkens van Brazilië). De dichtheid van steenzout is nauwelijks van de diepte afhankelijk en is lager dan de dichtheid van de meest voorkomende afzettingsgesteenten. Hierdoor kunnen instabiliteiten ontstaan die leiden tot de ontwikkeling van zoutkoepels (zoals bijvoorbeeld in de ondergrond van noordoost Nederland). De interaktie tussen vervormende zoutlichamen en tektonische processen is van invloed op de ontwikkeling van sedimentaire bekkens en op de verdeling van olie en gasvoorkomens hierin. Tenslotte worden zoutvoorkomens beschouwd als geschikte locaties voor de ondergrondse opslag van strategische olie- en gasreserves en mogelijk ook voor het opbergen van chemisch en radioactief afval.

Uit het bovenstaande is duidelijk dat het belangrijk is om het vloeigedrag van steenzout te kennen. Er is dan ook reeds veel onderzoek verricht naar de mechanische eigenschappen van steenzout, de vervormingsmechanismen (zowel door intrakristallijne vervorming als door drukoplossing) en de bijbehorende microstructurele ontwikkeling. Echter, ondanks het feit dat het bekend is dat de deformatie geschiedenis en deformatie geometrie het reologisch gedrag van steenzout kunnen beïnvloeden, is hiernaar nog geen systematisch onderzoek verricht. Verder bestaan in de literatuur nog onduidelijkheden over de details

van de vervormingsmechanismen (met name de intrakristallijne deformatieprocessen door dislocatiekruip), de microstructurele processen en de ontwikkeling van kristallografische voorkeursmaaksels die kunnen optreden in polykristallijn steenzout.

Dit onderzoek richt zich in het bijzonder op de invloed van deformatie geschiedenis en geometrie op het vloeigedrag van synthetisch steenzout. Hierbij wordt de vraag gesteld onder welke omstandigheden de aannames die ten grondslag liggen aan een veelgebruikte methode, om vloeiwetten, die gebaseerd zijn op axiaal-symmetrische vervormingsexperimenten, te extrapoleren naar de (drie-dimensionale) omstandigheden die in de aardkorst gelden. Deze extrapolatie van vloeiwetten wordt bijvoorbeeld gebruikt in numerieke modellen die het mechanisch gedrag van gesteentelichamen in de aarde simuleren. De gepresenteerde onderzoeksresultaten verschaffen niet alleen meer inzicht in het vloeigedrag van synthetisch steenzout, ook kunnen beginselen worden afgeleid die betrekking hebben op de invloed van deformatie geschiedenis en geometrie op het vloeigedrag van andere gesteentevormende mineralen.

In Hoofdstuk 1 worden de te onderzoeken vraagstellingen geïntroduceerd en nader toegelicht. Het in Hoofdstuk 2 beschreven onderzoek is gericht op het vloeigedrag van synthetisch steenzout in uniaxiale kompressie (samendrukking), in relatie tot de microstructurele evolutie, de ontwikkeling van kristallografische voorkeursmaaksels en de invloed van deformatie geschiedenis. Gedurende de experimenten, die werden uitgevoerd tussen 250 en 780 °C, werd de deformatiesnelheid (tussen 10^{-3} en 10^{-7} s^{-1}) constant gehouden of gevarieerd. Kurves die de relatie tussen de spanning en vervorming weergeven zijn berekend. Het vervormingsmechanisme is dislocatiekruip waarbij van 250 tot 450 °C de vervormingsnelheid bepaald wordt door diffusie door dislocatiekernen en tussen 500 en 780 °C bepaalt diffusie door het kristalrooster de vervormingsnelheid. Vloeiwetten die de relatie beschrijven tussen vervormingsnelheid, spanning en temperatuur zijn afgeleid.

In het temperatuurgebied 250-350 °C zijn vorming van "subgrains" (polygonisatie) en rotatie rekristallisatie de belangrijkste microstructurele processen die optreden. Met toenemende temperatuur wordt korrelgrens-migratie progressief belangrijker. De temperatuur waarbij korrelgrens-migratie de microstructurele evolutie overheerst, valt samen met de overgang van vloeigedrag, bepaald door diffusie door dislocatiekernen, naar vloeigedrag bepaald door diffusie door het kristalrooster. Deze waarneming is verklaard in de context van het dynamisch rekristallisatie model van Derby (1992) dat aantoont dat een dynamische

balans ontstaat tussen korrelgrens-migratiesnelheid en vormingsnelheid van nieuwe migrerende korrels.

Bij temperaturen tussen 250 en 450 °C heeft de deformatie geschiedenis een duidelijk effect op de microstructurele ontwikkeling en op het mechanisch gedrag van synthetisch steenzout. In dit temperatuursgebied heeft een verlaging van de deformatiesnelheid gedurende een experiment tot gevolg dat de spanningen hoger en dat de "subgrains" groter zijn dan de "steady state" waarden. Als gevolg hiervan is het steenzout relatief sterker en is de vervormingsnelheid minder afhankelijk van de spanning. Bij temperaturen boven 450 °C heeft de deformatiegeschiedenis geen invloed op de microstructurele ontwikkeling en op het mechanisch gedrag omdat korrelgrens-migratie de microstructuren op zeer efficiënte wijze "verjongt".

De kristallografische voorkeursmaaksels worden gekenmerkt door rotatie van de {110} <1$\bar{1}$0> slip-vlakken naar een orientatie loodrecht op de samendrukkingsrichting. Temperatuur en rekristallisatieprocessen schijnen geen invloed te hebben op de ontwikkeling van de kristallografische voorkeursmaaksels.

In Hoofdstuk 3 worden de onderzoeksresultaten gepresenteerd van schuifdeformatie-experimenten (simple shear) op synthetisch steenzout. Het onderzoek was erop gericht het vloeigedrag van synthetisch steenzout in schuifdeformatie te bestuderen, in relatie tot de microstructurele evolutie en de ontwikkeling van kristallografische voorkeursmaaksels. De experimenten, werden uitgevoerd tussen 250 en 600 °C en de deformatiesnelheid (tussen 10^{-5} en 10^{-7} s^{-1}) of de opgelegde spanning (tussen 0.6 en 2.75 MPa) werd constant gehouden. Kurves die de relatie tussen de schuifspanning en schuifvervorming weergeven worden gepresenteerd.

In temperatuursintervallen van 250 tot 450 °C en van 500 tot 600 °C traden dezelfde vervormingsmechanismen op als bij uniaxiale kompressie. Vloeiwetten die de relatie beschrijven tussen schuifvervormingsnelheid, schuifspanning en temperatuur zijn afgeleid. Ook werden dezelfde microstructurele processen waargenomen: polygonisatie en rotatie rekristallisatie zijn belangrijk tussen 250 en 365 °C en bij toenemende temperatuur wordt korrelgrens-migratie progressief belangrijker.

De kristallografische voorkeursmaaksels worden gekenmerkt door rotatie van het {110} glijvlak naar het schuifvlak en van de <111> kristallografische richting naar de schuifrichting. Het kristallografische voorkeurspatroon blijkt onafhankelijk van temperatuur te zijn. Echter, de intensiteit van de {110} component in het voorkeursmaaksel neemt toe boven 500 °C.

In Hoofdstuk 4 worden de resultaten verkregen, uit kompressie en schuifexperimenten, uitgevoerd tussen 250 en 350 °C, naast elkaar gezet. Het mechanisch gedrag voor deze twee deformatie geometrieën wordt vergeleken in termen van equivalente spanning en equivalente vervorming, zoals gedefinieerd in de theorie van perfecte isotrope plasticiteit. Bij eenzelfde equivalente vervormingsnelheid zijn de monsters gedeformeerd in kompressie, uitgedrukt in equivalente spanning, sterker. Uit een gedetailleerde analyse van de data blijkt dat het verschil in vloeispanning voornamelijk veroorzaakt wordt door de ontwikkeling van anisotropie gedurende de vervorming. Deze resultaten suggereren dat de aannames in zowel de klassieke theorie van isotrope plasticiteit als in de standaard methode om laboratorium vloeiwetten naar 3 dimensies te extrapoleren, niet van toepassing zijn op het onderhavige materiaal onder de onderzochte kondities.

In Hoofdstuk 5 wordt de vergelijking van het mechanisch gedrag tussen de twee bestudeerde deformatie geometrieën in meer detail verder uitgewerkt. Hierbij wordt gebruik gemaakt van de experimentele data gerapporteerd in Hoofdstukken 2 en 3.

Tussen 250 en 400 °C, dat wil zegggen onder condities waarbij de vervormingsnelheid afhankelijk is van diffusie door dislocatiekernen, zijn de equivalente spanningen gemeten in schuifvervorming altijd beduidend kleiner dan in kompressie (bij dezelfde equivalente vervormingsnelheid), gedurende zowel de "hardening" (verharding) als de steady state fase. Dus het verhardingsgedrag van steenzout is bij deze lage temperaturen anisotroop (afhankelijk van de opgelegde deformatiegeometrie). Bij temperaturen boven 400-450 °C, dat wil zeggen onder condities waarbij de vervormingsnelheid afhankelijk is van diffusie door het kristalrooster, is het mechanisch gedrag in kompressie en in schuifvervorming vergelijkbaar (isotroop oftewel onafhankelijk van de opgelegde deformatiegeometrie).

Vervolgens wordt beargumenteerd dat het verhardingsgedrag van synthetisch steenzout niet uniek is maar kan afhangen van het aantal en de kombinatie actieve slip-systemen die waarschijnlijk weer bepaald worden door de deformatiegeometrie. Deze koppeling tussen processen is waargenomen in polykristallijn koper (Cu) door Tomé et al. (1984) en kan ook in polykristallijn haliet optreden. Computermodelleringen van de ontwikkeling van kristallografische voorkeursmaaksels hebben aangetoond dat in het algemeen minder slip-systemen nodig zijn om een increment schuifvervorming te accommoderen dan een increment samendrukking, hierdoor treden ook minder dislocatie-interakties op.

Verder zijn de slip-systemen geactiveerd in schuifvervorming minder sterk en daardoor zullen de vloeispanningen in schuifvervorming lager zijn dan in kompressie. Het effect van deze twee processen is het grootst bij temperaturen onder 400 °C als de slip-systemen van haliet sterk uiteenlopende sterktes hebben. Verschillen in activatie-energie tussen de schuifvervorming- en kompressie-vloeiwetten die de vervormingsnelheid als functie van diffusie door dislocatiekernen beschrijven, zijn voorlopig verklaard door verschillen in de dislocatie-netwerken die ontstaan als gevolg van verschillen in aktieve slip-systemen.

Op basis van bovenstaande resultaten is het duidelijk dat de standaard methode om vloeiwetten te extrapoleren naar 3 dimensies niet geldig is voor synthetisch steenzout, waarbij het vervormingsmechanisme gecontroleerd wordt door diffusie door dislocatiekernen. Indien het vervormingsmechanisme afhankelijk is van diffusie door het kristalrooster kan de standaard extrapolatie-methode worden toegepast. In analogie hiermee geldt dat extrapolatie van laboratorium vloeiwetten van andere gesteente vormende mineralen, waarvan de slip-systemen uitlopende sterktes hebben en waarbij het vervormingsmechanisme gecontroleerd wordt door diffusie door dislocatiekernen, met gebruikmaking van de bovenbeschreven standaard methode kan leiden tot misleidende resultaten.

In Hoofdstuk 6 worden algemene conclusies en implicaties met betrekking tot de resultaten van Hoofdstukken 2 - 5 gepresenteerd. Hierin zijn ook suggesties voor aanvullend en verder onderzoek opgenomen.

NAWOORD

Eindelijk. Het is een moeilijke, doch dankbare taak om diegenen te bedanken die een bijdrage hebben geleverd aan het tot stand komen van dit proefschrift.

Allereerst gaat mijn dank uit naar Francine Spiering, wiens bijdrage aan dit proefschrift schier onvoorstelbaar is geweest. Om het kort en bondig te houden: zonder Francine was ik nooit klaargekomen!

Mijn copromotor Chris Spiers heeft een structurele bijdrage geleverd aan het opzetten van het onderzoek. Het overzicht en inzicht van Chris met betrekking tot mijn werk hebben mij keer op keer verbaasd, evenals zijn streven naar perfectie. Zijn bijdragen aan de 'final stages of writing up' zijn zeer wezenlijk geweest. Terugkijkend op meer dan tien jaar werken met Chris wil ik het volgende citaat aanhalen:

> *"The ethos is collegiate: ideas are there to be argued over; information is there to be shared. At its best the system works thus: a journalist proposes an idea for a leader, which is debated, refined and enriched at the editorial conference. Subsequently, a collegue from another section offers unexpected extra material which adds substance to the argument. The journalist writes the piece, a section head improves it and adds zip to the prose, and just before it goes to print someone else catches and corrects the only error.*
>
> *At its worst, it can mean the journalist's idea being strangled at birth by people more articulate and forceful then he is; or, when he has written his piece, his section head disagrees violently and rewrites it so thoroughly as to turn the argument on its head; or a heavy rubber removes every word of which he is proud along with every last trace of individuality."*

Genomen uit The Economist, (1993), Volume 328, number 7827.

Prof. Dr. Stan White was bereid het promotorschap op zich te nemen en mij van advies te dienen, zelfs gedurende zijn verblijf in het buitenland. Daarvoor mijn dank.

Jaren geleden werd met dit promotieonderzoek begonnen onder leiding van Prof. Dr. Henk Zwart. Ik wil Henk bedanken voor de onderzoeksvrijheid die hij me heeft gegund en voor het vertrouwen dat hij in mij heeft gesteld. Niet in de laatste plaats regelde Henk voor mij deelname aan de Texture-Schule van de Deutsche Akademie der Wissenschaften. Diese Winter-Schule war eine äußerst lehrreiche und unvergeßliche Erfahrung, besonders auch auf Grund der Gastfreundschaft von Prof. Dr. P. Bankwitz und Dr. H. Kämpf (beide ehemaliges ZIPE). Ein speziellen Dank an meinen Reisegenossen Prof. Dr. H. Siemes (RWTH Aachen).

Die Texturmessungen wurden von Dr. H.-G. Brokmeier von das GKSS Forschungszentrum in Geesthacht, BRD durchgeführt. Ich möchte mich bei Heinz-Günther bedanken für die gute Zusammen-arbeit und besonders für seine Gastfreundschaft. Die Texturberechnungen wurden von Dr. Michael Dahms (GKSS) durchgeführt. Reisgelden voor een werkbezoek aan het GKSS Forschungszentrum werden beschikbaar gesteld door de Nederlandse Organisatie voor Wetenschappelijk Onderzoek (NWO).

J'aimerais remercier le Prof. Dr. J.P. Poirier et Dr. S. Beauchesne de l'Institut de Physique du Globe de Paris pour m'avoir confié des copies de leurs récents programmes d'inversion, lesquels m'ont permis l'analyse de données de mecanique. Deze programma's werden door Jurriaan Gerretsen geschikt gemaakt voor Apple Macintosh™.

Een speciale dank gaat uit naar Gert Kastelein die in staat is gebleken het 'shear apparaat' te construeren en lopende te houden. Verder werd technische assistentie verleend door Peter van Krieken, Eimert de Graaff en Nelly Slaats (SEM) en Hans Schiet (rasterfotografie). De discussies met ex-mede-promovendi en met Colin Peach, Martyn Drury, Herman van Roermund, Jan Prij, Neville Carter, Hans-Rudolf Wenk, Werner Skrotzki, Alain Molinari en Stephen Cox gedurende verschillende fasen van het onderzoek zijn altijd door mij zeer gewaardeerd.

Magda Martens zorgde voor de papierwinkel die aan een promotie kleeft en ze trad regelmatig op als intermediair zoals alleen zij dat kan! Magda, daarvoor mijn hartelijke dank. Een woord van dank gaat zeker uit naar Ramon Loosveld, Peter Schutjens en Janos Urai die de moed hebben gehad delen van het manuscript te lezen en van commentaar te voorzien. Bas den Brok wordt bedankt omdat hij het hele manuscript heeft doorgewerkt met het doel vragen te verzinnen. Mike Naylor (Shell Research, KSEPL) is acknowledged as an excellent section head. Not in the least because Mike made it possible to hire Bert Janssen to do the graphic design of this thesis.

Tenslotte, tot diegenen die hierboven niet genoemd zijn zou ik willen zeggen:

"Immense have been the preparations for me,
faithful and friendly the arms that have help'd me".

Walt Whitman,
Song of Myself (1881)

Curriculum vitae

20-02-1959	Geboren te Heerlen
19-06-1977	Diploma Atheneum-B, Eijkhagencollege, Schaesberg
06-05-1980	Kandidaatsexamen Geologie, richting G3, Rijksuniversiteit Leiden
02-07-1984	Doctoraal examen Structurele Geologie met Geofysica (seismische methoden) en Materiaalkunde, Universiteit Utrecht
01-08-1984 tot 01-08-1988	Wetenschaplijk assistent Universiteit Utrecht
vanaf 01-02-1989	In dienst bij Koninklijke/Shell Exploratie en Produktie Laboratorium, Rijswijk als 'Research Geologist' bij de sectie 'Structural Geology'